Imperial College London
Department of Mathematics

Theory and computation of the stability of shear flows over compliant boundaries

Avni Chotai

Submitted for the degree of Doctor of Philosophy in Mathematics
February 2023

Declaration of Originality

I certify that this thesis, and the research to which it refers, are the product of my own work, and that any ideas or quotations from the work of other people, published or otherwise, are fully acknowledged in accordance with the standard referencing practices of the discipline.

Copyright Declaration

Acknowledgements

I would like to convey my sincerest gratitude towards my supervisor, Dr Andrew Walton, for his invaluable support and guidance. His enthusiasm has been a great source of inspiration for me. I also truly appreciate his endless patience with all my questions and his willingness to so generously share his time and expertise.

I would also like to acknowledge the EPSRC for financially supporting this research project.

I am deeply grateful to my family for their support in all of my endeavours. I would also like to thank my friends, with a special mention to Office 730/731 for all their useful advice.

Finally, I would like to express my heartfelt appreciation to Keval for his relentless encouragement and unwavering belief in me. He has been of immeasurable help throughout these years.

Abstract

Thread annular injection is a minimally invasive technique that entails transporting medical implants into the body via a thread moving through a fluid. It is desirable for this flow to remain laminar so as to ensure that the flow remains predictable and the thread does not suffer any lateral deviations. It is thus of practical interest to determine the range of Reynolds numbers for which this flow is stable. This flow can be modelled by annular Poiseuille-Couette flow (APCF), which is the flow driven by an axial pressure gradient through the annular region between a stationary outer cylinder and a sliding inner cylinder.

In this thesis, the linear stability properties of APCF to infinitesimal, axisymmetric disturbances are studied when the inner cylinder possesses a degree of flexibility. A cylindrical version of the Orr-Sommerfeld equation is derived with appropriate boundary conditions that encompass the compliance of the cylinder. This forms the foundation of our numerical studies at finite Reynolds numbers. It is found that there exist modes of instabilities that are not present in the case of a rigid inner cylinder.

At large Reynolds numbers, an asymptotic approach is used to gain insights into the different physical balances that give rise to neutrally stable modes. Distinguished scalings are found, including those that have no counterpart for a rigid inner cylinder. These asymptotic results are compared to those from our numerical studies.

The inviscid linear stability of this problem is also studied, and analogues to classical inviscid theorems for planar flow over rigid boundaries are provided.

In the final chapter of this thesis, our stability analysis focuses on vortex-wave interaction for planar Couette flow when the lower wall is modelled as compliant. The nonlinear equations governing this interaction are solved numerically, and finite-amplitude solutions are found.

Contents

List of Figures

Chapter 1

Introduction

A rich field central to fluid dynamics, hydrodynamic stability is concerned with whether a laminar flow is susceptible to the development of instabilities and, if so, how the flow eventually transitions to a turbulent state or a different laminar state [3, 4]. Laminar and turbulent flows exhibit different characteristics. The unsteady, irregular motion of a turbulent flow makes it preferable in certain applications, whilst disadvantageous in others. For example, a turbulent flow is more effective at mixing fluid than a comparable laminar flow [5], as is seen by Reynolds' [6] experiments.

Reynolds [6] performed a series of pioneering experiments that investigated the laminar-turbulent transition of the Hagen-Poiseuille flow through a pipe of circular cross-section. Adding dyed water to clear water flowing through three pipes of different diameters, Reynolds observed that the streak of dyed water extended in a straight line for sufficiently low flow velocities. Increasing the velocity incrementally, the dyed water mixed with the surrounding water. These experiments showed that increasing the dimensionless parameter

$$\frac{Va}{\nu}$$

beyond a critical value led to the breakdown of the laminar flow. Here V is defined to be the maximum velocity of the water in the pipe, a is the pipe radius and ν is the kinematic viscosity of water at the appropriate temperature. This important parameter is now known as the Reynolds number, and is a measure of the ratio of inertial forces to viscous forces in a fluid.

It is worth remarking that Hagen-Poiseuille flow through a circular pipe is known to be linearly stable. Furthermore, experiments have also shown transition in other linearly stable flows; the linear stability of plane Couette flow has been established by Romanov [7], though Tillmark and Alfredson [8] experimentally determine the transitional Reynolds

number to be $R \approx 360$, with R based on the channel half-width and half the velocity difference between the walls.

Experimental results also demonstrate that transition to turbulence for linearly unstable flows often occurs at Reynolds numbers much lower than the critical linear Reynolds number found theoretically for the flow. For example, Orszag [9] used a Chebyshev spectral method to numerically solve the Orr-Sommerfeld equation and determine the linear critical Reynolds number R_c of plane Poiseuille flow to be $R_c = 5772.2$, where the Reynolds number here is based on the channel half-width and centre-stream velocity. Despite this, transition in plane Poiseuille flow has been observed to occur for Reynolds numbers slightly greater than 1000 (Carlson et al. [10]) using the same basis for the Reynolds number.

The linear stability of a laminar flow can be determined by considering the evolution of an infinitesimal disturbance superimposed on the flow. If the disturbance grows in amplitude so that the flow does not return to its original laminar state, the flow is deemed to be linearly unstable. On the other hand, if the flow returns to its original laminar state with respect to every superimposed disturbance, the flow is linearly stable.

1.1 Linear stability of parallel flows

Expressing conservation of momentum and mass laws for a fluid, the Navier-Stokes equations are a set of nonlinear partial differential equations that govern the motion of a viscous flow. Let us consider a Cartesian coordinate system with (x^*, y^*, z^*) measuring distance in the streamwise, normal and spanwise directions, and denote the corresponding flow velocity components as (u^*, v^*, w^*). Let p^* denote the pressure of the flow and t^* denote time. For an incompressible fluid with constant density ρ and kinematic viscosity ν, the Navier-Stokes equations are given by

$$\frac{\partial u^*}{\partial x^*} + \frac{\partial v^*}{\partial y^*} + \frac{\partial w^*}{\partial z^*} = 0, \tag{1.1.1}$$

$$\frac{\partial u^*}{\partial t^*} + u^*\frac{\partial u^*}{\partial x^*} + v^*\frac{\partial u^*}{\partial y^*} + w^*\frac{\partial u^*}{\partial z^*} = -\frac{1}{\rho}\frac{\partial p^*}{\partial x^*} + \nu\left[\frac{\partial^2 u^*}{\partial x^{*2}} + \frac{\partial^2 u^*}{\partial y^{*2}} + \frac{\partial^2 u^*}{\partial z^{*2}}\right], \tag{1.1.2}$$

$$\frac{\partial v^*}{\partial t^*} + u^*\frac{\partial v^*}{\partial x^*} + v^*\frac{\partial v^*}{\partial y^*} + w^*\frac{\partial v^*}{\partial z^*} = -\frac{1}{\rho}\frac{\partial p^*}{\partial y^*} + \nu\left[\frac{\partial^2 v^*}{\partial x^{*2}} + \frac{\partial^2 v^*}{\partial y^{*2}} + \frac{\partial^2 v^*}{\partial z^{*2}}\right], \tag{1.1.3}$$

$$\frac{\partial w^*}{\partial t^*} + u^*\frac{\partial w^*}{\partial x^*} + v^*\frac{\partial w^*}{\partial y^*} + w^*\frac{\partial w^*}{\partial z^*} = -\frac{1}{\rho}\frac{\partial p^*}{\partial z^*} + \nu\left[\frac{\partial^2 w^*}{\partial x^{*2}} + \frac{\partial^2 w^*}{\partial y^{*2}} + \frac{\partial^2 w^*}{\partial z^{*2}}\right], \tag{1.1.4}$$

in the absence of an external body force. These are to be solved subject to appropriate boundary conditions.

Introducing a characteristic length scale L and velocity scale V with which to non-dimensionalise equations (1.1.1), we may write

$$(x^*, y^*, z^*) = L(x, y, z), \qquad (u^*, v^*, w^*) = V(u, v, w), \qquad p^* = \rho V^2 p, \qquad t^* = \frac{L}{V} t. \tag{1.1.5}$$

Substitution of (1.1.5) into (1.1.1) yields the Navier-Stokes equations in the dimensionless form,

$$\frac{\partial u}{\partial x} + \frac{\partial v}{\partial y} + \frac{\partial w}{\partial z} = 0, \tag{1.1.6}$$

$$\frac{\partial u}{\partial t} + u\frac{\partial u}{\partial x} + v\frac{\partial u}{\partial y} + w\frac{\partial u}{\partial z} = -\frac{\partial p}{\partial x} + \frac{1}{R}\left[\frac{\partial^2 u}{\partial x^2} + \frac{\partial^2 u}{\partial y^2} + \frac{\partial^2 u}{\partial z^2}\right], \tag{1.1.7}$$

$$\frac{\partial v}{\partial t} + u\frac{\partial v}{\partial x} + v\frac{\partial v}{\partial y} + w\frac{\partial v}{\partial z} = -\frac{\partial p}{\partial y} + \frac{1}{R}\left[\frac{\partial^2 v}{\partial x^2} + \frac{\partial^2 v}{\partial y^2} + \frac{\partial^2 v}{\partial z^2}\right], \tag{1.1.8}$$

$$\frac{\partial w}{\partial t} + u\frac{\partial w}{\partial x} + v\frac{\partial w}{\partial y} + w\frac{\partial w}{\partial z} = -\frac{\partial p}{\partial z} + \frac{1}{R}\left[\frac{\partial^2 w}{\partial x^2} + \frac{\partial^2 w}{\partial y^2} + \frac{\partial^2 w}{\partial z^2}\right], \tag{1.1.9}$$

where the Reynolds number R has been defined as

$$R = \frac{VL}{\nu}. \tag{1.1.10}$$

We see that R represents the ratio of inertial to viscous forces, as remarked upon earlier.

Assume that the set of equations (1.1.6) admits a steady solution,

$$u = U(x, y, z), \quad v = V(x, y, z), \quad w = W(x, y, z), \quad p = P(x, y, z), \tag{1.1.11}$$

which is known as our base flow. To study the linear stability of this flow, we study the evolution of an infinitesimal disturbance superimposed on (1.1.11). This is a complicated problem; we will make progress by considering a particular class of flows, namely those of the form

$$u = U(y), \quad v = 0, \quad w = 0, \quad p = P(x). \tag{1.1.12}$$

These are called parallel flows.

We consider the linear stability of a two-dimensional parallel shear flow between two plane boundaries at $y = -1$ and $y = 1$, with the basic flow given by (1.1.12). We will assume the two plane boundaries are rigid, so the base flow must satisfy the appropriate no-slip conditions given by

$$U = 0 \quad \text{on} \quad y = \pm 1. \tag{1.1.13}$$

Squire's theorem [11] states that if there exists a growing three-dimensional perturbation in a parallel flow, there exists a two-dimensional perturbation with a higher growth rate.

Furthermore, this two-dimensional perturbation becomes unstable at a lower Reynolds number than its three-dimensional counterpart. This theorem allows us to restrict our attention to two-dimensional perturbations, which simplifies the problem greatly. Perturbing our base flow (1.1.12) with a small amplitude two-dimensional disturbance, the flow velocities are

$$(u, v, w, p) = (U(y), 0, 0, P(x)) + \Delta(\tilde{u}, \tilde{v}, 0, \tilde{p}), \qquad \Delta \ll 1. \tag{1.1.14}$$

We will seek solutions of travelling-wave form, so that

$$\tilde{u} = \hat{u}(y)\mathrm{e}^{\mathrm{i}\alpha(x-ct)} + c.c, \quad v = \hat{v}(y)\mathrm{e}^{\mathrm{i}\alpha(x-ct)} + c.c, \quad p = \hat{p}(y)\mathrm{e}^{\mathrm{i}\alpha(x-ct)} + c.c, \tag{1.1.15}$$

where α is the streamwise wavenumber and c is the wavespeed of the mode. In a temporal stability analysis, α is assumed to be real and c taken to be complex-valued. Writing $c = c_r + \mathrm{i}c_i$, modes with $c_i < 0$ ($c_i > 0$) decay (grow) in time. If there exists a mode with $c_i > 0$, the flow is said to be linearly unstable.

Substituting (1.1.14) and (1.1.15) into (1.1.6) leads us to the linearised disturbance equations

$$\mathrm{i}\alpha\hat{u} + \frac{\mathrm{d}\hat{v}}{\mathrm{d}y} = 0, \tag{1.1.16a}$$

$$\mathrm{i}\alpha\left(U - c\right)\hat{u} + \hat{v}\frac{\mathrm{d}U}{\mathrm{d}y} = -\mathrm{i}\alpha\hat{p} + \frac{1}{R}\left[\frac{\mathrm{d}^2\hat{u}}{\mathrm{d}y^2} - \alpha^2\hat{u}\right], \tag{1.1.16b}$$

$$\mathrm{i}\alpha\left(U - c\right)\hat{v} = -\frac{\mathrm{d}\hat{p}}{\mathrm{d}y} + \frac{1}{R}\left[\frac{\mathrm{d}^2\hat{v}}{\mathrm{d}y^2} - \alpha^2\hat{v}\right]. \tag{1.1.16c}$$

These are to be solved with the no-slip conditions

$$\hat{u} = 0, \quad \hat{v} = 0 \quad \text{on } y = \pm 1. \tag{1.1.17}$$

After manipulation, (1.1.16) leads us to the result known as the Orr-Sommerfeld equation:

$$\left(U - c\right)\left(\frac{\mathrm{d}^2\hat{v}}{\mathrm{d}y^2} - \alpha^2\hat{v}\right) - \frac{\mathrm{d}^2U}{\mathrm{d}y^2}\hat{v} = \frac{1}{\mathrm{i}\alpha R}\left(\frac{\mathrm{d}^4\hat{v}}{\mathrm{d}y^4} - 2\alpha^2\frac{\mathrm{d}^2\hat{v}}{\mathrm{d}y^2} + \alpha^4\hat{v}\right). \tag{1.1.18}$$

A fourth order differential equation, (1.1.18) requires four boundary conditions. Using the continuity equation (1.1.16a) and the boundary conditions (1.1.17), we can formulate the boundary conditions of the Orr-Sommerfeld problem in terms of $\hat{v}$ and its derivative with respect to the wall normal coordinate:

$$\hat{v} = \frac{\mathrm{d}\hat{v}}{\mathrm{d}y} = 0 \quad \text{on } y = \pm 1. \tag{1.1.19}$$

Equations (1.1.18), (1.1.19) pose an eigenvalue equation that encapsulates the linear stability problem for parallel viscous flows. The locus of points in the (R, α) plane where there exists a mode with $c_i = 0$ form neutral stability curves.

1.2 Inviscid linear stability of parallel flows

For many flows of interest, the Reynolds number is large. The majority of the flow can then be modelled as inviscid, with viscous effects being confined to the flow in the vicinity of a boundary. In the limit

$$R \to \infty, \quad \alpha = O(1), \quad c = O(1), \tag{1.2.1}$$

the Orr-Sommerfeld equation (1.1.18) reduces to the Rayleigh equation:

$$(U - c)\left(\frac{\mathrm{d}^2\hat{v}}{\mathrm{d}y^2} - \alpha^2\hat{v}\right) - \frac{\mathrm{d}^2U}{\mathrm{d}y^2}\hat{v} = 0. \tag{1.2.2}$$

This is to satisfy impermeability conditions at the rigid boundaries, so that

$$\hat{v} = 0 \quad \text{on} \quad y = \pm 1. \tag{1.2.3}$$

This equation (1.2.2), introduced by Rayleigh [12], was found prior to the Orr-Sommerfeld equation.

Another early contribution to inviscid linear stability theory is Rayleigh's inflection-point theorem, which necessitates an inflection point in the base velocity profile in order for instability to exist. Fjørtoft's [3] theorem extends this result, providing a stronger condition for instability. Adding to this is Howard's [13] semicircle theorem, which bounds the wavespeeds of unstable modes with a semicircle in the complex c-plane.

For a neutrally stable mode with purely real wavespeed c_r, the Rayleigh equation (1.2.2) has a regular singular point $y = y_c$ where $U''(y_c) \neq 0$ and the base flow is equal to the wavespeed of the perturbation, so that $U(y_c) = c_r$.

Near the critical point $y = y_c$, the method of Frobenius gives two linearly independent solutions to the Rayleigh equation,

$$\hat{v}_1 = (y - y_c) + \cdots, \qquad \hat{v}_2 = 1 + \cdots + \frac{U_c''}{U_c'}\hat{v}_1 \log(y - y_c) + \cdots. \tag{1.2.4}$$

These are known as Tollmien's inviscid solutions ([14], cited in [3]). The second solution $\hat{v}_2$ (1.2.4) contains a logarithmic singularity at the critical point. In order to smooth out

this singularity, viscous effects can be incorporated in a region near the critical point (Lin [15], Stuart [16], Reid [17]). This analysis demonstrates that there is a phase change of magnitude π across this region, which we call a critical layer. If $U'(y_c) > 0$, we are to take

$$\ln(y - y_c) = \ln|y - y_c| \quad \text{for} \quad y > y_c, \tag{1.2.5}$$

$$\ln(y - y_c) = \ln|y - y_c| - \mathrm{i}\pi \quad \text{for} \quad y < y_c. \tag{1.2.6}$$

The critical layer singularity has been treated using other approaches, including the incorporation of nonlinear effects (for example, by Benney and Bergeron [18], and Davis [19]). Haberman [20] links the nonlinear and viscous critical layer theories.

1.3 Vortex-wave interaction

As mentioned earlier, linear stability theory is unable to explain transition for a number of flows, such as plane Couette flow and plane Poiseuille flow. The existence of exact coherent structures plays a key role in understanding transition. These structures include three-dimensional steady state or travelling-wave solutions of the Navier-Stokes equations.

By using a homotopy continuation method to numerically track three-dimensional solutions from Taylor-Couette flow with a narrow gap, Nagata [21] discovered the existence of steady three-dimensional finite-amplitude solutions in plane Couette flow. Other states have been found, including travelling-wave solutions in channel flow [22, 23] and three-dimensional steady states in plane Couette flow [22] by Waleffe.

Waleffe [24] proposed a mechanism for generating these structures in the form of a self-sustaining process. This theory, consisting of three interacting components, was developed through a series of papers, including those of Waleffe, Kim and Hamilton [25], Hamilton, Kim and Waleffe [26] and Waleffe [27]. Rolls in the cross-stream plane induce spanwise fluctuations in the streamwise velocity, leading to the formation of a streak flow. The spanwise inflections of the streak lead to an instability in which three-dimensional travelling waves develop. These waves then interact nonlinearly and reenergise the roll flow. There has since been further success. For example, Faisst and Eckhardt [28] and Wedin and Kerswell [29] followed the continuation technique proposed by Waleffe and obtained travelling-wave solutions in pipe flow.

This theory was established independently for asymptotically large Reynolds numbers, where it is often referred to as vortex-wave interaction. The framework was developed by Hall and Smith [30, 31, 32, 33], Bennett, Hall and Smith [34], Smith and Walton [35], Walton and Smith [36]. In vortex-wave interaction, the streak and roll flow are together referred to as a vortex flow. The wave may be governed by either inviscid or viscous dynamics, the former of which has been studied by Hall and Sherwin [37] in the context of Couette flow. An example of the latter is given by Dempsey and Walton [38] in their study of vortex/Tollmien-Schlichting wave interaction in the asymptotic suction boundary layer. In this thesis, we consider only the viscous wave situation.

1.4 Previous stability studies

The pressure-gradient-driven flow through the annular region formed by two concentric and stationary cylinders, annular Poiseuille flow (APF), can be characterised by the ratio of the radii of the inner cylinder to the outer cylinder, δ. An early study of the stability of concentric APF to infinitesimal, axisymmetric disturbances was conducted by Mott and Joseph [39]. They considered two stationary cylinders, focusing on the effect of the ratio of cylinder radii on linear stability. Their results from finite-difference techniques are presented for $0.3 \lesssim \delta \leq 1$. Mott and Joseph found that the critical Reynolds number increases monotonically with decreasing radius ratio, noting an increased skewing of the base velocity profile towards the inner cylinder as the radius ratio decreases. In the narrow-gap limit for which $\delta \to 1$, they show the critical Reynolds number of APF approaches that of plane Poiseuille flow (PPF).

Extending the work of Mott and Joseph, Mahadevan and Lilley [40] considered also the linear stability of APF to asymmetric disturbances with azimuthal wavenumbers $n = 1, 2$ and 3. For $\delta \lesssim 0.8$, they found that these asymmetric modes were less stable than the axisymmetric mode.

Heaton [41] found that APF is linearly unstable to axisymmetric disturbances for all $0 < \delta \leq 1$ and additionally concluded that asymmetric disturbances (with azimuthal wavenumbers $n = 1, 2$ and 3) become stable at all Reynolds numbers for δ less than critical finite values.

Before we consider the stability properties of this flow when the inner cylinder moves axially, we turn to the case of plane Poiseuille Couette flow (PPCF). The stability of this flow has been studied using asymptotic methods by Potter [42], who found that the superposition of a Couette component on PPF generally has a stabilising effect. In

fact, the flow was found to be linearly stable for all Reynolds numbers when the plate velocity exceeded 70% of the maximum velocity of the Poiseuille component of the flow. Subsequent studies on the stability of PPCF were carried out by Hains [43], Reynolds and Potter [44] and Cowley and Smith [45].

An asymptotic study carried out by Cowley and Smith [45] explored the linear and weakly nonlinear stability of PPCF for various relative sliding velocities. When the relative sliding velocity V is zero, the problem reduces to PPF, for which there exists one linear neutral stability curve [45]. Increasing V soon results in the appearance of two additional neutral curves, one of which disappears when V becomes slightly larger. We are eventually left with no neutral curves once V has been increased beyond a particular cut-off velocity that Cowley and Smith determine through the use of asymptotic methods.

Some years later, Sadeghi and Higgins [46] investigated the linear stability of concentric annular Poiseuille-Couette flow (APCF) to axisymmetric and asymmetric disturbances. For a fixed radius ratio of $\delta = 0.5$, they found that the sliding motion of the inner cylinder had an overall stabilising effect on the flow with respect to the neutral stability curves studied. Their numerical work illustrates that this increase in stability is not necessarily monotonic with the sliding velocity; for example, there are ranges of V in which an increase in sliding velocity is destabilising for the axisymmetric mode. For this choice of radii ratio, Sadeghi and Higgins additionally discovered that there exists a cut-off velocity for each mode studied, that is, a sliding velocity beyond which the mode is completely stabilised. Gittler [47] later illustrated the existence of multiple neutral curves in the (R, α) plane for $\delta = 0.5$ when analysing the linear stability of APCF to axisymmetric disturbances.

More recently, Walton [1] provided a thorough account of the axisymmetric linear stability of APCF. An asymptotic analysis was performed at high Reynolds numbers, the results of which were subsequently compared to numerical finite-Reynolds-number calculations. Obtaining the scalings of Cowley and Smith [45], Walton predicted the existence of multiple regions of instability and discussed the ultimate fate of the neutral modes found. He confirmed the existence of multiple neutral curves for certain choices of δ and V and studied how the neutral stability curves are modified as the inner cylinder sliding velocity is increased. The nonlinear stability of APCF has also been considered. In particular, an asymptotic study at high Reynolds numbers by Walton [48] demonstrates that finite-amplitude asymmetric neutral waves can be supported by basic thread-annular flow.

1.5 Previous stability studies with compliant surfaces

Thread-annular injection is a minimally invasive technique to transport medical implants into the body [48, 49]. With this application in mind, Frei, Lüscher and Wintermantel [49] conducted an experimental study of APCF, where a thread moved axially through a steel pipe. This motivates our work here in exploring the effects of compliance on linear stability.

Motivated by the experiments of Krämer [50], an early investigation on the effect of a flexible wall on the hydrodynamic stability of boundary layer flow was carried out by Benjamin [51]. He found that the Tollmien-Schlichting instability was stabilised by wall compliance, but destabilised by the dissipation in the wall. Benjamin [51, 52] and Landahl [53] categorise disturbances into three classes. Class A disturbances are destabilised by dissipation in the wall, and include the modified Tollmien-Schlichting waves. Conversely, class B waves are stabilised by the dissipation in the wall. Finally, class C are of a Kelvin-Helmholtz-type instability.

Carpenter and Garrad [54, 55] used a different classification, considering two types of instabilities for a passive surface: those which could not exist without viscosity (termed Tollmien-Schlichting type instabilities) and those that depend on the surface flexibility (termed flow-induced surface instabilities). They remark that this distinction may be artificial, particularly as the instabilities arise from the coupled system of the flow and compliant surface. Flow-induced surface instabilities include travelling wave flutter and static divergence [54]. It is possible for some instabilities to interact or coalesce with each other. For example, Carpenter, Gaster and Willis [56] identified modal coalescence between travelling wave flutter and Tollmien-Schlichting instabilities.

In their study, Carpenter and Garrad [54] modelled a Kramer-type compliant surface as spring-backed plate. An elastic plate is supported by an array of springs that rests on a rigid surface. A viscous fluid substrate also backs the plate. This model has been used extensively in various forms [57, 58, 59, 60]. For example, Gajjar and Sibanda [61] use a spring-backed plate model to investigate the stability of channel flow between one rigid wall and one compliant wall at large Reynolds numbers. They find an increase in wall damping to be destabilising on the Tollmien-Schlichting instability.

In this thesis we use a spring-backed plate model, but we note that viscoelastic continuum models for flexibility are used by, among others, Kumaran, Fredrickson and Pincus [62], Kumaran [63], and Shankar and Kumaran [64].

1.6 Thesis summary

The overall aim of this thesis is to develop an understanding of the effects of flexibility on the stability of annular flow. We are interested in exploring new instabilities that arise, in addition to exploring how instabilities of the rigid scenario are modified in the presence of a flexible wall.

In Chapter 2, we formulate the linear stability problem for annular Poiseuille-Couette flow when the inner cylinder is flexible, restricting our attention to axisymmetric disturbances. Using the linearised disturbance equations in cylindrical coordinates, we derive the circular Orr-Sommerfeld equation and its appropriate boundary conditions. Chapter 3 considers this linear stability problem at finite Reynolds numbers. We adopt a numerical approach to find the eigenvalues of the Orr-Sommerfeld equation and determine the stability regions of the flow in the (R, α) plane. Comparisons to the scenario of a rigid cylinder are made. Chapter 4 explores the circular Orr-Sommerfeld equation (pertaining to compliant APCF) in the long-wave limit, with the aim of finding the critical Reynolds number of the neutral curve as $\alpha \to 0$.

Before we move on to investigating the stability of compliant APCF at large Reynolds numbers, we focus on providing inviscid linear stability results in Chapter 5. Influential results due to Rayleigh [12], Fjørtoft [3], Howard [13], Høiland [65] are adapted for an annular flow over a flexible boundary following the methods of Yeo and Dowling [66], Yeo [67], Kumaran [68], and Shankar and Kumaran [69].

Chapters 6-8 study the linear stability of compliant APCF at high Reynolds numbers asymptotically. As in previous chapters, we focus only on axisymmetric disturbances. We use the method of matched asymptotics and a 'maximal interactions' approach to arrive at distinguished scalings for the different structures that arise for neutral modes in the flow. Chapter 9 provides a comparison of our numerical work at finite Reynolds numbers and our asymptotic results at large Reynolds numbers.

In Chapter 10, our focus shifts from compliant APCF to planar Couette flow with a lower flexible boundary. In the earlier chapters of this thesis, we conducted a linear stability analysis and therefore neglected terms that were nonlinear with respect to the disturbances. In this chapter, we determine the size of the disturbance that allows the flow to sustain a vortex-wave interaction at high Reynolds numbers. We formulate the equations that govern this interaction and discuss the numerical methods employed to solve these equations. We will then illustrate the co-existence of two finite-amplitude states with different flow structures.

Chapter 2

Linear stability of annular Poiseuille-Couette flow with a compliant inner cylinder: problem formulation

2.1 Governing equations

We consider an incompressible flow in the annular region between two infinitely long cylinders, where the ratio of radii of the undisturbed inner to outer cylinder is given by δ such that $0 < \delta < 1$. We use asterisks to denote dimensional quantities in what follows. With horizontally orientated cylinders that are concentric, the geometry of this problem naturally lends itself to the use of a cylindrical coordinate system whose axial axis aligns with that of the cylinders; we let x^*, r^* and θ be measured in the axial, radial and azimuthal directions respectively. The dimensional velocity components in these directions are given by u^*, v^* and w^* respectively.

The outer cylinder of radius a^* is rigid, while the inner cylinder possesses a degree of flexibility that we describe using the spring stiffness of its material. We use a spring-backed plate model for the compliant inner cylinder [57, 55], which we allow to flex only radially so as to preserve the axisymmetry of the problem. Additionally, the inner cylinder moves in the axial direction at a constant velocity V^*, maintaining its concentricity with the outer cylinder. Driven by a constant axial pressure gradient $-4g^*$, this incompressible flow of fluid with kinematic viscosity ν^* and constant density ρ^* is subject to no-slip conditions on the outer (inner) wall of the inner (outer) cylinder.

Dimensional time and fluid pressure are measured by t^* and p^* respectively. We neglect the effects of gravity on our flow, and adopt the non-dimensionalisation used by Walton [1]:

$$x^* = a^* x, \quad r^* = a^* r, \tag{2.1.1a}$$

$$u^* = \frac{g^* a^{*2}}{\rho^* \nu^*} u, \quad v^* = \frac{g^* a^{*2}}{\rho^* \nu^*} v, \quad V^* = \frac{g^* a^{*2}}{\rho^* \nu^*} V, \tag{2.1.1b}$$

$$t^* = \frac{\rho^* \nu^*}{g^* a^*} t, \quad p^* = \frac{g^{*2} a^{*4}}{\rho^* \nu^{*2}} p. \tag{2.1.1c}$$

The axisymmetry of this problem makes it reasonable to focus on flows with no azimuthal dependence. We further impose that there is no swirl in the flow, that is, the azimuthal component of our flow velocity is zero. With these simplifications, the unsteady non-dimensional Navier-Stokes and continuity equations that govern our fluid are reduced to

$$\frac{\partial u}{\partial x} + \frac{1}{r}\frac{\partial (rv)}{\partial r} = 0, \tag{2.1.2a}$$

$$\frac{\partial u}{\partial t} + u\frac{\partial u}{\partial x} + v\frac{\partial u}{\partial r} = -\frac{\partial p}{\partial x} + \frac{1}{R}\left[\frac{\partial^2 u}{\partial x^2} + \frac{1}{r}\frac{\partial}{\partial r}\left(r\frac{\partial u}{\partial r}\right)\right], \tag{2.1.2b}$$

$$\frac{\partial v}{\partial t} + u\frac{\partial v}{\partial x} + v\frac{\partial v}{\partial r} = -\frac{\partial p}{\partial r} + \frac{1}{R}\left[\frac{\partial^2 v}{\partial x^2} + \frac{1}{r}\frac{\partial}{\partial r}\left(r\frac{\partial v}{\partial r}\right) - \frac{v}{r^2}\right], \tag{2.1.2c}$$

where the Reynolds number, R, is a dimensionless parameter given by

$$R = \frac{g^* a^{*3}}{\rho^* \nu^{*2}}. \tag{2.1.3}$$

This form of the Reynolds number encapsulates the effects of a change in external axial pressure gradient, and is thus particularly relevant to thread-injection; for example, a decrease in g^* corresponds to an increased significance of the viscous terms in (2.1.2).

The system of partial differential equations (2.1.2) is to be solved in conjunction with no-slip conditions on the cylinder walls. On the outer cylinder, the fluid particles are at rest:

$$u = 0, \quad v = 0 \quad \text{on} \quad r = 1. \tag{2.1.4}$$

It is less straightforward to formulate the boundary conditions on our inner cylinder, which flexes radially and axisymmetrically. The effect of compliance on the cylinder's radial boundary can be expressed as a physical displacement to its unperturbed radius, so we write

$$r_s^*(x^*, t^*) = a^* \delta + \tilde{\eta}^*(x^*, t^*), \tag{2.1.5}$$

where $r_s^*(x, t)$ is the dimensional radial boundary of the inner cylinder and $\tilde{\eta}^*(x^*, t^*)$ represents a small dimensional perturbation in the radial direction.

Letting $\tilde{\eta}^*(x^*, t^*) = a^*\tilde{\eta}(x, t)$, this can be non-dimensionalised as

$$r_s(x, t) = \delta + \tilde{\eta}(x, t). \tag{2.1.6}$$

The flexibility of the cylinder affects only the radial velocity component of particles on the wall, and fluid particles on the cylinder wall must remain on the wall. Therefore we must have

$$u = V, \qquad v = \frac{\partial \tilde{\eta}}{\partial t} + u\frac{\partial \tilde{\eta}}{\partial x} \qquad \text{on} \quad r = r_s, \tag{2.1.7 a, b}$$

where the latter condition is the kinematic condition. Using a spring-backed plate model [54, 57] (see figure 2.1.1), we consider a balance of forces acting on the cylinder wall: the rate of change of momentum is balanced by a resistive force described by Hooke's law and forces due to perturbations in the fluid pressure $\tilde{p}^*$ and viscous shear stress. We neglect forces due to damping and plate tension. We also take the flexural rigidity of the inner cylinder to be zero, in order to maintain the axisymmetry of the problem. The wall motion is then governed by

$$m^*\frac{\partial^2 \tilde{\eta}^*}{\partial t^{*2}} = -\tilde{p}^* + 2\mu^*\frac{\partial \tilde{v}^*}{\partial r^*} - K^*\tilde{\eta}^* \quad \text{on} \quad r^* = r_s^*. \tag{2.1.8}$$

Here, the dimensional quantities m^* and K^* are respectively the mass per unit area and spring constant per unit area. The dynamic viscosity of the fluid μ^* is given by $\rho^*\nu^*$. Using the non-dimensionalisation

$$m^* = \rho^* a^* m, \quad K^* = \frac{\rho^*\nu^{*2}}{a^{*3}}K, \tag{2.1.9}$$

we obtain the non-dimensional dynamic condition

$$m\frac{\partial^2 \tilde{\eta}}{\partial t^2} = -\tilde{p} + \frac{2}{R}\frac{\partial \tilde{v}}{\partial r} - \frac{K}{R^2}\tilde{\eta} \quad \text{on} \quad r = r_s. \tag{2.1.10}$$

We have assumed here that the effect of the base pressure gradient on the displacement of the inner cylinder wall can be ignored. Alternatively, we may assume that body forces have been prescribed in the wall to balance the effect of the pressure gradient [57]. In their study of instabilities in a plane channel flow between compliant walls, Davies and Carpenter [57] explain that these assumptions are required in order to ensure a solution to the fluid/wall equations when the base flow is unperturbed. Like many others, they omit the contribution of the normal viscous stress, which should become negligible at large Reynolds numbers. This contribution is included by Nagata and Cole [58], and is also included in our wall equation (2.1.8) here. However, we do find that the viscous stress can be neglected at leading order in our asymptotic analysis for $R \gg 1$ in the later chapters of this thesis.

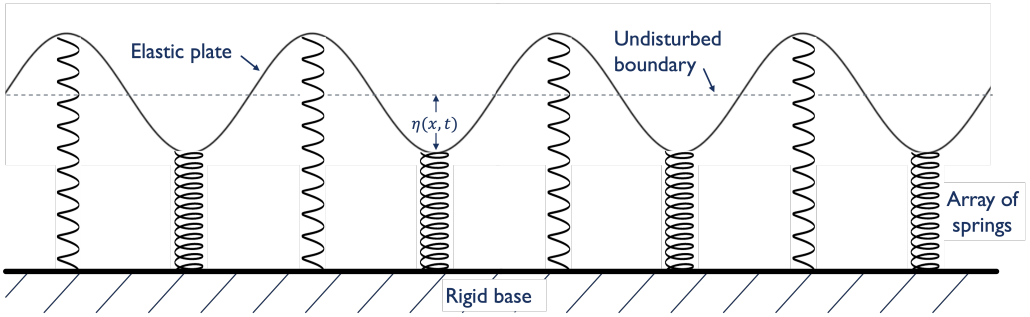

Figure 2.1.1: A depiction of the spring-backed plate model, shown in the planar case for clarity.

2.2 Basic flow

Our base flow is taken to be the steady, axial flow between the two cylinders, $(u, v) = (U_0(r), 0)$. Assumed to be unaffected by the inner cylinder's compliance, the base flow satisfies the no-slip conditions

$$U_0 = 0 \quad \text{on} \quad r = 1, \quad U_0 = V \quad \text{on} \quad r = \delta, \tag{2.2.1}$$

and is given by

$$U_0(r) = 1 - r^2 + \frac{(V - 1 + \delta^2)}{\log \delta} \log r, \quad \delta \leq r \leq 1. \tag{2.2.2}$$

This is an exact solution of the Navier-Stokes equations (2.1.2).

Assuming the pressure constant p_0 is the value of the non-dimensional pressure at $x = 0$, our base pressure $p = P(x)$ is given by

$$P(x) = p_0 - \frac{4x}{R}. \tag{2.2.3}$$

Figure 2.2.1 illustrates the basic velocity profile for various sliding velocities V and radii ratio δ. Before we embark on studying the linear stability of this flow, we close this section by commenting on the maximum value of the base flow. When $V < 1 - \delta^2 + 2\delta^2 \log \delta$, the base flow attains its maximum value in the interior of the flow, say at r_m such that $\delta < r_m < 1$. When $V \geq 1 - \delta^2 + 2\delta^2 \log \delta$, the maximum value of U_0 is achieved on the inner cylinder wall where $U_0 = V$.

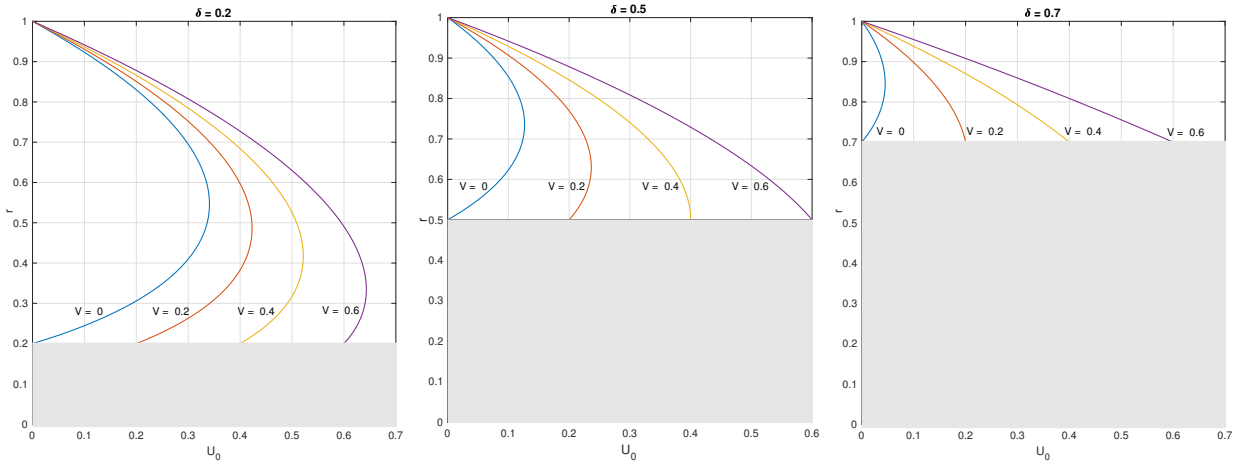

(a) $\delta = 0.2$ (b) $\delta = 0.5$ (c) $\delta = 0.7$

Figure 2.2.1: Depiction of the basic Poiseuille-Couette flow for various sliding velocities V and radii ratio δ.

2.3 Linearised disturbance equations

Our linear stability analysis focuses solely on swirl-free, axisymmetric perturbations of infinitesimal amplitude. To this end, we superimpose our base velocity and pressure field with travelling-wave disturbances of axial wavenumber α and wavespeed c:

$$u = U_0(r) + \Delta\hat{u}(r)\mathrm{e}^{\mathrm{i}\alpha(x-ct)} + c.c, \quad v = \Delta\hat{v}(r)\mathrm{e}^{\mathrm{i}\alpha(x-ct)} + c.c, \tag{2.3.1a}$$

$$p = p_0 - \frac{4x}{R} + \Delta\hat{p}(r)\mathrm{e}^{\mathrm{i}\alpha(x-ct)} + c.c, \tag{2.3.1b}$$

where $\Delta \ll 1$ is a non-dimensional amplitude and $\hat{u}(r), \hat{v}(r), \hat{p}(r)$ are disturbance shape functions. Specifically investigating temporal stability, the wavenumber α and the wavespeed c are assumed to be real and complex respectively.

To study the evolution of these perturbations in time, we substitute (2.3.1) into the non-dimensional Navier-Stokes equations (2.1.2). At order Δ, this yields the linearised disturbance equations

$$\mathrm{i}\alpha\hat{u} + \frac{\mathrm{d}\hat{v}}{\mathrm{d}r} + \frac{\hat{v}}{r} = 0, \tag{2.3.2a}$$

$$\mathrm{i}\alpha\left(U_0 - c\right)\hat{u} + \hat{v}\frac{\mathrm{d}U_0}{\mathrm{d}r} = -\mathrm{i}\alpha\hat{p} + \frac{1}{R}\left[\frac{\mathrm{d}^2\hat{u}}{\mathrm{d}r^2} + \frac{1}{r}\frac{\mathrm{d}\hat{u}}{\mathrm{d}r} - \alpha^2\hat{u}\right], \tag{2.3.2b}$$

$$\mathrm{i}\alpha\left(U_0 - c\right)\hat{v} = -\frac{\mathrm{d}\hat{p}}{\mathrm{d}r} + \frac{1}{R}\left[\frac{\mathrm{d}^2\hat{v}}{\mathrm{d}r^2} + \frac{1}{r}\frac{\mathrm{d}\hat{v}}{\mathrm{d}r} - \frac{\hat{v}}{r^2} - \alpha^2\hat{v}\right]. \tag{2.3.2c}$$

This system is to be paired with a set of linearised boundary conditions.

Conditions (2.1.4) indicate that on the outer cylinder, we must have

$$\hat{u} = 0, \quad \hat{v} = 0 \quad \text{on} \quad r = 1. \tag{2.3.3}$$

Before we linearise conditions (2.1.7), we impose that our perturbation $\tilde{\eta}$ takes the waveform

$$\tilde{\eta}(x,t) = \Delta\hat{\eta}\mathrm{e}^{\mathrm{i}\alpha(x-ct)} + c.c, \tag{2.3.4}$$

so our radial boundary (2.1.6) is now described by

$$r_s(x,t) = \delta + \Delta\hat{\eta}\mathrm{e}^{\mathrm{i}\alpha(x-ct)} + c.c. \tag{2.3.5}$$

We now consider a Taylor expansion of the axial velocity component about $r = \delta$, obtaining

$$u(r_s) = V + \Delta\mathrm{e}^{\mathrm{i}\alpha(x-ct)}\left(\hat{u}(\delta) + \hat{\eta}\frac{\mathrm{d}U_0}{\mathrm{d}r}\bigg|_{r=\delta}\right) + O(\Delta^2). \tag{2.3.6}$$

Since $u\left(r_s\right) = V$ (2.1.7), this indicates that we must have

$$\hat{u}(\delta) + \hat{\eta}U_0'(\delta) = 0. \tag{2.3.7}$$

Primes ($'$) denote derivatives with respect to r. Turning our attention to the kinematic condition (2.1.7b), a Taylor expansion about $r = \delta$ divulges the relation

$$\hat{v}(\delta) = \mathrm{i}\alpha(V - c)\hat{\eta}. \tag{2.3.8}$$

It is convenient to eliminate $\hat{\eta}$ using (2.3.7), and this provides us with our third boundary condition:

$$\mathrm{i}\alpha(V - c)\hat{u}(\delta) + v(\delta)U_0'(\delta) = 0. \tag{2.3.9}$$

In a similar manner to above, we linearise the dynamic condition (2.1.10) and eliminate η to obtain

$$\hat{p}(\delta) = \frac{2}{R}\hat{v}'(\delta) + \left(-\alpha^2c^2m + \frac{K}{R^2}\right)\frac{\hat{u}(\delta)}{U_0'(\delta)}, \qquad V \neq 1 - \delta^2 + 2\delta^2\log\delta. \tag{2.3.10}$$

We impose this restriction on V as this form of the dynamic condition requires that we have $U_0'(\delta) \neq 0$.

In summary, to investigate the linear stability of APCF with a flexible inner cylinder, we seek a solution to the equations (2.3.2) subject to the boundary conditions (2.3.3), (2.3.9), (2.3.10), repeated below for convenience:

$$\mathrm{i}\alpha\hat{u} + \frac{\mathrm{d}\hat{v}}{\mathrm{d}r} + \frac{\hat{v}}{r} = 0, \tag{2.3.11a}$$

$$\mathrm{i}\alpha\left(U_0 - c\right)\hat{u} + \hat{v}\frac{\mathrm{d}U_0}{\mathrm{d}r} = -\mathrm{i}\alpha\hat{p} + \frac{1}{R}\left[\frac{\mathrm{d}^2\hat{u}}{\mathrm{d}r^2} + \frac{1}{r}\frac{\mathrm{d}\hat{u}}{\mathrm{d}r} - \alpha^2\hat{u}\right], \tag{2.3.11b}$$

$$\mathrm{i}\alpha\left(U_0 - c\right)\hat{v} = -\frac{\mathrm{d}\hat{p}}{\mathrm{d}r} + \frac{1}{R}\left[\frac{\mathrm{d}^2\hat{v}}{\mathrm{d}r^2} + \frac{1}{r}\frac{\mathrm{d}\hat{v}}{\mathrm{d}r} - \frac{\hat{v}}{r^2} - \alpha^2\hat{v}\right]. \tag{2.3.11c}$$

subject to

$$\hat{u}(1) = 0, \quad \hat{v}(1) = 0, \tag{2.3.12}$$

$$\mathrm{i}\alpha(V - c)\hat{u}(\delta) + v(\delta)U_0'(\delta) = 0, \tag{2.3.13}$$

$$\hat{p}(\delta) = \frac{2}{R}\hat{v}'(\delta) + \left(-\alpha^2c^2m + \frac{K}{R^2}\right)\frac{\hat{u}(\delta)}{U_0'(\delta)}, \tag{2.3.14}$$

where $V \neq 1 - \delta^2 + 2\delta^2\log\delta$. The base flow U_0 is given by (2.2.2).

If there exists a perturbation with $\mathrm{Im}(c) > 0$, then the perturbation grows in time and our flow is linearly unstable. On the other hand, if all perturbations have $\mathrm{Im}(c) < 0$, all perturbations decay in time and our flow returns to its base state; in this case, we say our flow is linearly stable to axisymmetric disturbances.

At large Reynolds numbers, we analyse the problem asymptotically. This approach makes apparent the physical balances in the flow that give rise to different distinguished scalings for neutral modes. We discuss this in the later chapters of this thesis. Our approach at finite Reynolds numbers hinges on manipulating the system (2.3.11, 2.3.12-2.3.14) to form the cylindrical version of the Orr-Sommerfeld equation, which we describe below.

2.4 Circular Orr-Sommerfeld equation

The linearised disturbance equations (2.3.11) and boundary conditions (2.3.12-2.3.14) result in a generalised eigenvalue problem for the wavespeed c. Introducing the function

$$\phi(r) = r\hat{v}(r), \tag{2.4.1}$$

the continuity equation (2.3.11a) reveals that

$$\phi'(r) = -\mathrm{i}\alpha r\hat{u}(r). \tag{2.4.2}$$

Differentiating the axial momentum equation (2.3.11b) with respect to r and using the radial momentum equation (2.3.11c) to eliminate the pressure disturbance $\hat{p}$, we obtain the following circular version of the Orr-Sommerfeld equation after much manipulation:

$$(U_0 - c)\left(\phi'' - \frac{\phi'}{r} - \alpha^2\phi\right) + \phi\left(\frac{U_0'}{r} - U_0''\right) = \frac{1}{\mathrm{i}\alpha R}\left(\phi^{(4)} - \frac{2\phi^{(3)}}{r} + \left(\frac{3}{r^2} - 2\alpha^2\right)\phi'' + \left(\frac{2\alpha^2}{r} - \frac{3}{r^3}\right)\phi' + \alpha^4\phi\right). \quad (2.4.3)$$

It now remains to pose the boundary conditions with which to solve (2.4.3). Using the forms of $\phi(r)$ (2.4.1) and $\phi'(r)$ (2.4.2), the no-slip conditions on the outer cylinder (2.3.12) reveal

$$\phi(1) = 0, \quad \phi'(1) = 0, \quad (2.4.4)$$

and the kinematic condition (2.3.13) for the inner cylinder gives

$$(c - V)\,\phi'(\delta) + U_0'(\delta)\,\phi(\delta) = 0. \quad (2.4.5)$$

Forming the dynamic condition is less straightforward owing to the presence of the pressure term on the right hand side of (2.3.14). We begin by seeking an expression for $\hat{p}(\delta)$ in terms of $\phi(\delta)$ and higher derivatives. Evaluating the linearised axial momentum equation (2.3.11b) at $r = \delta$, we notice the left hand side of (2.3.11b) is zero as a result of the kinematic condition (2.3.13). We can therefore write

$$\mathrm{i}\alpha\hat{p}(\delta) = \frac{1}{R}\left(\hat{u}''(\delta) + \frac{\hat{u}'(\delta)}{\delta} - \alpha^2\hat{u}(\delta)\right). \quad (2.4.6)$$

Using the expression (2.4.2) to eliminate $\hat{u}$, this reveals

$$\hat{p}(\delta) = \frac{1}{\alpha^2 R}\left(\frac{\phi'''(\delta)}{\delta} - \frac{\phi''(\delta)}{\delta^2} + \frac{\phi'(\delta)}{\delta^3} - \alpha^2\frac{\phi'(\delta)}{\delta}\right). \quad (2.4.7)$$

It will also be helpful to note that differentiation of (2.4.1) gives

$$\hat{v}'(\delta) = \frac{\phi'(\delta)}{\delta} - \frac{\phi(\delta)}{\delta^2}. \quad (2.4.8)$$

The final boundary condition for (2.4.3) now follows from substitution of (2.4.7) into (2.3.14) and use of (2.4.2), (2.4.5), (2.4.8):

$$\left[\frac{2\mathrm{i}\alpha}{R}\left(\frac{3}{2}U_0'(\delta) + \frac{c - V}{\delta}\right) - \left(\frac{K}{R^2} - \alpha^2 c^2 m\right)\right]\phi'(\delta) = \frac{\mathrm{i}U_0'(\delta)}{\alpha R}\left[\phi^{(3)}(\delta) - \frac{\phi''(\delta)}{\delta} + \frac{\phi'(\delta)}{\delta^2}\right]. \quad (2.4.9)$$

The circular Orr-Sommerfeld equation (2.4.3) with boundary conditions (2.4.4, 2.4.5, 2.4.9) is an eigenvalue problem in c that can be solved numerically at various (R, α) combinations. Once we obtain the eigenvalues of the problem for a given pair of R and α, we consider the signs of the imaginary parts of the complex-valued wavespeeds. If a wavespeed has negative imaginary part, the associated mode of disturbance will decay in time. If there exists a wavespeed with positive imaginary part, the associated mode of disturbance will grow in time and the flow is linearly unstable. Finally, a mode with a purely real wavespeed, a so-called neutral mode, propagates with constant amplitude.

This motivates our next chapter, where we solve this Orr-Sommerfeld problem numerically using a Chebyshev collocation method and determine the linear stability regions for the flow in the (R, α) plane.

Chapter 3

Finite-Reynolds-number numerical computations

An early investigation of the effects of wall compliance on the stability of plane Poiseuille flow was carried out by Hains and Price [70]. The walls of the channel were assumed to be stretched flexible membranes with tension and damping. When damping was taken to be zero, flexibility was found to result in the formation of closed neutral stability curves and a reduced region of instability in comparison to the rigid-walled case. The region of instability becomes smaller and eventually disappears entirely as flexibility is increased, though it is noted that the low tension required for complete stability may not be easily attainable in practice. Further work was undertaken by Green and Ellen [71], who display a distorted Tollmien-Schlichting neutral curve joining onto the neutral curve of a higher-wavenumber region of instability. These two sections of the neutral curve exhibit different properties.

Davies and Carpenter [57] model the compliant walls of the channel as spring-backed plates that are constrained to move only in the vertical direction. Motivated by the stabilising effect of wall compliance on Tollmien-Schlichting waves, they focus their attention on symmetric disturbances. For untensioned spring-backed plates with no internal damping, increasing flexibility was found to shrink the neutral curve associated with the Tollmien-Schlichting instability into a closed curve that eventually disappears for sufficiently low values of plate flexural rigidity and spring stiffness. They also identified flow-induced surface instabilities termed divergence and travelling wave flutter. Nagata and Cole [58] supplement this work by considering the stability of plane Poiseuille flow without imposing predefined symmetry on the disturbances. They also use a spring-backed plate model, though include the contribution of viscous stress in their wall equation. In addition to neutral curves for the Tollmien-Schlichting and symmetric

travelling wave flutter modes, Nagata and Cole depict neutral curves for an antisymmetric travelling wave flutter mode. The authors illustrate that the critical Reynolds number of this antisymmetric disturbance can be lower than that of the symmetric disturbances. In the limit $\alpha \to 0$, the critical Reynolds number for the antisymmetric travelling wave flutter mode depends only on the spring stiffness of the walls.

In this chapter, we study the temporal linear stability of compliant annular Poiseuille-Couette flow to axisymmetric disturbances numerically. The linear stability of APCF in the context of two rigid cylinders has been studied extensively by Walton [1, 72], who investigated the effect of the sliding velocity on the stability of the flow both numerically and asymptotically for different cylinder radius ratios. He presents neutral stability curves in the (R, α) plane, finding parameter combinations of δ and nonzero V for which multiple neutral curves coexist. This is a more intricate situation than that of a stationary inner cylinder (APF), for which there exists a unique neutral curve. We anticipate that the introduction of wall compliance complicates the situation further.

3.1 Numerical method

In preparation of our numerical work, we restate for convenience the circular Orr-Sommerfeld problem (2.4.3) and associated boundary conditions (2.4.4, 2.4.5, 2.4.9) formulated in Section 2.4.

With the base flow U_0 (2.2.2) being given by

$$U_0(r) = 1 - r^2 + \frac{(V - 1 + \delta^2)}{\log \delta} \log r, \quad \delta \leq r \leq 1, \tag{3.1.1}$$

we wish to solve the eigenvalue problem

$$\begin{aligned}(U_0 - c)\left(\phi'' - \frac{\phi'}{r} - \alpha^2\phi\right) + \phi\left(\frac{U_0'}{r} - U_0''\right) \\ = \frac{1}{\mathrm{i}\alpha R}\left(\phi^{(4)} - \frac{2\phi^{(3)}}{r} + \left(\frac{3}{r^2} - 2\alpha^2\right)\phi'' + \left(\frac{2\alpha^2}{r} - \frac{3}{r^3}\right)\phi' + \alpha^4\phi\right)\end{aligned} \tag{3.1.2}$$

subject to the boundary conditions

$$\phi(1) = 0, \tag{3.1.3a}$$

$$\phi'(1) = 0, \tag{3.1.3b}$$

$$(c - V)\ \phi'(\delta) + U_0'(\delta)\,\phi(\delta) = 0, \tag{3.1.3c}$$

$$\left[\frac{2\mathrm{i}\alpha}{R}\left(\frac{3}{2}U_0'(\delta) + \frac{c-V}{\delta}\right) - \left(\frac{K}{R^2} - \alpha^2 c^2 m\right)\right]\phi'(\delta) = \frac{\mathrm{i}U_0'(\delta)}{\alpha R}\left[\phi^{(3)}(\delta) - \frac{\phi''(\delta)}{\delta} + \frac{\phi'(\delta)}{\delta^2}\right], \tag{3.1.3d}$$

where m and K are respectively the non-dimensional mass and spring stiffness of the inner cylinder per unit area.

Prompted by the methods of Nagata and Cole [58], we use the kinematic condition (3.1.3c) to reformulate the dynamic condition (3.1.3d) so that it is linear in c, and we write

$$\frac{K}{R^2} - \alpha^2 c^2 m = \frac{K}{R^2} - \alpha^2 c\left(\frac{V\phi'(\delta) - U_0'(\delta)\phi(\delta)}{\phi'(\delta)}\right) m. \tag{3.1.4}$$

A generalised eigenvalue problem for c, the system (3.1.2, 3.1.3a-c, 3.1.4) can be solved numerically by adopting a Chebyshev collocation method. This method is discussed in depth by Schmid and Henningson [4], and we provide a brief description here.

Introducing a linear transformation to map the domain from $r \in [\delta, 1]$ to $\xi \in [-1, 1]$, the function ϕ is approximated as a series of $(N+1)$ Chebyshev polynomials T_n, so that

$$\phi = \sum_{n=0}^{N} a_n T_n(\xi), \quad r = \frac{1}{2}\left[(1+\delta) - (1-\delta)\xi\right], \tag{3.1.5}$$

where $T_n(\xi) = \cos(n\cos^{-1}(\xi))$ and ξ is evaluated at the extrema of the N^{th} Chebyshev polynomial. Known as the Gauss-Lobatto points, these are given by

$$\xi_j = \cos\left(\frac{\pi j}{N}\right), \quad j = 0, ..., N. \tag{3.1.6}$$

After performing a change of variables from r to ξ in the Orr-Sommerfeld equation (3.1.2), we substitute expression (3.1.5) and require that the resulting equation holds at the interior Gauss-Lobatto points $j = 2, ..., N-2$. To supplement this, the four boundary conditions (3.1.3a-c, 3.1.4) are also expressed in Chebyshev form, with the inner and outer cylinders corresponding to $\xi = \xi_0$ and $\xi = \xi_N$ respectively.

This results in a system of $(N+1)$ equations that can be written as an eigenvalue problem

$$\mathbf{A}\mathbf{a} = c\mathbf{B}\mathbf{a}, \qquad \mathbf{a} = (a_0, ..., a_N)^T, \tag{3.1.7}$$

where the eigenvector $\mathbf{a}$ contains the coefficients of the Chebyshev polynomials in (3.1.5). The square matrices $\mathbf{A}$ and $\mathbf{B}$ are of the dimension $(N+1) \times (N+1)$ and depend on α and R, in addition to the cylinder properties δ, V, K and m. The first and last two rows of $\mathbf{A}$ and $\mathbf{B}$ have been chosen to enforce the boundary conditions, while the intermediate rows are used to describe the Orr-Sommerfeld equation at the interior Gauss-Lobatto points. Though this is a natural arrangement for $\mathbf{A}$ and $\mathbf{B}$, it is possible to interchange the rows so that, for example, the boundary conditions occupy the first four rows of the matrices.

The matrix equation (3.1.7) is solved using a QZ algorithm via a built-in MATLAB function. We are particularly interested in the sign of the imaginary part of the wavespeed for various combinations of wavenumber and Reynolds number, recalling that modes with $\mathrm{Im}(c) > 0$ are unstable. Having determined the eigenvalues, we are able to depict the stability regions of the flow in the (R, α) plane, which we will illustrate shortly.

It is also worth mentioning that the form of our matrix equation (3.1.7) hinges on our use of the dynamic condition (3.1.4) that is linear in c. Implementation of our original condition (3.1.3d) would have resulted in a polynomial eigenvalue problem that is more computationally expensive, owing to the presence of the quadratic c^2 term.

3.2 Numerical results

Using the methods outlined above, we illustrate the linear stability features of compliant APCF as we vary properties of the inner cylinder. There exists a copious number of parameter combinations one could explore. For the purposes of this thesis, we choose to display a carefully chosen selection that captures the effect of compliance.

Before continuing, we provide a preliminary check of our methods by comparing our results with those in previous literature. In figure 3.2.1a, we present the neutral stability curve obtained by Walton (see figure 18(a) of [1]) for a rigid inner cylinder with $\delta = 0.55$ and $V = 0$. Figure 3.2.1b depicts the corresponding neutral curve obtained from our computations. The two figures show good agreement. Figure 3.2.1c shows our neutral curve (black solid line) overlaid with data points from Walton's neutral curve (shown in pink asterisks). This was done using a web-based plot digitiser [2]. We remark that the boundary conditions (3.1.3c) and (3.1.3d) were replaced by $\phi(\delta) = 0$ and $\phi'(\delta) = 0$ when running our rigid computations.

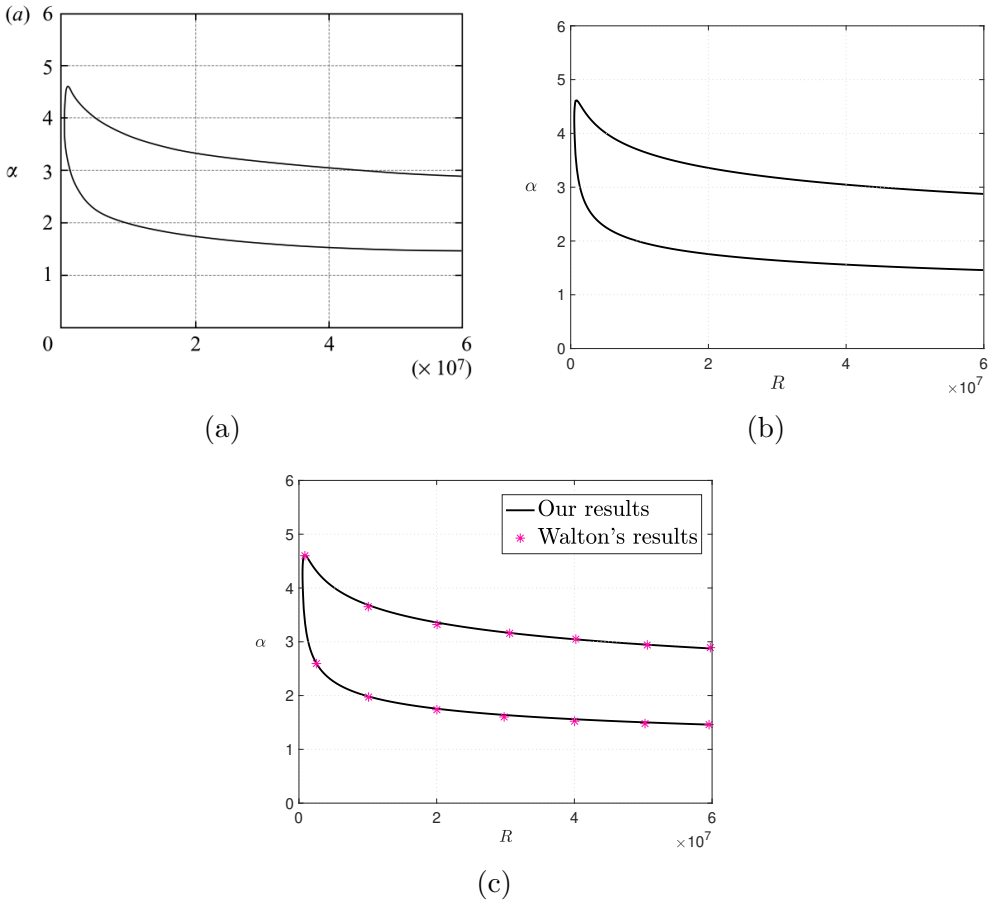

Figure 3.2.1: Neutral stability curve for a rigid inner cylinder with $\delta = 0.55$ and $V = 0$. A comparison between the reprinted results of Walton [1] (figure (a)) and our computations (figure (b)). Figure (c) overlays Walton's results (pink asterisks) onto our results (black line) using a web-based plot digitiser [2].

Varying spring stiffness

In order to determine the effect of flexibility and sliding velocity, we begin by considering the simplest case of a rigid inner cylinder at rest. The shaded area in figure 3.2.2a corresponds to the linearly unstable region of the flow with $\delta = 0.7$. We find exactly one unstable mode in this shaded region. Persisting in the absence of the compliant wall, this mode will be referred to as a flow-based instability.

Figure 3.2.2a shows growth contours of the unstable mode, whilst figure 3.2.2b displays contours of $\mathrm{Re}(c)$ of the unstable mode relative to the maximum value of the base flow. We observe that $\mathrm{Re}(c)$ of the unstable mode becomes larger as we approach the nose of the unstable region, but does not attain the maximum value of the base flow, $\max(U_0)$.

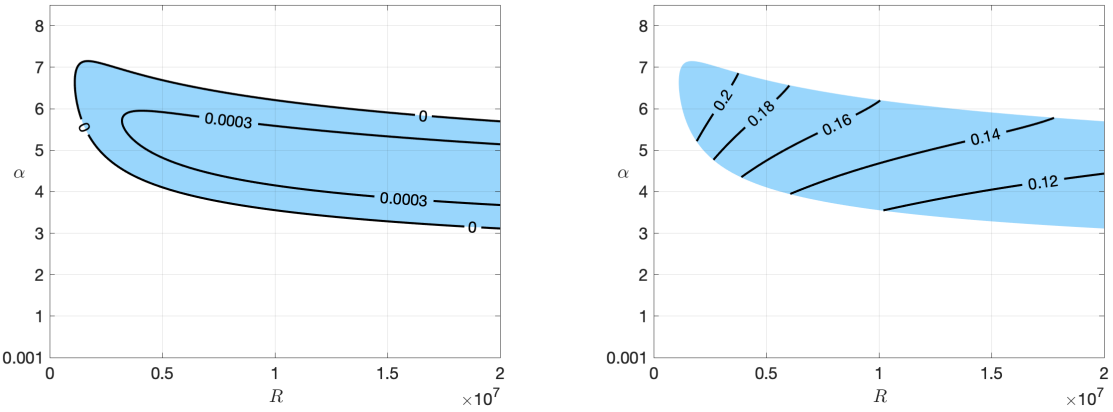

(a) Contours of $\mathrm{Im}(c)$ (b) Contours of $\mathrm{Re}(c)/\max(U_0)$

Figure 3.2.2: Stability properties for the flow with a rigid inner cylinder with $\delta = 0.7, V = 0$.

Figure 3.2.3 explores the effect of the inner cylinder's spring stiffness by considering a stationary inner cylinder with radius ratio $\delta = 0.7$ and mass $m = 0.1$. We focus on four spring stiffness values ($K = 5 \times 10^{11}$, $K = 1 \times 10^{11}$, $K = 5 \times 10^{9}$, $K = 5 \times 10^{8}$) and note that a lower spring stiffness indicates a more flexible cylinder. We remark that our choices of K are larger than those typically used by other authors. We choose these values so that we can see how the linear instabilities of the rigid case are modified as flexibility is increased.

The stability region plots shown in figure 3.2.3 reveal the number of unstable modes present for each (R, α) combination. The shaded regions correspond to the flexible case, whilst the dashed grey curves represent the neutral curve of the rigid case. Regions shaded in blue contain one linearly unstable mode, whilst red regions indicate the presence of two unstable modes. For the range of Reynolds numbers depicted, comparison with the dashed curve reveals that the band of unstable wavenumbers associated with the flow-based mode of figure 3.2.2 sinks lower as the spring stiffness decreases to $K \approx 5 \times 10^{9}$. As K decreases further, this effect becomes more localised to nearer the nose of the unstable region, which exists at a lower Reynolds number than its rigid counterpart. Note the range of Reynolds numbers illustrated is much smaller in figures 3.2.3d and 3.2.3e, and the figure corresponding to $K = 5 \times 10^{9}$ has been repeated for ease of comparison.

It is apparent that the flexibility of the cylinder has resulted in the emergence of a second instability, which has a much broader band of unstable wavenumbers than the modified flow-based mode. As the cylinder becomes more flexible, this instability materialises from the $\alpha = 0$ axis at lower Reynolds numbers, and also eventually engulfs the modified flow-based mode.

To provide a more complete picture of the nature of these instabilities, we supplement figure 3.2.3 with illustrations of the strength of the instabilities (figure 3.2.4) and illustrations of the real part of the wavespeed of instabilities (figure 3.2.5). Where there are two unstable modes, the contour pertains to the most unstable mode.

There is a stark contrast in the real parts of the wavespeed of the most unstable compliance-related and flow-based modes, which can be seen by the discontinuity in figures 3.2.5a and 3.2.5b. These discontinuities make apparent where strongest instability switches from being flow-based to compliance-related. Whilst there is a small region where the flow-based mode is more unstable for $K = 5 \times 10^{11}$ (figure 3.2.5a) and $K = 1 \times 10^{11}$ (figure 3.2.5b), generally the compliance-related mode attains much higher growth rates, as seen in figures 3.2.4a and 3.2.4b. In the region depicted, the compliance-related mode also has a much larger $\mathrm{Re}(c)$ than the flow-based mode and, in particular, achieves values greater than the maximum of the base flow.

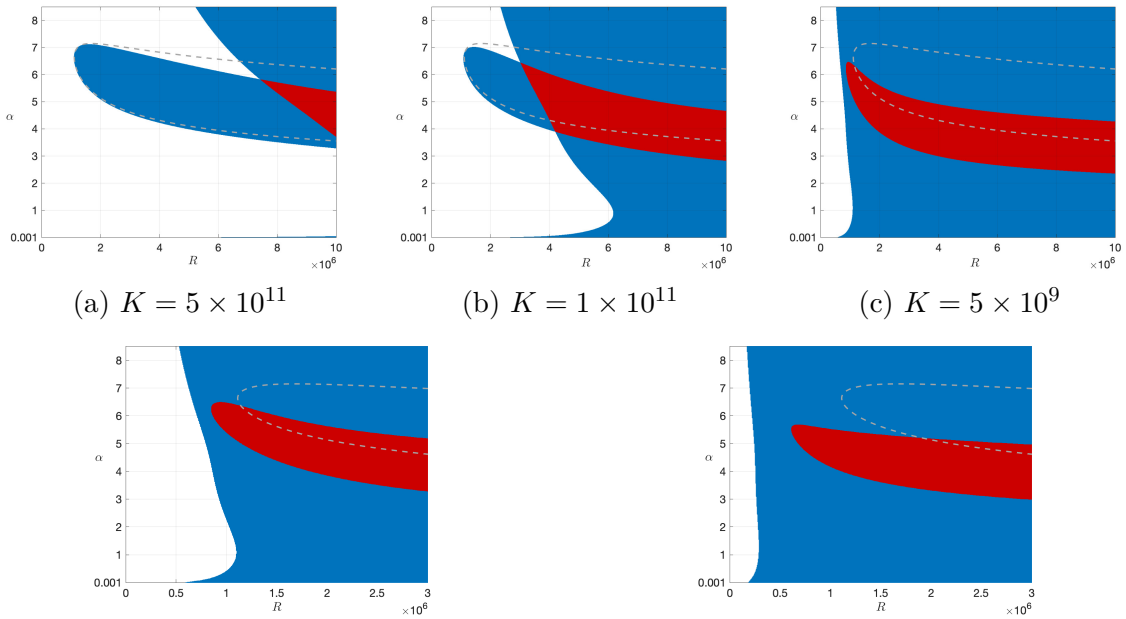

(a) $K = 5 \times 10^{11}$ (b) $K = 1 \times 10^{11}$ (c) $K = 5 \times 10^{9}$

(d) $K = 5 \times 10^{9}$ (repeated) (e) $K = 5 \times 10^{8}$

Figure 3.2.3: Shaded areas display the stability regions for $\delta = 0.7$, $V = 0$, $m = 0.1$, and varying K. Plots (d) and (e) depict a smaller range of Reynolds numbers than (a)-(c). Grey dashed curves depict the neutral curves of the rigid cases. Red regions contain two unstable modes, while blue regions contain only one unstable mode.

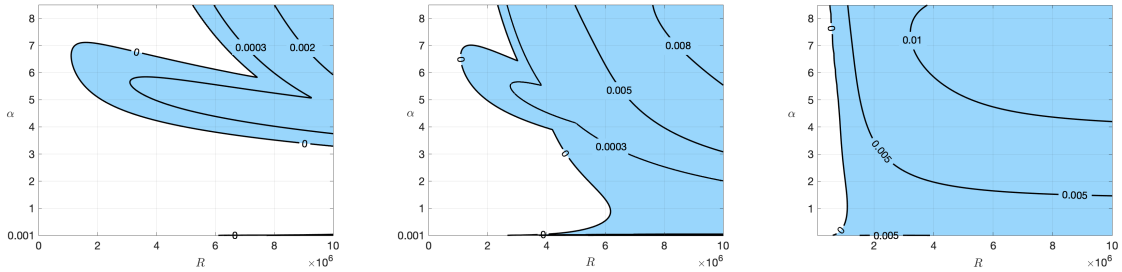

(a) $K = 5 \times 10^{11}$ (b) $K = 1 \times 10^{11}$ (c) $K = 5 \times 10^{9}$

Figure 3.2.4: Shaded areas display the stability regions for $\delta = 0.7$, $V = 0$, $m = 0.1$, and varying K. Black curves display contours of $\mathrm{Im}(c)$.

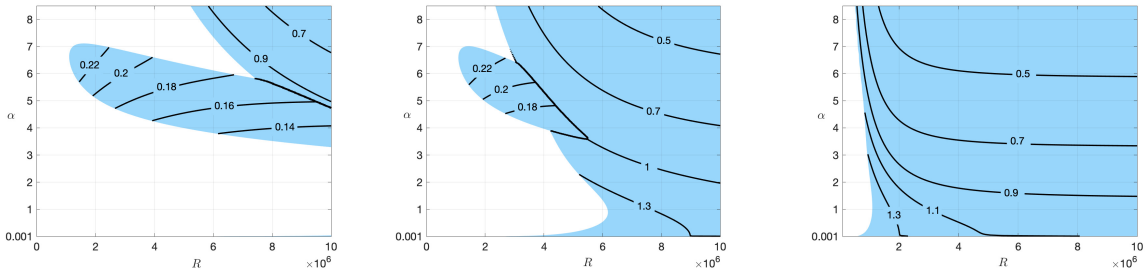

(a) $K = 5 \times 10^{11}$ (b) $K = 1 \times 10^{11}$ (c) $K = 5 \times 10^{9}$

Figure 3.2.5: Shaded areas display the stability regions for $\delta = 0.7$, $V = 0$, $m = 0.1$, and varying K. Black curves display contours of $\mathrm{Re}(c)/\max(U_0)$.

Varying mass

Thus far, we have explored the stability properties of a stationary cylinder with fixed mass $m = 0.1$. Figures 3.2.6, 3.2.7 and 3.2.8 illustrate the effect of increasing the cylinder mass when $\delta = 0.7$, $V = 0$ and $K = 5 \times 10^{11}$, with the scale of the Reynolds number on these plots being larger than on figure 3.2.3. As shown in figure 3.2.6, an increase in mass causes the upper branch of the flow-based mode to sink to lower values of α. The nose of the flow-based mode aligns with that of the rigid neutral curve for each of the masses considered. Though the compliance-related instability extends to lower Reynolds numbers as the mass increases, we notice that the critical Reynolds number R_c in the long-wave limit appears to be largely unaffected by a change in mass and remains at $R_c \approx 5.95 \times 10^6$. We explore this analytically in Chapter 4. This behaviour is reminiscent of the findings of Nagata and Cole [58], who noted the antisymmetric travelling wave flutter mode depended only on spring stiffness in the limit $\alpha \to 0$ in the case of plane Poiseuille flow between two compliant walls.

In figure 3.2.7, we see that the change in mass causes a distortion in the shape of the stability contours of the most unstable mode. Further, despite the depicted region of instability becoming larger as the mass is increased, the strength of instability has weakened for many (R, α) combinations.

The influence of mass is also seen through $\mathrm{Re}(c)$ of the most unstable mode (see figure 3.2.8). At large Reynolds number and large wavenumber in the regions depicted, $\mathrm{Re}(c)$ decreases as the mass becomes larger. Despite the surprising shape of the contour corresponding to $^{\mathrm{Re}(c)}/_{\max(U_0)} = 0.15$ when $m = 2$ (see figure 3.2.8c), we note that the analogous contour does not occur in the regions depicted for $m = 0.1$ and $m = 0.5$. It is therefore not possible to comment on whether the specific contour has been deformed due to the increase in mass, or has simply shifted into the depicted region.

From the discontinuity in $\mathrm{Re}(c)$, which is where the most unstable mode transitions from being the flow-based mode to the compliance-related mode, we also observe that the region in which the flow-based mode dominates becomes smaller with an increase in mass.

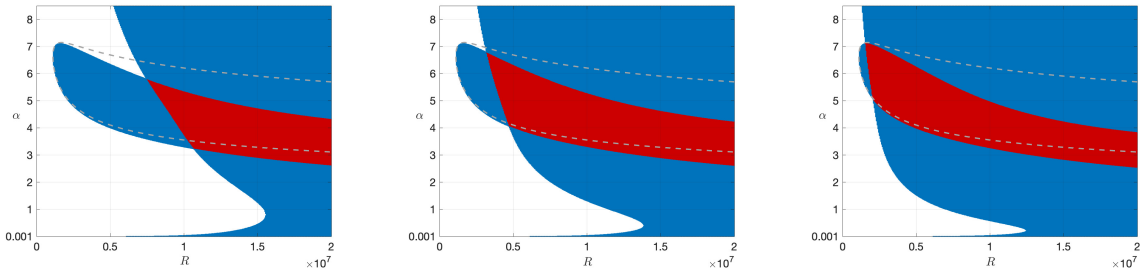

(a) $m = 0.1$ (b) $m = 0.5$ (c) $m = 2$

Figure 3.2.6: Stability regions for the case $\delta = 0.7$, $V = 0$, $K = 5 \times 10^{11}$ with mass (a) $m = 0.1$, (b) $m = 0.5$, (c) $m = 2$. Grey dashed curves depict the neutral curves of the rigid cases. Red regions contain two unstable modes, while blue regions contain only one unstable mode.

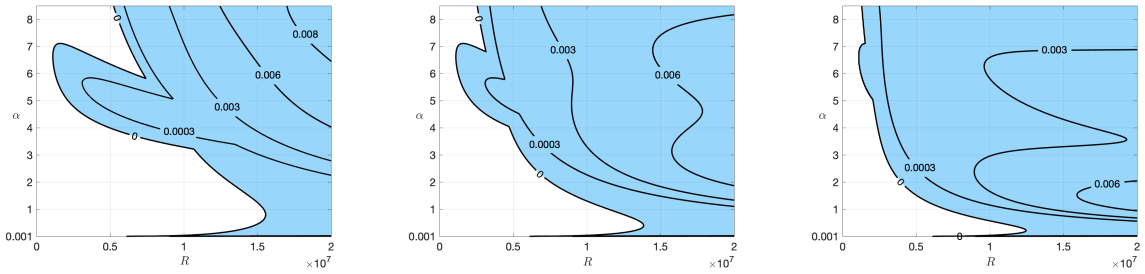

(a) $m = 0.1$ (b) $m = 0.5$ (c) $m = 2$

Figure 3.2.7: Contours of $\mathrm{Im}(c)$ in regions of instability for the case $\delta = 0.7$, $V = 0$, $K = 5 \times 10^{11}$ with mass (a) $m = 0.1$, (b) $m = 0.5$, (c) $m = 2$.

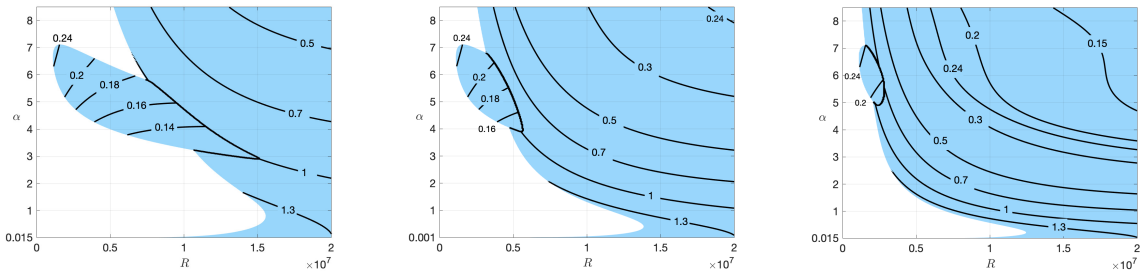

(a) $m = 0.1$ (b) $m = 0.5$ (c) $m = 2$

Figure 3.2.8: Contours of $\mathrm{Re}(c)/\max(U_0)$ in regions of instability for the case $\delta = 0.7$, $V = 0$, $K = 5 \times 10^{11}$ with mass (a) $m = 0.1$, (b) $m = 0.5$, (c) $m = 2$.

Varying sliding velocity

The effect of the sliding velocity on the stability properties for a rigid inner cylinder with $\delta = 0.55$ was studied extensively by Walton [1], and we briefly recount the results here. There exists a single neutral curve when $V = 0$. As V is increased slightly, this curve is sliced from right to left by a stable intrusion forming two distinct neutral curves (see the dashed curve in figure 3.2.9b). Increasing V further, the top curve becomes thinner and closes at finite R. Eventually, at a slightly higher V, the top curve disappears entirely. V is eventually increased to a particular 'cut-off' velocity where the lower curve retreats to infinity. Beyond this cut-off velocity, the flow is linearly stable for all Reynolds numbers.

In figure 3.2.9, the grey dashed curves represent neutral curves of the rigid case. Where we have chosen the same sliding velocities as Walton [1], our curves show good agreement with his results.

Now we explore the effect of varying the sliding velocity of a flexible cylinder. Similar to the rigid case, the modified flow-based mode is sliced from right to left (figure 3.2.9b) and eventually splits into two distinct closed regions (figure 3.2.9c). By $V = 0.01$, the upper region has entirely disappeared, though its rigid counterpart still exists at this sliding velocity. Increasing the velocity to $V = 0.03$, the lower region shrinks and we observe that an additional two modes of instability have emerged (see figures 3.2.9e, 3.2.9f). These modes do not seem to have rigid counterparts. Though we are not completely confident in the resolution of the stability regions beyond $R = 4 \times 10^7$, our asymptotic analysis in later chapters leads us to believe that the mode (shown in red) in the upper right corner of figure 3.2.9f exists.

Through this progression from $V = 0$ to $V = 0.03$, the stability region of the compliance-related instability already present in figure 3.2.9a when $V = 0$ seems to have remained unchanged.

Before exploring the strength of the unstable region, we make a few comments on the differences between the rigid and compliant cases. The upper region of the modified flow-based mode in the compliant case disappears at a lower velocity value than its analogue in the rigid case. Furthermore, as V is increased in the compliant case, the lower region does not retreat to infinity, but instead closes up and shrinks at finite Reynolds numbers before disappearing entirely. The main difference, however, lies in the number of unstable modes present; in total, we observe the existence of three compliance-related instabilities in the flow. Though we notice two of these additional instabilities only as V is increased, it is important to note that these figures do not allow us to rule out their presence for smaller values of V, or even $V = 0$. They may exist in a region of the (R, α) plane not shown here.

In figures 3.2.10 and 3.2.11 respectively, the contours of $\mathrm{Im}(c)$ and $\mathrm{Re}(c)/\max(U_0)$ of the (most) unstable compliance-related mode seem largely unchanged with an increase in V. We do note, though, that the depicted region for $V = 0.03$ attains a stronger instability than the regions for smaller V.

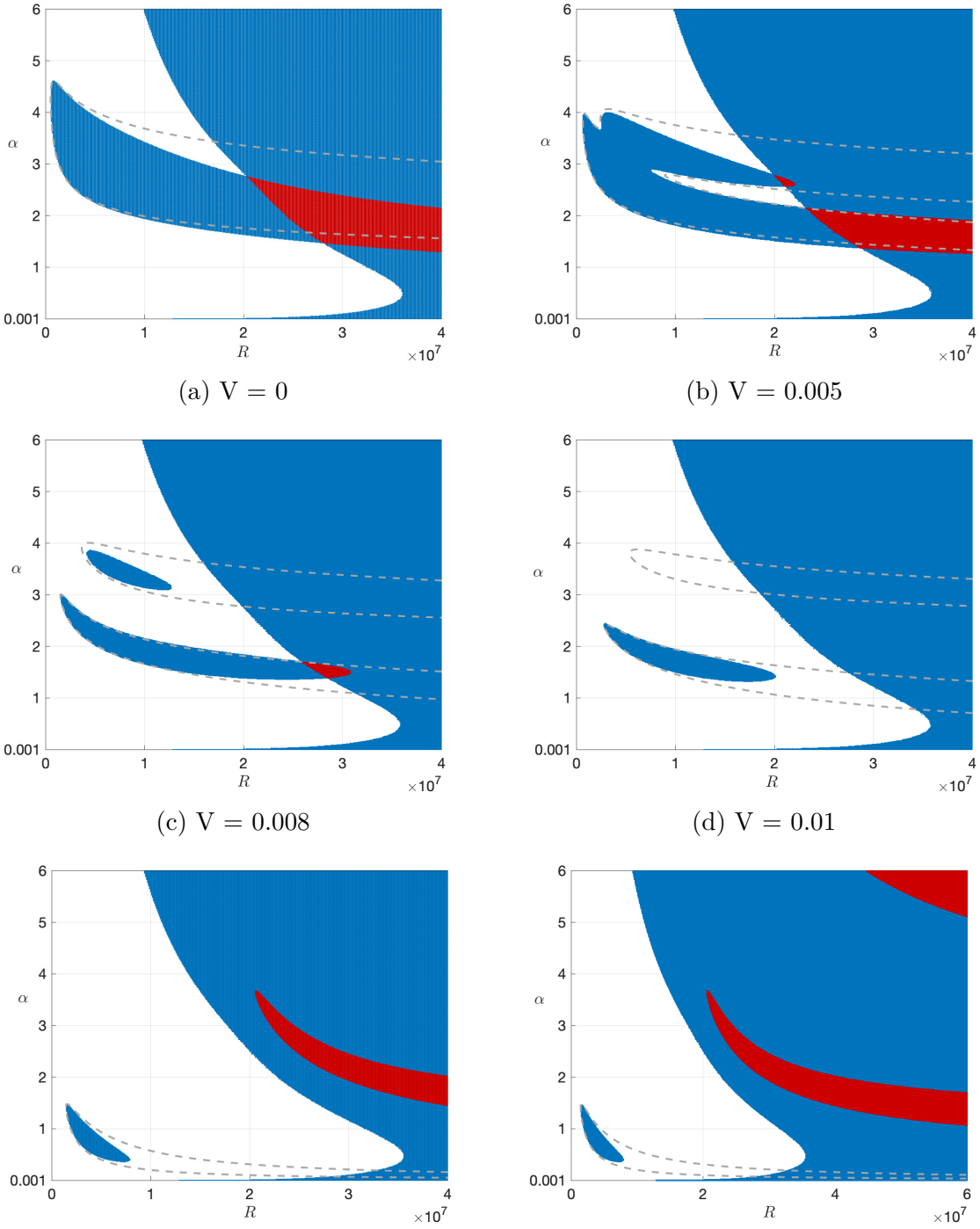

(a) V = 0

(b) V = 0.005

(c) V = 0.008

(d) V = 0.01

(e) V = 0.03

(f) $V = 0.03$ (repeated)*

Figure 3.2.9: Stability regions for the case $\delta = 0.55$, $K = 5 \times 10^{12}$, $m = 0.1$ with sliding velocity (a) $V = 0$, (b) $V = 0.005$, (c) $V = 0.008$, (d) $V = 0.01$, (e) $V = 0.03$ and (f) $V = 0.03$ (repeated). Grey dashed curves depict the neutral curves of the rigid cases. Red regions contain two unstable modes, while blue regions contain only one unstable mode. *We illustrate the stability regions for $V = 0.03$ over a larger range of Reynolds numbers. We are less confident in the resolution of the stability regions beyond $R = 4 \times 10^7$, but we choose to include this figure so as to showcase the emergence of a new mode in the top right corner of the figure.

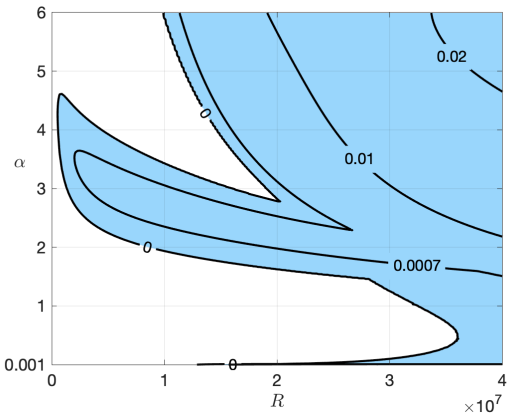

(a) V = 0

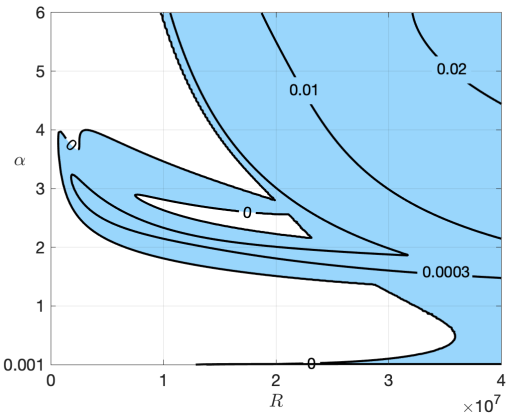

(b) V = 0.005

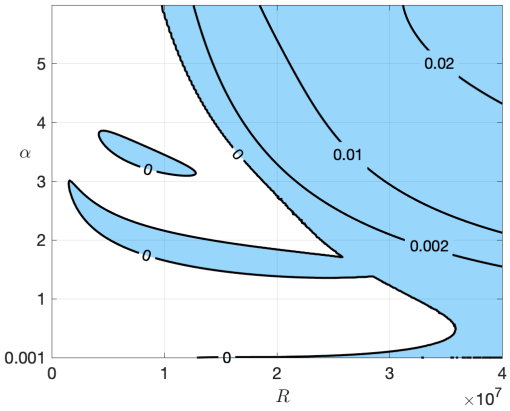

(c) V = 0.008

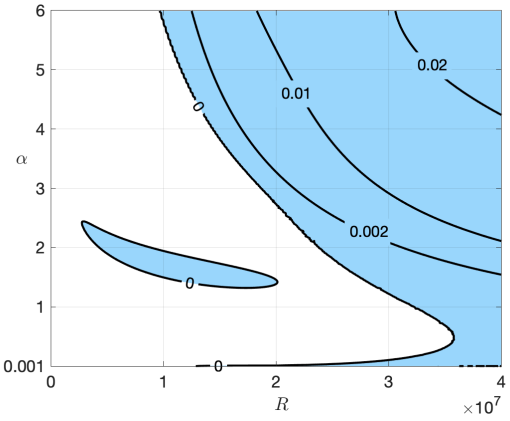

(d) V = 0.01

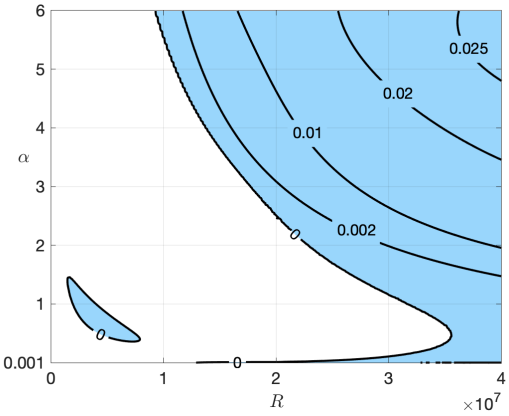

(e) V = 0.03

Figure 3.2.10: Contours of Im(c) in regions of instability for the case $\delta = 0.55$, $K = 5 \times 10^{12}$, $m = 0.1$ with sliding velocity (a) $V = 0$, (b) $V = 0.005$, (c) $V = 0.008$, (d) $V = 0.01$ and (e) $V = 0.03$.

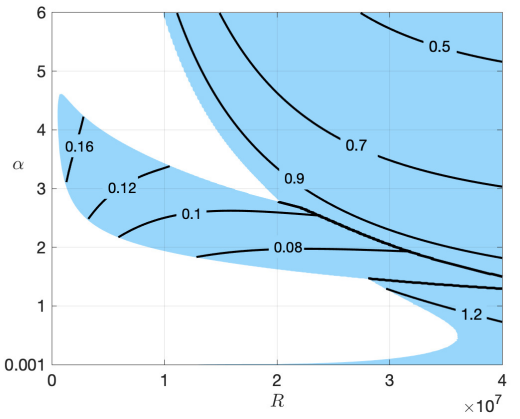

(a) V = 0

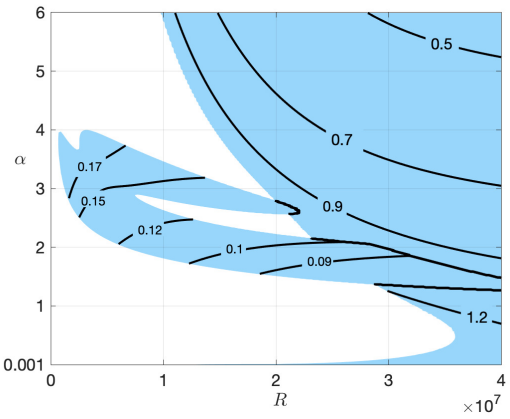

(b) V = 0.005

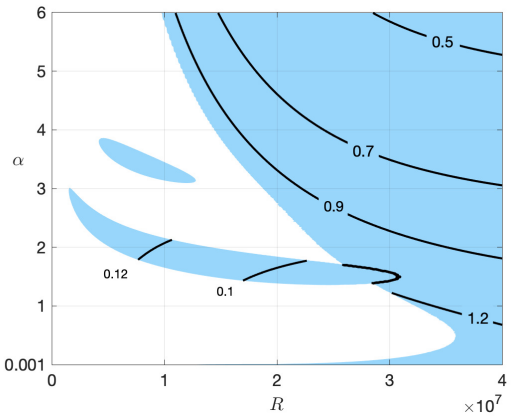

(c) V = 0.008

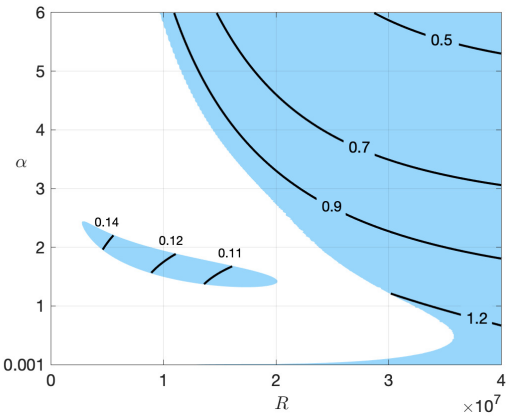

(d) V = 0.01

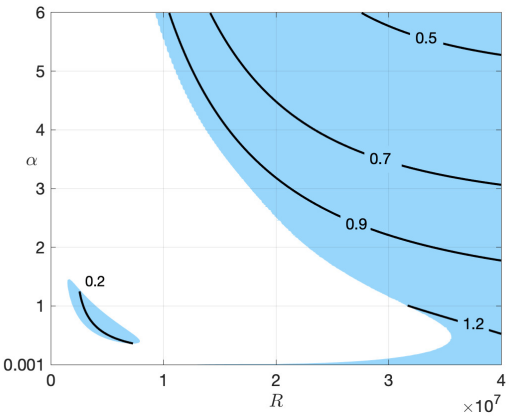

(e) V = 0.03

Figure 3.2.11: Contours of $\mathrm{Re}(c)/\max(U_0)$ in regions of instability for the case $\delta = 0.55$, $K = 5\times10^{12}$, $m = 0.1$ with sliding velocity (a) $V = 0$, (b) $V = 0.005$, (c) $V = 0.008$, (d) $V = 0.01$ and (e) $V = 0.03$.

3.3 Summary

To summarise, the aim of this chapter has been to study the effect of compliance on the linear stability of APCF at finite Reynolds numbers. To this end, we solved the circular Orr-Sommerfeld problem (3.1.2) using a Chebyshev collocation method and plotted regions of instability in the (R, α) plane.

For a rigid inner cylinder that is stationary and has $\delta = 0.7$, we find exactly one unstable mode for any given (R, α) combination inside the unstable region depicted in figure 3.2.2. We refer to this as a flow-based instability. When the inner cylinder possesses a degree of flexibility, we notice the existence of a so-called compliance-related mode of instability in addition to the now modified flow-based instability. As flexibility is increased, the critical Reynolds number of this compliance-related mode in the limit $\alpha \to 0$ is found to decrease, and the band of unstable wavenumbers pertaining to the flow-based mode becomes thinner.

The stability region diagrams become more complicated as we allow the inner cylinder to move axially with a strictly positive sliding velocity V (see figure 3.2.9). We see the appearance of additional compliance-related instabilities as V is increased, though we acknowledge that we have not determined whether these additional instabilities exist at smaller values of V (or even $V = 0$) outside of the (R, α) region shown.

Having now explored the linear stability problem of compliant APCF numerically, we seek to gain further insight into the stability properties of the flow through the use of analytic techniques. We recall that the critical Reynolds number in the limit $\alpha \to 0$ seems to be unaffected by the mass of the inner cylinder (see figure 3.2.6), and expect that an examination of the Orr-Sommerfeld problem (3.1.2, 3.1.3) in the long-wave limit also elucidates this behaviour.

Chapter 4

The Orr-Sommerfeld equation in the long-wave limit

To gain a more comprehensive understanding of the stability regions obtained in Chapter 3, it is useful to explore properties of the neutral curve that can be deduced analytically. We are particularly motivated by the set of figures 3.2.6, where the critical Reynolds number of the compliance-related mode along $\alpha = 0$ seems unaffected by the mass of the inner cylinder. Aiming to corroborate our numerical findings, we seek an analytical expression for the critical Reynolds number in the long-wave limit, $\alpha \to 0$.

To this end, in this chapter we study the Orr-Sommerfeld equation at finite Reynolds number with $\phi = O(1)$ as $\alpha \to 0$. The sliding velocity V, spring stiffness K and mass m of the inner cylinder are taken to be order one quantities. Focusing on the neutral curve, we seek a solution for modes with $\mathrm{Im}(c) = 0$. We recall that, as an eigenfunction, ϕ is defined up to some normalisation. We may therefore impose the normalisation condition $\phi(\delta) = 1$ without loss of generality.

Before continuing, we restate the circular Orr-Sommerfeld equation (2.4.3) and its associated boundary conditions (2.4.4, 2.4.5, 2.4.9) here for convenience:

$$(U_0 - c)\left(\phi'' - \frac{\phi'}{r} - \alpha^2\phi\right) + \phi\left(\frac{U_0'}{r} - U_0''\right) = \frac{1}{\mathrm{i}\alpha R}\left(\phi^{(4)} - \frac{2\phi^{(3)}}{r} + \left(\frac{3}{r^2} - 2\alpha^2\right)\phi'' + \left(\frac{2\alpha^2}{r} - \frac{3}{r^3}\right)\phi' + \alpha^4\phi\right), \quad (4.0.1)$$

subject to the boundary conditions

$$\phi(1) = 0, \tag{4.0.2a}$$

$$\phi'(1) = 0, \tag{4.0.2b}$$

$$(c - V)\ \phi'(\delta) + U_0'(\delta)\,\phi(\delta) = 0, \tag{4.0.2c}$$

$$\left[\frac{2\mathrm{i}\alpha}{R}\left(\frac{3}{2}U_0'(\delta) + \frac{c-V}{\delta}\right) - \left(\frac{K}{R^2} - \alpha^2 c^2 m\right)\right]\phi'(\delta) = \frac{\mathrm{i}U_0'(\delta)}{\alpha R}\left[\phi^{(3)}(\delta) - \frac{\phi''(\delta)}{\delta} + \frac{\phi'(\delta)}{\delta^2}\right], \tag{4.0.2d}$$

where V is chosen so that $U_0'(\delta) \neq 0$. Primes ($'$) denote differentiation with respect to r. The base flow U_0 (2.2.2) is given by

$$U_0(r) = 1 - r^2 + \frac{(V - 1 + \delta^2)}{\log\delta}\ \log r, \quad \delta \leq r \leq 1. \tag{4.0.3}$$

Expanding

$$R = R_0 + \cdots, \qquad \phi = \phi_0 + \alpha R_0\,\phi_1 + \cdots, \tag{4.0.4}$$

the Orr-Sommerfeld equation (4.0.1) suggests the leading order balance

$$\phi_0'''' - \frac{2}{r}\phi_0''' + \frac{3}{r^2}\phi_0'' - \frac{3}{r^3}\phi_0' = 0. \tag{4.0.5}$$

As a fourth-order differential equation, this requires four boundary conditions in order to solve for ϕ_0. The boundary conditions (4.0.2a), (4.0.2b), (4.0.2d) give

$$\phi_0(1) = 0, \qquad \phi_0'(1) = 0, \qquad \phi_0'''(\delta) - \frac{\phi_0''(\delta)}{\delta} + \frac{\phi_0'(\delta)}{\delta^2} = 0. \tag{4.0.6}$$

For the fourth condition, we invoke the normalisation condition to yield

$$\phi_0(\delta) = 1. \tag{4.0.7}$$

This allows us to uniquely determine ϕ_0 as

$$\phi_0 = \frac{r^2(2\log r - 1) + 1}{\delta^2(2\log\delta - 1) + 1}, \tag{4.0.8}$$

which we notice is independent of V, K and m. Writing

$$c = c_0 + \alpha c_1 + \cdots, \tag{4.0.9}$$

and substituting (4.0.7) into the kinematic condition (4.0.2c) reveals

$$(c_0 - V)\phi_0'(\delta) + U_0'(\delta) = 0, \tag{4.0.10}$$

which, upon use of (4.0.8), gives

$$c_0 = \frac{(1-\delta^2+2\delta^2\log\delta)^2 - V(1-\delta^2+2\delta^2\log\delta) + 4V(\delta\log\delta)^2}{4(\delta\log\delta)^2}. \tag{4.0.11}$$

This expression reveals that the leading order wavespeed of the neutral mode is unaffected by the mass and stiffness of the inner cylinder, but does in fact depend on the sliding velocity. Recalling that the sliding velocity is chosen such that $U_0'(\delta) \neq 0$, the condition (4.0.10) requires that $c_0 \neq V$. Repeated application of L'Hôpital's rule on (4.0.11) allows us to determine the limiting behaviour of c_0 with respect to δ. In the narrow-gap limit $\delta \to 1$, we see that $c_0 \to \frac{V}{2}$. As $\delta \to 0$, we have $c_0 \to +\infty$ for $V < 1$, whilst $c_0 \to -\infty$ for $V > 1$. We will later see that choosing $V = 1$ does not admit any solutions to our problem in the limit $\delta \to 0$.

At order α, substitution of (4.0.4) into the Orr-Sommerfeld equation (4.0.1) shows that ϕ_1 satisfies a forced analogue of (4.0.8). Specifically,

$$\phi_1'''' - \frac{2}{r}\phi_1''' + \frac{3}{r^2}\phi_1'' - \frac{3}{r^3}\phi_1' = \mathrm{i}(U_0 - c_0)\left(\phi_0'' - \frac{\phi_0'}{r}\right) + \mathrm{i}\left(\frac{U_0'}{r} - U_0''\right)\phi_0. \tag{4.0.12}$$

Seeking a neutral disturbance, we require that the wavespeed c is purely real. In Appendix B, we demonstrate that it must thus be the case that $c_1 = 0$. With this in mind, equation (4.0.12) is solved subject to

$$\phi_1(1) = 0, \qquad \phi_1'(1) = 0, \qquad \phi_1(\delta) = 0, \qquad (c_0 - V)\,\phi_1'(\delta) + U_0'(\delta)\phi_1(\delta) = 0. \tag{4.0.13}$$

The first and second of these conditions correspond to the boundary conditions on the outer cylinder (4.0.2a), (4.0.2b). The third condition imposes the normalisation we have chosen for ϕ, whilst the fourth condition arises from the kinematic condition on the inner cylinder (4.0.2c). Though written in this form for clarity, we note that the kinematic condition reduces to $\phi_1'(\delta) = 0$ in view of the third condition as $c_0 \neq V$.

It is possible to find a closed-form analytical expression for the purely imaginary ϕ_1. We note that (4.0.12) is a third-order differential equation for ϕ_1', and begin by solving the homogeneous analogue of (4.0.12) for the complementary solution of ϕ':

$$\phi_1'^{(CF)} = a_1 r^3 + a_2 r + a_3 r\log r \tag{4.0.14}$$

where a_1, a_2 and a_3 are constants of integration. Using a variation of parameters approach, we seek a particular solution of the form

$$\phi_1'^{(PS)} = A(r)r^3 + B(r)r + C(r)r\log r \tag{4.0.15}$$

and obtain

$$A'(r) = \frac{\mathcal{M}(r)}{4r}, \qquad B'(r) = -\frac{\mathcal{M}(r)}{4} r(1 - 2\log r), \qquad C'(r) = -\frac{\mathcal{M}(r)}{2} r, \tag{4.0.16}$$

where $\mathcal{M}(r)$ has been defined as the right-hand side of (4.0.12),

$$\mathcal{M}(r) = \mathrm{i}(U_0 - c_0)\left(\phi_0'' - \frac{\phi_0'}{r}\right) + \mathrm{i}\left(\frac{U_0'}{r} - U_0''\right)\phi_0. \tag{4.0.17}$$

The functions $A(r), B(r), C(r)$ can be found by integration of (4.0.16) using, for example, MAPLE. The constants of integration that arise can be absorbed into the homogeneous solution (4.0.14), and so are taken to be zero without loss of generality.

Integrating the sum of (4.0.14) and (4.0.15) gives the general solution for ϕ_1 to be

$$\phi_1{}^{(GS)} = \int \Big(A(r)r^3 + B(r)r + C(r)r\log r\Big)\mathrm{d}r + \frac{a_1}{4}r^4 + \frac{a_2}{2}r^2 - \frac{a_3}{4}r^2(1 - 2\log r) + a_4, \tag{4.0.18}$$

where the constants a_1, a_2, a_3, a_4 are determined by imposing the boundary conditions (4.0.13). The integral on the right-hand side was evaluated using MAPLE and is fully known, with the resulting constant of integration accounted for in a_4. While independent of K and m, ϕ_1 does depend on the sliding velocity of the inner cylinder.

With ϕ_1 fully determined, the dynamic condition (4.0.2d) provides us with a solvability condition for the problem. For prescribed δ, V and K, the neutral-mode solution exists for R_0 such that

$$\frac{K}{{R_0}^2} = -\frac{\mathrm{i}U_0'(\delta)}{\phi_0'(\delta)}\left(\phi_1'''(\delta) - \frac{\phi_1''(\delta)}{\delta}\right), \tag{4.0.19}$$

provided the right-hand side of (4.0.19) is real and positive. We emphasise that R_0 is dependent on the sliding velocity via U_0 and ϕ_1.

Introducing $\overline{\phi}_1$ such that $\phi_1 = \mathrm{i}\overline{\phi}_1$, rearrangement of (4.0.19) gives

$${R_0}^2 = \frac{\phi_0'(\delta)}{U_0'(\delta)}\left(\overline{\phi}_1'''(\delta) - \frac{\overline{\phi}_1''(\delta)}{\delta}\right)^{-1} K, \tag{4.0.20}$$

where δ and V are such that

$$\frac{\phi_0'(\delta)}{U_0'(\delta)}\left(\overline{\phi}_1'''(\delta) - \frac{\overline{\phi}_1''(\delta)}{\delta}\right)^{-1} > 0 \tag{4.0.21}$$

so as to ensure (4.0.20) admits a real solution for R_0.

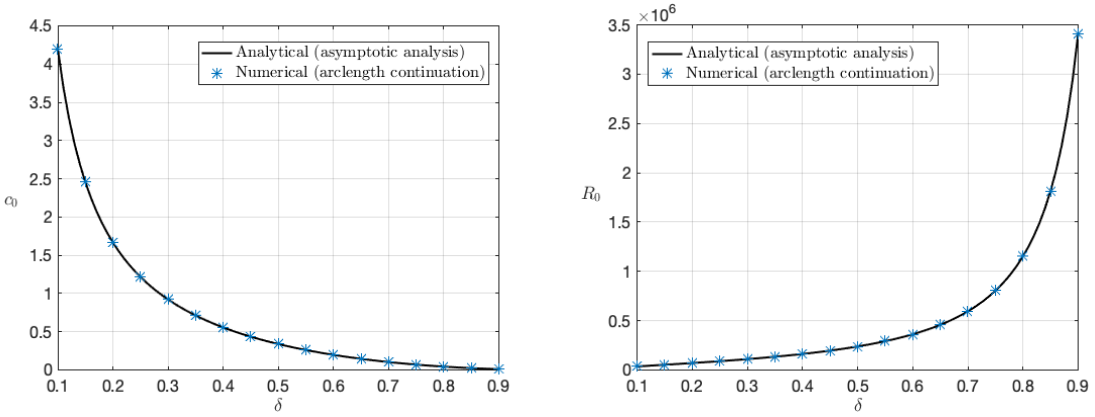

Figure 4.0.1: Illustrations showing how c_0 (left) and R_0 (right) vary with δ for $V = 0, K = 5 \times 10^9$. The solid black lines depict the behaviour as governed by the analytical expressions (4.0.11) and (4.0.20), whilst the blue asterisks represent numerical solutions to the Orr-Sommerfeld equation when $\alpha \approx 2 \times 10^{-6}$. For the numerical results, we have taken $m = 0.02$.

By examining expression (4.0.20), we see that the limit of the Reynolds number as $\alpha \to 0$ along the neutral curve is independent of the mass of the inner cylinder, confirming our expectations from the numerical results in Chapter 3. Whilst it is apparent that R_0 is proportional to $\sqrt{K}$, the behaviour of R_0 as we vary δ is more complicated and is illustrated in figure 4.0.1 for a stationary inner cylinder with stiffness $K = 5 \times 10^9$. We remark that the inequality (4.0.21) holds for $V = 0$ and $0 < \delta < 1$, so an admissible solution for R_0 exists for these parameters. As the radius ratio increases from $\delta = 0.1$ to $\delta = 0.9$ for this choice of V and K, the leading order wavespeed c_0 of the neutral mode decreases and the instability sets in at increasingly larger R_0.

Solving the Orr-Sommerfeld problem (4.0.1, 4.0.2), we use a continuation technique (adapted from Walton [1]) to numerically compute the eigenvalues and eigenfunctions of the neutral mode as $\alpha \to 0$. We modify the normalisation condition of Walton [1], instead imposing that $\phi(\delta) = 1$ for ease of comparison with our analytical solution.

For a stationary inner cylinder with $\delta = 0.6$, $m = 0.02$ and $K = 5 \times 10^9$, our numerical results show $R \approx 36240$ and $c \approx 0.19719$ when $\alpha = \tilde{\alpha} \approx 2.6778 \times 10^{-6}$. This is consistent with our analytical findings; figure 4.0.1 shows good agreement between our analytical and numerical solutions for c_0 and R_0 for various radius ratios with $V = 0$, $K = 5 \times 10^9$ and $m = 0.02$. Though the analytical solution is independent of the cylinder mass, we note that the numerical computations require an input value for m. Figure 4.0.2 compares our analytical and numerical solutions for ϕ, and suggests that our second-order analytic approximation appropriately captures the behaviour of the neutral mode in the limit $\alpha \to 0$.

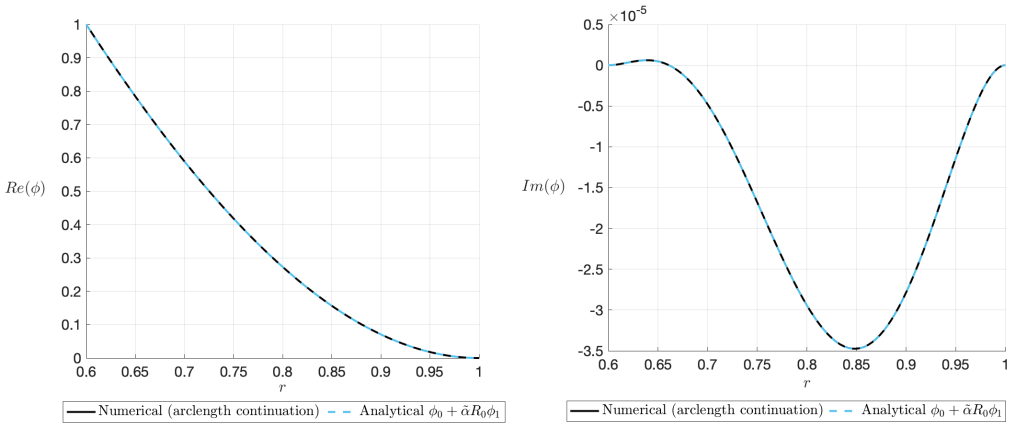

Figure 4.0.2: Illustration of ϕ for $\delta = 0.6$, $V = 0$ and $K = 5 \times 10^9$. We take $m = 0.02$ for our numerical solution. For our analytical solution, we plot $\phi \sim \phi_0 + \tilde{\alpha} R_0 \phi_1$, using (4.0.8), (4.0.20), (4.0.12) and $\tilde{\alpha} = 2.6777... \times 10^{-6}$.

The variation of R_0 with V is also of interest. With the application of thread-annular injection in mind, we focus only on non-negative values of V. For a given δ, our system only admits solutions for values of V such that the inequality (4.0.21) is satisfied. To find these values of V, we first analyse each factor on the left-hand side of (4.0.21) individually.

Differentiating ϕ_0 (4.0.8) with respect to r and evaluating the resulting derivative at $r = \delta$, we have

$$\phi'(\delta) = \frac{4\delta \log \delta}{2\delta^2 \log \delta - \delta^2 + 1}, \tag{4.0.22}$$

which is negative for $0 < \delta < 1$. With the base flow defined in (4.0.3), we determine

$$U_0'(\delta) = -2\delta + \frac{V - 1 + \delta^2}{\delta \log \delta}, \tag{4.0.23}$$

so that

$$U_0'(\delta) < 0 \quad \text{for} \quad V > 1 - \delta^2 + 2\delta^2 \log \delta \tag{4.0.24}$$

and

$$U_0'(\delta) > 0 \quad \text{for} \quad V < 1 - \delta^2 + 2\delta^2 \log \delta. \tag{4.0.25}$$

After much manipulation, consideration of ϕ_1 (4.0.18) enables us to write

$$\left(\overline{\phi}_1'''(\delta) - \frac{\overline{\phi}_1''(\delta)}{\delta} \right)^{-1} = \frac{\chi_0(\delta)}{\chi_1(\delta) + \chi_2(\delta) V} \tag{4.0.26}$$

where

$$\chi_0(\delta) = 12\delta \left(\log \delta\right)^2 \left(\delta^2 - 1\right) \left(2\delta^2 \log \delta - \delta^2 + 1\right) \left(\delta^2 \log \delta - \delta^2 + \log \delta + 1\right), \tag{4.0.27}$$

$$\chi_1(\delta) = \left(20\,\delta^8 - 12\,\delta^6 + 36\,\delta^4 - 44\,\delta^2\right)(\log\delta)^3 + \left(-54\,\delta^8 + 18\,\delta^6 + 126\,\delta^4 - 90\,\delta^2\right)(\log\delta)^2 + \left(39\,\delta^8 - 126\,\delta^6 + 144\,\delta^4 - 66\,\delta^2 + 9\right)\log\delta + 12\,(\delta^2-1)^4, \quad (4.0.28)$$

$$\chi_2(\delta) = \left(36\,\delta^6 + 24\,\delta^4 + 60\,\delta^2\right)(\log\delta)^3 + \left(-90\,\delta^6 - 36\,\delta^4 + 126\,\delta^2\right)(\log\delta)^2 + \left(63\,\delta^6 - 135\,\delta^4 + 81\,\delta^2 - 9\right)\log\delta + 12\,(\delta^2-1)^3. \quad (4.0.29)$$

While $\chi_0 > 0$ and $\chi_1 < 0$ for $0 < \delta < 1$, the behaviour of χ_2 is more complicated. We define δ_c to be such that $\chi_2(\delta_c) = 0$, which gives $\delta_c \approx 0.5076$ upon use of a root-solving algorithm in MATLAB. We have $\chi_2 > 0$ for $\delta < \delta_c$, whereas $\chi_2 < 0$ for $\delta > \delta_c$.

In order to determine the behaviour of (4.0.26), it is convenient to consider the cases $\delta < \delta_c$, $\delta = \delta_c$ and $\delta > \delta_c$ separately.

For $\delta < \delta_c$,

$$\left(\overline{\phi}_1'''(\delta) - \frac{\overline{\phi}_1''(\delta)}{\delta}\right)^{-1} > 0 \quad \text{for} \quad V > -\frac{\chi_1}{\chi_2} \quad (4.0.30)$$

and

$$\left(\overline{\phi}_1'''(\delta) - \frac{\overline{\phi}_1''(\delta)}{\delta}\right)^{-1} < 0 \quad \text{for} \quad V < -\frac{\chi_1}{\chi_2} \quad (4.0.31)$$

When $\delta = \delta_c$, (4.0.26) is independent of V and

$$\left(\overline{\phi}_1'''(\delta) - \frac{\overline{\phi}_1''(\delta)}{\delta}\right)^{-1} < 0. \quad (4.0.32)$$

Finally, we consider the case $\delta > \delta_c$, for which $\chi_2 < 0$. Restricting our attention to non-negative V, we have

$$\left(\overline{\phi}_1'''(\delta) - \frac{\overline{\phi}_1''(\delta)}{\delta}\right)^{-1} < 0 \quad \text{for} \quad V \geq 0. \quad (4.0.33)$$

It now remains to combine the analysis of the individual factors in (4.0.21) to determine the values of δ and V for which there exists an admissible solution for R_0 (4.0.19).

For $\delta < \delta_c$, consideration of (4.0.24, 4.0.25, 4.0.30, 4.0.31) indicates a neutral mode solution exists for

$$V < 1 - \delta^2 + 2\delta^2\log\delta \qquad \text{or} \qquad V > -\frac{\chi_1}{\chi_2}. \quad (4.0.34)$$

Here we have made use of the inequality

$$1 - \delta^2 + 2\delta^2 \log \delta < -\frac{\chi_1}{\chi_2} \quad \text{for} \quad 0 < \delta < \delta_c. \tag{4.0.35}$$

Finally, for $\delta \geq \delta_c$ we require

$$V < 1 - \delta^2 + 2\delta^2 \log \delta, \tag{4.0.36}$$

which follows from (4.0.25), (4.0.32), (4.0.33).

The inequalities in (4.0.34) confirm that we require $V \neq 1$ in the limit $\delta \to 0$, as remarked upon earlier.

The regions described by (4.0.34) and (4.0.36) are depicted in the $(\delta - V)$ plane in figure 4.0.3, where the shaded areas represent regions in which a neutral solution in the limit $\alpha \to 0$ exists. As we approach the boundaries of these regions from inside the shaded areas, R becomes asymptotically large. Increasing V from zero for a given a radius ratio, there exists a threshold velocity at which the solution ceases to exist. This threshold velocity approaches zero (from above) as $\delta \to 1$. For values of $\delta < \delta_c$, expression (4.0.20) predicts a subsequent re-emergence of the neutral solution once V has been sufficiently increased beyond the appropriate threshold value. As the radius ratio increases, the widening gap between the velocities at which the neutral mode disappears and re-emerges becomes infinitely large as $\delta \to \delta_c$.

The inequalities (4.0.34) and (4.0.36) are independent of the mass and stiffness of the inner cylinder, illustrating that the threshold velocities (and re-emergence velocities for $\delta < \delta_c$) depend only on the radius ratio of the inner cylinder.

In figure 4.0.4, we illustrate how R_0 varies with increasing V for fixed δ. For $\delta = \delta_c$ and $\delta = 0.7$, R_0 approaches infinity as V approaches the corresponding threshold velocities, $V \approx 0.393$ and $V \approx 0.160$ respectively. A similar phenomena occurs for $\delta = 0.3$, however here we additionally have R_0 reappearing once V has increased beyond $V \approx 1.507$. R_0 decreases from infinity as V is increased further. For a given sliding velocity, it appears that cylinders with a larger radius ratio have a higher critical Reynolds number in the long-wave limit, provided that a solution exists.

For $\delta = 0.7$, the predicted threshold velocity is $V \approx 0.1605$. We plot the stability regions corresponding to an inner cylinder that moves with $V = 0.16$ and $V = 0.161$ in figure 4.0.5. In agreement with figure 4.0.5a, our expression for R_0 (4.0.20) predicts that $R_0 \approx 9.38 \times 10^6$ when $V = 0.16$ and $K = 5 \times 10^9$. From our analytical work, we expect no neutral mode solution in the limit $\alpha \to 0$ for $V = 0.161$. This is consistent with figure 4.0.5b, where we have not found the neutral curve extending to $\alpha = 0$.

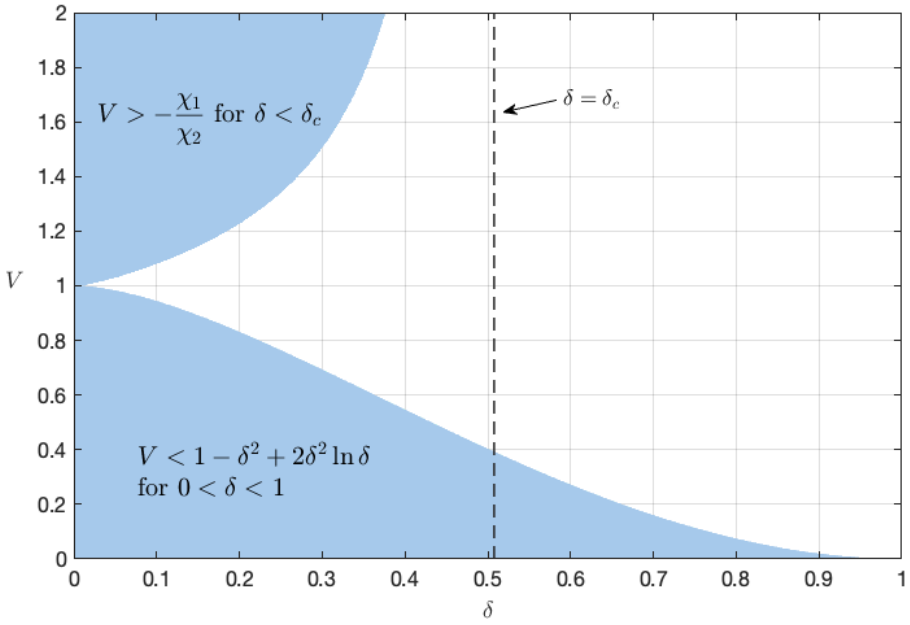

Figure 4.0.3: Shaded areas depict regions in the $(\delta - V)$ plane for which a long-wave neutral mode solution exists. For $\delta < \delta_c$, the upper shaded region extends to infinite V.

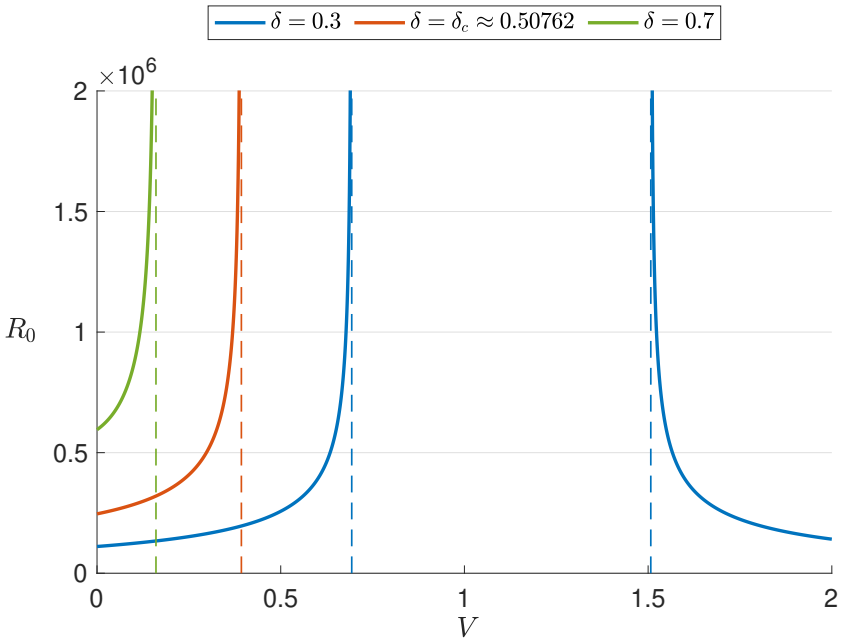

Figure 4.0.4: Solid lines illustrate how R_0 varies with increasing V for three fixed δ values, namely $\delta = 0.3$, $\delta = \delta_c$, and $\delta = 0.7$. Dashed lines represent the corresponding cut-off velocities as predicted by (4.0.34), (4.0.36).

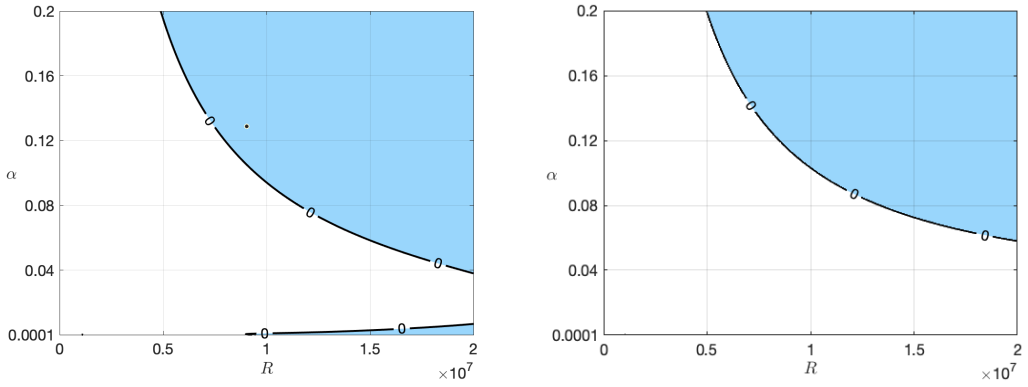

(a) (b)

Figure 4.0.5: Numerically determined neutral curves for an inner cylinder with $\delta = 0.7, K = 5 \times 10^9, m = 0.2$. The shaded regions are unstable. The cylinder has sliding velocities $V = 0.16$ (left) and $V = 0.161$ (right).

In this chapter, we examined the circular Orr-Sommerfeld problem (4.0.1, 4.0.2) pertaining to APCF with a flexible inner cylinder using asymptotic techniques. We deduced a mass-independent expression for the leading order critical Reynolds number of a compliance-related instability in the limit $\alpha \to 0$. This corroborated our findings in Chapter 3, where we found the critical Reynolds number in the long-wave limit was largely unaffected by a change in cylinder mass for the parameters $\delta = 0.7$, $V = 0$ and $K = 5 \times 10^{11}$ (see figure 3.2.6).

In addition, we determined sliding velocities V (as a function of radius ratio δ) for which a neutral solution exists in the limit $\alpha \to 0$. Where a solution exists, we studied the behaviour of R_0 with increasing V for selective values of δ.

Having analytically explored the neutral curve in the long-wave limit at finite Reynolds numbers, we aim to gain a fuller picture of the linear instabilities of compliant APCF by understanding the behaviour of neutral modes at high Reynolds numbers. In particular, we are interested in how the flow-based instability of the rigid case is modified in the presence of compliance. As a prelude to our high-Reynolds-number analysis, in the next chapter we seek to gain insights into the inviscid linear stability of compliant APCF.

Chapter 5

Inviscid linear stability of annular flow with a compliant inner cylinder

An inviscid analysis can often provide valuable insights into a viscous problem at large Reynolds numbers. In particular, inviscid results may act as guides for numerical computations, which often result in the existence of spurious modes of instability. With this in mind, our goal in this chapter is to derive modifications to classical inviscid theorems so as to account for the flexibility of our inner cylinder. Using the spring-backed plate model [54, 55], we will incorporate the effects of mass, spring stiffness and damping.

General criteria for the instability of inviscid parallel two-dimensional flows between two rigid boundaries have been obtained by Rayleigh [12] and Fjørtoft [3], both of whom provide necessary, but not sufficient, conditions for the instability of such flows.

Consider a two-dimensional planar inviscid flow with base velocity profile $U(y)$ in the streamwise direction, bounded by rigid boundaries at $y = y_1$ and $y = y_2$. Rayleigh's inflection-point theorem states that if the flow is unstable, there must be an inflection point in the base velocity profile $U(y)$ somewhere in the flow. Fjørtoft extended this theorem, providing a stronger condition for instability: if the flow is unstable, it is necessary that $U''(U - U_I) < 0$ somewhere in the flow, where $U_I = U(y_I)$ and y_I is such that $U''(y_I) = 0$.

Rayleigh also restricted the admissible complex-valued eigenvalues of the problem by stipulating that c_r lies within the range of $U(y)$ for modes with $c_i \neq 0$ [73]. Howard's semicircle theorem [13] adds to this result: the wavespeeds c of unstable modes are bounded by a semicircle that is located in the upper-half complex c-plane with diameter

$(\max_y U - \min_y U)$ and centre on the real axis at $c_r = \frac{1}{2}(\max_y U + \min_y U)$. Høiland [65] complements these theorems with an inequality relating the wavenumber of a disturbance with the imaginary part of its wavespeed.

The proofs of these theorems involve integrating over the region between the two plane rigid boundaries. In the case of rigid boundaries, the boundary terms that arise from an integration by parts have zero contribution as the inviscid impermeability conditions require the normal velocity of the disturbance to decrease to zero on the boundary. Along a compliant boundary, however, this normal velocity need not be zero and so these classical theorems do not readily apply to flows over a compliant surface.

The analysis that follows is closely related to the works of Yeo and Dowling [66], Yeo [67], Kumaran [68], and Shankar and Kumaran [69]. Yeo and Dowling [66] studied incompressible semi-bounded inviscid parallel flows over compliant walls and produced counterparts to well-known results by Rayleigh, Howard and Høiland. Yeo [67] provided further criteria for instability, including a modified Fjørtoft-type criterion. Building on this work, Kumaran [68] shows that classical results can be adapted to an inviscid flow in a flexible tube, both for axisymmetric and highly non-axisymmetric perturbations. Shankar and Kumaran [69] strengthen this work and generalise the inviscid results for non-axisymmetric perturbations for arbitrary n, where n is the azimuthal wavenumber of the perturbation.

In the remainder of this chapter, we study the inviscid stability of an axisymmetric flow through the annular region between two concentric cylinders. We begin our analysis by formulating the linear stability problem for this flow, and then consider the cylindrical analogue of Rayleigh's inflection point theorem when the cylinders are rigid. We subsequently modify classical stability theorems for the case of a flexible inner cylinder and apply these results to a base flow of the form (2.2.2). The results we discuss below are adaptations of those found in the above studies and we use similar methods to these authors.

5.1 Problem formulation

Consider an incompressible flow through the annular region between two concentric cylinders. The outer cylinder of radius 1 is stationary, while the inner cylinder of radius δ moves with axial velocity $V \geq 0$. Imposing that this inviscid flow is swirl-free, the governing Euler equations are

$$\frac{\partial u}{\partial x} + \frac{1}{r}\frac{\partial (rv)}{\partial r} = 0, \qquad \frac{\partial u}{\partial t} + u\frac{\partial u}{\partial x} + v\frac{\partial u}{\partial r} = -\frac{\partial p}{\partial x}, \qquad \frac{\partial v}{\partial t} + u\frac{\partial v}{\partial x} + v\frac{\partial v}{\partial r} = -\frac{\partial p}{\partial r}. \tag{5.1.1}$$

When both cylinders are rigid, the typical no-normal-flow conditions are expressed as

$$v(\delta) = v(1) = 0. \tag{5.1.2}$$

All quantities are assumed to be suitably non-dimensionalised. We will discuss the boundary conditions for a flexible inner cylinder shortly.

The base pressure is taken to be a constant, P_0. The unidirectional base flow, described by $(u, v) = (U(r), 0)$, then satisfies the Euler equations (5.1.1) and is assumed to be inviscid, steady and axisymmetric. The base flow is such that $U(\delta) = V$ and $U(1) = 0$.

We superimpose our base flow with axisymmetric travelling-wave disturbances of infinitesimal amplitude, and write

$$u = U(r) + \Delta\hat{u}(r)\mathrm{e}^{\mathrm{i}\alpha(x-ct)} + c.c, \quad v = \Delta\hat{v}(r)\mathrm{e}^{\mathrm{i}\alpha(x-ct)} + c.c, \tag{5.1.3a}$$

$$p = P_0 + \Delta\hat{p}(r)\mathrm{e}^{\mathrm{i}\alpha(x-ct)} + c.c, \tag{5.1.3b}$$

where $\Delta \ll 1$ is a non-dimensional amplitude and $\hat{u}(r), \hat{v}(r), \hat{p}(r)$ are disturbance shape functions. Specifically investigating temporal stability, the wavenumber α and the wavespeed c are assumed to be real and complex respectively.

At order Δ, substitution of (5.1.3) into (5.1.1) leads to the inviscid linearised disturbance equations

$$\mathrm{i}\alpha\hat{u} + \frac{\mathrm{d}\hat{v}}{\mathrm{d}r} + \frac{\hat{v}}{r} = 0, \qquad \mathrm{i}\alpha\left(U - c\right)\hat{u} + \hat{v}\frac{\mathrm{d}U}{\mathrm{d}r} = -\mathrm{i}\alpha\hat{p}, \qquad \mathrm{i}\alpha\left(U - c\right)\hat{v} = -\frac{\mathrm{d}\hat{p}}{\mathrm{d}r}. \tag{5.1.4 a,b,c}$$

For the scenario of two rigid cylinders, (5.1.2) and (5.1.3) give the conditions

$$\hat{v}(\delta) = \hat{v}(1) = 0. \tag{5.1.5}$$

Introducing the function $\phi(r) = r\hat{v}$, the equations (5.1.4) can be manipulated to form the circular Rayleigh equation

$$(U - c)\left[\frac{\mathrm{d}}{\mathrm{d}r}\left(\frac{\phi'}{r}\right) - \frac{\alpha^2\phi}{r}\right] - \frac{\mathrm{d}}{\mathrm{d}r}\left(\frac{U'}{r}\right)\phi = 0, \tag{5.1.6}$$

which is to be solved subject to

$$\phi(\delta) = \phi(1) = 0 \tag{5.1.7}$$

when both cylinders are rigid.

In what follows, the complex conjugate of ϕ is denoted as ϕ^*.

5.2 Inviscid annular flow between two rigid cylinders

When the outer and inner cylinders are rigid, typical no-normal-flow conditions (5.1.7) apply on both cylinder walls. Multiplying (5.1.6) by $\phi^*/(U-c)$ and integrating across the annulus, we find that

$$\int_\delta^1 \left\{ \frac{|\phi'|^2}{r} + \frac{\alpha^2|\phi|^2}{r} + \frac{|\phi|^2}{U-c}\frac{\mathrm{d}}{\mathrm{d}r}\left(\frac{U'}{r}\right)\right\}\mathrm{d}r = 0 \tag{5.2.1}$$

after performing an integration by parts for the first term. Taking the imaginary part of this equation,

$$c_i \int_\delta^1 \frac{\mathrm{d}}{\mathrm{d}r}\left(\frac{U'}{r}\right)\frac{|\phi|^2}{|U-c|^2}\,\mathrm{d}r = 0. \tag{5.2.2}$$

For an unstable flow, the quantity $\frac{\mathrm{d}}{\mathrm{d}r}\left(\frac{U'}{r}\right)$ must change sign somewhere in the interval $\delta \le r \le 1$. This result for an annular region is analogous to Rayleigh's inflection-point theorem.

For a base flow of the form (2.2.2),

$$U_0(r) = 1 - r^2 + \frac{(V-1+\delta^2)}{\log\delta}\log r, \quad \delta \le r \le 1, \tag{5.2.3}$$

we determine

$$\frac{\mathrm{d}}{\mathrm{d}r}\left(\frac{U_0'}{r}\right) = \frac{-2\,(V-1+\delta^2)}{r^3\log\delta}. \tag{5.2.4}$$

For fixed V and δ, this quantity does not change sign in the interval $r \in [\delta, 1]$. It is therefore not possible for the flow (5.2.3) to support linearly unstable inviscid modes when the inner cylinder is rigid, in view of equation (5.2.2). We note that the choice $V = 1-\delta^2$ yields $\phi(r) = 0$, which can be seen from equation (5.2.1) directly.

The results of Walton [1] show that viscous APCF subject to no-slip conditions is linearly unstable to axisymmetric disturbances at finite Reynolds numbers. In Chapter 3, we also illustrate neutral curves arising from solving the Orr-Sommerfeld problem (3.1.2) in the rigid scenario. Consider the case of a stationary inner cylinder. At asymptotically large Reynolds numbers, the upper and lower branches of the neutral curve are described by $\alpha \sim R^{-1/11}$ and $\alpha \sim R^{-1/7}$ respectively [1]. For a given positive value of α, we see that increasing the Reynolds number eventually leads us into a region of linear stability.

5.3 Inviscid annular flow with a flexible inner cylinder

Having examined the inviscid stability properties of a flow through two rigid concentric cylinders, we now explore the effect of compliance. We begin by forming the appropriate boundary conditions on the cylinder walls.

On the rigid outer cylinder, the inviscid impermeability condition gives

$$\phi(1) = 0. \tag{5.3.1}$$

In contrast to the rigid scenario, we do not impose zero normal flow on the inner cylinder wall. The boundary of the inner cylinder is expressed as

$$r_s(x,t) = \delta + \tilde{\eta}(x,t). \tag{5.3.2}$$

where $\tilde{\eta}$ is a small displacement due to compliance and points radially outwards from the inner cylinder. The perturbation $\tilde{\eta}$ takes the waveform (2.3.4)

$$\tilde{\eta}(x,t) = \Delta\hat{\eta}\mathrm{e}^{\mathrm{i}\alpha(x-ct)} + c.c. \tag{5.3.3}$$

With the inner cylinder moving radially, we impose the kinematic condition

$$v = \frac{\partial\tilde{\eta}}{\partial t} + u\frac{\partial\tilde{\eta}}{\partial x} \qquad \text{on} \quad r = r_s, \tag{5.3.4}$$

as seen in equation (2.3.9) of Chapter 2. A Taylor expansion of (5.3.4) about $r = \delta$ then yields

$$\hat{v}(\delta) = \mathrm{i}\alpha(V - c)\hat{\eta} \tag{5.3.5}$$

upon use of (5.1.3), (5.3.3), as we have $U(\delta) = V$.

Since $\phi = r\hat{v}$, the inviscid flow condition at the wall of the inner cylinder can now be expressed as

$$\phi(\delta) = \mathrm{i}\alpha\delta\,(V - c)\,\hat{\eta}. \tag{5.3.6}$$

Using the spring-backed plate model [54, 55], consideration of the forces acting on the flexible cylinder leads to the relation

$$\hat{p}(\delta) = \left(\alpha^2 c^2 \check{m} + \mathrm{i}\alpha c\check{D} - \check{K}\right)\hat{\eta}, \tag{5.3.7}$$

where $\check{m}$, $\check{D}$ and $\check{K}$ are non-dimensional constants that are associated with the mass, damping and spring stiffness of the system respectively. Naturally, these quantities do not correspond to the non-dimensionalisation described in (2.1.9), as viscosity is not a

parameter in the inviscid problem. In what follows, $\check{m}$, $\check{D}$ and $\check{K}$ are taken to be strictly positive constants unless stated otherwise.

When adapting the classical inviscid theorems to account for a flexible boundary, it will be useful to have expressions for the derivatives of ϕ on the cylinder walls. To this end, we use the continuity equation (5.1.4a) to find

$$\phi'(1) = -\mathrm{i}\alpha\hat{u}(1), \qquad \phi'(\delta) = -\mathrm{i}\alpha\delta\hat{u}(\delta). \tag{5.3.8 a,b}$$

To find $\hat{u}(\delta)$, we evaluate the axial momentum equation (5.1.4b) at $r = \delta$, obtaining

$$\hat{u}(\delta) = -\left[\frac{\alpha^2 c^2 \check{m} + \mathrm{i}\alpha c\check{D} - \check{K}}{V - c} + U'(\delta)\right]\hat{\eta} \tag{5.3.9}$$

upon substitution of (5.3.5) and (5.3.7).

In view of (5.3.8) and (5.3.9), it can now be shown that the derivative of ϕ on the inner cylinder wall is given by

$$\phi'(\delta) = \mathrm{i}\alpha\delta\left[\frac{\alpha^2 c^2 \check{m} + \mathrm{i}\alpha c\check{D} - \check{K}}{V - c} + U'(\delta)\right]\hat{\eta}. \tag{5.3.10}$$

We are now well-equipped to prove the following theorems for an inviscid flow between two concentric cylinders, where the inner flexible cylinder moves axially with constant velocity V and the outer rigid cylinder is stationary.

We strive for necessary conditions for instability involving the basic velocity profile to complement Rayleigh's inflection point theorem and Fjørtfort's theorem. Owing to the presence of non-zero boundary terms, we anticipate that the conditions found will be weaker than their rigid counterparts.

Theorem 1. *Let V be strictly positive. A temporally unstable axisymmetric mode with $c_r \leq 0$, $c_r \geq 2V$, or $c_i \geq c_r \geq V$ may exist only if $(U - V)\frac{\mathrm{d}}{\mathrm{d}r}\left(\frac{U'}{r}\right)$ is negative somewhere in the flow.*

Theorem 2. *Let $V = 0$. A temporally unstable axisymmetric mode may exist only if $U\frac{\mathrm{d}}{\mathrm{d}r}\left(\frac{U'}{r}\right)$ is negative somewhere in the flow.*

Theorem 3. *Let $V = 0$. A neutrally stable axisymmetric mode with $c_r \neq 0$ cannot exist if $\check{D}$ is strictly positive.*

We begin by considering an inner cylinder that moves axially with velocity $V \geq 0$ and later consider the cases $V > 0$ and $V = 0$ separately.

The following proof closely follows that of Rayleigh's inflection-point theorem. We first multiply the Rayleigh equation (5.1.6) by $\phi^*/(U-c)$ and then integrate from $r=\delta$ to $r=1$:

$$\int_\delta^1 \frac{|\phi'|^2}{r} + |\phi|^2\left[\frac{\alpha^2}{r} + \frac{1}{U-c}\frac{\mathrm{d}}{\mathrm{d}r}\left(\frac{U'}{r}\right)\right]\mathrm{d}r = \left[\frac{\phi^*\phi'}{r}\right]_\delta^1. \tag{5.3.11}$$

Differing from the scenario of rigid cylinders, the right-hand side of (5.3.11) is non-zero. Instead, the boundary terms (5.3.6) and (5.3.10) can be used to show that

$$\left[\frac{\phi^*\phi'}{r}\right]_\delta^1 = \alpha^2\delta|V-c|^2\left(-\frac{\alpha^2c^2\check{m}+\mathrm{i}\alpha c\check{D}-\check{K}}{(V-c)^2} - \frac{U'(\delta)}{V-c}\right)|\hat{\eta}|^2. \tag{5.3.12}$$

Substituting this into (5.3.11) and multiplying by $(V-c)$, we obtain

$$\int_\delta^1 \frac{(V-c)|\phi'|^2}{r} + |\phi|^2\left[\frac{\alpha^2(V-c)}{r} + \frac{V-c}{U-c}\frac{\mathrm{d}}{\mathrm{d}r}\left(\frac{U'}{r}\right)\right]\mathrm{d}r = \delta\alpha^2|V-c|^2\left[-\frac{\alpha^2c^2\check{m}+\mathrm{i}\alpha c\check{D}-\check{K}}{V-c} - U'(\delta)\right]|\hat{\eta}|^2. \tag{5.3.13}$$

The imaginary part of this equation yields

$$c_i\int_\delta^1 \frac{|\phi'|^2}{r} + |\phi|^2\left[\frac{\alpha^2}{r} + \frac{U-V}{|U-c|^2}\frac{\mathrm{d}}{\mathrm{d}r}\left(\frac{U'}{r}\right)\right]\mathrm{d}r = \delta\alpha^2\left[-\alpha^2\check{m}\left(|c|^2-2c_rV\right)c_i - \alpha\check{D}\left(|c|^2-c_rV\right) - \check{K}c_i\right]|\hat{\eta}|^2. \tag{5.3.14}$$

To analyse this expression and establish Theorems 1 and 2, we consider the cases $V>0$ and $V=0$ separately.

Case 1: $\mathbf{V>0}$. In this scenario, the inner cylinder moves in the positive axial direction at a constant velocity. Before continuing, we briefly state our aims. We wish to prove that the right-hand side of (5.3.14) is negative for unstable modes with $c_r\le 0$, $c_r\ge 2V$ or $c_i\ge c_r\ge V$. If this is the case, the left hand side of (5.3.14) must also be negative and we would require $(U-V)\frac{\mathrm{d}}{\mathrm{d}r}\left(\frac{U'}{r}\right)$ to be negative somewhere in the flow. This would prove our theorem.

We will consider each of the cases $c_r\le 0$, $c_r\ge 2V$ or $c_i\ge c_r\ge V$ individually.

(i). For an unstable mode with $c_r\le 0$, it can be seen that

$$|c|^2-2c_rV>0 \qquad \text{and} \qquad |c|^2-c_rV>0. \tag{5.3.15}$$

Since $c_i>0$, it follows that the right-hand side of (5.3.14) is negative for such a mode.

(ii). Now we consider an unstable mode with $c_r \geq 2V$. Let us first deduce the sign of $\left(|c|^2 - 2c_rV\right)$, which can be expanded as

$$\left(|c|^2 - 2c_rV\right) = c_i^2 + c_r^2 - 2c_rV. \tag{5.3.16}$$

Since c_r is strictly positive, we have

$$c_r^2 \geq 2c_rV, \tag{5.3.17}$$

so we can write

$$c_i^2 + c_r^2 - 2c_rV \geq c_i^2 + 2c_rV - 2c_rV = c_i^2 > 0. \tag{5.3.18}$$

This shows that

$$\left(|c|^2 - 2c_rV\right) > 0. \tag{5.3.19}$$

Adding (c_rV) to both sides of (5.3.19), it also follows that

$$\left(|c|^2 - c_rV\right) > 0. \tag{5.3.20}$$

In view of this, the right hand side of (5.3.14) must be negative.

(iii). Finally, we turn our attention to the condition $c_i \geq c_r \geq V$. These restrictions give

$$c_i^2 \geq c_rV \quad \text{and} \quad c_r^2 \geq c_rV, \tag{5.3.21}$$

so that

$$|c|^2 - 2c_rV = c_i^2 + c_r^2 - 2c_rV \geq c_rV + c_rV - 2c_rV = 0. \tag{5.3.22}$$

It also follows that

$$|c|^2 - c_rV > |c|^2 - 2c_rV \geq 0. \tag{5.3.23}$$

Thus the right hand side of (5.3.14) is negative.

To summarise, we have shown that for each of the cases (i)-(iii), the right-hand side of (5.3.14) is negative. It is thus necessary for the left-hand side of (5.3.14) to be negative. Therefore the existence of such instabilities requires that $(U-V)\frac{\mathrm{d}}{\mathrm{d}r}\left(\frac{U'}{r}\right)$ is negative somewhere in the flow. This completes the proof of Theorem 1.

Case 2: $\mathbf{V} = \mathbf{0}$. Under this restriction, (5.3.14) reduces to

$$c_i \int_\delta^1 \frac{|\phi'|^2}{r} + |\phi|^2 \left[\frac{\alpha^2}{r} + \frac{U}{|U-c|^2}\frac{\mathrm{d}}{\mathrm{d}r}\left(\frac{U'}{r}\right)\right] \mathrm{d}r = \delta\alpha^2|\hat{\eta}|^2 \left[-\alpha^2|c|^2\check{m}c_i - \alpha|c|^2\check{D} - \check{K}c_i\right]. \tag{5.3.24}$$

This equation is independent of the sign of c_r; this enables us to make a stronger statement than that of Theorem 1.

For an unstable mode, the right-hand side of (5.3.24) is negative. Therefore, the left-hand side must also be negative. This is only possible if the expression $U\frac{\mathrm{d}}{\mathrm{d}r}\left(\frac{U'}{r}\right)$ is negative somewhere in the flow. This proves Theorem 2.

We are able to deduce further results from equation (5.3.24). Assume that the damping coefficient $\check{D}$ is strictly positive and that we have a neutrally stable mode with $c_r \neq 0$. Then the left-hand side of (5.3.24) is zero, whilst the right-hand side is strictly negative. This is a contradiction, showing that the existence of neutrally stable modes with $c_r \neq 0$ is not possible in the presence of damping. This leads us to Theorem 3.

We can combine Theorems 2 and 3 to form a stronger statement:

Corollary 1. *Let $V = 0$. Assume that $U\frac{\mathrm{d}}{\mathrm{d}r}\left(\frac{U'}{r}\right) \geq 0$ everywhere in the flow, and that $\check{D} > 0$. Then all axisymmetric modes with $c_r \neq 0$ must be temporally damped.*

Under these assumptions, Theorem 2 allows us to conclude that there does not exist an unstable mode. Since $\check{D} > 0$, we further deduce that there exist no neutrally stable modes with $c_r \neq 0$ by Theorem 3. Therefore a mode with $c_r \neq 0$ must be damped. This proves Corollary 1.

In the special case $\check{D} = 0$, equation (5.3.24) simplifies to

$$c_i \int_\delta^1 \frac{|\phi'|^2}{r} + |\phi|^2 \left[\frac{\alpha^2}{r} + \frac{U}{|U-c|^2}\frac{\mathrm{d}}{\mathrm{d}r}\left(\frac{U'}{r}\right)\right] \mathrm{d}r = \delta\alpha^2|\hat{\eta}|^2 \left[-\alpha^2|c|^2\check{m} - \check{K}\right] c_i. \quad (5.3.25)$$

From this we are able to deduce the following corollary:

Corollary 2. *Let $V = 0$. Assume that $U\frac{\mathrm{d}}{\mathrm{d}r}\left(\frac{U'}{r}\right) \geq 0$ everywhere in the flow, and that $\check{D} = 0$. Then all axisymmetric modes must be neutrally stable.*

For such a flow, Theorem 2 implies that there exist no modes with $c_i > 0$. Suppose there exists a mode with $c_i < 0$. Then the left-hand side of (5.3.25) is strictly negative, while the right-hand side is strictly positive. This is a contradiction. Thus all modes must be neutrally stable, which is the statement of Corollary 2.

In the remainder of the analysis, we assume the damping coefficient $\check{D}$ is strictly positive.

The subsequent two theorems are reminiscent of the cylindrical analogue of Rayleigh's inflection-point theorem (see Section 5.2), albeit being much weaker.

Theorem 4. *Let $V > 0$. If we have $U'(\delta) \leq 0$, a temporally unstable axisymmetric mode with $c_r < 0$ or $c_r = V$ is only possible if $\frac{\mathrm{d}}{\mathrm{d}r}\left(\frac{U'}{r}\right) > 0$ somewhere in the flow.*

Theorem 5. *Let $V = 0$. If we have $U'(\delta) \leq 0$, a temporally unstable axisymmetric mode with $c_r < 0$ can exist only if $\frac{\mathrm{d}}{\mathrm{d}r}\left(\frac{U'}{r}\right) > 0$ somewhere in the flow. A similar result can be found for flows with $U'(\delta) \geq 0$.*

Following the proof of Rayleigh's inflection point theorem, we multiply the Rayleigh equation (5.1.6) by $\phi^*/(U-c)$ and integrate from $r = \delta$ to $r = 1$. This yields (5.3.11), into which we substitute (5.3.12). Thus far, this is identical to our proof of Theorems 1-3.

Now taking the imaginary part of the resulting equation, we obtain

$$c_i \int_\delta^1 \frac{|\phi|^2}{|U-c|^2} \frac{\mathrm{d}}{\mathrm{d}r}\left(\frac{U'}{r}\right) \mathrm{d}r = \\ -\alpha^2 \delta |\hat{\eta}|^2 \left[\alpha^2 \check{m}\left(\frac{2c_i V(c_r V - |c|^2)}{|V-c|^2}\right) + \alpha \check{D}\left(\frac{c_r(V^2+|c|^2) - 2V|c|^2}{|V-c|^2}\right) - \frac{2\check{K} c_i (V - c_r)}{|V-c|^2} + U'(\delta) c_i\right]. \tag{5.3.26}$$

Case 1: $\mathbf{V > 0}$. We first consider the case of a strictly positive sliding velocity. It will be useful to note that when $c_r < 0$,

$$c_r V - |c|^2 < 0 \quad \text{and} \quad c_r(V^2 + |c|^2) - 2V|c|^2 < 0. \tag{5.3.27}$$

In addition, when $c_r = V$,

$$c_r V - |c|^2 = c_r V - c_r^2 - c_i^2 = -c_i^2 < 0 \tag{5.3.28}$$

and

$$c_r(V^2 + |c|^2) - 2V|c|^2 = V(V^2 + |c|^2) - 2V|c|^2 = V^3 - V|c|^2 = -V c_i^2 < 0. \tag{5.3.29}$$

For a flow with $U'(\delta) \leq 0$, we use the inequalities (5.3.27)-(5.3.29) to deduce that an unstable mode with $c_r < 0$ or $c_r = V$ results in the right-hand side of (5.3.26) being positive. Therefore such an instability can exist only if $\frac{\mathrm{d}}{\mathrm{d}r}\left(\frac{U'}{r}\right)$ is positive somewhere in the flow.

It is less straightforward to comment on flows with $U'(\delta) \geq 0$ without making assumptions on the parameters, so we now let $V = 0$.

Case 2: $\mathbf{V} = \mathbf{0}$. For a stationary inner cylinder, (5.3.26) can be simplified to

$$c_i \int_\delta^1 \frac{|\phi|^2}{|U-c|^2} \frac{\mathrm{d}}{\mathrm{d}r}\left(\frac{U'}{r}\right) \mathrm{d}r = -\alpha^2 \delta |\hat{\eta}|^2 \left[\alpha \check{D} c_r + \frac{2\check{K} c_i c_r}{|c|^2} + c_i U'(\delta)\right]. \tag{5.3.30}$$

For a flow with $U'(\delta) \leq 0$, an unstable mode with $c_r < 0$ is only possible if $\frac{\mathrm{d}}{\mathrm{d}r}\left(\frac{U'}{r}\right) > 0$ somewhere in the flow. We make a similar deduction for flows with $U'(\delta) \geq 0$; for a flow with $U'(\delta) \geq 0$, an unstable mode with $c_r > 0$ is only possible if $\frac{\mathrm{d}}{\mathrm{d}r}\left(\frac{U'}{r}\right) < 0$ somewhere in the flow.

We also note that if $U'(\delta)$ is strictly positive (negative), then an unstable mode with $c_r = 0$ is only possible if $\frac{\mathrm{d}}{\mathrm{d}r}\left(\frac{U'}{r}\right)$ is strictly negative (positive) somewhere in the flow.

This completes the proofs for Theorems 4 and 5.

Another useful theorem for inviscid parallel flows over rigid boundaries includes Rayleigh's restriction for the real part of wavespeeds to lie in the range of the basic velocity when $c_i \neq 0$ [73]. We seek a similar result for inviscid annular flow with a flexible inner cylinder, obtaining:

Theorem 6. *Let $V \geq 0$. All temporally unstable axisymmetric modes must have c_r such that*

$$U_L < c_r < U_U,$$

where

$$U_L = \min[U_{\min}, 0], \qquad U_U = \max[U_{\max}, 0]$$

and

$$U_{\min} = \min_{r\in[\delta,1]} U, \qquad U_{\max} = \max_{r\in[\delta,1]} U.$$

To prove this theorem, we introduce a function g such that

$$g = \frac{\phi}{U-c}. \tag{5.3.31}$$

We may then write the Rayleigh equation (5.1.6) in terms of g, obtaining

$$\frac{\mathrm{d}}{\mathrm{d}r}\left(\frac{(U-c)^2 g'}{r}\right) - \frac{\alpha^2 (U-c)^2 g}{r} = 0. \tag{5.3.32}$$

Upon multiplying this by g^* and integrating across the annular region, we have

$$\int_\delta^1 \frac{(U-c)^2}{r}\left(|g'|^2 + \alpha^2 |g|^2\right) \mathrm{d}r = \left[\frac{(U-c)^2 g^* g'}{r}\right]_\delta^1. \tag{5.3.33}$$

From our boundary conditions (5.3.1), (5.3.6), (5.3.8a), (5.3.10), we deduce that

$$g(1) = 0, \qquad g'(1) = \frac{\mathrm{i}\alpha\hat{u}(1)}{c}, \tag{5.3.34a}$$

$$g(\delta) = \mathrm{i}\alpha\delta\hat{\eta}, \qquad g'(\delta) = \frac{\mathrm{i}\alpha\delta\left(\alpha^2c^2\check{m} + \mathrm{i}\alpha c\check{D} - \check{K}\right)\hat{\eta}}{(V-c)^2}. \tag{5.3.34b}$$

using the definition of g (5.3.31). Substituting these into (5.3.33) and defining a real, positive function Q such that $Q = |g'|^2 + \alpha^2|g|^2$ yields

$$\int_\delta^1 \frac{(U-c)^2}{r}\, Q \,\mathrm{d}r = -\alpha^2\delta\left(\alpha^2c^2\check{m} + \mathrm{i}\alpha c\check{D} - \check{K}\right)|\hat{\eta}|^2. \tag{5.3.35}$$

The imaginary part of this equation,

$$2c_i\int_\delta^1 \frac{(U-c_r)}{r}\, Q \,\mathrm{d}r = \alpha^2\delta c_r\left(2\alpha^2\check{m}c_i + \alpha\check{D}\right)|\hat{\eta}|^2, \tag{5.3.36}$$

reveals bounds on the wavespeeds of temporally unstable modes. We make the following observations:

i. Say $U_{\max} > 0$. Suppose there exists an unstable mode with $c_r \geq U_{\max}$. This means $U - c_r \leq 0$ throughout the flow, so the left-hand side of (5.3.36) is non-positive. However the right-hand side of (5.3.36) is positive. This gives a contradiction. Therefore, an unstable mode must have $c_r < U_{\max}$.

ii. Say $U_{\max} \leq 0$. Suppose there exists an unstable mode with $c_r \geq 0$. Since $U(r)$ is not identically zero, U must be strictly negative somewhere in the flow. Thus the left-hand side of (5.3.36) is negative. On the other hand, the right-hand side of (5.3.36) must be non-negative since $c_r \geq 0$. This leads to a contradiction. Therefore, an unstable mode must have $c_r < 0$.

iii. Now consider the situation where $U_{\min} \geq 0$. Suppose there exists an unstable mode with $c_r \leq 0$. Assuming $U(r)$ is not zero throughout the flow, the left-hand side must be positive. However, the right-hand side of (5.3.36) is non-positive. This is a contradiction. Therefore, an unstable mode must have $c_r > 0$.

iv. Finally, consider $U_{\min} < 0$. Suppose there exists an unstable mode with $c_r \leq U_{\min}$. Then $U - c_r \geq 0$ throughout the flow. Thus, the left-hand side of (5.3.36) is non-negative. However, since $c_r < 0$, the right-hand side of (5.3.36) is negative. We again have a contradiction. Therefore, an unstable mode must have $c_r > U_{\min}$.

Considering these together, we arrive at the conclusion that all unstable modes must be such that

$$\min[U_{\min}, 0] < c_r < \max[U_{\max}, 0], \tag{5.3.37}$$

which we note is the statement of Theorem 6.

Before progressing to our next theorem, we briefly comment on how this result differs from its rigid counterpart by Rayleigh, which would bound c_r in the range of U so that $U_{\min} < c_r < U_{\max}$.

Consider a flow with $U_{\min} > 0$ and $U_{\max} > 0$. According to Theorem 6, the resulting bound for an unstable mode is $0 < c_r < U_{\max}$. We therefore have not ruled out unstable modes with $0 < c_r \leq U_{\min}$. In this sense, Theorem 6 is weaker than its rigid analogue.

A natural next step is to seek a modification of Howard's semicircle theorem [13].

Theorem 7. *Let $V \geq 0$. If $U \geq 0$ everywhere (and $U > 0$ somewhere), all temporally unstable axisymmetric modes must satisfy $|c|^2 - c_r \max_{r\in[\delta,1]} U < 0$.*

We begin by formulating expressions that will be useful in our proof of Theorem 7. Rearrangement of (5.3.36) allows us to write

$$\int_\delta^1 \frac{U\,Q}{r}\,\mathrm{d}r = \alpha^2\delta|\hat{\eta}|^2\left(\alpha^2\check{m} + \frac{\alpha\check{D}}{2c_i}\right)c_r + \int_\delta^1 \frac{c_r\,Q}{r}\,\mathrm{d}r. \tag{5.3.38}$$

Taking the real part of (5.3.35), we obtain

$$\int_\delta^1 \frac{\left[(U-c_r)^2 - c_i^2\right]\,Q}{r}\,\mathrm{d}r = -\alpha^2\delta|\hat{\eta}|^2\left(\alpha^2\check{m}\left(c_r^2 - c_i^2\right) - \alpha\check{D}c_i - \check{K}\right). \tag{5.3.39}$$

Expanding the left-hand side of (5.3.39) gives

$$\int_\delta^1 \frac{\left[(U-c_r)^2 - c_i^2\right]\,Q}{r}\,\mathrm{d}r = \int_\delta^1 \frac{U^2Q}{r}\,\mathrm{d}r - 2c_r\int_\delta^1 \frac{UQ}{r}\,\mathrm{d}r + c_r^2\int_\delta^1 \frac{Q}{r}\,\mathrm{d}r - c_i^2\int_\delta^1 \frac{Q}{r}\,\mathrm{d}r. \tag{5.3.40}$$

Upon simplification, substituting (5.3.38) for the second integral on the right-hand side of (5.3.40) reveals

$$\int_\delta^1 \frac{\left[(U-c_r)^2 - c_i^2\right]\,Q}{r}\,\mathrm{d}r = \int_\delta^1 \frac{U^2Q}{r}\,\mathrm{d}r - 2\alpha^2\delta|\hat{\eta}|^2\left(\alpha^2\check{m} + \frac{\alpha\check{D}}{2c_i}\right)c_r^2 - c_r^2\int_\delta^1 \frac{Q}{r}\,\mathrm{d}r - c_i^2\int_\delta^1 \frac{Q}{r}\,\mathrm{d}r, \tag{5.3.41}$$

which can be written as

$$\int_\delta^1 \frac{\left[(U-c_r)^2 - c_i^2\right] Q}{r}\,\mathrm{d}r = \int_\delta^1 \frac{U^2 Q}{r}\,\mathrm{d}r - 2\alpha^2\delta|\hat{\eta}|^2\left(\alpha^2\check{m} + \frac{\alpha\check{D}}{2c_i}\right)c_r^2 - |c|^2\int_\delta^1 \frac{Q}{r}\,\mathrm{d}r. \tag{5.3.42}$$

Together with (5.3.39), this gives

$$\int_\delta^1 \frac{U^2\,Q}{r}\,\mathrm{d}r = \alpha^2\delta|c|^2|\hat{\eta}|^2\left(\alpha^2\check{m} + \frac{\alpha\check{D}}{c_i} + \frac{\check{K}}{|c|^2}\right) + \int_\delta^1 \frac{|c|^2\,Q}{r}\,\mathrm{d}r. \tag{5.3.43}$$

after some manipulation. We will find the relations (5.3.38) and (5.3.43) helpful in what follows.

Letting $U_{\max} = \max_{r\in[\delta,1]} U$ and $U_{\min} = \min_{r\in[\delta,1]} U$, it is evident that

$$\int_\delta^1 (U - U_{\max})\,(U - U_{\min})\,\frac{Q}{r}\,\mathrm{d}r \le 0. \tag{5.3.44}$$

since Q is positive.

This is possible if and only if

$$\int_\delta^1 \left(U^2 - U_{\max}U + U_{\min}\,(U_{\max} - U)\right)\frac{Q}{r}\,\mathrm{d}r \le 0, \tag{5.3.45}$$

which can be written as

$$\int_\delta^1 \left(\frac{U^2 Q}{r} - U_{\max}\frac{UQ}{r} + U_{\min}\,(U_{\max} - U)\,\frac{Q}{r}\right)\mathrm{d}r \le 0. \tag{5.3.46}$$

Upon rearrangement, substitution of (5.3.43) and (5.3.38) into the first two terms yields

$$\int_\delta^1 \frac{Q}{r}\,\left(|c|^2 - c_r U_{\max}\right)\,\mathrm{d}r + \alpha^2\delta|\hat{\eta}|^2\left[\alpha^2\check{m}\left(|c|^2 - c_r U_{\max}\right) + \frac{\alpha\check{D}}{c_i}\left(|c|^2 - \frac{c_r U_{\max}}{2}\right)\right] + \alpha^2\delta|\hat{\eta}|^2\check{K} + U_{\min}\int_\delta^1 (U_{\max} - U)\,\frac{Q}{r}\,\mathrm{d}r \le 0. \tag{5.3.47}$$

We will focus on flows with $U \ge 0$ everywhere (and $U > 0$ somewhere), so that $U_{\min} \ge 0$ and $U_{\max} > 0$. Suppose that we have a temporally unstable mode with

$$|c|^2 - c_r U_{\max} \ge 0. \tag{5.3.48}$$

From Theorem 6, we know that $c_r > 0$. This means

$$|c|^2 - \frac{1}{2}c_r U_{\max} > |c|^2 - c_r U_{\max} \tag{5.3.49}$$

and so, in view of (5.3.48),

$$|c|^2 - \frac{1}{2} c_r U_{\max} > 0. \tag{5.3.50}$$

This leads us to a contradiction, as it suggests that the left hand side of (5.3.47) is strictly positive. Therefore, we require that all unstable modes satisfy

$$|c|^2 - c_r U_{\max} < 0, \tag{5.3.51}$$

which is equivalent to writing

$$\left(c_r - \frac{U_{\max}}{2}\right)^2 + c_i^2 < \left(\frac{U_{\max}}{2}\right)^2. \tag{5.3.52}$$

This concludes the proof of Theorem 7.

The result (5.3.52) is analogous to Howard's semicircle theorem for parallel flows over rigid boundaries, which states that unstable modes satisfy

$$\left(c_r - \frac{1}{2}\left(U_{\min} + U_{\max}\right)\right)^2 + c_i^2 < \left(\frac{1}{2}\left(U_{\max} - U_{\min}\right)\right)^2. \tag{5.3.53}$$

Recall that our criteria accounting for flexibility considers basic flows with the property $U \geq 0$. When $U_{\min} = 0$, the inequalities for the rigid (5.3.53) and flexible (5.3.52) cases both offer the same restriction. In the case $U_{\min} > 0$, however, the semicircle described for the rigid case (5.3.53) has a smaller radius than that of (5.3.52).

Theorems 6 and 7 lead us to the following corollary:

Corollary 3. *Let $V \geq 0$. For a flow with $U \geq 0$ everywhere (and $U > 0$ somewhere), all temporally unstable axisymmetric modes must satisfy $|c|^2 < (\max_{r\in[\delta,1]} U)^2$.*

Since $U > 0$ somewhere in the flow, we have $U_{\max} > 0$. Using Theorem 6, we then deduce that an unstable mode has $c_r < U_{\max}$. This means

$$c_r U_{\max} < (U_{\max})^2. \tag{5.3.54}$$

Using Theorem 7 (specifically inequality (5.3.51)), we have

$$|c|^2 < c_r U_{\max}. \tag{5.3.55}$$

By transitivity, combining (5.3.54) and (5.3.55) gives

$$|c|^2 < (U_{\max})^2, \tag{5.3.56}$$

completing the proof of Corollary 3.

We are able to establish a stronger version of this corollary that does not restrict the base profile $U(r)$ to be positive. This forms our next theorem.

Theorem 8. *Let $V \geq 0$. For a flow such as this, an unstable axisymmetric mode must have a wavespeed c such that $|c|^2 < (\max |U|)^2$.*

To prove this theorem, we will draw upon equations we have derived previously. Multiplying (5.3.36) and (5.3.39) by c_r and c_i respectively, and subsequently adding the resulting equations, yields

$$c_i \int_\delta^1 \left(U^2 - |c|^2\right) \frac{Q}{r}\, \mathrm{d}r = \alpha^2 \delta |\hat{\eta}|^2 |c|^2 \left(\alpha^2 \check{m} c_i + \alpha \check{D} + \frac{\check{K} c_i}{|c|^2}\right) \tag{5.3.57}$$

For an unstable mode,

$$c_i \int_\delta^1 \left(U^2 - |c|^2\right) \frac{Q}{r}\, \mathrm{d}r \leq c_i \int_\delta^1 \left(\max\left(U^2\right) - |c|^2\right) \frac{Q}{r}\, \mathrm{d}r, \tag{5.3.58}$$

which, in view of (5.3.57), implies that

$$c_i \left(\max\left(U^2\right) - |c|^2\right) \int_\delta^1 \frac{Q}{r}\, \mathrm{d}r \geq \alpha^2 \delta |\hat{\eta}|^2 |c|^2 \left(\alpha^2 \check{m} c_i + \alpha \check{D} + \frac{\check{K} c_i}{|c|^2}\right). \tag{5.3.59}$$

Since c_i is assumed to be positive, the right-hand side of (5.3.59) is strictly positive. The left-hand side must thus also be strictly positive, and so we conclude that

$$|c|^2 < \max\left(U^2\right), \tag{5.3.60}$$

as desired. This completes the proof of Theorem 8.

As expressed by Drazin and Howard [73], a result due to Høiland relates the wavenumber of a disturbance to the imaginary part of its wavespeed:

$$\alpha c_i \leq \frac{\max_{r\in[\delta,1]} |U'|}{2}. \tag{5.3.61}$$

In the subsequent theorems, we strive to relate the wavenumber of an unstable mode with the strength of its instability when the basic velocity is not constant.

Theorem 9. *Let $V = 0$. Assume $U(r)$ is not constant. Temporally unstable axisymmetric modes must satisfy $\alpha c_i < \frac{\max_{r\in[\delta,1]} |U'|}{2}$.*

Theorem 10. *Let $V > 0$. Assume $U(r)$ is not constant. A temporally unstable axisymmetric mode with $c_r > 2V$ must satisfy $\alpha c_i < \frac{\max_{r\in[\delta,1]} |U'|}{2}$.*

Following the methods in Drazin and Howard [73], we introduce a function G such that

$$G = \frac{\phi}{(U-c)^{1/2}}. \tag{5.3.62}$$

Upon use of the Rayleigh equation (5.1.6), we can form a differential equation in G:

$$\frac{\mathrm{d}}{\mathrm{d}r}\left[(U-c)\,G'\right] - \frac{(U-c)G'}{r} + \frac{U'\,G}{2r} - G\left[\frac{U''}{2} + \alpha^2(U-c) + \frac{(U')^2}{4(U-c)}\right] = 0. \tag{5.3.63}$$

Multiplying by $\frac{G^*}{r}$ and integrating across the annular region reveals

$$\int_\delta^1 \frac{(U-c)\,|G'|^2}{r}\,\mathrm{d}r - \int_\delta^1 \frac{U'\,|G|^2}{2r^2}\,\mathrm{d}r + \int_\delta^1 \frac{|G|^2}{r}\left(\frac{U''}{2} + \alpha^2\,(U-c) + \frac{(U')^2}{4\,(U-c)}\right)\,\mathrm{d}r = \left[\frac{G^*G'\,(U-c)}{r}\right]_\delta^1. \tag{5.3.64}$$

The boundary conditions (5.3.1), (5.3.6), (5.3.8a), (5.3.10) can be used to find

$$\left[\frac{G^*G'\,(U-c)}{r}\right]_\delta^1 = -\alpha^2\delta|\hat{\eta}|^2|V-c|\left(\frac{\alpha^2c^2\check{m} + \mathrm{i}\alpha c\check{D} - \check{K}}{V-c} + \frac{U'(\delta)}{2}\right). \tag{5.3.65}$$

We substitute (5.3.65) into (5.3.64), take the imaginary part of the resulting equation and multiply by c_i. This gives

$$c_i^2\int_\delta^1 \frac{|G'|^2}{r}\,\mathrm{d}r + c_i^2\int_\delta^1 \frac{\alpha^2|G|^2}{r}\,\mathrm{d}r - \frac{c_i^2}{4}\int_\delta^1 \frac{|G|^2}{r}\frac{(U')^2}{|U-c|^2}\,\mathrm{d}r = -\frac{\alpha^2\delta|\hat{\eta}|^2c_i}{|V-c|}\left[\alpha^2\check{m}c_i\left(|c|^2 - 2Vc_r\right) + \alpha\check{D}\left(|c|^2 - c_rV\right) + \check{K}c_i\right]. \tag{5.3.66}$$

Since

$$|U-c|^2 = (U-c_r)^2 + c_i^2 \geq c_i^2, \tag{5.3.67}$$

we may write

$$\int_\delta^1 \frac{|G|^2}{r}\frac{(U')^2}{|U-c|^2}\,\mathrm{d}r \leq \frac{(\max|U'|)^2}{c_i^2}\int_\delta^1 \frac{|G|^2}{r}\,\mathrm{d}r. \tag{5.3.68}$$

Using (5.3.66), this gives

$$\int_\delta^1 \frac{|G|^2}{r}\left(\alpha^2c_i^2 - \frac{(\max|U'|)^2}{4}\right)\,\mathrm{d}r \leq -\frac{\alpha^2\delta|\hat{\eta}|^2c_i}{|V-c|}\left(\alpha^2\check{m}c_i\left(|c|^2 - 2Vc_r\right) + \alpha\check{D}\left(|c|^2 - c_rV\right) + \check{K}c_i\right). \tag{5.3.69}$$

Case 1: $\mathbf{V = 0}$. Let us first look at the case of two stationary cylinders. In this scenario, (5.3.69) simplifies to

$$\int_\delta^1 \frac{|G|^2}{r}\left(\alpha^2 c_i^2 - \frac{(\max|U'|)^2}{4}\right)\,\mathrm{d}r \leq -\alpha^2\delta|\hat{\eta}|^2|c|\left(\alpha^2\check{m}c_i + \alpha\check{D} + \frac{\check{K}c_i}{|c|^2}\right)c_i. \tag{5.3.70}$$

For an unstable mode, the right-hand side of (5.3.70) is strictly negative. The left-hand side must also then be strictly negative, and so we deduce that

$$\alpha c_i < \frac{\max|U'|}{2}, \tag{5.3.71}$$

as stated in Theorem 9.

Case 2: $\mathbf{V > 0}$. We now look for a bound on c_i when the inner cylinder moves. Suppose we have an unstable mode with $c_r > 2V$. Then

$$|c|^2 - 2c_rV > 0 \qquad \text{and} \qquad |c|^2 - c_rV > 0, \tag{5.3.72}$$

and the right-hand side of (5.3.69) is strictly negative. We thus require that

$$\alpha c_i < \frac{\max|U'|}{2}, \tag{5.3.73}$$

which proves Theorem 10.

Having derived modified versions of classical inviscid theorems to account for a flexible inner cylinder, it is worthwhile to see what stability properties we can learn about a base flow of the form (2.2.2).

5.4 Applying the modified inviscid theorems

Armed with the theorems above, we can make some statements regarding the inviscid instability of a base flow of the form (2.2.2), repeated below:

$$U_0(r) = 1 - r^2 + \frac{(V - 1 + \delta^2)}{\log\delta}\log r, \quad \delta \leq r \leq 1.$$

For this base flow,

$$\frac{\mathrm{d}}{\mathrm{d}r}\left(\frac{U_0'}{r}\right) = \frac{-2\,(V - 1 + \delta^2)}{r^3\log\delta}. \tag{5.4.1}$$

We explore the flexible case for different choices of V, noting that U_0 is a flow that is non-negative everywhere, and strictly positive somewhere.

Case 1: $V = 0$. For a stationary inner cylinder, $U_0 \frac{\mathrm{d}}{\mathrm{d}r}\left(\frac{U_0'}{r}\right) = 2U_0\left(\frac{1-\delta^2}{r^3 \log \delta}\right) < 0$ for $r \in (\delta, 1)$. Using Theorems 6, 7 and 9, we deduce all temporally unstable modes must be such that

$$0 < c_r < U_{\max}, \quad |c|^2 - c_r U_{\max} < 0, \quad \alpha c_i < \frac{\max_{r\in[\delta,1]} |U_0'|}{2}, \tag{5.4.2}$$

where

$$U_{\max} = U_0(r_1), \qquad r_1 = \sqrt{\frac{\delta^2 - 1}{2\log\delta}}. \tag{5.4.3}$$

Case 2: $0 < V < 1 - \delta^2 + 2\delta^2 \log \delta$. For this range of V, the quantity $\frac{\mathrm{d}}{\mathrm{d}r}\left(\frac{U_0'}{r}\right)$ is negative throughout the flow. The maximum value of U_0 is greater than V, so there is a region in the flow where $(U_0 - V)$ is positive. Therefore, $(U_0 - V)\frac{\mathrm{d}}{\mathrm{d}r}\left(\frac{U_0'}{r}\right)$ is negative somewhere in the flow. Theorems 6 and 7 allow us to conclude that all unstable modes must be such that

$$0 < c_r < U_{\max}, \quad |c|^2 - c_r U_{\max} < 0, \tag{5.4.4}$$

where

$$U_{\max} = U_0(r_2), \qquad r_2 = \sqrt{\frac{V + \delta^2 - 1}{2\log\delta}}. \tag{5.4.5}$$

Further to this, unstable modes with $c_r > 2V$ must satisfy

$$\alpha c_i < \frac{\max_{r\in[\delta,1]} |U_0'|}{2} \tag{5.4.6}$$

in line with Theorem 10.

Case 3: $V \geq 1 - \delta^2 + 2\delta^2 \log \delta$. The base velocity attains its maximum value at the wall of the inner cylinder, so $U_{\max} = V$. In such a case, any instability must be such that $0 < c_r < V$ to comply with Theorem 6. In this scenario, Theorem 10 does not shed more light on the problem, as we know unstable modes cannot have $c_r > 2V$.

In contrast to the scenario involving both a rigid inner and rigid outer cylinder, we are unable to rule out inviscid instability when the inner cylinder is flexible. However, we have been able to provide bounds for the wavespeeds of unstable modes (provided they exist).

5.5 Summary

In summary, this chapter explored the inviscid linear stability of axisymmetric, swirl-free flows through an annular region between a flexible inner cylinder and rigid outer cylinder. Following the work of previous literature [66, 67, 68, 69] to account for the presence of a flexible inner cylinder, we derived theorems reminiscent of Rayleigh's inflection point theorem and Fjørtfot's theorem. We also modified results such as Rayleigh's wavespeed restriction for non-neutral modes, Howard's semi-circle theorem and Høiland's theorem. Owing to our boundary conditions, our results are weaker than their classical counterparts. To conclude the chapter, we applied these theorems to a base flow that pertains to APCF.

Having studied the inviscid problem, we return to the full viscous problem (2.3.11, 2.3.12-2.3.14) and seek to understand the behaviour of neutral modes at asymptotically large Reynolds numbers. Though the bulk of the flow will be dominated by inertial forces, we will incorporate the effects of viscosity near the cylinder walls.

Chapter 6

An asymptotic approach at large Reynolds numbers: a lower-branch analysis

Smith and Cowley [45] conducted an asymptotic analysis into the linear and weakly non-linear stability of plane Poiseuille-Couette flow, noting that the linear lower-branch neutral mode of plane Poiseuille flow has a wavenumber that is such that $\alpha = O(R^{-1/7})$ when the Reynolds number becomes asymptotically large. This has previously been shown by Lin [74], who studied the asymptotic behaviour of the neutral curve by direct consideration of the Orr-Sommerfeld equation, and has also been demonstrated by Cowley and Wu [75].

In their account detailing the use of asymptotic linear theory as a means to understand transition, Cowley and Wu [75] discuss how to arrive at distinguished scalings for the lower and upper branch of the neutral curve. They adopt a 'maximal-interactions' approach when considering the different processes that occur in the flow, and explain that the different structures for a lower and upper branch mode are indicative of the different physical balances in the flow for each mode. This guides our analysis below.

Walton [48] used asymptotic methods to study the stability of APCF when the inner cylinder is rigid. He provided a detailed analysis of the lower-branch and upper-branch scalings of the neutral curve at large Reynolds numbers, in addition to studying what he has termed a hybrid scaling. In this thesis, we adapt this work to account for the flexibility of the inner cylinder, and seek new scalings that arise as a result of the cylinder flexibility. This chapter is concerned with lower-branch scalings and, and in later chapters, we explore upper-branch and the hybrid scalings.

Before commencing our analysis, it will be helpful to briefly revisit the linearised disturbance equations (2.3.11) of Chapter 2, which are repeated here for convenience.

We superimpose our base velocity and pressure field with travelling-wave disturbances of axial wavenumber α and wavespeed c,

$$u = U_0(r) + \Delta\hat{u}(r)\mathrm{e}^{\mathrm{i}\alpha(x-ct)} + c.c, \quad v = \Delta\hat{v}(r)\mathrm{e}^{\mathrm{i}\alpha(x-ct)} + c.c, \tag{6.0.1a}$$

$$p = p_0 - \frac{4x}{R} + \Delta\hat{p}(r)\mathrm{e}^{\mathrm{i}\alpha(x-ct)} + c.c, \quad \Delta \ll 1, \tag{6.0.1b}$$

where the base flow (2.2.2) is given by

$$U_0(r) = 1 - r^2 + \frac{(V - 1 + \delta^2)}{\log\delta}\ \log r, \quad \delta \le r \le 1. \tag{6.0.2}$$

We have seen that the disturbance shape functions $\hat{u}(r), \hat{v}(r)$ and $\hat{p}(r)$ are governed by the linearised disturbance equations (2.3.11),

$$\mathrm{i}\alpha\hat{u} + \frac{\mathrm{d}\hat{v}}{\mathrm{d}r} + \frac{\hat{v}}{r} = 0, \tag{6.0.3a}$$

$$\mathrm{i}\alpha\left(U_0 - c\right)\hat{u} + \hat{v}\frac{\mathrm{d}U_0}{\mathrm{d}r} = -\mathrm{i}\alpha\hat{p} + \frac{1}{R}\left[\frac{\mathrm{d}^2\hat{u}}{\mathrm{d}r^2} + \frac{1}{r}\frac{\mathrm{d}\hat{u}}{\mathrm{d}r} - \alpha^2\hat{u}\right], \tag{6.0.3b}$$

$$\mathrm{i}\alpha\left(U_0 - c\right)\hat{v} = -\frac{\mathrm{d}\hat{p}}{\mathrm{d}r} + \frac{1}{R}\left[\frac{\mathrm{d}^2\hat{v}}{\mathrm{d}r^2} + \frac{1}{r}\frac{\mathrm{d}\hat{v}}{\mathrm{d}r} - \frac{\hat{v}}{r^2} - \alpha^2\hat{v}\right], \tag{6.0.3c}$$

subject to

$$\hat{u}(1) = 0, \quad \hat{v}(1) = 0, \tag{6.0.4}$$

$$\mathrm{i}\alpha(V - c)\hat{u}(\delta) + \hat{v}(\delta)U_0'(\delta) = 0, \tag{6.0.5}$$

$$\hat{p}(\delta) = \frac{2}{R}\hat{v}'(\delta) + \left(-\alpha^2c^2m + \frac{K}{R^2}\right)\frac{\hat{u}(\delta)}{U_0'(\delta)}, \tag{6.0.6}$$

where $V \neq 1 - \delta^2 + 2\delta^2\log\delta$.

Seeking the behaviour of a neutrally stable disturbance, we take c to be real in what follows.

6.1 Lower-branch analysis I: a mode with $\alpha = O\left(R^{-1/7}\right)$

At asymptotically large Reynolds numbers, we anticipate that the bulk of the flow is dominated by inertial forces. Near the cylinder walls, however, viscous forces become significant and there is a balance between the inertial, pressure and viscous terms in the governing linear disturbance equations. For sufficiently small sliding velocities, we anticipate that the lower-branch mode behaviour will be captured by a three-zone structure (see figure 6.1.1) consisting of an inviscid core surrounded by viscous wall layers. Critical layers are situated where the basic velocity is equal to the wavespeed of the mode. A critical layer is assumed to be embedded in the upper viscous layer and, if the sliding velocity of the inner cylinder is smaller than the disturbance wavespeed of the lower-branch mode, the lower viscous wall layer.

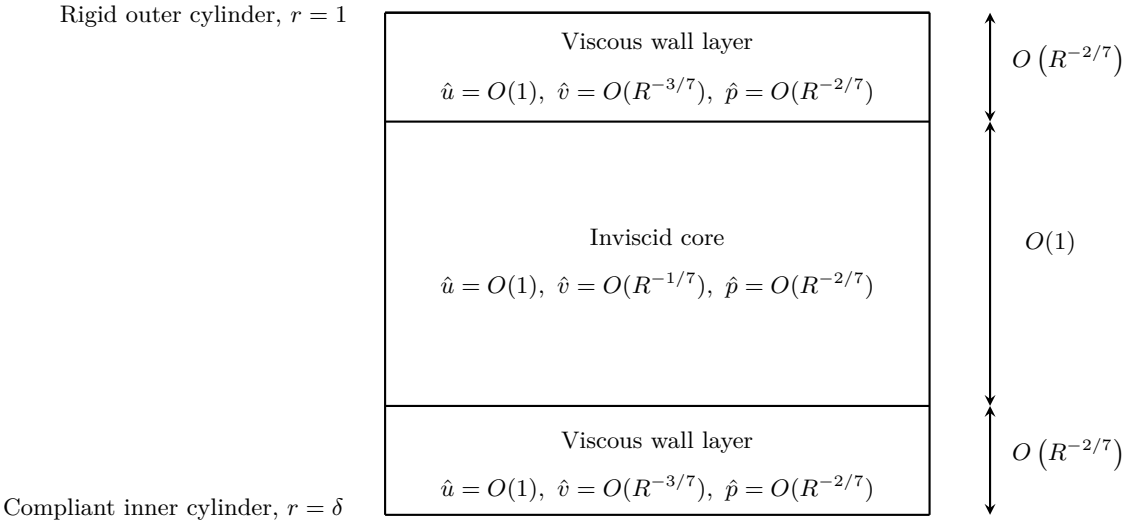

Figure 6.1.1: Schematic of the asymptotic structure of the lower-branch mode with $\alpha = O\left(R^{-1/7}\right)$ and $c = O\left(R^{-2/7}\right)$. The cylinder properties are $V = O\left(R^{-2/7}\right)$, $K = O\left(R^{12/7}\right)$ and $m = O\left(R^{4/7}\right)$.

We will seek a solution to the disturbance equations for asymptotically large Reynolds numbers and small sliding velocities V such that

$$V = \epsilon^2 V_0, \quad \epsilon \ll 1, \tag{6.1.1}$$

where ϵ is a small parameter that will be determined in terms of the Reynolds number.

The base velocity (6.0.2) may now be expressed as

$$U_0 = U_{00} + \epsilon^2\, U_{01}, \tag{6.1.2a}$$

with

$$U_{00} = 1 - r^2 - (1-\delta^2)\frac{\log r}{\log \delta} \quad \text{and} \quad U_{01} = V_0 \frac{\log r}{\log \delta}. \tag{6.1.2b}$$

Much of the analysis that follows will focus on near-wall dynamics. To facilitate this, we preemptively explore here the behaviour of the base velocity U_0 near the cylinder walls by performing Taylor expansions of (6.1.2b) about $r = 1$ and $r = \delta$. Near the outer cylinder, where $r \to 1^-$,

$$U_{00} \sim \lambda_+^{(0)}(1-r) + \lambda_+^{(10)}(1-r)^2, \qquad U_{01} \sim \lambda_+^{(1)}(1-r), \tag{6.1.3a}$$

and near the inner cylinder, where $r \to \delta^+$,

$$U_{00} \sim \lambda_-^{(0)}(r-\delta) + \lambda_-^{(10)}(r-\delta)^2, \qquad U_{01} \sim V_0 + \lambda_-^{(1)}(r-\delta), \tag{6.1.4a}$$

where

$$\lambda_+^{(0)} = \quad 2 + \frac{(1-\delta^2)}{\log \delta}, \qquad \lambda_+^{(10)} = -1 + \frac{(1-\delta^2)}{2\log \delta}, \qquad \lambda_+^{(1)} = -\frac{V_0}{\log \delta}, \tag{6.1.5a}$$

$$\lambda_-^{(0)} = -2\delta - \frac{(1-\delta^2)}{\delta \log \delta}, \qquad \lambda_-^{(10)} = -1 + \frac{(1-\delta^2)}{2\delta^2 \log \delta}, \qquad \lambda_-^{(1)} = \frac{V_0}{\delta \log \delta}. \tag{6.1.5b}$$

The core region

It seems natural to begin by considering the size of the lower-branch disturbance in the bulk of the flow. As the Reynolds number becomes asymptotically large, the wavenumbers on the lower branch of our neutral stability curve in the (R, α) plane become small. With this in mind, we write $\alpha = O(\epsilon)$. We also suppose that c is small, so that $c = O(q)$ where $q \ll 1$ will be determined during the course of our analysis. Numerical computations provide motivation for these choices for α and c.

Seeking a linear disturbance, we let $\hat{u} = O(1)$ without loss of generality. The linearised continuity equation (6.0.3a) then suggests that $\hat{v} = O(\epsilon)$. The basic flow is much larger than c in this region, and we anticipate $\hat{p} = O(\epsilon^2)$ so as to preserve the inertia and pressure terms in the linearised radial momentum equation (6.0.3c). Our disturbance expansion to leading order is thus

$$\hat{u} = F_0 + \cdots, \quad \hat{v} = \epsilon G_0 + \cdots, \quad \hat{p} = \epsilon^2 P_0 + \cdots, \quad \alpha = \epsilon \alpha_0 + \cdots, \quad c = q c_0 + \cdots. \tag{6.1.6a}$$

Substituting these expansions into the governing linearised disturbance equations (6.0.3), we find to leading order the inviscid system

$$\mathrm{i}\alpha_0 F_0 + \frac{\mathrm{d}G_0}{\mathrm{d}r} + \frac{G_0}{r} = 0, \quad \mathrm{i}\alpha_0 U_{00} F_0 + G_0 \frac{\mathrm{d}U_{00}}{\mathrm{d}r} = 0, \quad \mathrm{i}\alpha_0 U_{00} G_0 + \frac{\mathrm{d}P_0}{\mathrm{d}r} = 0. \tag{6.1.7a,b,c}$$

We can manipulate these equations to form a first order separable differential equation for G_0, specifically

$$\frac{\mathrm{d}G_0}{\mathrm{d}r} + \left(\frac{1}{r} - \frac{1}{U_0}\frac{\mathrm{d}U_0}{\mathrm{d}r}\right) G_0 = 0. \tag{6.1.8}$$

This has the solution

$$G_0 = -\mathrm{i}\alpha_0 A_0 \frac{U_0}{r}, \tag{6.1.9}$$

where A_0 is an unknown constant. F_0 and P_0 are now straightforward to find; upon rearrangement of the continuity equation (6.1.7a) and integration of the radial momentum equation (6.1.7c), we obtain

$$F_0 = \frac{A_0 U_{00}'}{r} \quad \text{and} \quad P_0 = \hat{P}_0 + \alpha_0^2 A_0 I(r), \tag{6.1.10}$$

where $\hat{P}_0$ is a constant and

$$I(r) = \int_r^1 \frac{{U_{00}}^2}{\tilde{r}}\,\mathrm{d}\tilde{r}. \tag{6.1.11}$$

It is useful to examine the behaviour of the disturbance as we approach the cylinder walls as this will motivate our scalings in the viscous regions. As $r \to 1^-$,

$$F_0 \to -A_0\lambda_+^{(0)}, \quad G_0 \sim -\mathrm{i}\alpha_0 A_0 \lambda_+^{(0)}\,(1-r)\,, \quad P_0 \to \hat{P}_0, \tag{6.1.12}$$

and as $r \to \delta^+$,

$$F_0 \to \frac{A_0\lambda_-^{(0)}}{\delta}, \quad G_0 \sim -\frac{\mathrm{i}\alpha_0 A_0 \lambda_-^{(0)}}{\delta}\,(r-\delta)\,, \quad P_0 \to \hat{P}_0 + \alpha_0^2 A_0 I(\delta). \tag{6.1.13}$$

The upper viscous wall layer

Assuming that the thickness of the viscous wall layer is given by h, we write $r = 1 - hy_+$, where h is to be determined and y_+ is an order one variable. The behaviour of the disturbance in the core as it approaches the outer cylinder guides our scalings in the upper viscous wall layer; we observe that $F_0 = O(1)$, $G_0 = O(h)$ and $P_0 = O(1)$ as we approach the outer cylinder, suggesting the scalings $\hat{u} = O(1)$, $\hat{v} = O(\epsilon h)$ and $\hat{p} = O(\epsilon^2)$ for the disturbance in the wall layer.

A critical layer is embedded within the upper viscous wall layer, requiring that $U_0 \sim c$. The behaviour of U_0 near the outer cylinder is described by (6.1.3a) and can be written as

$$U_0 = \lambda_+^{(0)} h y_+ + \cdots = O(h). \tag{6.1.14}$$

Hence we observe that the wavespeed must be of the same magnitude as the thickness of the wall layer, that is, $c = O(h)$. It now remains to find a relationship between ϵ and h. In the viscous region, we seek a balance between the inertia, pressure and viscous terms in the axial momentum equation (6.0.3b):

$$\mathrm{i}\alpha\left(U_0 - c\right)\hat{u} \sim \mathrm{i}\alpha\hat{p} \sim \frac{1}{R}\frac{\mathrm{d}^2\hat{u}}{\mathrm{d}r^2} \implies \epsilon h \sim \epsilon^3 \sim R^{-1}h^{-2}. \tag{6.1.15}$$

From this we deduce that the thickness h of the layer is of the order ϵ^2, where

$$\epsilon = R^{-1/7}, \tag{6.1.16}$$

and we can write

$$\alpha = R^{-1/7}\alpha_0 + \cdots, \qquad c = R^{-2/7}c_0 + \cdots. \tag{6.1.17}$$

Using the above considerations, we have to leading order

$$\hat{u} = u_+ + \cdots, \quad \hat{v} = -\epsilon^3 v_+ + \cdots, \quad \hat{p} = \epsilon^2 p_+ + \cdots, \quad \alpha = \epsilon\alpha_0 + \cdots, \quad c = \epsilon^2 c_0 + \cdots, \tag{6.1.18a}$$

$$U_0 = \epsilon^2 \lambda_+^{(0)} y_+ + \cdots, \quad r = 1 - \epsilon^2 y_+. \tag{6.1.18b}$$

Substituting these expansions into the governing linearised system (6.0.3), we find that the disturbance must satisfy to leading order

$$\mathrm{i}\alpha_0 u_+ + \frac{\mathrm{d}v_+}{\mathrm{d}y_+} = 0, \tag{6.1.19a}$$

$$\mathrm{i}\alpha_0\left(\lambda_+^{(0)} y_+ - c_0\right) u_+ + \lambda_+^{(0)} v_+ = -\mathrm{i}\alpha_0 p_+ + \frac{\mathrm{d}^2 u_+}{\mathrm{d}y_+^2}, \tag{6.1.19b}$$

$$\frac{\mathrm{d}p_+}{\mathrm{d}y_+} = 0, \tag{6.1.19c}$$

subject to the no-slip conditions (6.0.4) on the outer cylinder, which give

$$u_+ = v_+ = 0 \quad \text{on} \quad y_+ = 0. \tag{6.1.20}$$

Matching the core solution, the disturbance must satisfy

$$p_+ = \hat{P}_0 \ \text{ for all } \ y_+, \tag{6.1.21}$$

and

$$u_+ \to -A_0 \lambda_+^{(0)} \ \text{ as } \ y_+ \to \infty \tag{6.1.22}$$

in view of (6.1.12). We differentiate the axial momentum equation (6.1.19b), and upon simplification with the continuity equation (6.1.19a), obtain

$$\frac{\mathrm{d}^3 u_+}{\mathrm{d}y_+^3} - \mathrm{i}\alpha_0\left(\lambda_+^{(0)} y_+ - c_0\right)\frac{\mathrm{d}u_+}{\mathrm{d}y_+} = 0. \tag{6.1.23}$$

We reduce the order of this differential equation by introducing a new variable $\tau_+(y_+)$ such that $\tau_+(y_+) = \frac{\mathrm{d}u_+}{\mathrm{d}y_+}$, and then apply the linear transformation $\xi_+ = a_+ y_+ + b_+$, where

$$a_+ = \left(\mathrm{i}\alpha_0 \lambda_+^{(0)}\right)^{1/3} \quad \text{and} \quad b_+ = -\frac{\mathrm{i}\alpha_0 c_0}{\left(\mathrm{i}\alpha_0\lambda_+^{(0)}\right)^{2/3}}. \tag{6.1.24}$$

The evolution of τ_+ with respect to ξ_+ is described exactly by the Airy equation

$$\frac{\mathrm{d}^2\tau_+}{\mathrm{d}\xi_+^2} - \xi_+\tau_+ = 0, \tag{6.1.25}$$

the solutions of which are well-known. Hence we have

$$\tau_+ = C_1 \mathrm{Ai}\left(\xi_+\right) + C_2 \mathrm{Bi}\left(\xi_+\right), \tag{6.1.26}$$

where $\mathrm{Ai}\left(\xi_+\right)$ and $\mathrm{Bi}\left(\xi_+\right)$ are the linearly independent Airy functions of the first and second kind respectively, and C_1 and C_2 are constants to be determined. The asymptotic behaviour of the Airy functions are well-known [76]. It is reasonable to require that τ_+ remains bounded as $y_+ \to \infty$, so we impose $C_2 = 0$. Integrating (6.1.26) with respect to y_+ yields

$$u_+(y_+) = \frac{C_1}{a_+}\int_{b_+}^{\xi_+} \mathrm{Ai}\left(\xi_+\right)\mathrm{d}\xi_+ \tag{6.1.27}$$

upon using our condition (6.1.20) and performing a change of variables. It remains to find the constant C_1. Letting $\xi_+ \to \infty$, we see that

$$u_+ \to \frac{C_1}{a_+}\int_{b_+}^{\infty} \mathrm{Ai}\left(\xi_+\right)\mathrm{d}\xi_+. \tag{6.1.28}$$

In order to satisfy the condition $u_+ = -A_0\lambda_+^{(0)}$ as $\xi_+ \to \infty$ (6.1.22), we demand that

$$C_1 = -\frac{A_0\lambda_+^{(0)} a_+}{\kappa(b_+)}, \quad \text{where we have defined} \quad \kappa(b_+) = \int_{b_+}^{\infty} \mathrm{Ai}\left(\xi_+\right) d\xi_+. \tag{6.1.29}$$

This leads us to

$$u_+(y_+) = -\frac{A_0\lambda_+^{(0)}}{\kappa(b_+)}\int_{b_+}^{\xi_+} \mathrm{Ai}\left(\xi_+\right)\mathrm{d}\xi_+. \tag{6.1.30}$$

It now remains to find an expression for $\hat{P}_0$. We evaluate the leading order axial momentum equation (6.1.19b) on $y_+ = 0$. Recalling that $u_+ = v_+ = 0$ on $y_+ = 0$ (6.1.20) and $p_+ = \hat{P}_0$ (6.1.21), we have

$$\left.\frac{\mathrm{d}^2 u_+}{\mathrm{d}y_+^2}\right|_{y_+=0} = \mathrm{i}\alpha_0 \hat{P}_0. \tag{6.1.31}$$

Substituting our expression (6.1.30) for u_+ and rearranging yields

$$\hat{P}_0 = \frac{A_0 \left(\mathrm{i}\lambda_+^{(0)}\right)^{5/3} \mathrm{Ai}'(b_+)}{\alpha_0^{1/3}\kappa(b_+)}. \tag{6.1.32}$$

This is our first pressure-displacement relation.

The lower viscous wall layer

The analysis in this region closely follows that of the upper viscous wall layer, however there is a key difference: the inner cylinder boundary is compliant. The effect of this will be seen through the boundary conditions of our system. Following the scaling arguments in the upper layer, the appropriate expansions in this region are

$$\hat{u} = u_- + \cdots, \quad \hat{v} = \epsilon^3 v_- + \cdots, \quad \hat{p} = \epsilon^2 p_- + \cdots, \quad \alpha = \epsilon\alpha_0 + \cdots, \quad c = \epsilon^2 c_0 + \cdots, \tag{6.1.33a}$$

$$U_0 = \epsilon^2\left(\lambda_-^{(0)} y_- + V_0\right) + \cdots, \quad r = \delta + \epsilon^2 y_-, \tag{6.1.33b}$$

where y_- is an order one variable. Substituting these expansions into the linearised disturbance equations (6.0.3), we find that the leading order terms must satisfy

$$\mathrm{i}\alpha_0 u_- + \frac{\mathrm{d}v_-}{\mathrm{d}y_-} = 0, \tag{6.1.34a}$$

$$\mathrm{i}\alpha_0\left(\lambda_-^{(0)} y_- + V_0 - c_0\right) u_- + \lambda_-^{(0)} v_- = -\mathrm{i}\alpha_0 p_- + \frac{\mathrm{d}^2 u_-}{\mathrm{d}y_-^2}, \tag{6.1.34b}$$

$$\frac{\mathrm{d}p_-}{\mathrm{d}y_-} = 0, \tag{6.1.34c}$$

subject to matching the core. Consideration of the conditions (6.1.13) reveals that

$$u_- \to \frac{A_0 \lambda_-^{(0)}}{\delta} \quad \text{as} \quad y_- \to \infty, \tag{6.1.35}$$

and, in combination with (6.1.34c), that

$$p_- = \hat{P}_0 + \alpha_0^2 A_0 I(\delta) \quad \text{for all} \quad y_-. \tag{6.1.36}$$

Recalling that $p_+ = \hat{P}_0$ (6.1.21), we are able to rewrite this to show that the behaviour of p_+ and p_- are connected through the relation

$$p_- = p_+ + \alpha_0^2 A_0 I(\delta). \tag{6.1.37}$$

We remark that the effects of compliance have not yet entered our analysis of the lower-branch structure. We see presently that the cylinder flexibility influences the structure through the boundary conditions on the inner cylinder.

We recall the dynamic condition (6.0.6):

$$\hat{p}(\delta) = \frac{2}{R}\hat{v}'(\delta) + \left(-\alpha^2 c^2 m + \frac{K}{R^2}\right)\frac{\hat{u}(\delta)}{U_0'(\delta)}. \tag{6.1.38}$$

We are interested in exploring the situation where changing the spring stiffness and mass of our inner cylinder has a leading order effect on the system. With this in mind, we seek to establish a balance between $\hat{p}(\delta)$ and the second term on the right-hand side of (6.1.38). Since $\alpha = O(\epsilon)$, $c = O(\epsilon^2)$, $\hat{p}(\delta) = O(\epsilon^2)$ (6.1.33a) and $R^{-1} \sim \epsilon^7$ (6.1.16), we prescribe

$$K = O\left(\epsilon^{-12}\right), \qquad m = O\left(\epsilon^{-4}\right). \tag{6.1.39}$$

Using (6.0.5) and (6.0.6), the boundary conditions to be satisfied may now be expressed as

$$\lambda_-^{(0)} v_- + \mathrm{i}\alpha_0 \left(V_0 - c_0\right) u_- = 0 \quad \text{on} \quad y_- = 0, \tag{6.1.40a}$$

$$p_- = \frac{\widetilde{K}\, u_-}{\lambda_-^{(0)}} \quad \text{on} \quad y_- = 0, \tag{6.1.40b}$$

where we have defined

$$\widetilde{K} = K_0 - \alpha_0^2 c_0^2 m_0. \tag{6.1.41}$$

K_0 and m_0 are order one quantities defined such that $K_0 = \epsilon^{12} K$ and $m_0 = \epsilon^4 m$.

We seek a solution for u_- (y_-) following the same methods as in the upper viscous region, finding

$$u_-(y_-) = \frac{\lambda_-^{(0)}\left(\hat{P}_0 + \alpha_0^2 A_0 I(\delta)\right)}{\widetilde{K}} + \frac{\lambda_-^{(0)}}{\kappa(b_-)}\left[\frac{A_0}{\delta} - \frac{\hat{P}_0 + \alpha_0^2 A_0 I(\delta)}{\widetilde{K}}\right]\int_{b_-}^{\xi_-} \mathrm{Ai}(\xi_-)\mathrm{d}\xi_-. \tag{6.1.42}$$

Here, we have introduced

$$\xi_- = a_- y_- + b_-, \qquad a_- = \left(\mathrm{i}\alpha_0 \lambda_-^{(0)}\right)^{1/3}, \qquad b_- = -\frac{\mathrm{i}\alpha_0(c_0 - V_0)}{\left(\mathrm{i}\alpha_0\lambda_-^{(0)}\right)^{2/3}}, \tag{6.1.43}$$

$$\kappa(b_-) = \int_{b_-}^{\infty} \mathrm{Ai}\left(\xi_-\right) \mathrm{d}\xi_-. \tag{6.1.44}$$

Our objective now is to find another expression for $\hat{P}_0$. Turning our attention back to the axial momentum equation (6.1.34b) and evaluating this at $y_- = 0$, we have

$$\left.\frac{\mathrm{d}^2 u_-}{\mathrm{d}y_-^2}\right|_{y_-=0} = \mathrm{i}\alpha_0 \left(\hat{P}_0 + \alpha_0^2 A_0 I(\delta)\right). \tag{6.1.45}$$

With our solution for $u_-(y_-)$ in (6.1.42), this leads us to the pressure-displacement relation

$$\hat{P}_0 + \alpha_0^2 A_0 I(\delta) = \frac{a_-^2 \mathrm{Ai}'(b_-) A_0 \lambda_-^{(0)} \widetilde{K}}{\delta \lambda_-^{(0)} a_-^2 \mathrm{Ai}'(b_-) + \mathrm{i}\alpha_0 \delta \widetilde{K} \kappa(b_-)}. \tag{6.1.46}$$

Our aim now is to use (6.1.32) and (6.1.46) to form an eigenrelation for the lower-branch mode.

Lower-branch eigenrelation

We begin by defining a function g such that

$$g(s) = \mathrm{i}^{5/3} \frac{\mathrm{Ai}'(-\mathrm{i}^{1/3} s)}{\kappa(-\mathrm{i}^{1/3} s)}, \tag{6.1.47}$$

and introducing variables s_+ and s_-, where

$$s_+ = \frac{\alpha_0 c_0}{\left(\alpha_0 \lambda_+^{(0)}\right)^{2/3}} \quad \text{and} \quad s_- = \frac{\alpha_0 \left(c_0 - V_0\right)}{\left(\alpha_0 \lambda_-^{(0)}\right)^{2/3}}, \tag{6.1.48}$$

so that

$$b_+ = -\mathrm{i}^{1/3} s_+ \quad \text{and} \quad b_- = -\mathrm{i}^{1/3} s_-. \tag{6.1.49}$$

Details on calculating $g(s)$ are found in Appendix A. Figure A.0.1 illustrates how the complex-valued function $g(s)$ varies with s.

Subtracting the pressure-displacement relation (6.1.32) from (6.1.46) and making use of (6.1.43), (6.1.47), (6.1.48) and (6.1.49) allows us to form the eigenrelation

$$\frac{\left(\lambda_-^{(0)}\right)^{5/3} g(s_-)}{\tilde{K}}\left[\alpha_0^{7/3} I(\delta) + \left(\lambda_+^{(0)}\right)^{5/3} g(s_+)\right] = \alpha_0^{1/3}\left[\alpha_0^{7/3} I(\delta) + \left(\lambda_+^{(0)}\right)^{5/3} g(s_+) + \frac{\left(\lambda_-^{(0)}\right)^{5/3} g(s_-)}{\delta}\right]. \quad (6.1.50)$$

It will be useful to remove the explicit dependence on α_0 here, and so we manipulate (6.1.48) to yield the relation

$$\alpha_0{}^{1/3} V_0 = \left(\lambda_+^{(0)}\right)^{2/3} s_+ - \left(\lambda_-^{(0)}\right)^{2/3} s_-. \quad (6.1.51)$$

Multiplying (6.1.50) by $V_0{}^8$ and using (6.1.51) results in the eigenrelation

$$\mathrm{t}(s_+, s_-)\left[(\mathrm{t}(s_+, s_-))^7 I(\delta) + \frac{1}{\delta} V_0{}^7 \left(\lambda_-^{(0)}\right)^{5/3} g(s_-) + V_0{}^7 \left(\lambda_+^{(0)}\right)^{5/3} g(s_+)\right] -$$
$$\frac{1}{\widetilde{K}}\left[(\mathrm{t}(s_+, s_-))^7 I(\delta) V_0 \left(\lambda_-^{(0)}\right)^{5/3} g(s_-) + V_0{}^8 \left(\lambda_+^{(0)}\right)^{5/3} \left(\lambda_-^{(0)}\right)^{5/3} g(s_+) g(s_-)\right] = 0, \quad V_0 \neq 0, \quad (6.1.52)$$

where we have introduced

$$\mathrm{t}(s_+, s_-) = \left(\lambda_+^{(0)}\right)^{2/3} s_+ - \left(\lambda_-^{(0)}\right)^{2/3} s_-. \quad (6.1.53)$$

Using the definition of s_+ (6.1.48) and $\mathrm{t}(s_+, s_-)$ (6.1.53), $\widetilde{K}$ can be written in terms of s_+ and s_- as

$$\widetilde{K} = K_0 - \frac{{s_+}^2 \left(\lambda_+^{(0)}\right)^{4/3} (\mathrm{t}(s_+, s_-))^4}{V_0{}^4} m_0, \quad (6.1.54)$$

upon recollection that $\widetilde{K} = K_0 - \alpha_0^2 c_0^2 m_0$ (6.1.41).

A complex-valued relation, eigenrelation (6.1.52) forms a system of two real equations that can be solved numerically for s_+ and s_-, given V_0, K_0, m_0 and δ. The wavespeed and wavenumber of the neutral mode along the lower-branch can then be determined through the use of (6.1.48).

In the rigid limit $\widetilde{K} \to \infty$ with $\alpha_0 = O(1)$ and $c_0 = O(1)$, the eigenrelation (6.1.52) collapses to

$$\left(\left(\lambda_+^{(0)}\right)^{2/3} s_+ - \left(\lambda_-^{(0)}\right)^{2/3} s_-\right)^7 I(\delta) + {V_0}^7 \left(\frac{1}{\delta}\left(\lambda_-^{(0)}\right)^{5/3} g(s_-) + \left(\lambda_+^{(0)}\right)^{5/3} g(s_+)\right) = 0, \tag{6.1.55}$$

which is precisely the lower-branch eigenrelation found by Walton [1] for the case of a rigid inner cylinder.

To find pairs of solutions s_+ and s_- of the eigenrelation (6.1.52), we follow the approach used by Walton [1] in the rigid case. We plot contours of the real and imaginary parts of the left-hand side of (6.1.52). Where the zero-level contours intersect, we have solutions s_+ and s_- of our neutral mode.

Since we are considering only non-negative sliding velocities, examination of (6.1.51) reveals that

$$s_+ \geq \left(\frac{\lambda_-^{(0)}}{\lambda_+^{(0)}}\right)^{2/3} s_-. \tag{6.1.56}$$

We therefore restrict ourselves to the region in the (s_+, s_-) plane described by (6.1.56).

For a rigid inner cylinder with $\delta = 0.7$, Walton [1] finds a unique solution until V_0 is increased to $V_0 \approx 0.6$. Two additional modes then form, one of which has a shortening wavelength as $V_0 \to \infty$. The solution of the rigid problem, described by (6.1.55), is illustrated in figures 6.1.2 and 6.1.3. Once close approximations to s_+ and s_- have been found via our contour plots (figure 6.1.2), we use a solver in MATLAB to refine our solutions and determine α_0 and c_0 using (6.1.48).

Figure 6.1.3 illustrates how the 'rigid' wavenumber varies with V_0. For $\delta = 0.7$, we see that there are three branches of solutions. The curve corresponding to Root 1 exists for all sliding velocities $V_0 \geq 0$. Roots 2 and 3 appear at a larger sliding velocity, emerging from the same solution at $V_0 \approx 0.6$. As $V_0 \to \infty$, Root 3 behaves in such a way that s_+ becomes large while s_- remains order one (figure 6.1.2).

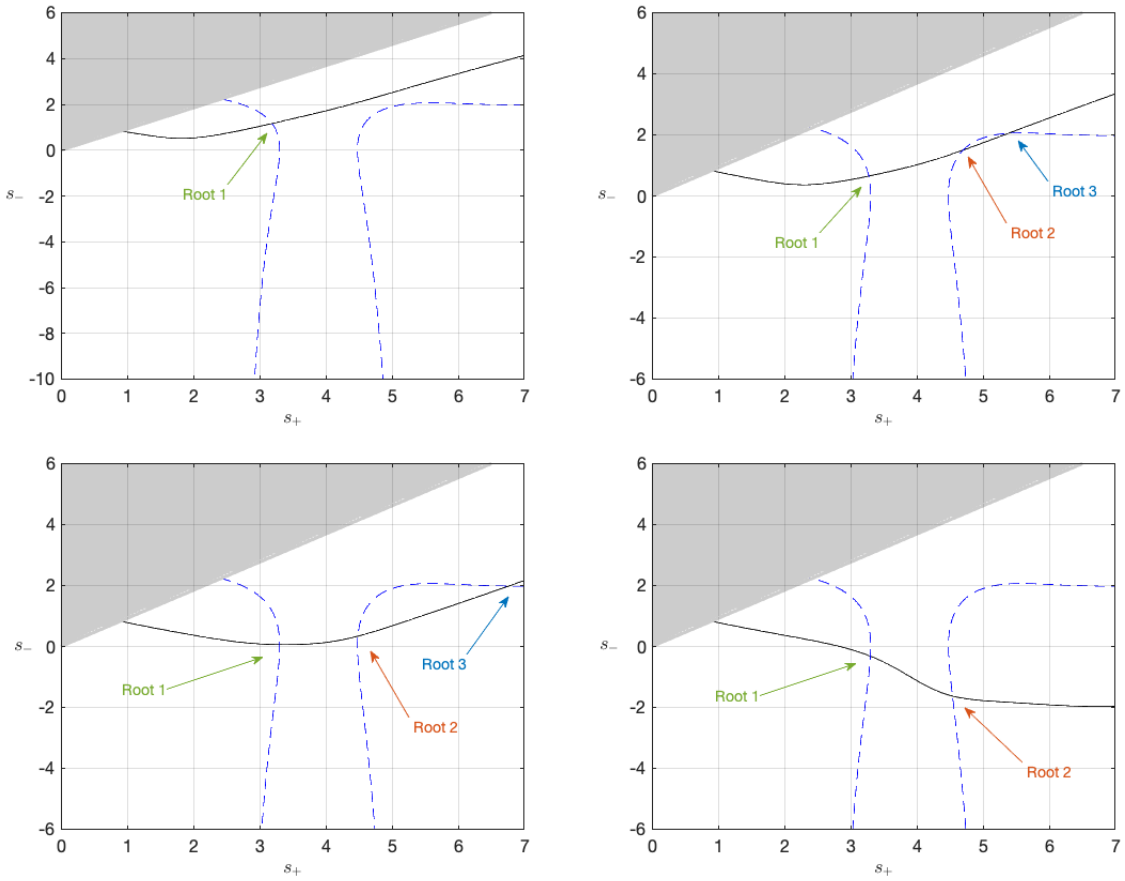

Figure 6.1.2: Solutions of the rigid eigenrelation (6.1.55) for $\delta = 0.7$ and various V: (a) $V = 0.5$, (b) $V = 0.7$, (c) $V = 1$, (d) $V = 2.5$. Note Root 3 exists beyond the values of s_+ shown in figure (d).

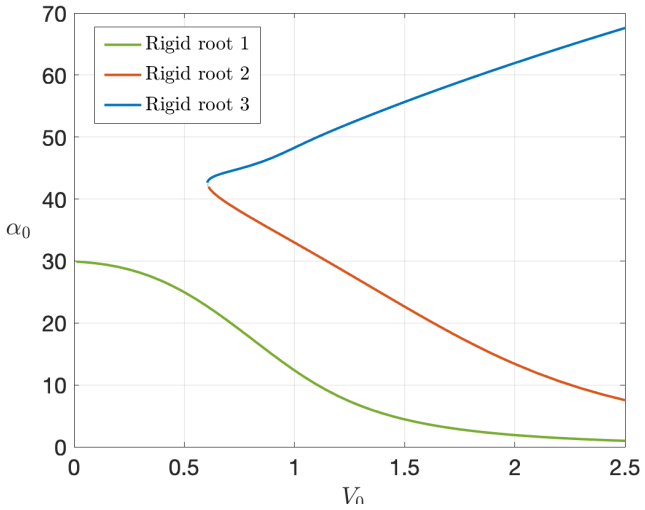

Figure 6.1.3: Solutions of the rigid eigenrelation (6.1.48) and (6.1.55) for $\delta = 0.7$ as V_0 varies.

In figures 6.1.4 and 6.1.5 we investigate the effect of compliance on the leading order wavenumber. For simplicity, the mass of the cylinder is taken to be $m_0 = 0$. Whilst Root 3 still exists at large sliding velocities for $K_0 = 0.5$ and $K_0 = 2$, Roots 1 and 2 now merge and disappear at a finite sliding velocity, say $V_0 = {V_0}^{(1,2)}$. This means the range of sliding velocities for which all three solutions coexist is dramatically reduced. As the spring stiffness of our inner cylinder decreases, ${V_0}^{(1,2)}$ also decreases. In addition to these changes, figure 6.1.4f showcases the emergence of two additional neutral modes once V_0 is sufficiently increased. These emerge from the same solution. As the sliding velocity is increased further to $V_0 = 5$, the wavenumber of Root 4 decreases with $\frac{\mathrm{d}\alpha_0}{\mathrm{d}V_0}$ becoming less negative (figure 6.1.6). We emphasise we have not found analogous roots to Roots 4 and 5 in the rigid case with $\delta = 0.7$.

We look at the effect of compliance on each of Roots 1, 2 and 3 separately. In figure 6.1.5a, the compliant curves describing Root 2 intersect their rigid counterpart, though we note that this intersection does not necessarily occur at the same sliding velocity for each K_0. This means that, for each K_0, there exists a sliding velocity for which that particular spring stiffness does not influence the leading order wavenumber obtained from Root 2. Beyond the intersection, the effect of compliance becomes more prominent as V_0 is increased to ${V_0}^{(1,2)}$.

We now focus on the first root, shown in figure 6.1.5a. For small values of V_0, a more compliant cylinder yields a lower leading order wavenumber. This trend does not continue, and eventually compliance results in a wavenumber that is larger than its rigid counterpart. As in Root 2, the deviation from the rigid scenario is more pronounced as V_0 increases to ${V_0}^{(1,2)}$.

A lower spring stiffness results in a lower wavenumber for Root 3, though the difference between the rigid and compliant cases seem to become less apparent as the sliding velocity increases (see figure 6.1.5b). This is unlike the cases for Roots 1 and 2.

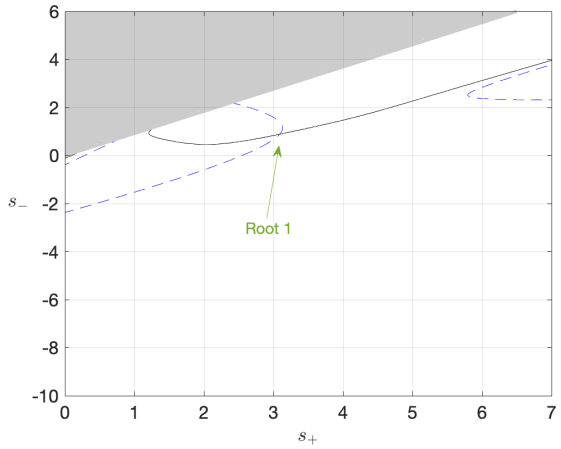

(a) $V = 0.5$

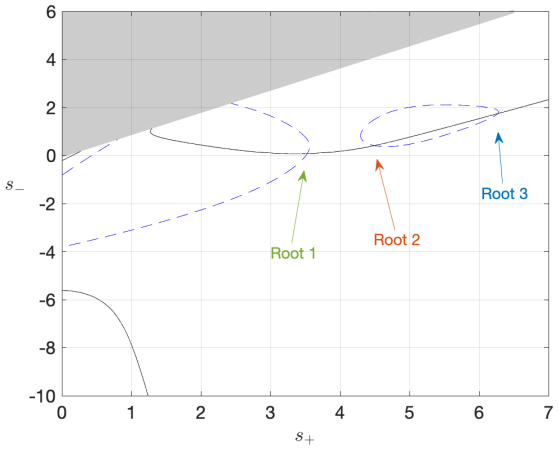

(b) $V = 0.85$

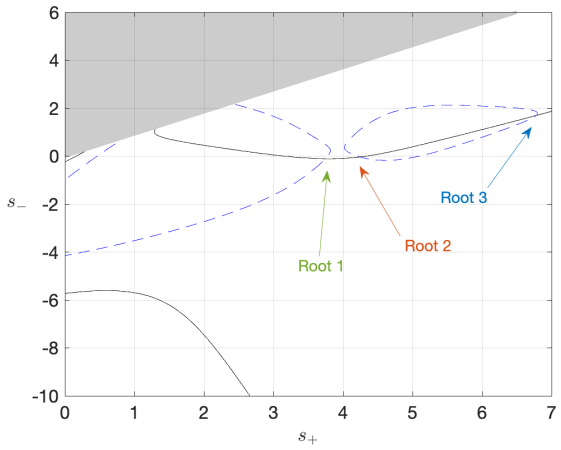

(c) $V = 0.95$

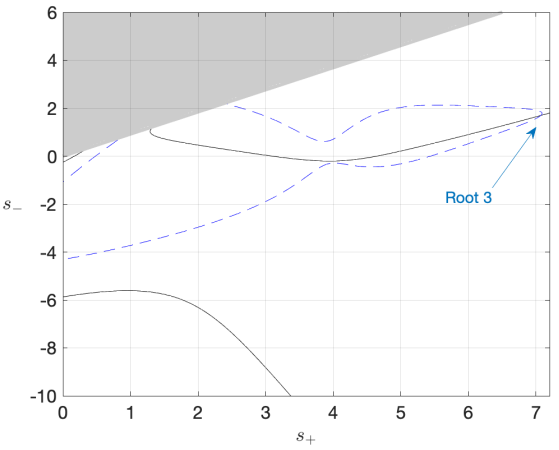

(d) $V = 1$

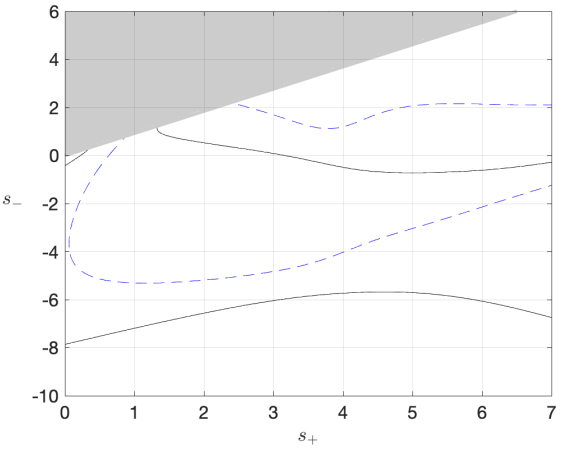

(e) $V = 1.5$

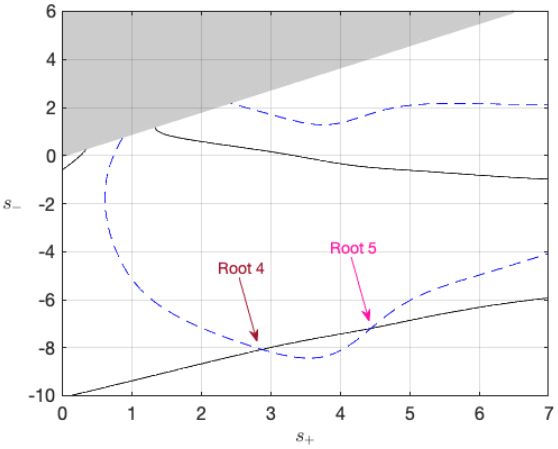

(f) $V = 2$

Figure 6.1.4: Solutions of the flexible eigenrelation (6.1.48) and (6.1.52) for $\delta = 0.7$ and various V. Note Root 3 exists beyond the values of s_+ shown in figures (e) and (f).

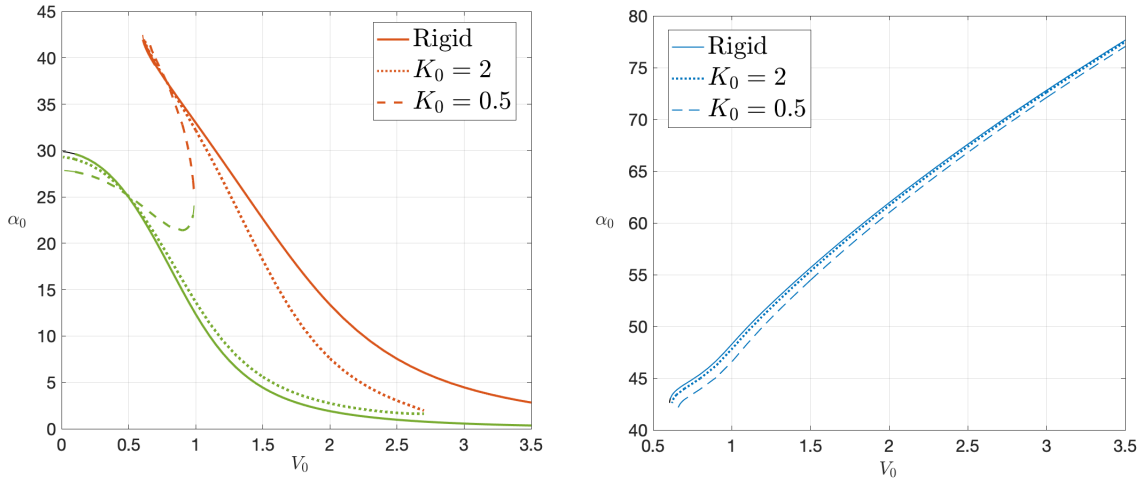

(a) Depiction of Roots 1 (green) and 2 (orange).

(b) Depiction of Root 3.

Figure 6.1.5: Solutions of the eigenrelation (6.1.48) and (6.1.52) in the flexible case, for $K_0 = 0.5$ and $K_0 = 2$ with $m_0 = 0$. The rigid solution is plotted for reference. The labelling of the roots follows figure 6.1.3, with Root 3 plotted separately to Roots 1 and 2.

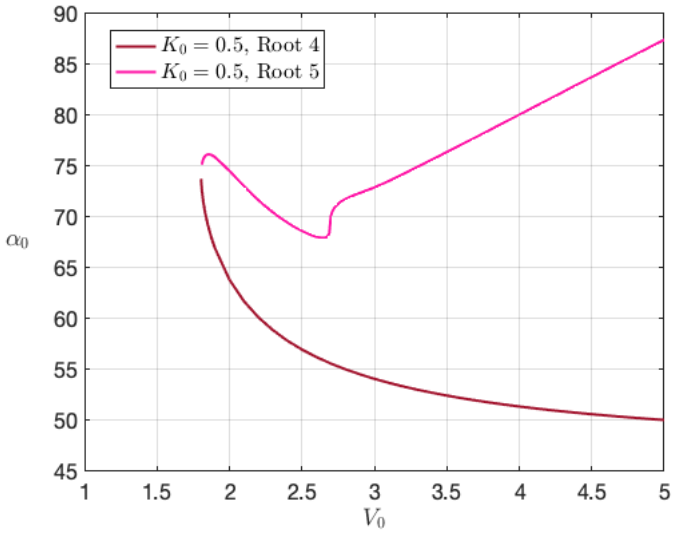

Figure 6.1.6: Solutions of the eigenrelation (6.1.48) and (6.1.52) in the flexible case, for $K_0 = 0.5$ with $m_0 = 0$. Depiction of Roots 4 and 5.

Motivated by the rigid scenario, we seek the limiting behaviour for Root 3 in the limit $V_0 \to \infty$ with $s_+ \to \infty$ and $s_- = O(1)$ and explore the effect of the introduction of compliance. In this limit, use of (6.1.51) shows that

$$\left(\lambda_+^{(0)}\right)^{2/3} s_+ \sim {\alpha_0}^{1/3} V_0. \tag{6.1.57}$$

To find the behaviour of α_0 and c_0 as $V_0 \to \infty$, we revisit the eigenrelation (6.1.50), which we rewrite here

$$\frac{\left(\lambda_-^{(0)}\right)^{5/3} g(s_-)}{K_0}\left[\alpha_0^{7/3} I(\delta) + \left(\lambda_+^{(0)}\right)^{5/3} g(s_+)\right] = \alpha_0^{1/3}\left[\alpha_0^{7/3} I(\delta) + \left(\lambda_+^{(0)}\right)^{5/3} g(s_+) + \frac{\left(\lambda_-^{(0)}\right)^{5/3} g(s_-)}{\delta}\right] \tag{6.1.58}$$

for a massless inner cylinder. The behaviour of $g(s)$ is given by

$$g(s) \sim s + \mathrm{e}^{\mathrm{i}\pi/4} s^{-1/2} \tag{6.1.59}$$

in the limit $s \to \infty$ [1]. Considering (6.1.60) for $s_+ \to \infty$ and $s_- = O(1)$ then leads to the balance

$$\frac{\left(\lambda_-^{(0)}\right)^{5/3} g(s_-)}{K_0}\left[\alpha_0^{7/3} I(\delta) - \left(\lambda_+^{(0)}\right)^{5/3} s_+\right] \sim \alpha_0^{1/3}\left[\alpha_0^{7/3} I(\delta) - \left(\lambda_+^{(0)}\right)^{5/3} s_+\right]. \tag{6.1.60}$$

We first consider the balance

$$\alpha_0^{1/3} \sim \frac{\left(\lambda_-^{(0)}\right)^{5/3} g(s_-)}{K_0} \tag{6.1.61}$$

and demonstrate that this is not possible. Since α_0 is real, we require the right-hand side of (6.1.61) to be real. The unique root of $\operatorname{Im} g(s_-) = 0$ for $s_- = O(1)$ is given by $s_- = s_0 \approx 2.2972$. From figure A.0.1, we see that $\operatorname{Re}(g(s_0))$ is negative. Since K_0 and $\lambda_-^{(0)}$ are positive, this leads to a contradiction.

We deduce that we must instead have

$$\alpha_0^{7/3} I(\delta) \sim \left(\lambda_+^{(0)}\right)^{5/3} s_+, \tag{6.1.62}$$

which, upon consideration of (6.1.57), gives

$$\alpha_0 \sim \left(\frac{\lambda_+^{(0)}}{I(\delta)}\right)^{1/2} {V_0}^{1/2} \quad \text{as } V_0 \to \infty, \tag{6.1.63}$$

which is independent of the spring stiffness of the cylinder. This is in agreement with our findings in figure 6.1.5b. Since s_- is order one, we find the leading order wavespeed to be such that

$$c_0 \sim V_0 \quad \text{as} \quad V_0 \to \infty. \tag{6.1.64}$$

As V_0 increases, we expect that the upper critical layer of the structure moves away from the outer cylinder whilst the lower critical layer remains in the viscous wall layer. We discuss the structure that arises in Chapter 8.

Importance of mass

We see in this section that the introduction of $\widetilde{K}$ provides valuable insights into our problem. Focusing on the case $V = 0$ to highlight the role of $\widetilde{K}$, we wish to determine the leading order wavenumber and wavespeed for a stationary inner cylinder at various values of $\widetilde{K}$. We make use of (6.1.48) to write s_- in terms of α_0 and s_+. Substituting this form of s_- into the eigenrelation (6.1.50) yields a relation in s_+ and α_0, which we solve using MATLAB. Once s_+ and α_0 are known, we are able to make use of (6.1.48) to find c_0. Figure 6.1.7 illustrates how the scaled wavenumbers of the lower-branch neutral modes vary with $\widetilde{K}$. We note that it does not pose a problem to prescribe $\widetilde{K}$ despite its dependence on the wavenumber and wavespeed; once α_0 and c_0 have been determined, it is possible to choose K_0 and m_0 appropriately so as to yield the prescribed $\widetilde{K}$.

There exists only one neutral mode for positive $\tilde{K}$ in figure 6.1.7, and the wavenumber in the rigid limit is approached from below as $\widetilde{K}$ is increased. As $\widetilde{K}$ is decreased, the wavenumber of this mode decreases and eventually becomes very small at large negative $\widetilde{K}$.

The situation when $\widetilde{K}$ is negative is made more interesting by the existence of a second neutral mode, whose presence seems to be attributed to the flexibility of the inner cylinder. This 'elastic' mode possesses an ever-increasing wavenumber as $\widetilde{K} \to 0^-$.

A massless inner cylinder would be characterised by a positive value of $\widetilde{K}$. The incorporation of mass as a descriptor for our inner cylinder allows $\widetilde{K}$ to acquire negative values, and thus also allows for the existence of the elastic mode described above.

Figure 6.1.7 hints at the possibility of there being two structures that more intricately describe the lower-branch mode, specifically when $\widetilde{K} \to -\infty$ with $\alpha_0 \to 0^+$ and when $\tilde{K} \to 0^-$ with $\alpha_0 \to \infty$. The former limit corresponds to $c_0 \to \infty$ and the latter limit, which we explore in the next section, is associated with $c_0 \to 0$.

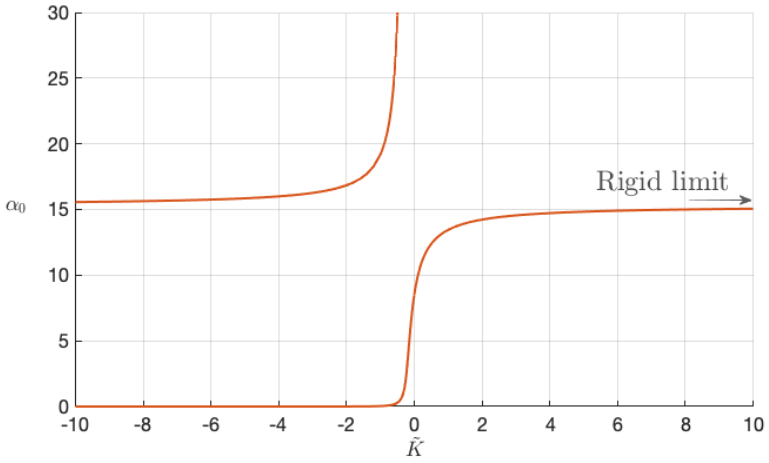

Figure 6.1.7: Solutions α_0 of the lower-branch eigenrelation for various $\widetilde{K} = K_0 - {\alpha_0}^2 {c_0}^2 m_0$ and fixed $\delta = 0.5,\ V = 0$.

6.1.1 Large-wavenumber limit of the lower-branch mode

We begin by considering the lower-branch eigenrelation in the limit $\widetilde{K} \to 0^-$ and $\alpha_0 \to \infty$. Later we explore how the structure changes in this limit, and we will find a distinguished scaling for $\widetilde{K}$ and α_0 in terms of the Reynolds number.

A numerical investigation into how s_+ and s_- (6.1.48) vary along each curve illustrated in figure 6.1.7 suggests that we look for a structure in which s_+ and s_- remain order one quantities. We rewrite the eigenrelation (6.1.50) in a form that lends itself to the subsequent analysis:

$$\left(\alpha_0^{1/3} - \frac{\left(\lambda_-^{(0)}\right)^{5/3} g(s_-)}{\tilde{K}}\right)\left(\alpha_0^{7/3} I(\delta) + \left(\lambda_+^{(0)}\right)^{5/3} g(s_+)\right) + \alpha_0^{1/3} \frac{\left(\lambda_-^{(0)}\right)^{5/3} g(s_-)}{\delta} = 0. \tag{6.1.65}$$

We note that this form of the eigenrelation holds for $V_0 \geq 0$. In the limit $\alpha_0 \to \infty$, with $s_+ = O(1),\ s_- = O(1)$ and $\widetilde{K} \to 0^-$, the dominant balance in this equation must be

$$\alpha_0^{1/3} \sim \frac{\left(\lambda_-^{(0)}\right)^{5/3} g(s_-)}{\tilde{K}}. \tag{6.1.66}$$

Introducing a small, positive parameter Ψ, we therefore take $\widetilde{K} \sim -k_0 \Psi$ and $\alpha_0 \sim \overline{\alpha}_0 \Psi^{-3}$ for positive k_0 and $\overline{\alpha}_0$. Since α_0 is real, we must have that $\mathrm{Im}(g(s_-)) = 0$ for relation (6.1.66) to hold.

Under these deductions, the eigenrelation (6.1.65) reduces to

$$\overline{\alpha}_0 = -\frac{{\lambda_-^{(0)}}^5 \left(g(s_0)\right)^3}{{k_0}^3}, \qquad s_0 \approx 2.2972, \tag{6.1.67}$$

where s_0 is such that $\mathrm{Im}\left(g(s_0)\right) = 0$. Figure A.0.1 demonstrates that $g(s_0)$ is negative, so we conclude that the right-hand side of (6.1.67) is positive.

Recalling the definitions of s_+ and s_- (6.1.48),

$$s_+ = \frac{{\alpha_0}^{1/3} c_0}{\left(\lambda_+^{(0)}\right)^{2/3}} \quad \text{and} \quad s_- = \frac{{\alpha_0}^{1/3}\left(c_0 - V_0\right)}{\left(\lambda_-^{(0)}\right)^{2/3}}. \tag{6.1.68}$$

Since s_+ remains order one, we require that $\left(\alpha_0^{1/3} c_0\right) = O(1)$. This prompts the scaling $c_0 \sim \overline{c}_0\,\Psi$. We would like the sliding velocity to have a leading order effect in our structure, so turning to the expression for s_-, we take $V_0 \sim \overline{V}_0\,\Psi$. Under these scalings, a rearrangement of the definition of s_- leads to

$$\overline{c}_0 = -\frac{s_0 k_0}{\lambda_-^{(0)} g(s_0)} + \overline{V}_0. \tag{6.1.69}$$

With c_0 becoming smaller as $\widetilde{K} \to 0^-$, we expect the critical layer in the upper viscous wall layer to move closer to the outer cylinder. We use the above scalings to guide us in our search for a new structure.

In what follows, we try to discern how the lower-branch structure changes in the 'large-α_0, small-$\tilde{K}$' limit described above. As suggested by the analysis in 6.1.1, we suppose that

$$\alpha_0 \sim \overline{\alpha}_0\,\widetilde{K}^{-3}, \qquad c_0 \sim \overline{c}_0\,\widetilde{K}, \qquad V_0 \sim \overline{V}_0\,\widetilde{K}, \qquad \widetilde{K} \to 0^-. \tag{6.1.70}$$

Recalling the definition of $\widetilde{K}$ as

$$\widetilde{K} = K_0 - \alpha_0^2\, c_0^2\, m_0, \tag{6.1.71}$$

we take

$$K_0 \sim \overline{K}_0\,\widetilde{K}, \qquad m_0 \sim \overline{m}_0\,\widetilde{K}^5, \tag{6.1.72}$$

in order to preserve the effect of spring stiffness and mass in this limit.

We emphasise that $\widetilde{K}$ is negative here, meaning $\overline{\alpha}_0, \overline{c}_0, \overline{V}_0, \overline{K}_0$ and $\overline{m}_0$ are also negative.

Exploring the lower-branch structure in this limit, we seek scalings on the flow quantities that enable us retain as many terms as possible in the Reynolds-number-independent equations governing the core region (6.1.7), upper wall layer (6.1.19) and lower wall layer (6.1.34).

The core region

The analysis in this region is based on the expansions (6.1.6) and equations (6.1.7).

Beginning with the core region, we seek a scaling for our disturbance quantities F_0, G_0 and P_0, as defined in (6.1.9), (6.1.10). We take $P_0 = O(1)$ without loss of generality and, in what follows, determine the sizes of A_0 and $\hat{P}_0$. It is apparent from (6.1.9) and (6.1.10) that

$$F_0 = O(A_0\,\overline{F}_0), \qquad G_0 = O(A_0\,\overline{G}_0\widetilde{K}^{-3}). \tag{6.1.73}$$

Balancing the radial momentum equation (6.1.7c) then gives us $A_0 = O(\widetilde{K}^6)$, so that

$$F_0 = O\left(\widetilde{K}^6\right), \qquad G_0 = O\left(\widetilde{K}^3\right). \tag{6.1.74}$$

Substituting

$$F_0 \sim \widetilde{K}^6\ \overline{F}_0, \qquad G_0 \sim \widetilde{K}^3\ \overline{G}_0, \qquad P_0 \sim \overline{P}_0 \tag{6.1.75}$$

into the core equations (6.1.7), we obtain

$$\mathrm{i}\overline{\alpha}_0\overline{F}_0 + \frac{\mathrm{d}\overline{G}_0}{\mathrm{d}r} + \frac{\overline{G}_0}{r} = 0, \quad \mathrm{i}\overline{\alpha}_0 U_{00}\overline{F}_0 + \overline{G}_0\frac{\mathrm{d}U_{00}}{\mathrm{d}r} = 0, \quad \mathrm{i}\overline{\alpha}_0 U_{00}\overline{G}_0 + \frac{\mathrm{d}\overline{P}_0}{\mathrm{d}r} = 0. \tag{6.1.76a}$$

These equations are identical to those in (6.1.7), though with the use of barred quantities instead. Examining the disturbance behaviour as we approach the inner cylinder, (6.1.13) suggests

$$F_0 = O\left(\widetilde{K}^6\right), \qquad G_0 = O\left(\widetilde{K}^3(r-\delta)\right), \qquad P_0 = O(1). \tag{6.1.77}$$

As we approach the outer cylinder, (6.1.12) gives

$$F_0 = O\left(\widetilde{K}^6\right), \qquad G_0 = O\left(\widetilde{K}^3(1-r)\right), \qquad P_0 \to O\left(\hat{P}_0\right), \tag{6.1.78}$$

where the size of $\hat{P}_0$ will be determined.

The upper viscous wall layer

In this region, our analysis relates to the expansions (6.1.18) and equations (6.1.19). We have $r = 1 - \epsilon^2 y_+$, where y_+ will be determined in terms of $\widetilde{K}$.

To match the core, we take $u_+ \sim \widetilde{K}^6\ \overline{u}_+$ here in view of (6.1.78). Balancing the terms in the axial momentum equation (6.1.19b) reveals that $\hat{P}_0 = O\left(\widetilde{K}^7\right)$ and

$$v_+ \sim \overline{v}_+\ \widetilde{K}^4, \qquad p_+ \sim \overline{p}_+\ \widetilde{K}^7, \qquad y_+ \sim \overline{y}_+\ \widetilde{K}. \tag{6.1.79}$$

In this region, the basic velocity (6.1.18b) behaves as $U_0 \sim \lambda_+^{(0)} \widetilde{K}\ \overline{y}_+$ and is of the same size as the disturbance wavespeed, supporting the existence of a critical layer in this region. Using (6.1.79), the equations (6.1.19) become

$$\mathrm{i}\overline{\alpha}_0 \overline{u}_+ + \frac{\mathrm{d}\overline{v}_+}{\mathrm{d}\overline{y}_+} = 0, \tag{6.1.80a}$$

$$\mathrm{i}\overline{\alpha}_0 \left(\lambda_+^{(0)} \overline{y}_+ - \overline{c}_0\right) \overline{u}_+ + \lambda_+^{(0)} \overline{v}_+ = -\mathrm{i}\overline{\alpha}_0 \overline{p}_+ + \frac{\mathrm{d}^2 \overline{u}_+}{\mathrm{d}\overline{y}_+^2}, \tag{6.1.80b}$$

$$\frac{\mathrm{d}\overline{p}_+}{\mathrm{d}\overline{y}_+} = 0. \tag{6.1.80c}$$

These are subject to no-slip conditions on the outer cylinder, and the disturbance quantities must match the core as $\overline{y}_+ \to \infty$.

Lower wall layer

The analysis here pertains to the expansions (6.1.33) and equations (6.1.34). We have $r = \delta + \epsilon^2 y_-$, where y_- is to be determined in terms of $\widetilde{K}$.

As $\widetilde{K}$ becomes small, the lower viscous wall layer splits into an upper inviscid layer that matches to the core region and a lower viscous layer. This is depicted in figure 6.1.8. In the analysis of both layers below, u_-, v_-, p_- and y_- are as in the expansions (6.1.33).

Inviscid layer. To match the core solution, we expect from (6.1.77) that

$$u_- \sim \overline{u}_-^{(I)}\ \widetilde{K}^6, \qquad p_- \sim \overline{p}_-. \tag{6.1.81}$$

Balancing the inertia and pressure terms in the axial momentum equation (6.1.34b), we take $y_- \sim \overline{y}_-^{(I)}\ \widetilde{K}^{-6}$ and $v_- \sim \overline{v}_-^{(I)}\ \widetilde{K}^{-3}$ in this region. With these scalings, the equations (6.1.34) reduce to

$$\frac{\mathrm{d}\overline{u}_-^{(I)}}{\mathrm{d}\overline{y}_-^{(I)}} = 0, \qquad \frac{\mathrm{d}\overline{p}_-}{\mathrm{d}\overline{y}_-^{(I)}} = 0, \qquad \lambda_-^{(0)} \left(\mathrm{i}\overline{\alpha}_0 \overline{y}_-^{(I)} \overline{u}_-^{(I)} + \overline{v}_-^{(I)}\right) = -\mathrm{i}\overline{\alpha}_0 \overline{p}_-. \tag{6.1.82}$$

As $\overline{y}_- \to \infty$, the disturbance quantities are required to match the core. The expansions in this inviscid layer do not allow for the boundary conditions (6.1.40) to be satisfied, nor do they account for the critical layer in the original structure. This highlights the need for the viscous layer that is described below.

Viscous layer. Anticipating that the pressure disturbance is constant across this layer in accordance with (6.1.34c), we take

$$p_- \sim \overline{p}_- \tag{6.1.83}$$

to match the inviscid layer above. Recalling the scalings (6.1.70), the boundary conditions (6.1.40) on the inner cylinder then propose that

$$u_- \sim \widetilde{K}^{-1}\,\overline{u}_-^{(II)}, \quad v_- \sim \widetilde{K}^{-3}\,\overline{v}_-^{(II)}. \tag{6.1.84}$$

A balance in the continuity equation (6.1.34a) gives the thickness of the layer to be

$$y_- \sim \overline{y}_-^{(II)}\,\widetilde{K}. \tag{6.1.85}$$

This means that this viscous wall layer becomes thinner in the limit $\widetilde{K} \to 0^-$. Using (6.1.33) and (6.1.70), we see that this scaling on y_- maintains the balance of the base velocity and the disturbance wavespeed, which is consistent with the existence of a critical layer in this region.

With consideration of (6.1.83)-(6.1.85), the equations (6.1.34) become

$$\mathrm{i}\overline{\alpha}_0\overline{u}_-^{(II)} + \frac{\mathrm{d}\overline{v}_-^{(II)}}{\mathrm{d}\overline{y}_-^{(II)}} = 0, \tag{6.1.86a}$$

$$\mathrm{i}\overline{\alpha}_0\left(\lambda_-^{(0)}\overline{y}_-^{(II)} + \overline{V}_0 - \overline{c}_0\right)\overline{u}_-^{(II)} + \lambda_-^{(0)}\overline{v}_-^{(II)} = -\mathrm{i}\overline{\alpha}_0\overline{p}_- + \frac{\mathrm{d}^2\overline{u}_-^{(II)}}{\mathrm{d}\overline{y}_-^{(II)\,2}}, \tag{6.1.86b}$$

$$\frac{\mathrm{d}\overline{p}_-}{\mathrm{d}\overline{y}_-^{(II)}} = 0, \tag{6.1.86c}$$

where the disturbance quantities are subject to matching the inviscid layer as $\overline{y}_-^{(II)} \to \infty$ and, using (6.1.40),

$$\lambda_-^{(0)}\,\overline{v}_-^{(II)} + \mathrm{i}\overline{\alpha}_0\left(\overline{V}_0 - \overline{c}_0\right)\overline{u}_-^{(II)} = 0 \quad \text{on} \quad \overline{y}_-^{(II)} = 0, \tag{6.1.87a}$$

$$\overline{p}_- = \frac{\left(\overline{K}_0 - \overline{\alpha}_0^2\overline{c}_0^2\overline{m}_0\right)\overline{u}_-^{(II)}}{\lambda_-^{(0)}} \quad \text{on} \quad \overline{y}_-^{(II)} = 0. \tag{6.1.87b}$$

Figure 6.1.8 encapsulates the behaviour of the lower-branch mode in the limit $\widetilde{K} \to 0^-$. We observe that the size of the inviscid layer becomes comparable to that of the core when $\widetilde{K}$ decreases to an order of $R^{-1/21}$. When this occurs, the equations that govern the dynamics of the core change and the inviscid layer merges with this 'new' core. In addition, the size of wavenumber increases to $\alpha_0 = O(R^{1/7})$ while that of the wavespeed decreases to $c_0 = O(R^{-1/21})$. We discuss in more depth the changes that occur when $\widetilde{K} = O(R^{-1/21})$ in the following section.

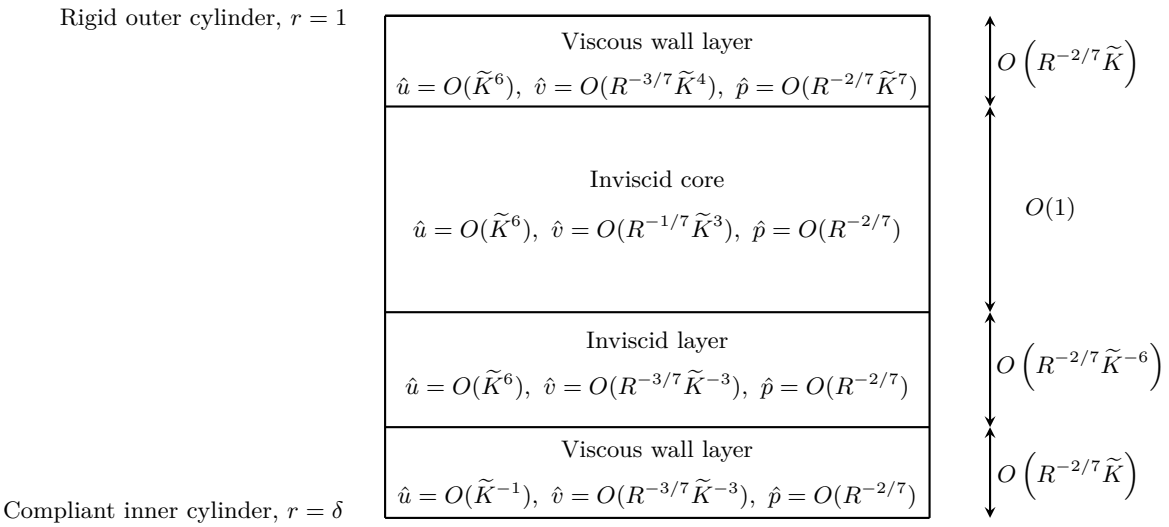

Figure 6.1.8: Schematic of the asymptotic structure of the lower-branch mode in the limit $\widetilde{K} \to 0^-$, where $\alpha = O\left(R^{-1/7}\widetilde{K}^{-3}\right)$, $c = O\left(R^{-2/7}\widetilde{K}\right)$ and $V = O\left(R^{-2/7}\widetilde{K}\right)$.

To summarise our findings here, we briefly revisit the original expansions of the lower-branch structure. Using (6.1.1), (6.1.17), (6.1.16), (6.1.39), we recall the mode has

$$\alpha = R^{-1/7}\alpha_0 + \cdots, \qquad c = R^{-2/7}c_0 + \cdots \tag{6.1.88}$$

with the inner cylinder properties

$$V = R^{-2/7}V_0, \qquad K = R^{12/7}K_0, \qquad m = R^{4/7}m_0. \tag{6.1.89}$$

In the limit $\widetilde{K} \to 0^-$, we have seen that we may take

$$\alpha_0 = O(\widetilde{K}^{-3}), \quad c_0 = O(\widetilde{K}), \quad V_0 = O(\widetilde{K}), \quad K_0 = O(\widetilde{K}), \quad m_0 = O(\widetilde{K}^5) \tag{6.1.90}$$

as in (6.1.70), (6.1.72), so that

$$\alpha = O(R^{-1/7}\widetilde{K}^{-3}), \quad c = O(R^{-2/7}\widetilde{K}), \tag{6.1.91}$$

$$V = O(R^{-2/7}\widetilde{K}), \quad K = O(R^{12/7}\widetilde{K}), \quad m = O(R^{4/7}\widetilde{K}^5). \tag{6.1.92}$$

As discussed above, once $\widetilde{K}$ has decreased to an order of $R^{-1/21}$, this original lower-branch structure breaks. When this occurs, the scalings (6.1.91) become

$$\alpha = O\left(R^{-1/7}R^{1/7}\right), \quad c = O\left(R^{-2/7}R^{-1/21}\right), \tag{6.1.93a}$$

$$V = O\left(R^{-2/7}R^{-1/21}\right), \quad K = O\left(R^{12/7}R^{-1/21}\right), \quad m = O\left(R^{4/7}R^{-5/21}\right), \tag{6.1.93b}$$

and we anticipate a new structure with the scalings

$$\alpha = O\left(1\right), \quad c = O\left(R^{-1/3}\right), \tag{6.1.94a}$$

$$V = O\left(R^{-1/3}\right), \quad K = O\left(R^{5/3}\right), \quad m = O\left(R^{1/3}\right). \tag{6.1.94b}$$

This structure will be the focus of our next section.

6.2 Lower-branch analysis II: a mode with $\alpha = O(1)$

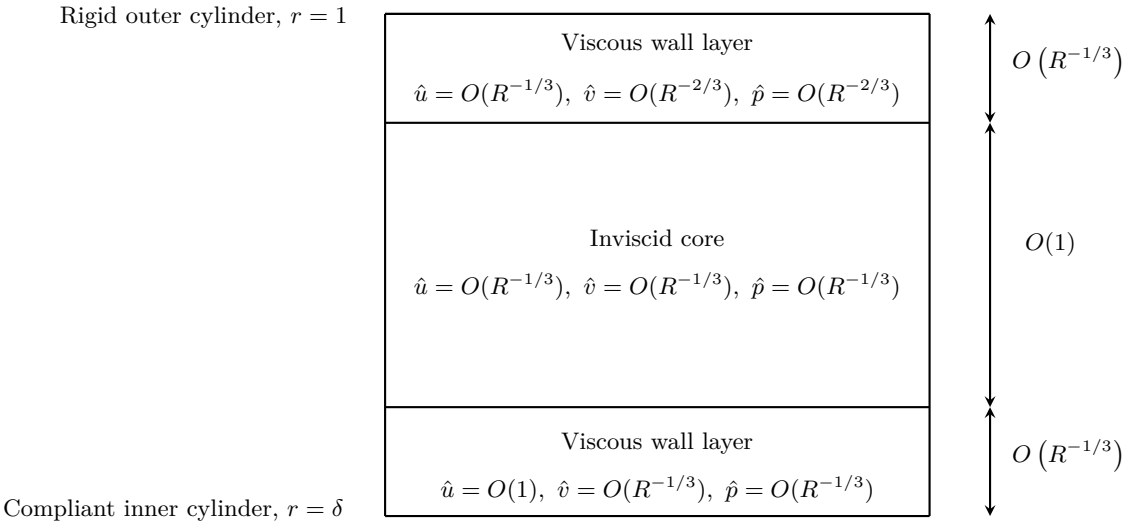

Figure 6.2.1: Schematic of the asymptotic structure of the lower-branch Rayleigh mode, where $\alpha = O(1)$ and $c = O(R^{-1/3})$. The cylinder properties are $V = O\left(R^{-1/3}\right)$, $K = O\left(R^{5/3}\right)$ and $m = O\left(R^{1/3}\right)$.

In this section, we discuss the emergence of a lower-branch mode when the cylinder properties are such that

$$K - \alpha^2 c^2 m < 0. \tag{6.2.1}$$

Guided by the analysis above, we anticipate a three-zone structure: an inviscid core surrounded by viscous wall layers of thickness $R^{-1/3}$.

We also expect

$$\alpha = \overline{\alpha}_0 + \cdots, \qquad c = R^{-1/3}\,\overline{c}_0 + \cdots, \tag{6.2.2}$$

where the cylinder properties are

$$V = R^{-1/3}\overline{V}_0, \qquad K = R^{5/3}\,\overline{K}_0, \qquad m = R^{1/3}\,\overline{m}_0. \tag{6.2.3}$$

We depict our new regime in figure 6.2.1, where we have included the scalings of our flow quantities in each region. We remark that we have rescaled the linear disturbance suggested by figure 6.1.8 so that the pressure disturbance in the core has size $R^{-1/3}$.

The Rayleigh core

In the core region, we may write

$$\hat{u} = R^{-1/3}\overline{F}_0 + \cdots, \qquad \hat{v} = R^{-1/3}\overline{G}_0 + \cdots, \qquad \hat{p} = R^{-1/3}\overline{P}_0 + R^{-2/3}\overline{P}_1 + \cdots. \tag{6.2.4}$$

Substitution of (6.2.2) and (6.2.4) into the linearised disturbance equations (6.0.3) yields the governing equations

$$\mathrm{i}\overline{\alpha}_0\overline{F}_0 + \frac{\mathrm{d}\overline{G}_0}{\mathrm{d}r} + \frac{\overline{G}_0}{r} = 0, \quad \mathrm{i}\overline{\alpha}_0 U_{00}\overline{F}_0 + \overline{G}_0\frac{\mathrm{d}U_{00}}{\mathrm{d}r} = -\mathrm{i}\overline{\alpha}_0\overline{P}_0, \quad \mathrm{i}\overline{\alpha}_0 U_{00}\overline{G}_0 + \frac{\mathrm{d}\overline{P}_0}{\mathrm{d}r} = 0. \tag{6.2.5a,b,c}$$

We note the existence of a pressure term on the right-hand side of the axial momentum equation (6.2.5b), which is not present in the core equation (6.1.7b) of our previous lower-branch structure.

The equations (6.2.5) can be manipulated to form the Rayleigh pressure equation with zero wavespeed:

$$\overline{P}_0{}''(r) + \left(\frac{1}{r} - \frac{2U_{00}{}'(r)}{U_{00}(r)}\right)\overline{P}_0{}'(r) - \overline{\alpha}_0^2\,\overline{P}_0(r) = 0. \tag{6.2.6}$$

A linear equation, (6.2.6) admits any multiple of $\overline{P}_0$ as a solution. Therefore we prescribe $\overline{P}_0(\delta) = 1$ without loss of generality. To match the upper viscous layer, we also require $\overline{P}_0$ to decay as $r \to 1$. Therefore, we solve (6.2.6) subject to

$$\overline{P}_0(\delta) = 1, \qquad \overline{P}_0(1) = 0. \tag{6.2.7}$$

We employ the Frobenius method to find series solutions of $\overline{P}_0$ near $r = 1$ and $r = \delta$. These series solutions then enable us to also express $\overline{F}_0$ and $\overline{G}_0$ as we approach the viscous layers. Near $r = \delta$, we find

$$\overline{P}_0 = 1 - \frac{\overline{\alpha}_0{}^2}{2}(r-\delta)^2 + \cdots, \qquad \overline{G}_0 = -\frac{\mathrm{i}\overline{\alpha}_0}{\lambda_-^{(0)}} + \cdots, \qquad \overline{F}_0 = \frac{1}{\lambda_-^{(0)}}\left(\frac{2\lambda_-^{(10)}}{\lambda_-^{(0)}} - \frac{1}{\delta}\right)\log(r-\delta) + \cdots. \tag{6.2.8}$$

Near $r = 1$, we have

$$\overline{P}_0 = A(r-1)^3 + \cdots, \qquad \overline{G}_0 = \mathrm{i}\frac{3A(1-r)}{\overline{\alpha}_0\lambda_+^{(0)}} + \cdots, \qquad \overline{F}_0 = \frac{3A}{\overline{\alpha}_0{}^2\lambda_+^{(0)}} + \cdots, \tag{6.2.9}$$

where A is a constant to be determined. At the next order, we must have

$$\overline{P}_1 = \overline{\hat{P}}_0 + \cdots \tag{6.2.10}$$

near $r = 1$, where $\overline{\hat{P}}_0$ is also an undetermined constant.

Upper viscous wall layer

In this region, the disturbance quantities to leading order are

$$\hat{u} = R^{-1/3}\overline{u}_+, \qquad \hat{v} = -R^{-2/3}\overline{v}_+, \qquad \hat{p} = R^{-2/3}\overline{p}_+, \qquad r = 1 - R^{-1/3}\overline{y}_+. \tag{6.2.11}$$

Substituting these expansions into the linearised disturbance equations (6.0.3) gives the governing equations

$$\mathrm{i}\overline{\alpha}_0\overline{u}_+ + \frac{\mathrm{d}\overline{v}_+}{\mathrm{d}\overline{y}_+} = 0, \tag{6.2.12a}$$

$$\mathrm{i}\overline{\alpha}_0\left(\lambda_+^{(0)}\overline{y}_+ - \bar{c}_0\right)\overline{u}_+ + \overline{v_+}\lambda_+^{(0)} = -\mathrm{i}\overline{\alpha}_0\overline{p}_+ + \frac{\mathrm{d}^2\overline{u}_+}{\mathrm{d}\overline{y}_+^2}, \tag{6.2.12b}$$

$$\frac{\mathrm{d}\overline{p}_+}{\mathrm{d}\overline{y}_+} = 0. \tag{6.2.12c}$$

These are subject to no-slip conditions on the outer cylinder (6.0.4) and matching conditions as we approach the core. In view of (6.2.9), these are expressed as

$$\overline{u}_+ = \overline{v}_+ = 0 \qquad \text{on} \quad y = 0, \tag{6.2.13a}$$

$$\overline{u}_+ \to \frac{3A}{\overline{\alpha}_0{}^2\lambda_+^{(0)}} \qquad \text{as} \quad y \to \infty. \tag{6.2.13b}$$

The radial momentum equation (6.2.12c) reveals that the pressure is constant in $\bar{y}_+$. To match the pressure disturbance (6.2.10) in the core, we must have

$$\overline{p}_+ = \overline{\hat{P}}_0. \tag{6.2.14}$$

Solving (6.2.12a,b) subject to (6.2.13), the axial disturbance is found to be

$$\overline{u}_+\left(\overline{y}_+\right) = \frac{3A}{\overline{\alpha}_0{}^2\lambda_+^{(0)}}\frac{1}{\kappa(\bar{b}_+)}\int_{\bar{b}_+}^{\infty}\mathrm{Ai}\left(\overline{\xi}_+\right)\mathrm{d}\overline{\xi}_+, \tag{6.2.15}$$

where

$$\overline{\xi}_+ = \overline{a}_+\overline{y}_+ + \overline{b}_+, \qquad \overline{a}_+ = \left(\mathrm{i}\overline{\alpha}_0\lambda_+^{(0)}\right)^{1/3}, \qquad \overline{b}_+ = -\frac{\mathrm{i}\overline{\alpha}_0\overline{c}_0}{\left(\mathrm{i}\overline{\alpha}_0\lambda_+^{(0)}\right)^{2/3}}, \tag{6.2.16}$$

$$\kappa(\overline{b}_+) = \int_{\overline{b}_+}^{\infty} \mathrm{Ai}\left(\overline{\xi}_+\right) \mathrm{d}\overline{\xi}_+. \tag{6.2.17}$$

Evaluating the axial momentum equation (6.2.12b) at $\overline{y}_+ = 0$ and using (6.2.15), we find the relation

$$-\overline{\alpha}_0{}^{7/3}\left(\lambda_+^{(0)}\right)^{1/3}\widehat{\overline{P}}_0 = 3A\, g(\overline{s}_+), \tag{6.2.18}$$

where we have defined

$$\overline{s}_+ = \frac{\overline{\alpha}_0\overline{c}_0}{\left(\overline{\alpha}_0\lambda_+^{(0)}\right)^{2/3}}. \tag{6.2.19}$$

Lower viscous wall layer

Here, the expansions to leading order are

$$\hat{u} = \overline{u}_-, \quad \hat{v} = R^{-1/3}\overline{v}_-, \quad \hat{p} = R^{-1/3}\overline{p}_-, \quad U_0 = R^{-1/3}\left(\lambda_-^{(0)}\overline{y}_- + \overline{V}_0\right), \quad r = \delta + R^{-1/3}\overline{y}_-. \tag{6.2.20}$$

with

$$V = R^{-1/3}\overline{V}_0, \quad K = R^{5/3}\overline{K}_0, \quad m = R^{1/3}\overline{m}_0, \tag{6.2.21}$$

Whilst $\hat{u}$ is of order one in this region, we recall that the axial disturbance in the core (6.2.4, 6.2.8) approaches the lower viscous wall layer with an amplitude of order $R^{-1/3}\log R$. We expect, then, for $\hat{u}$ in this viscous layer to decay as we approach the core. Substitution of (6.2.20) into the linearised disturbance equations (6.0.3) shows that the leading order dynamics in this layer are governed by

$$\mathrm{i}\overline{\alpha}_0\overline{u}_- + \frac{\mathrm{d}\overline{v}_-}{\mathrm{d}\overline{y}_-} = 0, \tag{6.2.22a}$$

$$\mathrm{i}\overline{\alpha}_0\left(\lambda_-^{(0)}\overline{y}_- + \overline{V}_0 - \overline{c}_0\right)\overline{u}_- + \lambda_-^{(0)}\overline{v}_- = -\mathrm{i}\overline{\alpha}_0\overline{p}_- + \frac{\mathrm{d}^2\overline{u}_-}{\mathrm{d}\overline{y}_-^2}, \tag{6.2.22b}$$

$$\frac{\mathrm{d}\overline{p}_-}{\mathrm{d}\overline{y}_-} = 0. \tag{6.2.22c}$$

subject to the boundary conditions (6.0.5) and (6.0.6), which give

$$\mathrm{i}\overline{\alpha}_0\left(\overline{V}_0 - \overline{c}_0\right)\overline{u}_- + \lambda_-^{(0)}\overline{v}_- = 0 \quad \text{on} \quad \overline{y}_- = 0, \tag{6.2.23a}$$

$$\overline{p}_- = \frac{\left(\overline{K}_0 - \overline{\alpha}_0{}^2\overline{c}_0{}^2\overline{m}_0\right)\,\overline{u}_-}{\lambda_-^{(0)}} \quad \text{on} \quad \overline{y}_- = 0. \tag{6.2.23b}$$

As discussed above, we must also have that

$$\overline{u}_- \to 0 \quad \text{as} \quad \overline{y}_- \to \infty. \tag{6.2.24}$$

in order to be able to match the core solution.

It can be seen from (6.2.22c) that $\overline{p}_-$ is constant across this layer. Matching the pressure solution (6.2.8) in the core, we must have $\overline{p}_- = 1$. This allows us to write the dynamic condition (6.2.23b) as

$$\overline{u}_- = \frac{\lambda_-^{(0)}}{\overline{K_0} - \overline{\alpha}_0{}^2\overline{c}_0{}^2\overline{m}_0} \quad \text{on} \quad \overline{y}_- = 0. \tag{6.2.25}$$

Solving (6.2.22a,b) subject to (6.2.23a), (6.2.25) , we obtain the axial disturbance

$$\overline{u}_-(\overline{y}_-) = \frac{\lambda_-^{(0)}}{\overline{K_0} - \overline{\alpha}_0{}^2\overline{c}_0{}^2\overline{m}_0}\left(1 - \frac{1}{\kappa(\overline{b}_-)}\int_{\overline{b}_-}^{\overline{\xi}_-} \mathrm{Ai}\left(\overline{\xi}_-\right)\mathrm{d}\overline{\xi}_-\right), \tag{6.2.26}$$

where

$$\overline{\xi}_- = \overline{a}_-\overline{y}_- + \overline{b}_-, \qquad \overline{a}_- = \left(\mathrm{i}\overline{\alpha}_0\lambda_-^{(0)}\right)^{1/3}, \qquad \overline{b}_- = -\frac{\mathrm{i}\overline{\alpha}_0\left(\overline{c}_0 - \overline{V}_0\right)}{\left(\mathrm{i}\alpha_0\lambda_-^{(0)}\right)^{2/3}}, \tag{6.2.27}$$

$$\kappa(\overline{b}_-) = \int_{\overline{b}_-}^{\infty} \mathrm{Ai}\left(\overline{\xi}_-\right)\mathrm{d}\overline{\xi}_-. \tag{6.2.28}$$

Now, evaluating the axial momentum equation (6.2.22b) on $\overline{y}_- = 0$ gives

$$\left.\frac{\mathrm{d}^2\overline{u}_-}{\mathrm{d}\overline{y}_-^2}\right|_{\overline{y}_-=0} = \mathrm{i}\overline{\alpha}_0 \tag{6.2.29}$$

where we have made use of the kinematic condition (6.2.23a) to simplify the resulting expression.

After some manipulation, substitution of (6.2.26) into (6.2.29) reveals

$$\overline{\alpha}_0{}^{1/3} = \frac{\left(\lambda_-^{(0)}\right)^{5/3}}{\overline{K_0} - \overline{\alpha}_0{}^2\overline{c}_0{}^2\overline{m}_0}\, g(s), \tag{6.2.30}$$

where the function g is defined as

$$g(s) = \mathrm{i}^{5/3}\frac{\mathrm{Ai}'(-\mathrm{i}^{1/3}s)}{\kappa(-\mathrm{i}^{1/3}s)}, \tag{6.2.31}$$

and the variable s as

$$s = \frac{\overline{\alpha}_0\left(\overline{c}_0 - \overline{V}_0\right)}{\left(\overline{\alpha}_0\lambda_-^{(0)}\right)^{2/3}}, \tag{6.2.32}$$

so that

$$\bar{b}_- = -\mathrm{i}^{1/3} s. \tag{6.2.33}$$

To gain more insight into relation (6.2.30), we make use of the fact that the wavenumber must be real and positive. We notice that the left-hand side of (6.2.30) is real. Therefore, the right-hand must also be real. The unique finite root of $\mathrm{Im}(g(s)) = 0$ is given by $s = s_0$, where

$$s_0 \approx 2.2972. \tag{6.2.34}$$

Figure A.0.1 illustrates that $\mathrm{Re}(g(s_0))$ is negative, and so we also require that

$$\overline{K_0} - \overline{\alpha}_0{}^2 \, \bar{c}_0{}^2 \, \overline{m}_0 < 0 \tag{6.2.35}$$

in order for the right-hand side of (6.2.30) to be positive.

Combining this together, we find that the leading order wavenumber of the neutral mode is found by solving

$$\overline{\alpha}_0{}^{1/3} = \frac{\left(\lambda_-^{(0)}\right)^{5/3}}{\overline{K_0} - \overline{\alpha}_0{}^2 \bar{c}_0{}^2 \overline{m}_0} \, g(s_0), \tag{6.2.36}$$

for given $\overline{V}_0, \overline{K}_0, \overline{m}_0$, provided (6.2.35) holds. We will soon see that, so long as $\overline{m}_0$ is nonzero, we are able to find a solution to (6.2.36) that has (6.2.35).

We note that (6.2.36) is in agreement with the eigenrelation (6.1.67) we found in the limit $\alpha_0 \to \infty, \ \tilde{K} \to 0^-$ of the $\alpha = O\left(R^{-1/7}\right)$ structure.

The relation (6.2.36) can be manipulated to form a seventh degree polynomial equation in $\overline{\alpha}_0{}^{1/3}$,

$$\overline{m}_0 \overline{V_0}^2 \overline{\alpha}_0^{7/3} + 2\overline{m}_0 \overline{V}_0 \lambda_-^{(0)\,2/3} s_0 \overline{\alpha}_0{}^2 + \overline{m}_0 \lambda_-^{(0)\,4/3} s_0{}^2 \overline{\alpha}_0^{5/3} - \overline{K_0} \overline{\alpha}_0{}^{1/3} + \lambda_-^{(0)\,5/3} g\,(s_0) = 0. \tag{6.2.37}$$

This has at least one real solution for $\overline{\alpha}_0 > 0$ when $\overline{m}_0 > 0$. When $\overline{m}_0$ is zero, the polynomial equation yields no admissible solutions, as expected by the requirement that $\overline{K_0} - \overline{\alpha}_0{}^2 \, \bar{c}_0{}^2 \, \overline{m}_0 < 0$.

Paired with a rearrangement of the definition of s (6.2.32),

$$\bar{c}_0 = \overline{V}_0 + \frac{\lambda_-^{(0)\,2/3} s_0}{\overline{\alpha}_0{}^{1/3}}, \tag{6.2.38}$$

it can be shown that the relation (6.2.37) provides us with a unique solution for the leading order wavenumber and wavespeed given $\overline{K}_0$, $\overline{V}_0$ and non-zero $\overline{m}_0$.

It is also illuminative to prescribe $\overline{\widetilde{K}}$, where

$$\overline{\widetilde{K}} = \overline{K}_0 - \overline{\alpha}_0^2\,\overline{c}_0^2\,\overline{m}_0, \tag{6.2.39}$$

and solve (6.2.36) and (6.2.38) for the leading order wavenumber and wavespeed. For a stationary inner cylinder with $\delta = 0.7$, figure 6.2.2 illustrates that as $|\overline{\widetilde{K}}|$ becomes increasingly small, $\overline{\alpha}_0$ grows without bound, while $\overline{c}_0$ approaches zero linearly with respect to $\overline{\widetilde{K}}$.

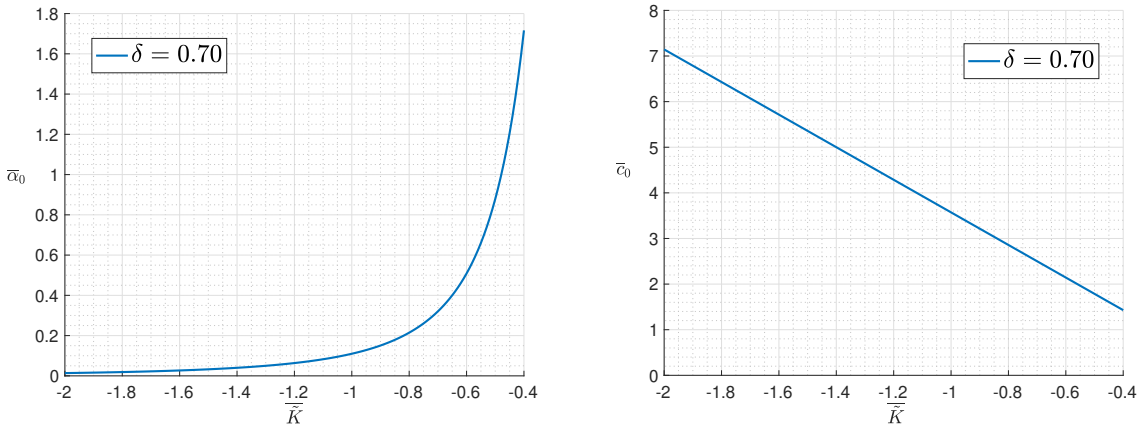

(a) (b)

Figure 6.2.2: Illustration of the behaviour of the (a) leading order wavenumber and (b) leading order wavespeed as we vary with $\overline{\widetilde{K}}$ for a stationary inner cylinder with $\delta = 0.7$.

Before moving on from this structure, we consider it worthwhile to examine more closely the pressure disturbance in the core region.

Pressure in the Rayleigh core

We remind ourselves that the Rayleigh pressure equation governing the core, and its associated boundary conditions, are given by (6.2.6), (6.2.7):

$$\overline{P}_0''(r) + \left(\frac{1}{r} - \frac{2U_{00}'(r)}{U_{00}(r)}\right)\overline{P}_0'(r) - \overline{\alpha}_0^2 P_0(r) = 0, \tag{6.2.40}$$

$$\overline{P}_0(\delta) = 1, \qquad \overline{P}_0(1) = 0. \tag{6.2.41}$$

Using the method of Frobenius, the behaviour of $\overline{P}_0$ as we approach the outer cylinder from within the core is captured by the infinite series

$$\overline{P}_0 = A(r-1)^3 - \frac{3A}{4\lambda_+^{(0)}}\left(\lambda_+^{(0)} + 2\lambda_+^{(10)}\right)(r-1)^4 + ..., \tag{6.2.42}$$

where A is an undetermined constant.

As we approach the inner cylinder instead, we have

$$\overline{P}_0 = 1 - \frac{\overline{\alpha}_0^2}{2}(r-\delta)^2 - \frac{\overline{\alpha}_0{}^2(2\delta\lambda_-^{(10)} - \lambda_-^{(0)})}{3\delta\lambda_-^{(0)}}(r-\delta)^3\log(r-\delta) + M(r-\delta)^3 + \ldots, \tag{6.2.43}$$

where M is an undetermined constant.

We use a matching procedure to determine the behaviour of the leading order pressure perturbation in the core. This entails an initial guess, say A_1 and M_1, for A and M. We can now use the first 20 terms in our series expansion (6.2.43) to evaluate $\overline{P}_0$ and $\overline{P}_0'$ very close to the inner cylinder wall, say at $r = \delta + \epsilon$ for ϵ small and positive. This provides the initial values in our subsequent Runge-Kutta procedure: we march from $r = \delta + \epsilon$ using the Rayleigh equation (6.2.40), finally obtaining values for $\overline{P}_0$ and its derivative at $r = r_1^-$, where we have taken $r_1 = 1/2 + \delta/2$. A similar procedure is carried out to approximate $\overline{P}_0$ and its derivative at $r = r_1^+$ using the expansion (6.2.42) and marching from $r = 1 - \epsilon$. Newton's method allows us to iterate on A_1 and M_1 until

$$\overline{P}_0(r_1^-) = \overline{P}_0(r_1^+) \quad \text{and} \quad \overline{P}_0'(r_1^-) = \overline{P}_0'(r_1^+).$$

Once A and M are determined, our Runge-Kutta solutions together form a smooth solution for $\overline{P}_0$ across the core. $\overline{F}_0$ and $\overline{G}_0$ can then be found via manipulation of (6.2.5). These solutions are depicted in figure 6.2.3 for $\overline{\alpha}_0 = 1.5,\ \delta = 0.2$.

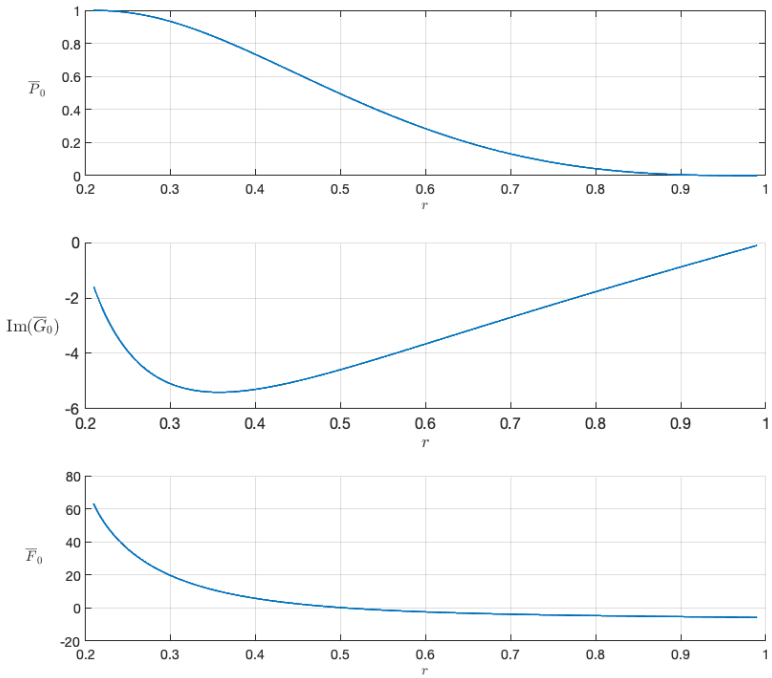

Figure 6.2.3: Illustration of the disturbance quantities $\overline{P}_0, \overline{G}_0$ and $\overline{F}_0$ in the core for $\overline{\alpha}_0 = 1.5,\ \delta = 0.2$. Recall the core is situated at a distance of $O\left(R^{-1/3}\right)$ from the walls.

We can study the behaviour of the pressure disturbance as $\overline{\alpha}_0$ becomes small by solving (6.2.40), (6.2.41) in the limit $\overline{\alpha}_0 \to 0$. In this limit, the problem reduces to

$$\overline{P}_0{}''(r) + \left(\frac{1}{r} - \frac{2U_{00}{}'(r)}{U_{00}(r)}\right)\overline{P}_0{}'(r) = 0, \qquad \overline{P}_0(\delta) = 1, \qquad \overline{P}_0(1) = 0.$$

This has the solution

$$\overline{P}_0 = \frac{I(r)}{I(\delta)}, \qquad I(r) = \int_r^1 \frac{U_{00}{}^2}{\tilde{r}}\,\mathrm{d}\tilde{r}, \tag{6.2.44}$$

which behaves as

$$\overline{P}_0 = -\frac{\lambda_+^{(0)2}}{3I(\delta)}(r-1)^3 + \cdots \quad \text{near} \quad r = 1. \tag{6.2.45}$$

Comparing this to (6.2.42) reveals that

$$\lim_{\overline{\alpha}_0 \to 0} A = -\frac{\lambda_+^{(0)2}}{3I(\delta)}. \tag{6.2.46}$$

Figure 6.2.4 illustrates this relation; we plot A (as found by our matching procedure for solving (6.2.40), (6.2.41)) as $\overline{\alpha}_0 \to 0$ and notice that the graph approaches the value on the right-hand side of (6.2.46). This value can be used as an initial guess for the matching procedure described above.

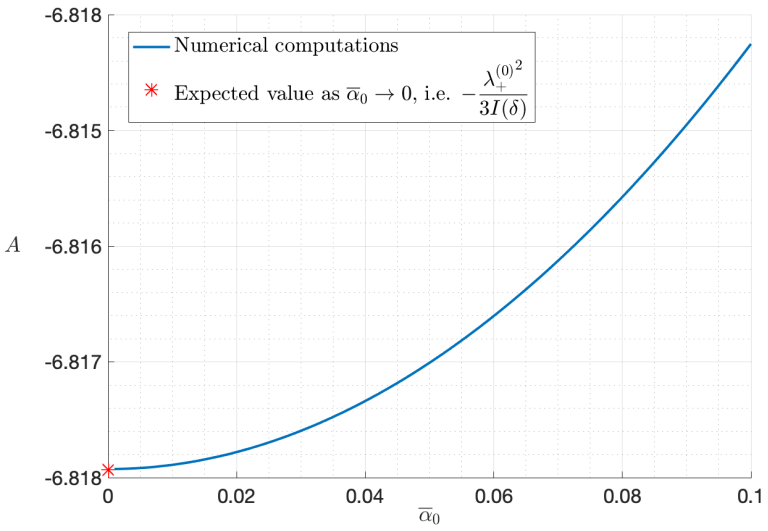

Figure 6.2.4: Plot of A as $\overline{\alpha}_0 \to 0$ for $\delta = 0.2$.

6.3 Summary

Before continuing, we summarise our work in this chapter. To begin, we were motivated by the existence of a lower-branch mode of wavenumber $\alpha = O(R^{-1/7})$ in rigid APCF, and we sought to incorporate the effects of compliance into this structure. For the cylinder properties studied, we observed the existence of two neutral modes that were not present in the rigid case.

We also found it fruitful to study this structure in various limits. As has been done by Walton [48] in the rigid case, we examined the $\alpha = O(R^{-1/7})$ lower-branch structure as the scaled sliding velocity became large. We found that the upper critical layer moves away from the outer cylinder in this limit. The resulting structure is discussed in Chapter 8.

Later exploring the large-wavenumber limiting behaviour of the $\alpha = O(R^{-1/7})$ lower-branch structure, we found a distinguished scaling for a neutral mode with $\alpha = O(1)$. A key component of this new structure is that it hinges on the cylinder and wave properties being such that

$$K - \alpha^2 c^2 m < 0 \tag{6.3.1}$$

and, as such, has no rigid counterpart. We emphasise that it is necessary for the mass of the inner cylinder to be non-zero in order for the inequality (6.3.1) to hold, since K is a positive quantity.

In the next chapter, we seek to understand the behaviour of upper-branch neutral modes.

Chapter 7

An asymptotic approach at large Reynolds numbers: an upper-branch analysis

7.1 Upper-branch structure I: two critical layers

As with the lower-branch analysis at asymptotically large Reynolds numbers, the effects of viscosity are confined to near the cylinder walls. A key difference here, however, is that the magnitude of the disturbance wavespeed on the upper branch is typically greater than that on the lower branch, which gives rise to critical layers that are not embedded within the viscous wall layers. This upper-branch mode behaviour is encapsulated in the intricate, nine-zone asymptotic structure described below (see also figure 7.1.1).

The bulk of the fluid is modelled by an inviscid core. Surrounding this core on both sides are inviscid shear layers where the base velocity is of the same order as that of the disturbance wavespeed. A viscous critical layer forms in these regions to smooth out the singularity that arises where the base velocity exactly equals the disturbance wavespeed. Lastly, close to the cylinder walls, we have thin viscous wall layers that modify the disturbance behaviour so that the appropriate boundary conditions on the cylinder walls are satisfied.

As in the lower-branch analysis, we seek a disturbance solution for $V \ll 1$. With this in mind, we write

$$V = \epsilon^2 \, V_0, \qquad U_0 = U_{00} + \epsilon^2 U_{01} \tag{7.1.1}$$

where ϵ is a small parameter that will be determined in the analysis that follows. The base quantities U_{00} and U_{01} are defined in (6.1.2b), and their near wall behaviour is given by (6.1.3a)-(6.1.5).

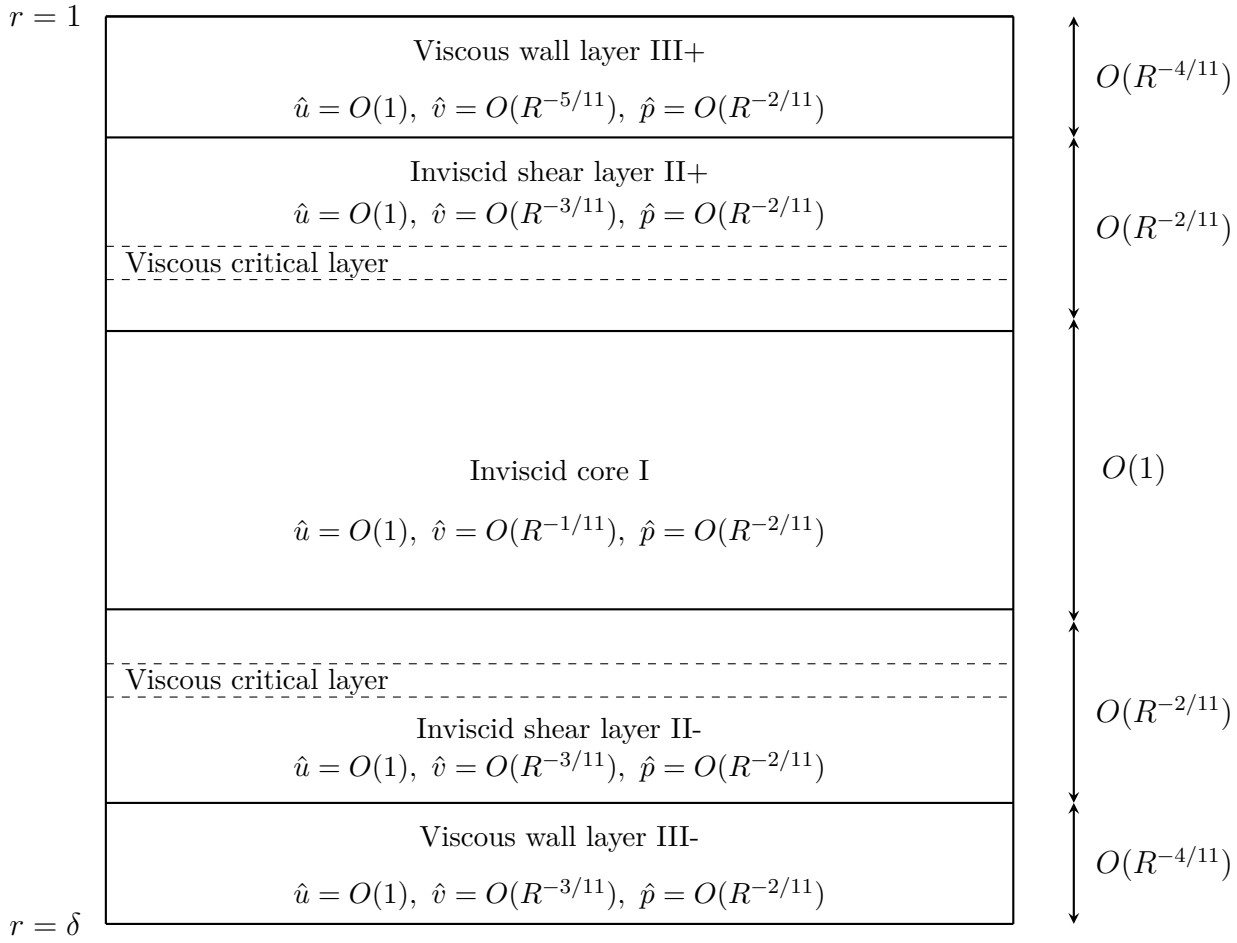

Figure 7.1.1: Schematic of the asymptotic structure of the upper-branch mode, where $\alpha = O(R^{-1/11})$ and $c = O(R^{-2/11})$. The cylinder properties are $V = O\left(R^{-2/11}\right)$, $K = O\left(R^{20/11}\right)$ and $m = O\left(R^{4/11}\right)$.

Inviscid core I

Following the scaling arguments of the lower-branch analysis in Chapter 6, Section 6.1, we begin by investigating the disturbance behaviour in the inviscid core and expand our flow quantities as follows:

$$\hat{u} = F_0 + \epsilon^2 F_1 + \cdots, \quad \hat{v} = \epsilon G_0 + \epsilon^3 G_1 + \cdots, \quad \hat{p} = \epsilon^2 P_0 + \epsilon^4 P_1 + \cdots, \tag{7.1.2a}$$

$$\alpha = \epsilon\alpha_0 + \epsilon^3\alpha_1 + \cdots, \quad c = \epsilon^2 c_0 + \epsilon^4 c_1 + \cdots. \tag{7.1.2b}$$

We note that the small parameter ϵ here is not the same as that of the lower-branch analysis in Section 6.1. For the present structure, we will determine ϵ in terms of the Reynolds number in the analysis that follows.

Upon substituting the expansions (7.1.2) into the linearised disturbance equations (2.3.11), we focus on the leading order dynamics to obtain

$$\mathrm{i}\alpha_0 F_0 + \frac{\mathrm{d}G_0}{\mathrm{d}r} + \frac{G_0}{r} = 0, \quad \mathrm{i}\alpha_0 U_{00} F_0 + G_0 \frac{\mathrm{d}U_{00}}{\mathrm{d}r} = 0, \quad \mathrm{i}\alpha_0 U_{00} G_0 + \frac{\mathrm{d}P_0}{\mathrm{d}r} = 0. \tag{7.1.3a,b,c}$$

Requiring that we have zero normal velocity on the outer cylinder wall, we recall that this is exactly the system studied in the inviscid core region of the lower-branch mode in Section 6.1. The solutions are thus

$$F_0 = \frac{A_0}{r}\frac{\mathrm{d}U_{00}}{\mathrm{d}r}, \quad G_0 = -\frac{\mathrm{i}\alpha_0 A_0}{r}\, U_{00}, \quad P_0 = \hat{P}_0 + \alpha_0^2 A_0 I(r), \tag{7.1.4}$$

where $I(r)$ is as defined in (6.1.11). Without loss of generality, we assume the phase of F_0, G_0 and P_0 is such that A_0 is real, noting that $(F_0, G_0, P_0)e^{\mathrm{i}\theta}$ is a solution of (7.1.3) for any $\theta \in \mathbb{R}$.

At the next order, substitution of the expansions (7.1.2) into the linearised disturbance equations (2.3.11) gives

$$\mathrm{i}\alpha_0 F_1 + \mathrm{i}\alpha_1 F_0 + \frac{\mathrm{d}G_1}{\mathrm{d}r} + \frac{G_1}{r} = 0, \tag{7.1.5a}$$

$$\mathrm{i}\alpha_0 U_{00} F_1 + \mathrm{i}\alpha_0 (U_{01} - c_0) F_0 + \mathrm{i}\alpha_1 U_{00} F_0 + G_0 \frac{\mathrm{d}U_{01}}{\mathrm{d}r} + G_1 \frac{\mathrm{d}U_{00}}{\mathrm{d}r} = -\mathrm{i}\alpha_0 P_0, \tag{7.1.5b}$$

$$\mathrm{i}\alpha_0 U_{00} G_1 + \mathrm{i}\alpha_0 (U_{01} - c_0) G_0 + \mathrm{i}\alpha_1 U_{00} G_0 = -\frac{\mathrm{d}P_1}{\mathrm{d}r}. \tag{7.1.5c}$$

Using the solutions for the leading order terms (7.1.4), we find G_1 and P_1 to be

$$G_1(r) = -\mathrm{i}\alpha_0 A_1 \frac{U_{00}}{r} + \text{imaginary terms}, \quad P_1(r) = P_+^{(1)} + \alpha_0^2 A_1 I(r) + \text{real terms}, \tag{7.1.6}$$

where A_1 and $P_+^{(1)}$ are unknown complex constants.

It will be useful to note the behaviour of $\hat{u}, \hat{v}$ and $\hat{p}$ as we approach each cylinder. As $r \to 1^-$,

$$F_0 \to -A_0\lambda_+^{(0)}, \quad G_0 \sim -\mathrm{i}\alpha_0 A_0 \lambda_+^{(0)}(1-r), \quad P_0 \to \hat{P}_0, \tag{7.1.7a}$$

$$\mathrm{Re}\{G_1\} \sim \alpha_0 \,\mathrm{Im}\{A_1\}\lambda_+^{(0)}(1-r), \quad \mathrm{Im}\{P_1\} \to \mathrm{Im}\Big\{P_+^{(1)}\Big\}. \tag{7.1.7b}$$

Similarly, as $r \to \delta^+$,

$$F_0 \to \frac{A_0\lambda_-^{(0)}}{\delta}, \quad G_0 \sim -\frac{\mathrm{i}\alpha_0 A_0 \lambda_-^{(0)}}{\delta}(r-\delta), \quad P_0 \to \hat{P}_0 + \alpha_0^2 A_0 I(\delta), \tag{7.1.8a}$$

$$\mathrm{Re}\{G_1\} \sim \frac{\alpha_0 \,\mathrm{Im}\{A_1\}\lambda_-^{(0)}}{\delta}(r-\delta), \quad \mathrm{Im}\{P_1\} \to \mathrm{Im}\Big\{P_+^{(1)}\Big\} + \alpha_0^2 \,\mathrm{Im}\{A_1\} I(\delta). \tag{7.1.8b}$$

We will see that these matching conditions provide us with an insight into how to formulate the appropriate scalings for the disturbance field in the neighbouring regions.

Inviscid shear layer II+

In this region, the basic velocity is of the same order as that of the disturbance wavespeed. Near $r = 1$, we recall that the basic velocity expands as in (6.1.3a), which gives

$$U_0 = \lambda_+^{(0)}(1-r) + \lambda_+^{(10)}(1-r)^2 + \epsilon^2\lambda_+^{(1)}(1-r) + \cdots \tag{7.1.9}$$

with $\lambda_+^{(0)}$, $\lambda_+^{(10)}$ and $\lambda_+^{(1)}$ as defined in (6.1.5). With (7.1.2b), we also have that

$$c = O(\epsilon^2). \tag{7.1.10}$$

Hence we require that $(1-r) = O(\epsilon^2)$ and we write

$$r = 1 - \epsilon^2 Y_+ \quad \text{where} \quad Y_+ = O(1). \tag{7.1.11}$$

Turning our attention back to the matching conditions (7.1.7), we see the disturbance in the core approaches this region as

$$F_0 \to -A_0\lambda_+^{(0)} = O(1), \quad G_0 \sim -\mathrm{i}\epsilon^2\alpha_0 A_0 \lambda_+^{(0)} Y_+ = O(\epsilon^2), \quad P_0 \to \hat{P}_0 = O(1). \tag{7.1.12}$$

In view of (7.1.2a), this suggests that the appropriate scalings for the disturbance quantities in the inviscid shear region are $\hat{u} = O(1)$, $\hat{v} = O(\epsilon^3)$ and $\hat{p} = O(\epsilon^2)$.

We thus write the flow expansions as

$$U_0 = \epsilon^2 \lambda_+^{(0)} Y_+ + \epsilon^4 \left(\lambda_+^{(10)} Y_+^2 + \lambda_+^{(1)} Y_+ \right) + \cdots, \quad r = 1 - \epsilon^2 Y_+, \tag{7.1.13a}$$

$$\hat{u} = u_+^{(0)} + \epsilon^2 u_+^{(1)} \cdots, \quad \hat{v} = -\epsilon^3 v_+^{(0)} - \epsilon^5 v_+^{(1)} - \cdots, \quad \hat{p} = \epsilon^2 p_+^{(0)} + \epsilon^4 p_+^{(1)} + \cdots, \tag{7.1.13b}$$

$$\alpha = \epsilon \alpha_0 + \epsilon^3 \alpha_1 + \cdots, \quad c = \epsilon^2 c_0 + \epsilon^4 c_1 + \cdots. \tag{7.1.13c}$$

Substituting these expansions into the disturbance equations (2.3.11), we find to leading order

$$\mathrm{i}\alpha_0 u_+^{(0)} + \frac{\mathrm{d}v_+^{(0)}}{\mathrm{d}Y_+} = 0, \tag{7.1.14a}$$

$$\mathrm{i}\alpha_0 \left(\lambda_+^{(0)} Y_+ - c_0 \right) u_+^{(0)} + \lambda_+^{(0)} v_+^{(0)} + \mathrm{i}\alpha_0 p_+^{(0)} = 0, \tag{7.1.14b}$$

$$\frac{\mathrm{d}p_+^{(0)}}{\mathrm{d}Y_+} = 0. \tag{7.1.14c}$$

Differentiation of the axial momentum equation (7.1.14b) with respect to Y_+ and use of the continuity equation (7.1.14a) gives

$$\mathrm{i}\alpha_0 (\lambda_+^{(0)} Y_+ - c_0) \frac{\mathrm{d}u_+^{(0)}}{\mathrm{d}y} = 0. \tag{7.1.15}$$

Solving equations (7.1.14a), (7.1.14c) and (7.1.15) subject to the matching conditions (7.1.12) illustrates that, at leading order, the disturbance quantities $\hat{u}$ and $\hat{p}$ exhibit constant behaviour (with respect to Y_+) across the extent of region II+ whilst $\hat{v}$ decreases linearly in Y_+ as we approach the outer cylinder. More specifically, we have

$$u_+^{(0)} = -A_0 \lambda_+^{(0)}, \qquad v_+^{(0)} = \mathrm{i}\alpha_0 A_0 \left(\lambda_+^{(0)} Y_+ - c_0 \right) - \frac{\mathrm{i}\alpha_0 \hat{P}_0}{\lambda_+^{(0)}}, \qquad p_+^{(0)} = \hat{P}_0. \tag{7.1.16}$$

In an inviscid flow, there is no normal flow at the surface of the outer cylinder and it is therefore reasonable to expect that $v_+^{(0)} \to 0$ as $r \to 1$. To satisfy this, the following pressure-displacement relation must hold true:

$$A_0 c_0 + \frac{\hat{P}_0}{\lambda_+^{(0)}} = 0. \tag{7.1.17}$$

At the next order, the dynamics become more complicated. From substitution of (7.1.13a) into (2.3.11), the governing equations are

$$\mathrm{i}\alpha_1 u_+^{(0)} + \mathrm{i}\alpha_0 u_+^{(1)} + \frac{\mathrm{d}v_+^{(1)}}{\mathrm{d}Y_+} - v_+^{(0)} = 0, \tag{7.1.18a}$$

$$\begin{aligned}\mathrm{i}\alpha_0\left(\lambda_+^{(10)}Y_+^2 + \lambda_+^{(1)}Y_+ - c_1\right)u_+^{(0)} + \left(\lambda_+^{(0)}Y_+ - c_0\right)\left(\mathrm{i}\alpha_0 u_+^{(1)} + \mathrm{i}\alpha_1 u_+^{(0)}\right) + \\ \left(2\lambda_+^{(10)}Y_+ + \lambda_+^{(1)}\right)v_+^{(0)} + \lambda_+^{(0)}v_+^{(1)} + \mathrm{i}\alpha_1 p_+^{(0)} + \mathrm{i}\alpha_0 p_+^{(1)} = 0,\end{aligned} \tag{7.1.18b}$$

$$\frac{\mathrm{d}p_+^{(1)}}{\mathrm{d}Y_+} = 0. \tag{7.1.18c}$$

Equation (7.1.18c) demonstrates that $p_+^{(1)}$ is constant with respect to Y_+, and we write

$$p_+^{(1)} = P_+. \tag{7.1.19}$$

To match the core pressure as $Y_+ \to \infty$, the behaviour in (7.1.7b) shows it must be the case that

$$\mathrm{Im}\{P_+\} = \mathrm{Im}\{P_+^{(1)}\}. \tag{7.1.20}$$

Introducing the variable $\zeta_+ = \lambda_+^{(0)}Y_+ - c_0$, we find that

$$v_+^{(1)} = \mathrm{i}\alpha_0 A_+^{(1)}\zeta_+ - \frac{\mathrm{i}\alpha_0 P_+}{\lambda_+^{(0)}} - \frac{\mathrm{i}\alpha_0 \hat{P}_0}{\lambda_+^{(0)}}\left(\frac{2\lambda_+^{(10)}}{{\lambda_+^{(0)}}^2} + \frac{1}{\lambda_+^{(0)}}\right)\zeta_+\log(\zeta_+) + \text{imaginary terms}, \quad \zeta_+ \neq 0, \tag{7.1.21}$$

where $A_+^{(1)}$ is an unknown complex constant. A thin linear critical layer manifests where the base velocity equals the wavespeed ($\zeta_+ = 0$) to smooth out the singularity arising in the log term of $v_+^{(1)}$. As we cross the layer, there exists a jump in velocity which we express by writing $\log(\zeta_+) = \log|\zeta_+|$ for $\zeta_+ > 0$, and $\log(\zeta_+) = \log|\zeta_+| - \mathrm{i}\pi$ for $\zeta_+ < 0$. The details of such layers have been studied by, for example, Lin [15], Stuart [16], and Reid [17].

Our aim now is to uncover a relation between the constants of integration $A_+^{(1)}$ and A_1. Matching the real part of $v_+^{(1)}$ (7.1.21) as $Y_+ \to \infty$ in the shear region with the real part of G_1 as $r \to 1$ in the core region (7.1.7b), we obtain

$$\mathrm{Im}\left\{A_+^{(1)}\right\} = \mathrm{Im}\{A_1\}. \tag{7.1.22}$$

We conclude this section by considering the disturbance behaviour as we approach the viscous wall layer, that is, as $Y_+ \to 0$. It is important to acknowledge that $\zeta_+ \to -c_0$ and becomes negative as $Y_+ \to 0$, so we must account for the phase shift of $-\pi$ here.

In the limit $\zeta_+ \to -c_0$, the solutions (7.1.16) give

$$u_+^{(0)} = -A_0\lambda_+^{(0)} \tag{7.1.23a}$$

$$p_+^{(0)} = \hat{P}_0. \tag{7.1.23b}$$

Using (7.1.22) to eliminate $A_+^{(1)}$, consideration of (7.1.16) and (7.1.21) in the limit $\zeta_+ \to -c_0$ gives

$$v_+^{(0)} \to \mathrm{i}\alpha_0 A_0 \lambda_+^{(0)} Y_+, \tag{7.1.24a}$$

$$\mathrm{Re}\left\{v_+^{(1)}\right\} \to \alpha_0 c_0 \,\mathrm{Im}\{A_1\} + \frac{\alpha_0 c_0 \hat{P}_0}{\lambda_+^{(0)}}\left(\frac{1}{\lambda_+^{(0)}} + \frac{2\lambda_+^{(10)}}{\lambda_+^{(0)\,2}}\right)\pi + \frac{\alpha_0 \,\mathrm{Im}\left\{P_+^{(1)}\right\}}{\lambda_+^{(0)}}. \tag{7.1.24b}$$

These expressions provide us with the matching conditions to be satisfied by the disturbance quantities in the viscous wall layer, and indicate to us the possible scalings in this region. We now investigate this in more detail.

Viscous wall layer III+

Our initial motive here is to determine the thickness of the upper viscous wall layer, which we will denote as q. In view of the behaviour (7.1.23), it is evident that $\hat{u} = O(1)$ and $\hat{p} = O(\epsilon^2)$ as $Y_+ \to 0$ in the inviscid shear region. This drives the scalings for the disturbance quantities in this upper viscous region to be $\hat{u} = O(1)$ and $\hat{p} = O(\epsilon^2)$. We will determine the scaling for $\hat{v}$ presently.

From the continuity equation (2.3.11a), we expect

$$\mathrm{i}\alpha\hat{u} \sim \frac{\mathrm{d}\hat{v}}{\mathrm{d}r}, \tag{7.1.25}$$

which gives $O(\hat{v}) = \epsilon q$. Matching this to $v_+^{(1)}$ (7.1.21) as $Y_+ \to 0$ in the inviscid shear region, we require the balance $\epsilon q \sim \epsilon^5$. This determines the thickness of the layer to be

$$q \sim \epsilon^4. \tag{7.1.26}$$

In this region, the basic velocity is of order ϵ^4 and is much smaller than the wavespeed. The axial momentum equation (2.3.11b) enables us to find ϵ in terms of the Reynolds number. We expect the dominant balance in (2.3.11b) to be given by

$$\mathrm{i}\alpha c\hat{u} \sim \frac{1}{R}\frac{\mathrm{d}^2\hat{u}}{\mathrm{d}r^2}, \tag{7.1.27}$$

from which we deduce $\epsilon^3 \sim R^{-1}q^{-2}$ since $\alpha = O(\epsilon)$ and $c = O(\epsilon^2)$ (7.1.2b).

Using the relationship between q and ϵ in (7.1.26), this reveals

$$\epsilon \sim R^{-1/11}. \tag{7.1.28}$$

We note that this is the upper-branch scaling deduced by Lin [74] for plane Poiseuille flow.

We now write the expansions in this region as

$$\hat{u} = \bar{u}_+ + \cdots, \quad \hat{v} = -\epsilon^5 \bar{v}_+ - \cdots, \quad \hat{p} = \epsilon^2 \bar{p}_+ + \cdots, \tag{7.1.29a}$$

$$U_0 = \epsilon^4 \lambda_+^{(0)} \bar{y}_+ + \cdots, \quad r = 1 - \epsilon^4 \bar{y}_+. \tag{7.1.29b}$$

Substituting (7.1.29) into the linearised disturbance equations (2.3.11), we seek a solution to the leading order equations

$$\mathrm{i}\alpha_0 \bar{u}_+ + \frac{\mathrm{d}\bar{v}}{\mathrm{d}\bar{y}_+} = 0, \tag{7.1.30a}$$

$$\frac{\mathrm{d}^2 \bar{u}_+}{\mathrm{d}\bar{y}_+^2} + \mathrm{i}\alpha_0 c_0 \bar{u}_+ - \mathrm{i}\alpha_0 \bar{p}_+ = 0, \tag{7.1.30b}$$

$$\frac{\mathrm{d}\bar{p}_+}{\mathrm{d}\bar{y}_+} = 0, \tag{7.1.30c}$$

subject to the matching conditions (7.1.23) and the viscous no-slip condition $\bar{u}_+ = \bar{v}_+ = 0$ on $y_+ = 0$. We find that

$$\bar{u}_+ = \frac{\hat{P}_0}{c_0}\left[1 - \exp\left(-m_+ \bar{y}_+\right)\right], \quad \bar{v}_+ = -\frac{\mathrm{i}\alpha_0 \hat{P}_0}{c_0}\left[\bar{y}_+ + \frac{\exp\left(-m_+ \bar{y}_+\right)}{m_+} - \frac{1}{m_+}\right], \tag{7.1.31}$$
$$\bar{p}_+ = \hat{P}_0, \quad m_+ = (1 - \mathrm{i})\left(\tfrac{1}{2}\alpha_0 c_0\right)^{1/2}.$$

For the normal disturbance to be continuous across the annular region, we require that the real part of $\hat{v}$ as we approach the inviscid shear layer from the viscous layer is equal to the real part $\hat{v}$ as we approach the viscous layer from the inviscid shear layer, that is

$$\lim_{\bar{y}_+ \to \infty} \mathrm{Re}\{\hat{v}(\bar{y}_+)\} = \lim_{Y_+ \to 0} \mathrm{Re}\{\hat{v}(Y_+)\}.$$

Taking the real part of $\bar{v}_+$ as $\bar{y}_+ \to \infty$ and using (7.1.24) elicits a second pressure-displacement relation,

$$-\frac{\hat{P}_0}{c_0\left(2\alpha_0 c_0\right)^{1/2}} = c_0 \,\mathrm{Im}\{A_1\} + \frac{\mathrm{Im}\left\{P_+^{(1)}\right\}}{\lambda_+^{(0)}} + \frac{\hat{P}_0}{\lambda_+^{(0)}}\left(\frac{2\lambda_+^{(10)}}{{\lambda_+^{(0)}}^2} + \frac{1}{\lambda_+^{(0)}}\right)\pi c_0. \tag{7.1.32}$$

This completes the analysis for the upper layers. We expect that the lower layers will be influenced by the sliding velocity, spring stiffness and mass of the inner cylinder, and we explore this in what follows.

Lower inviscid shear layer II-

The analysis for the lower inviscid shear layer follows closely that of the upper inviscid shear layer. With a critical layer in this region, we must again have that the size of the disturbance wavespeed c is of the same order as the basic flow U_0. We assume $(c_0 - V_0) = O(1)$ with $c_0 > V_0$ and, upon recalling the near wall behaviour of U_0 (6.1.4), (6.1.5), we write

$$U_0 - c \sim \lambda_-^{(0)}(r-\delta) - \epsilon^2(c_0 - V_0) + \cdots . \tag{7.1.33}$$

For these two terms to be in balance, we require $(r-\delta) = O(\epsilon^2)$. Thus we write $r = \delta + \epsilon^2 Y_-$ for an order one variable Y_-. In view of the matching conditions (7.1.8) and core expansions (7.1.2a), we see that the disturbance quantities in the core approach the inner cylinder with $\hat{u} = O(1)$, $\hat{v} = O(\epsilon(r-\delta))$ and $\hat{p} = O(\epsilon^2)$. We anticipate the expansions in this lower shear region are then

$$U_0 = \epsilon^2\left(V_0 + \lambda_-^{(0)}Y_-\right) + \epsilon^4\left(\lambda_-^{(10)}Y_-^2 + \lambda_-^{(1)}Y_-\right) + \cdots , \quad r = \delta + \epsilon^2 Y_-, \tag{7.1.34a}$$

$$\hat{u} = u_-^{(0)} + \epsilon^2 u_-^{(1)} + \cdots , \quad \hat{v} = -\epsilon^3 v_-^{(0)} - \epsilon^5 v_-^{(1)} - \cdots , \quad \hat{p} = \epsilon^2 p_-^{(0)} + \epsilon^4 p_-^{(1)} + \cdots , \tag{7.1.34b}$$

$$\alpha = \epsilon\alpha_0 + \epsilon^3\alpha_1 + \cdots , \quad c = \epsilon^2 c_0 + \epsilon^4 c_1 + \cdots . \tag{7.1.34c}$$

Substituting these expansions into the linearised disturbance equations (2.3.11), we see that the leading order terms are governed by

$$\frac{\mathrm{d}v_-^{(0)}}{\mathrm{d}Y_-} - \mathrm{i}\alpha_0 u_-^{(0)} = 0, \tag{7.1.35a}$$

$$\mathrm{i}\alpha_0\left(\lambda_-^{(0)}Y_- + V_0 - c_0\right)u_-^{(0)} + \mathrm{i}\alpha_0 p_-^{(0)} - \lambda_-^{(0)}v_-^{(0)} = 0, \tag{7.1.35b}$$

$$\frac{\mathrm{d}p_-^{(0)}}{\mathrm{d}Y_-} = 0. \tag{7.1.35c}$$

Solving (7.1.35c) subject to the matching condition (7.1.8a) reveals that

$$p_-^{(0)} = \hat{P}_0 + \alpha_0^2 A_0 I(\delta). \tag{7.1.36}$$

Turning now to the velocity disturbances, the matching condition for $u_-^{(0)}$ (7.1.8a) can be expressed as

$$u_-^{(0)} \to \frac{A_0\lambda_-^{(0)}}{\delta} \quad \text{as} \quad Y_- \to \infty. \tag{7.1.37}$$

Writing $\zeta_- = \lambda_-^{(0)}Y_- + V_0 - c_0$, the solutions for (7.1.35a) and (7.1.35b) are found to be

$$u_-^{(0)} = \frac{A_0\lambda_-^{(0)}}{\delta}, \qquad v_-^{(0)} = \frac{\mathrm{i}\alpha_0 A_0}{\delta}\zeta_- + \frac{\mathrm{i}\alpha_0}{\lambda_-^{(0)}}\left(\hat{P}_0 + \alpha_0^2 A_0 I(\delta)\right). \tag{7.1.38a}$$

A distinguishing feature between the analysis here and in the upper inviscid shear region is the lack of a 'no normal flow' condition as $r \to \delta$. This is due to the compliant nature of the inner cylinder.

At the next order, substitution of the expansions (7.1.34) into (2.3.11) yields

$$\mathrm{i}\alpha_1 u_-^{(0)} + \mathrm{i}\alpha_0 u_-^{(1)} - \frac{\mathrm{d}v_-^{(1)}}{\mathrm{d}Y_-} - \frac{v_-^{(0)}}{\delta} = 0, \tag{7.1.39a}$$

$$\begin{aligned}\mathrm{i}\alpha_0 \left(\lambda_-^{(10)} Y_-^2 + \lambda_-^{(1)} Y_- - c_1\right) u_-^{(0)} + \left(\lambda_-^{(0)} Y_- + V_0 - c_0\right)\left(\mathrm{i}\alpha_0 u_-^{(1)} + \mathrm{i}\alpha_1 u_-^{(0)}\right) \\ - \left(2\lambda_-^{(10)} Y_- + \lambda_-^{(1)}\right) v_-^{(0)} - \lambda_-^{(0)} v_-^{(1)} + \mathrm{i}\alpha_1 p_-^{(0)} + \mathrm{i}\alpha_0 p_-^{(1)} = 0,\end{aligned} \tag{7.1.39b}$$

$$\frac{\mathrm{d}p_-^{(1)}}{\mathrm{d}Y_-} = 0. \tag{7.1.39c}$$

From (7.1.39c), we see the pressure term is constant and may be written as

$$p_-^{(1)} = P_-^{(1)}, \tag{7.1.40}$$

where we determine

$$\mathrm{Im}\left\{P_-^{(1)}\right\} = \mathrm{Im}\left\{P_+^{(1)}\right\} + \alpha_0^2 \,\mathrm{Im}\{A_1\} I(\delta) \tag{7.1.41}$$

upon matching (7.1.40) to the core using (7.1.8b).

Solving (7.1.39) for $v_-^{(1)}$, we find that the normal velocity disturbance exhibits a singularity where $\zeta_- = 0$. This term can be expressed as

$$v_-^{(1)} = \frac{\mathrm{i}\alpha_0}{\lambda_-^{(0)}}\left(\frac{2\lambda_-^{(10)}}{{\lambda_-^{(0)}}^2} - \frac{1}{\delta\lambda_-^{(0)}}\right)\left(\hat{P}_0 + \alpha_0^2 A_0 I(\delta)\right)\zeta_- \log\left(\zeta_-\right) - \mathrm{i}\alpha_0 A_-^{(1)}\zeta_- + \frac{\mathrm{i}\alpha_0 P_-^{(1)}}{\lambda_-^{(0)}} + \text{imaginary terms}, \quad \zeta_- \neq 0, \tag{7.1.42}$$

As in the upper shear layer, a critical layer smooths out this behaviour and when crossed, there exists a phase jump of magnitude π. We write $\log(\zeta_-) = \log|\zeta_-|$ for $\zeta_- > 0$ and $\log(\zeta_-) = \log|\zeta_-| - \mathrm{i}\pi$ for $\zeta_- < 0$ ([15], [16], [17]).

In order to relate the constants $A_-^{(1)}$ and A_1, we match expression (7.1.42) in the limit $\zeta_- \to \infty$ to the core using (7.1.8b). This gives the relation

$$\mathrm{Im}\left\{A_-^{(1)}\right\} = -\frac{\mathrm{Im}\{A_1\}}{\delta}. \tag{7.1.43a}$$

To complete this section, we study the disturbance behaviour as we approach the viscous wall layer. As $r \to \delta$, we have $\zeta_- \to V_0 - c_0$ and we find

$$u_-^{(0)} = \frac{A_0 \lambda_-^{(0)}}{\delta}, \qquad v_-^{(0)} \to \frac{\mathrm{i}\alpha_0 A_0}{\delta}(V_0 - c_0) + \frac{\mathrm{i}\alpha_0}{\lambda_-^{(0)}}\left(\hat{P}_0 + \alpha_0^2 A_0 I(\delta)\right), \tag{7.1.44a}$$

$$p_-^{(0)} = \hat{P}_0 + \alpha_0^2 A_0 I(\delta), \qquad p_-^{(1)} = P_-^{(1)}. \tag{7.1.44b}$$

Since $(V_0 - c_0) < 0$, we have $\log \zeta_- \to \log(c_0 - V_0) - \mathrm{i}\pi$ as $r \to \delta$, so finally, we also have

$$\mathrm{Re}\left\{v_-^{(1)}\right\} \to \frac{\alpha_0}{\lambda_-^{(0)}}\left(\frac{2\lambda_-^{(10)}}{\lambda_-^{(0)}} - \frac{1}{\delta\lambda_-^{(0)}}\right)\left(\hat{P}_0 + \alpha_0^2 A_0 I(\delta)\right)(V_0 - c_0)\pi - \alpha_0(V_0 - c_0)\frac{\mathrm{Im}\{A_1\}}{\delta} - \frac{\alpha_0 \,\mathrm{Im}\left\{P_-^{(1)}\right\}}{\lambda_-^{(0)}}. \tag{7.1.45}$$

We reiterate that the leading order normal velocity term is not presumed to vanish in this limit. The normal velocity here thus motivates us to take $\hat{v} = O(\epsilon^3)$ in the lower viscous wall layer. In contrast, we had $\hat{v} = O(\epsilon^5)$ in the upper viscous layer. We now look at the lower layer in more depth.

Viscous wall layer III-

We repeat the analysis performed for the upper viscous layer, highlighting the differences that arise from being near a compliant, non-stationary cylinder.

The behaviour of the disturbance as we approach the viscous wall layer (as seen in (7.1.44)) proposes that we take $\hat{u} = O(1)$ and $\hat{p} = O(\epsilon^2)$. With these scalings, consideration of a dominant balance between

$$\mathrm{i}\alpha(U_0 - c)\hat{u} \sim \mathrm{i}\alpha\hat{p} \sim R^{-1}\hat{u}'' \tag{7.1.46}$$

in the axial momentum equation (2.3.11b) suggests that the thickness q_- of the viscous wall layer is found to be of order ϵ^4. We note that the upper viscous wall layer also endorses a balance between the inertial, pressure and viscous terms in the axial momentum equation, and has a thickness of ϵ^4.

One key difference between the upper and lower viscous layers is the size of $\hat{v}$, which was of order ϵ^5 in the upper layer. The matching condition (7.1.44) suggests that $\hat{v} = O(\epsilon^3)$ here. Since $\alpha\hat{u} = O(\epsilon)$, the continuity equation (2.3.11a) then reveals the leading order term of $\hat{v}$ must be constant with respect to Y_-. We see this presently.

The expansions in the viscous wall layer near $r = \delta$ are given by

$$U_{00} = \epsilon^4 \lambda_-^{(0)} \bar{y} + \epsilon^8 \lambda_-^{(10)} \bar{y}^2 + \cdots, \quad U_{01} = V_0 + \epsilon^4 \lambda_-^{(1)} \bar{y} + \cdots, \quad r = \delta + \epsilon^4 \bar{y}_-, \tag{7.1.47a}$$

$$\hat{u} = \bar{u}_-^{(0)} + \epsilon^2 \bar{u}_-^{(1)} \cdots, \quad \hat{v} = -\epsilon^3 \bar{v}_-^{(0)} - \epsilon^5 \bar{v}_-^{(1)} - \cdots, \quad \hat{p} = \epsilon^2 \bar{p}_-^{(0)} + \epsilon^4 \bar{p}_-^{(1)} \cdots, \tag{7.1.47b}$$

$$\alpha = \epsilon \alpha_0 + \epsilon^3 \alpha_1 + \cdots, \quad c = \epsilon^2 c_0 + \epsilon^4 c_1 + \cdots. \tag{7.1.47c}$$

Substituting these expansions into the linearised disturbance equations (2.3.11), the leading order equations governing the dynamics in this layer are

$$\frac{\mathrm{d}\bar{v}_-^{(0)}}{\mathrm{d}\bar{y}_-} = 0, \tag{7.1.48a}$$

$$\frac{\mathrm{d}^2 \bar{u}_-^{(0)}}{\mathrm{d}\bar{y}^2} - \mathrm{i}\alpha_0 \bar{p}_-^{(0)} + \lambda_-^{(0)} \bar{v}_-^{(0)} - \mathrm{i}\alpha_0 (V_0 - c_0) \bar{u}_-^{(0)} = 0, \tag{7.1.48b}$$

$$\frac{\mathrm{d}\bar{p}_-^{(0)}}{\mathrm{d}\bar{y}_-} = 0. \tag{7.1.48c}$$

Enforcing a match with the inviscid shear layer above using (7.1.44), the solutions are

$$\bar{u}_-^{(0)} = \tilde{A} \exp(-m_- \bar{y}) + \frac{A_0 \lambda_-^{(0)}}{\delta}, \tag{7.1.49a}$$

$$\bar{v}_-^{(0)} = \mathrm{i}\alpha_0 \left(\frac{A_0 (V_0 - c_0)}{\delta} + \frac{\hat{P}_0 + \alpha_0^2 A_0 I(\delta)}{\lambda_-^{(0)}} \right), \tag{7.1.49b}$$

$$\bar{p}_-^{(0)} = \hat{P}_0 + \alpha_0^2 A_0 I(\delta), \tag{7.1.49c}$$

where $m_- = \frac{1}{\sqrt{2}}(1 - \mathrm{i})\sqrt{\alpha_0 (c_0 - V_0)}$ and $\tilde{A}$ is a constant to be determined.

To find $\tilde{A}$, we turn to the boundary conditions on the inner cylinder. We recall the dynamic condition (2.3.14) is

$$\hat{p}(\delta) = \frac{2}{R} \hat{v}'(\delta) + \left(-\alpha^2 c^2 m + \frac{K}{R^2} \right) \frac{\hat{u}(\delta)}{U_0'(\delta)}, \tag{7.1.50}$$

where $'$ denotes differentiation with respect to r. Upon use of (7.1.47), we notice that

$$\hat{u}(\delta) = O(1), \quad \hat{p}(\delta) = O(\epsilon^2), \quad \frac{2}{R} \hat{v}(\delta) = O(\epsilon^{12}), \tag{7.1.51}$$

$$\alpha^2 c^2 m = O(\epsilon^6 m) \quad \frac{K}{R^2} = O(\epsilon^{22} K) \tag{7.1.52}$$

since $\epsilon = R^{-1/11}$ (7.1.28).

Invoking a balance between the pressure terms and the term pertaining to the cylinder's compliance in (7.1.50) so that

$$\hat{p}(\delta) \sim R^{-2} K \hat{u}(\delta) \sim \alpha^2 c^2 m \hat{u}(\delta), \tag{7.1.53}$$

we prescribe that

$$K = O(\epsilon^{-20}), \quad m = O(\epsilon^{-4}). \tag{7.1.54}$$

We note that these are the scalings used by Gajjar and Sibanda [61] in their upper-branch analysis of channel flow with compliant boundaries.

Writing $K = \epsilon^{-20} K_0$ for $K_0 = O(1)$ and $m = \epsilon^{-4} m_0$ for $m_0 = O(1)$, from (7.1.50) we obtain to leading order

$$\bar{p}_-^{(0)} = \frac{\widetilde{K}\, \bar{u}_-^{(0)}}{\lambda_-^{(0)}}, \tag{7.1.55}$$

where $\widetilde{K} = K_0 - {\alpha_0}^2 {c_0}^2 m_0$. We substitute our solutions (7.1.49) into (7.1.55), obtaining an expression for $\tilde{A}$ that incorporates the compliance of the inner cylinder. We find

$$\tilde{A} = -\lambda_-^{(0)} \left(\frac{A_0}{\delta} - \frac{\hat{P}_0 + \alpha_0^2 A_0 I(\delta)}{\widetilde{K}} \right). \tag{7.1.56}$$

The second condition to be imposed on the boundary $r = \delta$ is the kinematic condition (2.3.13),

$$\mathrm{i}\alpha \left(V - c\right) \hat{u}(\delta) + \hat{v}(\delta) \frac{\mathrm{d}U_0}{\mathrm{d}r} = 0. \tag{7.1.57}$$

Using our expansions (7.1.47), to leading order this condition is expressed as

$$\mathrm{i}\alpha_0 \bar{u}_-^{(0)} \left(V_0 - c_0\right) - \lambda_-^{(0)} \bar{v}_-^{(0)} = 0. \tag{7.1.58}$$

This gives us a second expression for $\tilde{A}$ upon substitution of (7.1.49):

$$\tilde{A} = \frac{\hat{P}_0 + \alpha_0^2 A_0 I(\delta)}{V_0 - c_0}. \tag{7.1.59}$$

Combining (7.1.56) and (7.1.59) enables us to form a pressure-displacement relation between A_0 and $\hat{P}_0$:

$$\frac{A_0 \left(V_0 - c_0\right)}{\delta} + \left(\hat{P}_0 + \alpha_0^2 A_0 I(\delta)\right) \left(\frac{1}{\lambda_-^{(0)}} - \frac{V_0 - c_0}{\widetilde{K}} \right) = 0. \tag{7.1.60}$$

Turning to the dynamics at the next order, substitution of the expansions (7.1.47) into (2.3.11) gives the equations

$$\mathrm{i}\alpha_0\bar{u}_-^{(0)} - \frac{\mathrm{d}\bar{v}_-^{(1)}}{\mathrm{d}\bar{y}_-} = 0, \tag{7.1.61a}$$

$$\begin{aligned}(V_0 - c_0)\left(\mathrm{i}\alpha_1\bar{u}_-^{(0)} + \mathrm{i}\alpha_0\bar{u}_-^{(1)}\right) + \mathrm{i}\alpha_0\left(\lambda_-^{(0)}\bar{y}_- - \bar{c}_1\right)\bar{u}_-^{(0)} - \lambda_-^{(1)}\bar{v}_-^{(0)} - \lambda_-^{(0)}\bar{v}_-^{(1)} \\ + \mathrm{i}\alpha_0\bar{p}_-^{(1)} + \mathrm{i}\alpha_1\bar{p}_-^{(0)} - \frac{\mathrm{d}^2\bar{u}_-^{(1)}}{\mathrm{d}\bar{y}_-^2} = 0,\end{aligned} \tag{7.1.61b}$$

$$\frac{\mathrm{d}\bar{p}_-^{(1)}}{\mathrm{d}\bar{y}_-} = 0. \tag{7.1.61c}$$

Using our solution for $\bar{u}_-^{(0)}$ (7.1.49), the continuity equation (7.1.61a) reveals that the normal velocity possesses the solution

$$\bar{v}_-^{(1)} = \mathrm{i}\alpha_0\left[\frac{A_0\lambda_-^{(0)}\bar{y}_-}{\delta} - \frac{\hat{P}_0 + \alpha_0^2 A_0 I(\delta)}{m_-\left(V_0 - c_0\right)}\exp\left(-m_-\bar{y}_-\right)\right] + \mathrm{i}\alpha_0\tilde{D}, \tag{7.1.62}$$

where $\tilde{D}$ is a complex-valued constant of integration. In the limit $\bar{y}_- \to \infty$,

$$\mathrm{Re}\left\{\bar{v}_-^{(1)}\right\} \to -\alpha_0\,\mathrm{Im}\left\{\tilde{D}\right\}. \tag{7.1.63}$$

Applying the matching condition

$$\lim_{\bar{y}_-\to\infty}\mathrm{Re}\{\hat{v}(\bar{y}_-)\} = \lim_{Y_-\to 0}\mathrm{Re}\{\hat{v}(Y_-)\},$$

we equate expressions (7.1.63) and (7.1.45) to acquire the relation

$$\mathrm{Im}\left\{\tilde{D}\right\} = \frac{\hat{P}_0 + \alpha_0^2 A_0 I(\delta)}{\lambda_-^{(0)}}\left(\frac{2\lambda_-^{(10)}}{\lambda_-^{(0)}} - \frac{1}{\delta\lambda_-^{(0)}}\right)(c_0 - V_0)\pi + (c_0 - V_0)\,\mathrm{Im}\left\{A_-^{(1)}\right\} + \frac{\mathrm{Im}\left\{P_-^{(1)}\right\}}{\lambda_-^{(0)}}. \tag{7.1.64}$$

In what follows, we seek to form a pressure-displacement relation independent of $\tilde{D}$. In the upper viscous layer, where the nearby cylinder was rigid, it was sufficient to impose the condition of no normal flow in order to determine the constant of integration that arose in $\bar{v}_+$. The boundary conditions on a compliant cylinder are not so straightforward and require us to seek solutions at the next order for $\hat{u}$ and $\hat{p}$.

Solving (7.1.61c) and enforcing a match to the inviscid shear layer using (7.1.44b), we find the pressure disturbance is given by

$$\bar{p}_-^{(1)} = P_-^{(1)}. \tag{7.1.65}$$

Using our known solutions (7.1.49), (7.1.62), (7.1.65), we solve (7.1.61b) for $\bar{u}_-^{(1)}$. We ensure that $\bar{u}_-^{(1)}$ remains finite as $\bar{y}_- \to \infty$ and apply the kinematic condition (7.1.57) at order $O(\epsilon^5)$, which is

$$\mathrm{i}\alpha_0 (c_0 - V_0)\, \bar{u}_-^{(1)} + [\mathrm{i}\alpha_0 c_1 + \mathrm{i}\alpha_1 (c_0 - V_0)]\, \bar{u}_-^{(0)} + \lambda_-^{(1)} \bar{v}_-^{(0)} + \lambda_-^{(0)} \bar{v}_-^{(1)} = 0 \quad \text{on} \quad \bar{y}_- = 0. \tag{7.1.66}$$

This leads us to the solution

$$\bar{u}_-^{(1)} = -C(\bar{y}_-) \exp(-m_- \bar{y}_-) + B, \tag{7.1.67}$$

where $C(\bar{y}_-)$ is a second order polynomial in $\bar{y}_-$ and B is a constant such that

$$\mathrm{Im}\{C\} = \frac{\mathrm{Im}\{P_-^{(1)}\}}{c_0 - V_0} + \frac{\lambda_-^{(0)} \left(\hat{P}_0 + \alpha_0^2 A_0 I(\delta)\right)}{(c_0 - V_0)^2 \sqrt{2\alpha_0 (c_0 - V_0)}} \quad \text{on} \quad \bar{y}_- = 0, \tag{7.1.68a}$$

$$\mathrm{Im}\{B\} = \frac{\mathrm{Im}\{P_-^{(1)}\} - \lambda_-^{(0)} \mathrm{Im}\{\tilde{D}\}}{c_0 - V_0}. \tag{7.1.68b}$$

Combining these provides us with an expression for the imaginary part of $\bar{u}_-^{(1)}$ on $\bar{y}_- = 0$. Using the expansions (7.1.47), we turn our attention to the dynamic condition (7.1.50) and obtain at second order

$$\frac{\lambda_-^{(0)} \bar{p}_-^{(1)}}{\widetilde{K}} = \bar{u}_-^{(1)} - \frac{\lambda_-^{(1)} \bar{u}_-^{(0)}}{\lambda_-^{(0)}} \quad \text{on} \quad \bar{y}_- = 0. \tag{7.1.69}$$

Setting $\bar{y}_- = 0$ in (7.1.49a) and using expression (7.1.59) for $\tilde{A}$, we may write

$$\bar{u}_-^{(0)}(0) = \frac{\hat{P}_0 + \alpha_0^2 A_0 I(\delta)}{V_0 - c_0} + \frac{A_0 \lambda_-^{(0)}}{\delta}. \tag{7.1.70}$$

From this, we observe that $\bar{u}_-^{(0)}$ is purely real on $\bar{y}_- = 0$.

Taking the imaginary part of (7.1.69) and substituting our expressions for $\bar{p}_-^{(1)}$ (7.1.65) and $\bar{u}_-^{(1)}$ (7.1.67), we learn that

$$\mathrm{Im}\{\tilde{D}\} = -\frac{\mathrm{Im}\{P_-^{(1)}\}}{\widetilde{K}} (c_0 - V_0) - \frac{\hat{P}_0 + \alpha_0^2 A_0 I(\delta)}{(c_0 - V_0) \sqrt{2\alpha_0 (c_0 - V_0)}}, \tag{7.1.71}$$

after some manipulation and use of (7.1.68).

We close this section by combining expressions (7.1.64) and (7.1.71) to eliminate $\tilde{D}$ and form the relation

$$\frac{\hat{P}_0 + \alpha_0^2 A_0 I(\delta)}{(c_0 - V_0)\sqrt{2\alpha_0 (c_0 - V_0)}} = \frac{\mathrm{Im}\{A_1\}}{\delta}(c_0 - V_0) - \mathrm{Im}\left\{P_-^{(1)}\right\}\left(\frac{1}{\lambda_-^{(0)}} + \frac{c_0 - V_0}{\widetilde{K}}\right) - \frac{\hat{P}_0 + \alpha_0^2 A_0 I(\delta)}{\lambda_-^{(0)}}\left(\frac{2\lambda_-^{(10)}}{\lambda_-^{(0)2}} - \frac{1}{\delta\lambda_-^{(0)}}\right)(c_0 - V_0)\,\pi. \quad (7.1.72)$$

We use this pressure-displacement relation to form an eigenrelation for the upper-branch mode.

Forming the upper eigenrelation

Our aim here is to solve for the leading order disturbance wavenumber and wavespeed. Using (7.1.17) to eliminate A_0, rearrangement of (7.1.60) yields an expression for ${\alpha_0}^2$:

$${\alpha_0}^2 = \frac{(c_0 - V_0)\,\gamma}{\delta I(\delta)} + \frac{c_0 \lambda_+^{(0)}}{I(\delta)}, \quad (7.1.73)$$

where

$$\gamma = \left(\frac{1}{\lambda_-^{(0)}} + \frac{c_0 - V_0}{\widetilde{K}}\right)^{-1}. \quad (7.1.74)$$

Upon simplification using (7.1.17), (7.1.41) and (7.1.60), a linear combination of (7.1.32) and (7.1.72) results in a second relation between α_0 and c_0,

$$\frac{\lambda_+^{(0)}}{c_0\sqrt{2\alpha_0 c_0}} - \frac{\gamma}{(c_0 - V_0)\sqrt{2\alpha_0 (c_0 - V_0)}}\left(1 - \frac{{\alpha_0}^2 I(\delta)}{c_0 \lambda_+^{(0)}}\right) - \frac{\gamma}{\lambda_-^{(0)}}\left(1 - \frac{{\alpha_0}^2 I(\delta)}{c_0 \lambda_+^{(0)}}\right)\left(\frac{2\lambda_-^{(10)}}{\lambda_-^{(0)2}} - \frac{1}{\delta\lambda_-^{(0)}}\right)(c_0 - V_0)\,\pi + \left(\frac{2\lambda_+^{(10)}}{\lambda_+^{(0)2}} + \frac{1}{\lambda_+^{(0)}}\right) c_0 \pi = 0. \quad (7.1.75)$$

Two equations with two unknowns, (7.1.73) and (7.1.75) can be solved numerically using MATLAB. Recalling that α_0 is non-negative, we find that there is a unique solution for α_0 and c_0 for prescribed values of $V_0, \widetilde{K}$ and δ.

We verify that in the rigid limit where $\widetilde{K} \to \infty$ (with $\alpha_0, c_0, V_0 = O(1)$), we have $\gamma \to \lambda_-^{(0)}$ and the resulting eigenrelation,

$$\frac{\lambda_+^{(0)}}{c_0\sqrt{2\alpha_0 c_0}} - \frac{\lambda_-^{(0)}}{(c_0-V_0)\sqrt{2\alpha_0\,(c_0-V_0)}}\left(1-\frac{{\alpha_0}^2 I(\delta)}{c_0\lambda_+^{(0)}}\right)$$
$$-\left(1-\frac{{\alpha_0}^2 I(\delta)}{c_0\lambda_+^{(0)}}\right)\left(\frac{2\lambda_-^{(10)}}{{\lambda_-^{(0)}}^2}-\frac{1}{\delta\lambda_-^{(0)}}\right)(c_0-V_0)\,\pi+\left(\frac{2\lambda_+^{(10)}}{{\lambda_+^{(0)}}^2}+\frac{1}{\lambda_+^{(0)}}\right)c_0\pi=0, \quad (7.1.76)$$

is exactly that which was derived by Walton [1] for the rigid case.

In figure 7.1.2, we illustrate solutions α_0 (left) and $(c_0 - V_0)$ (right) of the eigenrelations (7.1.73), (7.1.75) as V_0 varies. For all choices of $\widetilde{K}$ in figure 7.1.2, it is evident that the wavenumber increases with the sliding speed. However, the curve representing $\widetilde{K} = 0.1$ increases with an increasing gradient near $V_0 = 0$, whereas the second derivative of α_0 with respect to V_0 is negative near $V_0 = 0$ for the curves corresponding to other choices of $\widetilde{K}$. We see that for a given $V_0 \lesssim 2$, a smaller $\widetilde{K}$ yields a lower wavenumber. This influence of compliance on α_0 appears greatest at small sliding velocities, and becomes less prominent as V_0 increases. In fact, we see that all the curves eventually merge at large V_0. We speculate that the leading order wavenumber is independent of the spring stiffness at large sliding velocities, and investigate this in the following section.

To explore the wavespeed of the neutral mode as V_0 increases, we find it more illustrative to plot $(c_0 - V_0)$ against V_0 (figure 7.1.2). For very small sliding velocities, we observe the largest wavespeed is associated with the smallest value of $\widetilde{K}$ and the smallest wavespeed is associated with the rigid case. As V_0 is increased beyond $V_0 \approx 0.2$, this situation reverses. For our choices of $\widetilde{K}$, we observe that $(c_0 - V_0)$ decreases with an increase in sliding velocity. In fact, as V_0 becomes large, we find the quantity $(c_0 - V_0)$ approaches zero. This motivates our analysis in the next section.

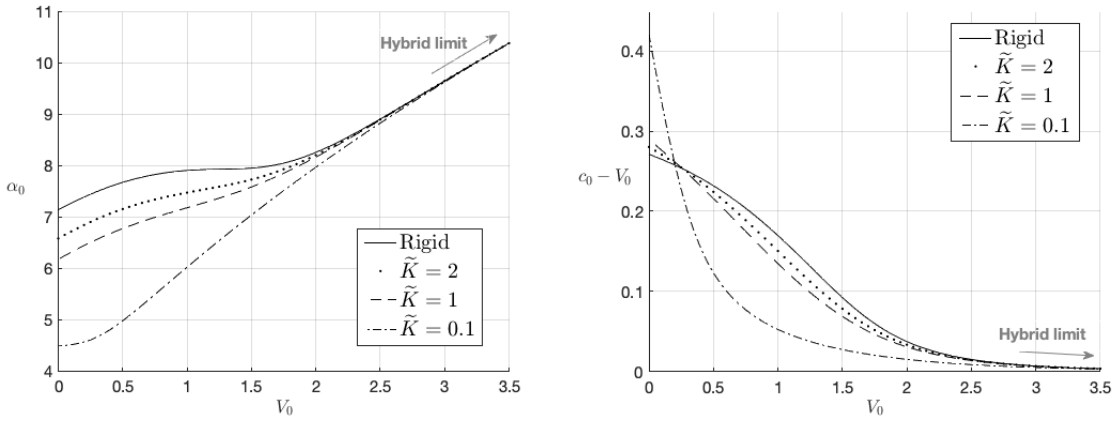

Figure 7.1.2: Fixing $\delta = 0.3$, this figure describes the solutions α_0 (left) and $(c_0 - V_0)$ (right) of the eigenrelations (7.1.73), (7.1.75) as V_0 varies. This is done for $\widetilde{K} = 0.1$, $\widetilde{K} = 1$, and $\widetilde{K} = 2$. The rigid solution is included for comparison.

7.1.1 Upper-branch structure in the limit $V_0 \to \infty$

It is interesting to explore the behaviour of the disturbance wavespeed and wavenumber as V_0 becomes large. In figure 7.1.2, we illustrated solutions to the upper-branch eigenrelations (7.1.73), (7.1.75) as V_0 varies. We observed that the quantity $(c_0 - V_0)$ approaches zero as V_0 becomes large. In view of this finding, we anticipate

$$c_0 \sim V_0 \tag{7.1.77}$$

when V_0 is asymptotically large.

Motivated by the rigid scenario in which γ remains order one as $V_0 \to \infty$, we will demand that γ (7.1.74) in our flexible scenario also remains an order one quantity as V_0 becomes large. With α_0 assumed to be positive, we suppose that $\alpha_0 \sim \beta_0 V_0^{\rho_0}$ for $\beta_0 > 0$. Investigating relation (7.1.73) in the limit $V_0 \to \infty$, it becomes apparent that we must have

$$\beta_0^2 V_0^{2\rho_0} \sim \frac{V_0 \lambda_+^{(0)}}{I(\delta)} \implies \rho_0 = \frac{1}{2}, \quad \beta_0 = \left(\frac{\lambda_+^{(0)}}{I(\delta)}\right)^{1/2}. \tag{7.1.78}$$

Proceeding onto the higher order terms in the expansions of α_0 and c_0, we write

$$\alpha_0 \sim \left(\frac{\lambda_+^{(0)}}{I(\delta)}\right)^{1/2} V_0^{1/2} + \tilde{\beta}_1 V_0^{\rho_1}, \quad c_0 \sim V_0 + \tilde{\beta}_2 V_0^{\rho_2} \quad \text{as } V_0 \to \infty, \tag{7.1.79}$$

where $\tilde{\beta}_1, \tilde{\beta}_2, \rho_1$ and ρ_2 are to be determined in the analysis that follows. Before we substitute these expansions into the upper-branch eigenrelation (7.1.75), we stipulate that the term encompassing the inner cylinder's compliance scales appropriately with V_0 so as to be retained in γ; this requires $\widetilde{K} = O\left(V_0^{\rho_2}\right)$ and we let $\widetilde{K} \sim k_0 V_0^{\rho_2}$ for some quantity k_0. With this, the expression for γ (7.1.74) suggests

$$\gamma \sim \frac{k_0 \lambda_-^{(0)}}{k_0 + \tilde{\beta}_2 \lambda_-^{(0)}} \quad \text{as} \quad V_0 \to \infty. \tag{7.1.80}$$

In light of the expansions (7.1.79), we turn again to (7.1.73). This suggests the balance

$$2\delta \left(\lambda_+^{(0)} I(\delta)\right)^{1/2} \tilde{\beta}_1 V_0^{\rho_1 + 1/2} \sim \left(\frac{k_0 \lambda_-^{(0)}}{k_0 + \lambda_-^{(0)} \tilde{\beta}_2} + \delta \lambda_+^{(0)}\right) \tilde{\beta}_2 V_0^{\rho_2}, \tag{7.1.81}$$

which evokes the relation

$$\rho_1 + \frac{1}{2} = \rho_2. \tag{7.1.82}$$

Equating the coefficients of the terms in (7.1.81) reveals

$$\frac{\lambda_+^{(0)}\lambda_-^{(0)}}{k_0}\tilde{\beta}_2{}^2+\left(\frac{\lambda_-^{(0)}}{\delta}+\lambda_+^{(0)}-\frac{2\lambda_-^{(0)}I(\delta)^{1/2}\lambda_+^{(0)1/2}\tilde{\beta}_1}{k_0}\right)\tilde{\beta}_2-2I(\delta)^{1/2}\lambda_+^{(0)1/2}\tilde{\beta}_1=0. \quad (7.1.83)$$

Now we turn to the upper-branch eigenrelation. Letting V_0 become asymptotically large, we study each term in (7.1.75) individually and find

$$\frac{\lambda_+^{(0)}}{c_0\left(2\alpha_0 c_0\right)^{1/2}}=O\left(V_0^{-7/4}\right), \quad (7.1.84a)$$

$$\frac{\gamma}{\left(c_0-V_0\right)\sqrt{2\alpha_0\left(c_0-V_0\right)}}\left(1-\frac{\alpha_0{}^2I(\delta)}{c_0\lambda_+^{(0)}}\right)=O\left(V_0^{-(2\rho_2+5)/4}\right), \quad (7.1.84b)$$

$$-\frac{\gamma}{\lambda_-^{(0)}}\left(1-\frac{\alpha_0{}^2I(\delta)}{c_0\lambda_+^{(0)}}\right)\left(\frac{2\lambda_-^{(10)}}{\lambda_-^{(0)2}}-\frac{1}{\delta\lambda_-^{(0)}}\right)\left(c_0-V_0\right)\pi=O\left(V_0^{-1}\right), \quad (7.1.84c)$$

$$\left(\frac{2\lambda_+^{(10)}}{\lambda_+^{(0)2}}+\frac{1}{\lambda_+^{(0)}}\right)c_0\pi=O\left(V_0\right). \quad (7.1.84d)$$

Since terms (7.1.84a) and (7.1.84c) become negligible, we must have a balance between terms (7.1.84b) and (7.1.84d). This results in $\rho_2=-9/2$, and hence $\rho_1=-5$ as a result of (7.1.82). Defining $B_2=\tilde{\beta}_2{}^{1/2}$, the eigenrelation (7.1.75) suggests that

$$\lambda_-^{(0)2}+\pi\delta\sqrt{2}\left(\frac{\lambda_+^{(0)}}{I(\delta)}\right)^{1/4}\left(\frac{2\lambda_+^{(10)}}{\lambda_+^{(0)}}+1\right)\left(B_2+2\left(\frac{\lambda_-^{(0)}}{k_0}\right)B_2{}^3+\left(\frac{\lambda_-^{(0)}}{k_0}\right)^2B_2{}^5\right)=0 \quad (7.1.85)$$

in the limit $V_0\to\infty$. It can be shown that this quintic in B_2 admits only one real root.

It is natural to expect that the disturbance wavespeed we seek here collapses into the disturbance wavespeed of the rigid analogue to our problem as $k_0\to\infty$. The asymptotics of the rigid case, as studied by Walton [1], are

$$\alpha_{0,R}\sim\left(\frac{\lambda_+^{(0)}}{I(\delta)}\right)^{1/2}V_0^{1/2}+\beta_{1,R}V_0^{-5}, \quad c_{0,R}\sim V_0+\beta_{2,R}V_0^{-9/2} \quad \text{as} \quad V_0\to\infty, \quad (7.1.86)$$

where $\beta_{1,R}$ and $\beta_{2,R}$ are constants given by

$$\beta_{1,R}=-\frac{\lambda_-^{(0)2}\lambda_+^{(0)}}{16\pi^2\delta^6\log\delta}\left(1-\delta^2+2\delta^2\log\delta\right)^2, \quad (7.1.87)$$

$$\beta_{2,R}=\frac{I(\delta)^{1/2}\lambda_-^{(0)2}\lambda_+^{(0)3/2}}{8\pi^2\left(1-\delta^2\right)^2\delta^4}\left(1-\delta^2+2\delta^2\log\delta\right)^2. \quad (7.1.88)$$

We verify that equations (7.1.83) and (7.1.85), in the limit $k_0 \to \infty$, elicit the behaviour described in (7.1.86) and (7.1.87).

We anticipate the real solution of (7.1.85) will be of the form $B_2 = \phi {\beta_{2,R}}^{1/2}$, where ϕ is a real and unique function of k_0 and δ, and is such that $\phi \to 1$ in the rigid limit. Substitution into (7.1.85) illustrates that ϕ must satisfy

$$\phi^5 + \frac{2}{A}\phi^3 + \frac{1}{A^2}\phi - \frac{1}{A^2} = 0, \tag{7.1.89}$$

where

$$A = \frac{{\lambda_-^{(0)}}^5}{2\pi^2\delta^2 k_0}\left(\frac{2\lambda_+^{(10)}}{\lambda_+^{(0)}} + 1\right)^{-2}\left(\frac{I(\delta)}{\lambda_+^{(0)}}\right)^{1/2} \in \mathbb{R}_{>0}. \tag{7.1.90}$$

We confirm that (7.1.89) has only one real solution for A as described in (7.1.90). Since A becomes small as the inner cylinder becomes rigid, (7.1.89) confirms that

$$\phi \to 1 \quad \text{as} \quad k_0 \to \infty. \tag{7.1.91}$$

Having established that there exists a solution $B_2 = \phi {\beta_{2,R}}^{1/2}$, where ϕ satisfies (7.1.89) and obeys the property outlined in (7.1.91), we can write down explicit forms for $\tilde{\beta}_1$ and $\tilde{\beta}_2$. Since $\tilde{\beta}_2 = {B_2}^2$, we have

$$\tilde{\beta}_2 = \phi^2 \beta_{2,R} \tag{7.1.92}$$

and so

$$\tilde{\beta}_2 = \frac{I(\delta)^{1/2}{\lambda_-^{(0)}}^2{\lambda_+^{(0)}}^{3/2}}{8\pi^2\left(1-\delta^2\right)^2\delta^4}\left(1 - \delta^2 + 2\delta^2\log\delta\right)^2\phi^2. \tag{7.1.93}$$

Rearranging (7.1.83) to isolate $\tilde{\beta}_1$,

$$\tilde{\beta}_1 = \frac{\left(\lambda_+^{(0)} I\left(\delta\right)\right)^{-1/2}}{2} \cdot \frac{k_0}{\lambda_-^{(0)}\tilde{\beta}_2 + k_0}\left(\frac{\lambda_+^{(0)}\lambda_-^{(0)}}{{k_0}^2}{\tilde{\beta}_2}^2 - \frac{\left(1-\delta^2\right)^2}{\delta^2\log\delta}\tilde{\beta}_2\right). \tag{7.1.94}$$

These expressions allow us to see that in the rigid limit, α_0 and c_0 behave precisely as $\alpha_{0,R}$ and $c_{0,R}$ (7.1.86, 7.1.87), as expected.

To summarise, we recall (7.1.79) and describe the upper-branch mode behaviour with

$$\alpha_0 \sim \left(\frac{\lambda_+^{(0)}}{I(\delta)}\right)^{1/2} V_0^{1/2} + \tilde{\beta}_1 V_0^{-5}, \quad c_0 \sim V_0 + \tilde{\beta}_2 V_0^{-9/2} \quad \text{as } V_0 \to \infty, \tag{7.1.95}$$

where $\tilde{\beta}_1$ and $\tilde{\beta}_2$ are as in (7.1.94) and (7.1.93).

Before we approach the end of this analysis, we determine the appropriate sizes for K_0 and m_0. Recall that $\rho_2 = -9/2$ and that $\widetilde{K} = O(V_0^{\rho_2})$ to preserve the effect of compliance.

Then the definition of $\widetilde{K}$,

$$\widetilde{K} = K_0 - {\alpha_0}^2 {c_0}^2 m_0,$$

suggests that we take

$$K_0 = O(V_0^{-9/2}), \quad m_0 = O(V_0^{-15/2}) \quad \text{as } V_0 \to \infty. \tag{7.1.96}$$

in view of the scalings for α_0 and c_0 (7.1.95).

At increasingly large sliding velocities, $c_0 \to V_0^+$ and we expect the lower critical layer to move closer to the wall of the inner cylinder, eventually into the lower viscous wall. Whilst the lower layers now resemble the lower-branch mode, the upper layers are largely unaffected by V_0 becoming asymptotically large. We expect that they retain the upper-branch structure, though perhaps not with the same thicknesses deduced above.

We anticipate that this coalescence of structures naturally gives rise to a mode that encompasses characteristics of both the upper- and lower-branch modes. In Chapter 8, we deduce the magnitude of V at which the new structure forms and study the behaviour of the resulting mode. We will refer to this as a 'hybrid' mode, following the terminology of Walton [1].

Having studied the upper-branch structure in the limit $V_0 \to \infty$, we now investigate the behaviour of the structure in the limit $\widetilde{K} \to 0^-$.

7.1.2 Upper-branch structure in the limit $\widetilde{K} \to 0^-$

As in the lower-branch analysis, we consider the upper-branch structure in the limit $\widetilde{K} \to 0^-$. To emphasise the effect of compliance, we concentrate on the dynamics of a stationary cylinder.

To begin, we examine the upper-branch eigenrelation (7.1.75) in the limit $\widetilde{K} \to 0^-$, $\alpha_0 \to \infty$ and $c_0 \to 0$. This will help us to later find a distinguished scaling for $\widetilde{K}$ in terms of the Reynolds number.

The upper-branch eigenrelation for a stationary inner cylinder is given by (7.1.75) with $V_0 = 0$, that is

$$\begin{aligned}&\frac{\lambda_+^{(0)}}{c_0\sqrt{2\alpha_0 c_0}} - \frac{\gamma}{c_0\sqrt{2\alpha_0 c_0}}\left(1 - \frac{{\alpha_0}^2 I(\delta)}{c_0\lambda_+^{(0)}}\right)\\ &\quad - \frac{\gamma}{\lambda_-^{(0)}}\left(1 - \frac{{\alpha_0}^2 I(\delta)}{c_0\lambda_+^{(0)}}\right)\left(\frac{2\lambda_-^{(10)}}{{\lambda_-^{(0)}}^2} - \frac{1}{\delta\lambda_-^{(0)}}\right)c_0\pi + \left(\frac{2\lambda_+^{(10)}}{{\lambda_+^{(0)}}^2} + \frac{1}{\lambda_+^{(0)}}\right)c_0\pi = 0.\end{aligned} \tag{7.1.97}$$

This is to be solved with (7.1.73) and (7.1.74), where we again let $V_0 = 0$:

$$\alpha_0{}^2 = \frac{c_0\gamma}{\delta I(\delta)} + \frac{c_0\lambda_+^{(0)}}{I(\delta)}, \qquad \gamma = \left(\frac{1}{\lambda_-^{(0)}} + \frac{c_0}{\widetilde{K}}\right)^{-1}. \tag{7.1.98}$$

Since we consider the limit in which α_0 grows and c_0 decays with $\widetilde{K} \to 0^-$, it must be the case that γ grows with decreasing $\widetilde{K}$. We have omitted the details here, however a balance of the terms in the eigenrelation (7.1.97), along with a consideration of (7.1.98), reveals that

$$\alpha_0 \sim -\frac{{\lambda_-^{(0)}}^7}{2\pi^2}\left(\frac{2\lambda_-^{(10)}}{{\lambda_-^{(0)}}^2} - \frac{1}{\delta\lambda_-^{(0)}}\right)^{-2}\widetilde{K}^{-5}, \tag{7.1.99a}$$

$$c_0 \sim -\frac{1}{\lambda_-^{(0)}}\widetilde{K} - \frac{4\pi^4}{\delta I(\delta){\lambda_-^{(0)}}^{15}}\left(\frac{2\lambda_-^{(10)}}{{\lambda_-^{(0)}}^2} - \frac{1}{\delta\lambda_-^{(0)}}\right)^{4}\widetilde{K}^{12}. \tag{7.1.99b}$$

We use the above scalings to guide us in our search for a new structure.

Large-wavenumber limit of the upper-branch mode

Here, we try to discern how the upper-branch structure changes in the 'large-α_0, small-$\tilde{K}$' limit described above. As suggested by the scalings (7.1.99), we suppose that

$$\alpha_0 \sim \overline{\alpha}_0\,\widetilde{K}^{-5}, \qquad c_0 \sim \overline{c}_0\,\widetilde{K}, \qquad \widetilde{K} \to 0^-. \tag{7.1.100}$$

We will seek scalings on the flow quantities that enable us retain as many terms as possible in the Reynolds-number-independent equations governing the core region (7.1.3), inviscid shear layers (7.1.14), (7.1.35) and viscous wall layers (7.1.30), (7.1.48) of the upper-branch structure.

In what follows, the inner cylinder is taken to be stationary ($V = 0$).

Core region

Beginning with the core region, the analysis here corresponds to expansions (7.1.2) and equations (7.1.3). We seek a scaling for our disturbance quantities F_0, G_0 and P_0, as defined in (7.1.4). We take $P_0 = O(1)$ without loss of generality and, in what follows, determine the sizes of A_0 and $\hat{P}_0$.

It is apparent from (7.1.4) that

$$F_0 = O(A_0), \qquad G_0 = O(A_0 \widetilde{K}^{-5}). \tag{7.1.101}$$

Balancing the radial momentum equation (7.1.3c) gives us $A_0 \sim \overline{A}_0\, \widetilde{K}^{10}$, so that

$$F_0 = O\left(\widetilde{K}^{10}\right), \qquad G_0 = O\left(\widetilde{K}^{5}\right). \tag{7.1.102}$$

Substituting

$$F_0 = \widetilde{K}^{10}\overline{F}_0, \qquad G_0 = \widetilde{K}^{5}\overline{G}_0, \qquad P_0 = \overline{P}_0, \tag{7.1.103}$$

into the core equations (7.1.3), the governing equations for these barred disturbance quantities are

$$\mathrm{i}\overline{\alpha}_0\overline{F}_0 + \frac{\mathrm{d}\overline{G}_0}{\mathrm{d}r} + \frac{\overline{G}_0}{r} = 0, \quad \mathrm{i}\overline{\alpha}_0 U_{00}\overline{F}_0 + \overline{G}_0\frac{\mathrm{d}U_{00}}{\mathrm{d}r} = 0, \quad \mathrm{i}\overline{\alpha}_0 U_{00}\overline{G}_0 + \frac{\mathrm{d}\overline{P}_0}{\mathrm{d}r} = 0. \tag{7.1.104a}$$

These equations are unchanged from (7.1.3). Examining the disturbance behaviour as we approach the inner cylinder,

$$\overline{F}_0 = O\left(\widetilde{K}^{10}\right), \qquad \overline{G}_0 = O\left(\widetilde{K}^{5}(r-\delta)\right), \qquad \overline{P}_0 = O(1). \tag{7.1.105}$$

As we approach the outer cylinder,

$$\overline{F}_0 = O\left(\widetilde{K}^{10}\right), \qquad \overline{G}_0 = O\left(\widetilde{K}^{5}(1-r)\right), \qquad \overline{P}_0 \to O\left(\hat{P}_0\right), \tag{7.1.106}$$

where the size of $\hat{P}_0$ is not yet determined.

Upper inviscid shear layer

Following the expansions in (7.1.13a), here we take $(1-r) = \epsilon^2 Y_+$, where the size of Y_+ is to be determined in terms of $\widetilde{K}$. In what follows, $u_+^{(0)}, v_+^{(0)}, p_+^{(0)}$ refer to the quantities introduced in (7.1.13b), though they are no longer assumed to be of size order one. Anticipating that $u_+^{(0)} = O(\widetilde{K}^{10})$ in order to match the core (7.1.106), we note that a balance in the continuity equation (7.1.14a) is achieved with $v_+^{(0)} = O(\widetilde{K}^5\, Y_+)$. This is consistent with (7.1.106). A balance in the axial momentum equation (7.1.14b) requires that $Y_+ = O(\widetilde{K})$ and $\hat{P}_0 = O(\widetilde{K}^{11})$. Therefore in this region, we write

$$u_+^{(0)} = \widetilde{K}^{10}\,\overline{u}_+^{(0)}, \qquad v_+^{(0)} = \widetilde{K}^{6}\,\overline{v}_+^{(0)}, \qquad p_+^{(0)} = \widetilde{K}^{11}\,\overline{p}_+^{(0)}, \qquad (1-r) = \epsilon^2\widetilde{K}\,\overline{Y}_+. \tag{7.1.107}$$

Upon substitution in the inviscid shear equations (7.1.14), we obtain

$$\mathrm{i}\overline{\alpha}_0\overline{u}_+^{(0)} + \frac{\mathrm{d}\overline{v}_+^{(0)}}{\mathrm{d}\overline{Y}_+} = 0, \tag{7.1.108a}$$

$$\mathrm{i}\overline{\alpha}_0\left(\lambda_+^{(0)}\overline{Y}_+ - \overline{c}_0\right)\overline{u}_+^{(0)} + \lambda_+^{(0)}\overline{v}_+^{(0)} + \mathrm{i}\overline{\alpha}_0\overline{p}_+^{(0)} = 0, \tag{7.1.108b}$$

$$\frac{\mathrm{d}\overline{p}_+^{(0)}}{\mathrm{d}\overline{Y}_+} = 0. \tag{7.1.108c}$$

We remark that this set of equations is unchanged from (7.1.14).

Matching the core, the barred quantities $\overline{u}_+^{(0)}$ and $\overline{p}_+^{(0)}$ are constant throughout this region. Therefore $u_+^{(0)}$ and $p_+^{(0)}$ approach the outer cylinder wall with sizes $\widetilde{K}^{10}$ and $\widetilde{K}^{11}$ respectively. The radial velocity term $\overline{v}_+^{(0)}$ depends linearly on $\overline{Y}_+$, and the unbarred $v_+^{(0)}$ approaches the upper viscous wall layer with $v_+^{(0)} = O(\widetilde{K}^6\,\overline{Y}_+)$.

These scalings are in agreement with the existence of a critical layer in this region.

Upper viscous wall layer

The quantities $\bar{u}_+$, $\bar{v}_+$, $\bar{p}_+$ in the analysis of this layer refer to the leading order terms in the expansions (7.1.29). In this region we have $(1-r) = \epsilon^4\bar{y}_+$, where the size of $\bar{y}_+$ is to be determined in terms of $\widetilde{K}$. Taking $\bar{u}_+ = \widetilde{K}^{10}\,\bar{U}_+$ and $\bar{p}_+ = \widetilde{K}^{11}\,\bar{P}_+$ here to match the inviscid shear layer (7.1.107), balancing the terms in the axial momentum equation (7.1.30b) reveals that $\bar{y}_+ = \widetilde{K}^2\bar{Y}_+$. The continuity equation (7.1.30a) then gives us that $\bar{v}_+ = \widetilde{K}^7\bar{V}_+$.

Substituting these scalings into the viscous wall layer equations (7.1.30), we find the governing equations

$$\mathrm{i}\overline{\alpha}_0\bar{U}_+ + \frac{\mathrm{d}\bar{V}_+}{\mathrm{d}\bar{Y}_+} = 0, \tag{7.1.109a}$$

$$\frac{\mathrm{d}^2\bar{U}_+}{\mathrm{d}\bar{Y}_+^2} + \mathrm{i}\overline{\alpha}_0\bar{c}_0\bar{U}_+ - \mathrm{i}\overline{\alpha}_0\bar{P}_+ = 0, \tag{7.1.109b}$$

$$\frac{\mathrm{d}\bar{P}_+}{\mathrm{d}\bar{Y}_+} = 0. \tag{7.1.109c}$$

These are subject to no-slip conditions on the outer cylinder, and the disturbance quantities must match the inviscid shear layer as $\bar{Y}_+ \to \infty$. These equations are also unchanged (7.1.30).

Lower inviscid shear layer

The analysis in this region relates to the expansions (7.1.34) and equations (7.1.35).

In this region, we have $(r-\delta) = \epsilon^2 Y_-$, where Y_- will be determined in terms of $\widetilde{K}$. As $\tilde{K}$ becomes small, the lower inviscid layer splits into two inviscid regions with different dominant balances. The size of Y_- will be determined for each sub-layer.

Upper inviscid region: inviscid shear layer II(a)-. To match the core solution (7.1.105), we expect that

$$u_-^{(0)} = \overline{u}_-^{(0)}\ \widetilde{K}^{10}, \qquad p_-^{(0)} = \overline{p}_-^{(0)}. \tag{7.1.110}$$

Seeking to retain as many terms as possible in the continuity (7.1.35a) and axial momentum (7.1.35b) equations, we see that these scalings suggest that

$$v_-^{(0)} = \widetilde{K}^{-5}\,\overline{v}_-^{(0)}, \qquad Y_- = \widetilde{K}^{-10}\overline{Y}_-. \tag{7.1.111}$$

Substituting these scalings, along with (7.1.110) into (7.1.35), we learn that the equations that govern this layer are

$$\mathrm{i}\overline{\alpha}_0\overline{u}_-^{(0)} - \frac{\mathrm{d}\overline{v}_-^{(0)}}{\mathrm{d}\overline{Y}_-} = 0, \qquad \mathrm{i}\overline{\alpha}_0\lambda_-^{(0)}\overline{Y}_-\overline{u}_-^{(0)} - \lambda_-^{(0)}\overline{v}_-^{(0)} + \mathrm{i}\overline{\alpha}_0\overline{p}_- = 0, \qquad \frac{\mathrm{d}\overline{p}_-^{(0)}}{\mathrm{d}\overline{Y}_-} = 0. \tag{7.1.112}$$

Note the second equation here differs from (7.1.35b). As $\overline{y}_- \to \infty$, the disturbance quantities are required to match the core. It can be seen that $\overline{u}_-^{(0)}$ and $\overline{p}_-^{(0)}$ are constant throughout this region, whilst $\overline{v}_-^{(0)}$ varies linearly with $\overline{Y}_-$.

The expansions in this inviscid layer do not account for the critical layer present in the original structure. This highlights the need for the second layer described below.

Lower inviscid region: inviscid shear layer II(b)-. Anticipating that the pressure and axial velocity disturbances are constant (in Y_-) across this layer in accordance with (7.1.35), we take $p_-^{(0)} = \overline{p}_-^{(0)}$ and $u_-^{(0)} = \widetilde{K}^{10}\,\overline{u}_-^{(0)}$ to match the inviscid layer above. The existence of a critical layer proposes that $Y_- = \widetilde{K}\,\overline{Y}_{2-}$ since $c_0 = O(\widetilde{K})$ (7.1.100). The axial momentum equation (7.1.35b) then suggests that $v_-^{(0)} = \widetilde{K}^{-5}\,\overline{v}_{2-}^{(0)}$. Upon substitution of these scalings into (7.1.35), we obtain

$$\frac{\mathrm{d}\overline{v}_{2-}^{(0)}}{\mathrm{d}\overline{Y}_{2-}} = 0, \qquad \frac{\mathrm{d}\overline{p}_-^{(0)}}{\mathrm{d}\overline{Y}_{2-}} = 0, \qquad \lambda_-^{(0)}\overline{v}_{2-}^{(0)} - \mathrm{i}\overline{\alpha}_0\overline{p}_-^{(0)} = 0. \tag{7.1.113}$$

These equations differ from (7.1.35). It is evident that $\overline{v}_{2-}^{(0)}$ is constant in this region and must approach the lower viscous wall layer with order $\widetilde{K}^{-5}$.

Lower viscous wall layer

The analysis of this region follows the expansions (7.1.47) and is based on the equations (7.1.48). In this region, we have $(r-\delta) = \epsilon^4 \bar{y}_-$ where $\bar{y}_-$ will be determined in terms of $\widetilde{K}$. As $\widetilde{K}$ becomes small, the lower viscous layer also splits into two regions. These are described below.

Upper viscous sub-layer: viscous wall layer III(a)-. Here, $\bar{u}_-^{(0)}$, $\bar{v}_-^{(0)}$, $\bar{p}_-^{(0)}$ refer to the leading order quantities in the expansions (7.1.47b). To match the inviscid layer above, we expect that $\bar{u}_-^{(0)} = \widetilde{K}^{10}\bar{U}_-$ and $\bar{p}_-^{(0)} = \bar{P}_-$. We take $\bar{v}_-^{(0)} = \widetilde{K}^{-5}\bar{V}_-$ and $y_- = \widetilde{K}^{15/2}\,\bar{Y}_-$ to retain as many terms as possible in the axial momentum equation (7.1.48b). Substitution of these scalings into (7.1.48) yields

$$\frac{\mathrm{d}\bar{V}_-}{\mathrm{d}\bar{Y}_-} = 0, \qquad -\lambda_-^{(0)}\bar{V}_- = -\mathrm{i}\overline{\alpha}_0\bar{P}_- + \frac{\mathrm{d}^2\bar{U}_-}{\mathrm{d}\bar{Y}_-^2}, \qquad \frac{\mathrm{d}\bar{P}_-}{\mathrm{d}\bar{Y}_-} = 0. \tag{7.1.114}$$

The second equation here differs from (7.1.48b). The expansions in this region do not allow for the boundary conditions on the inner cylinder to be satisfied. This leads us to the layer described below.

Lower viscous sub-layer: viscous wall layer III(b)-. Assuming that the leading order pressure term is constant in this layer, in accordance with (7.1.48c), we take $\bar{p}_-^{(0)} = \bar{P}_-$. The boundary conditions (7.1.55) and (7.1.58) on the inner cylinder propose that

$$\bar{u}_-^{(0)} = \widetilde{K}^{-1}\,\bar{U}_-^{(2)}, \qquad \bar{v}_-^{(0)} = \widetilde{K}^{-5}\,\bar{V}_-^{(2)}. \tag{7.1.115}$$

A balance in the axial momentum equation (7.1.48b) requires that $y_- = \widetilde{K}^2\,\bar{Y}_-^{(2)}$. This means that our viscous wall layer becomes thinner in the limit $\widetilde{K} \to 0^-$.

Substituting these scalings into the equations (7.1.48), we find

$$\frac{\mathrm{d}\bar{V}_-^{(2)}}{\mathrm{d}\bar{Y}_-^{(2)}} = 0, \tag{7.1.116a}$$

$$\mathrm{i}\overline{\alpha}_0\bar{c}_0\bar{U}_-^{(2)} + \lambda_-^{(0)}\bar{V}_-^{(2)} - \mathrm{i}\overline{\alpha}_0\bar{P}_- + \frac{\mathrm{d}^2\bar{U}_-^{(2)}}{\mathrm{d}\bar{Y}_-^{(2)^2}} = 0, \tag{7.1.116b}$$

$$\frac{\mathrm{d}\bar{P}_-}{\mathrm{d}\bar{Y}_-^{(2)}} = 0, \tag{7.1.116c}$$

where the disturbance quantities are subject to matching the viscous layer above as

$\overline{y}_{2-} \to \infty$ and

$$\lambda_-^{(0)}\,\bar{V}_-^{(2)} - \mathrm{i}\overline{\alpha}_0\,\overline{c}_0\,\bar{U}_-^{(2)} = 0 \quad \text{on} \quad \bar{Y}_-^{(2)} = 0, \tag{7.1.117a}$$

$$\bar{P}_- = \frac{\bar{U}_-^{(2)}}{\lambda_-^{(0)}} \quad \text{on} \quad \bar{Y}_-^{(2)} = 0. \tag{7.1.117b}$$

Figure 7.1.3 encapsulates the behaviour of the upper-branch mode in the limit $\widetilde{K} \to 0^-$.

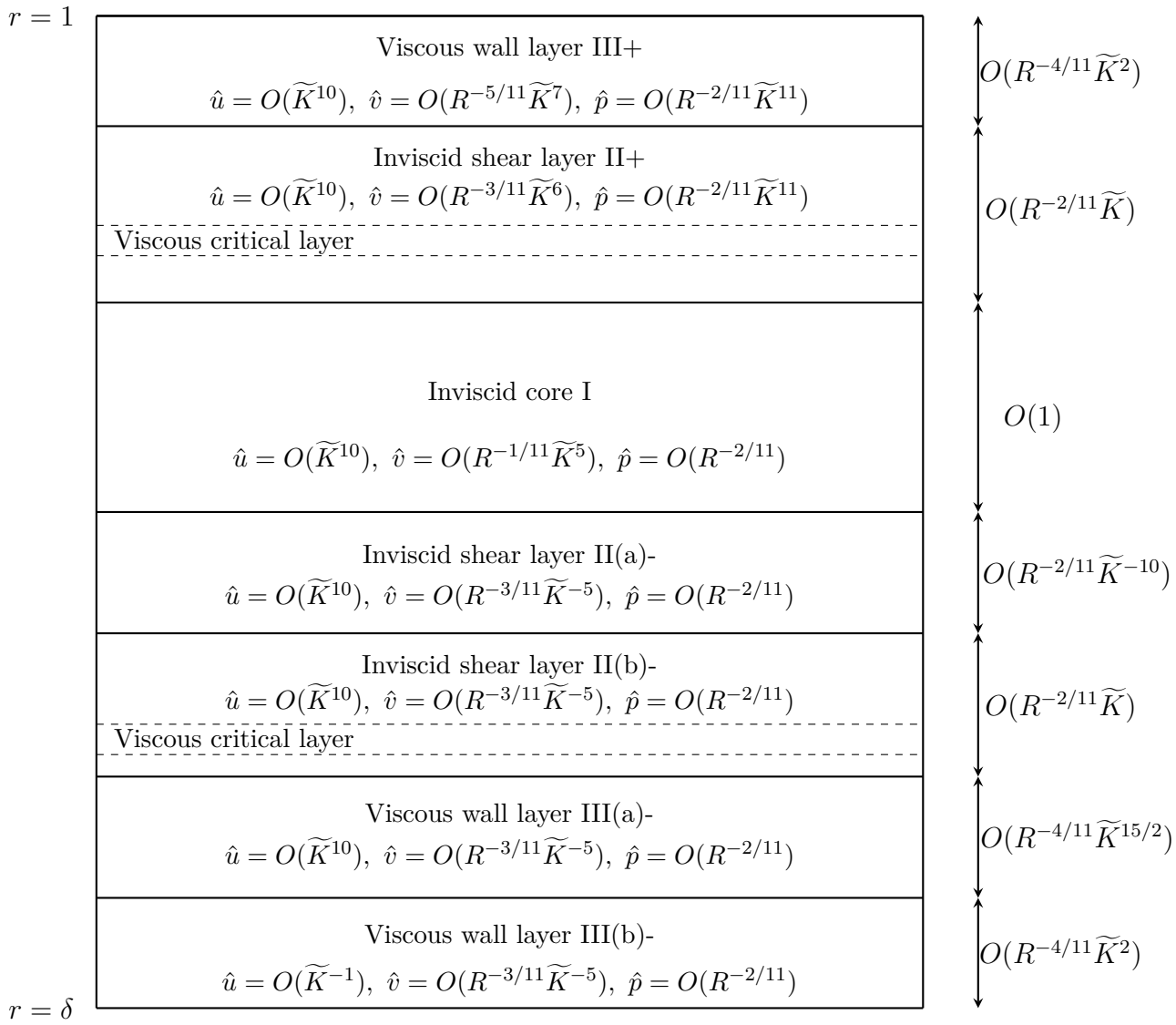

Figure 7.1.3: Schematic of the asymptotic structure of the upper-branch mode in the limit $\widetilde{K} \to 0^-$ with $\alpha = O\left(R^{-1/11}\widetilde{K}^{-5}\right)$ and $c = O\left(R^{-2/11}\widetilde{K}\right)$. The inner cylinder is stationary ($V = 0$) and has properties $K = O\left(R^{20/11}\widetilde{K}\right)$ and $m = O\left(R^{4/11}\widetilde{K}^{9}\right)$.

It is of interest to determine the size of $\widetilde{K}$ at which this structure breaks down. To this end, we look at the dynamics of *Inviscid shear layer II-(a)* more closely here.

Recalling the expansions (7.1.34) in the lower inviscid shear layer, the radial velocity disturbance in this region can be written as

$$\hat{v} = -R^{-3/11} v_-^{(0)} - R^{-5/11} v_-^{(1)}, \tag{7.1.118}$$

where we have used that $\epsilon = R^{-1/11}$. In view of (7.1.111), we observe that $v_-^{(0)} = O\left(\tilde{K}^{-5}\right)$ in the limit $\widetilde{K} \to 0^-$. It is also of interest to consider the size of $v_-^{(1)}$ in this limit.

The solution for $v_-^{(1)}$ was found to be (7.1.42), which we repeat here for convenience:

$$v_-^{(1)} = \frac{\mathrm{i}\alpha_0}{\lambda_-^{(0)}} \left(\frac{2\lambda_-^{(10)}}{\lambda_-^{(0)2}} - \frac{1}{\delta \lambda_-^{(0)}} \right) \left(\hat{P}_0 + \alpha_0^2 A_0 I(\delta) \right) \zeta_- \log(\zeta_-) - \mathrm{i}\alpha_0 A_-^{(1)} \zeta_- + \frac{\mathrm{i}\alpha_0 P_-^{(1)}}{\lambda_-^{(0)}} + \text{imaginary terms}, \quad \zeta_- \neq 0, \tag{7.1.119}$$

where $\zeta_- = \lambda_-^{(0)} Y_- - c_0$ for a stationary inner cylinder. In our analysis of the *Inviscid shear layer II(a)-*, we found that $Y_- = \widetilde{K}^{-10} \overline{Y}_-$ (7.1.111). It is also helpful to recall that we have found $A_0 = O(\widetilde{K}^{10})$, $\hat{P}_0 = O(\widetilde{K}^{11})$ in the limit $\widetilde{K} \to 0^-$ during our analysis of the core region and upper inviscid layer in Section 7.1.2. In addition, we have $\alpha_0 = O(\widetilde{K}^{-5})$, $c_0 = O(\widetilde{K})$ from (7.1.100).

With these scalings, the first term of $v_-^{(1)}$ (7.1.119) is expected to grow as $\widetilde{K} \to 0^-$. We see

$$\frac{\mathrm{i}\alpha_0}{\lambda_-^{(0)}} \left(\frac{2\lambda_-^{(10)}}{\lambda_-^{(0)2}} - \frac{1}{\delta \lambda_-^{(0)}} \right) \left(\hat{P}_0 + \alpha_0^2 A_0 I(\delta) \right) \zeta_- \log(\zeta_-) = O\left(\widetilde{K}^{-15} \log\left(\widetilde{K}^{-10} \right) \right). \tag{7.1.120}$$

Therefore we write the expansion (7.1.118) as

$$\hat{v} = -R^{-3/11} \tilde{K}^{-5} \overline{v}_-^{(0)} - R^{-5/11} \tilde{K}^{-15} \log\left(\tilde{K}^{-10} \right) \overline{v}_-^{(1)}, \tag{7.1.121}$$

where $\overline{v}_-^{(0)}$ and $\overline{v}_-^{(1)}$ are of order one in the limit $\widetilde{K} \to 0^-$. We consider whether this asymptotic expansion is well-ordered in this limit and note that when $\tilde{K}^{-10} \sim \frac{R^{2/11}}{\log\left(R^{2/11}\right)}$, we have $\tilde{K}^{-10} \log\left(\tilde{K}^{-10}\right) \sim R^{2/11}$ and the two terms in (7.1.121) become comparable in size. The structure thus no longer holds when

$$\tilde{K} \sim \left(\frac{\log R}{R^{2/11}} \right)^{1/10}. \tag{7.1.122}$$

This completes the analysis of the upper-branch structure in the limit

$$\alpha_0 \sim \overline{\alpha}_0 \widetilde{K}^{-5}, \qquad c_0 \sim \overline{c}_0 \widetilde{K}, \qquad \widetilde{K} \to 0^-. \tag{7.1.123}$$

We will not explore the new structure that is expected to arise. Instead, in the next section we investigate an upper-branch mode with our original scalings

$$\alpha = R^{-1/11}\alpha_0, \qquad c = R^{-2/11}c_0, \qquad V = R^{-2/11}V_0, \tag{7.1.124}$$

where we now stipulate that $c < V$ so that there exists only one critical layer in the structure.

7.2 Upper-branch structure II: one critical layer

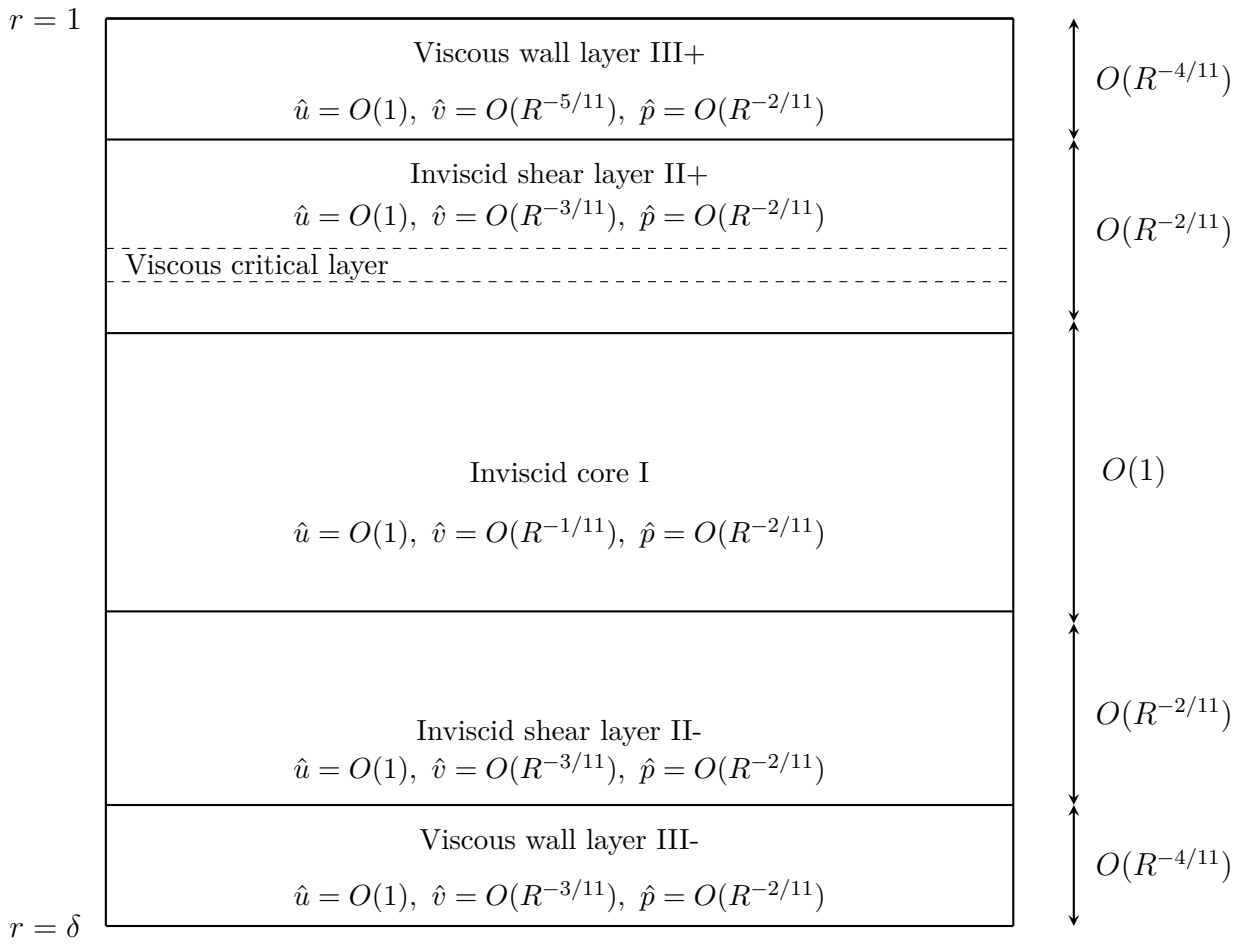

Figure 7.2.1: Schematic of the asymptotic structure of the upper branch mode with one critical layer, where $\alpha = O\left(R^{-1/11}\right)$ and $c = O\left(R^{-2/11}\right)$. The cylinder properties are $V = O\left(R^{-2/11}\right)$, $K = O\left(R^{20/11}\right)$ and $m = O\left(R^{4/11}\right)$.

In Section 7.1, we investigated an upper-branch structure that consisted of two critical layers, each situated in an inviscid shear layer that neighbours the core region. However it is possible to have a structure with only one of these critical layers, specifically the critical layer closer to the outer cylinder. Depicted in figure 7.2.1, it is this structure that we discuss in the remainder of this section.

The crucial element in this analysis is that the disturbance wavespeed c is less than sliding velocity V of the inner cylinder. This ensures that there is no critical layer near the inner cylinder (see figure 7.2.2). In Chapter 9, we will see an example of a numerical stability curve corresponding to this structure.

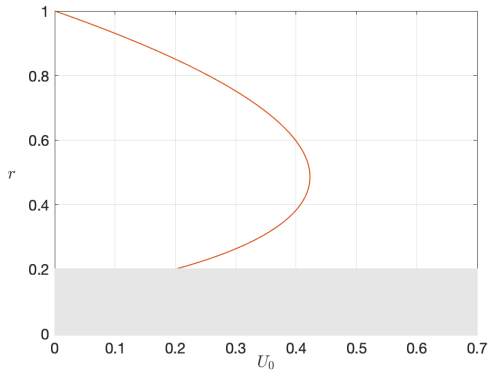

Figure 7.2.2: Depiction of the base flow $U_0(r)$ for $\delta = 0.2, V = 0.2$.

This structure is largely similar to that which is described in Section 7.1, with the scalings in each region being unchanged. In fact, the dynamics of the core region, upper inviscid shear layer, and upper viscous wall layer are entirely unchanged. The analysis of the lower layers closely resembles that of Section 7.1, though there are distinguishing features that differentiate between the two structures.

We omit details of the analysis here, but instead briefly describe the disturbance solutions in each region so as to emphasise the similarities and differences between an upper-branch structure with one critical layer and two critical layers.

As in the previous upper branch structure (Chapter 7, Section 7.1), we scale the inner cylinder properties as

$$V = \epsilon^2 \, V_0, \qquad K = \epsilon^{-20} K_0, \qquad m = \epsilon^{-4} m_0 \tag{7.2.1}$$

where $\epsilon = R^{-1/11}$. The disturbance wavenumber and wavespeed expand as in (7.1.2b)

$$\alpha = \epsilon\alpha_0 + \epsilon^3\alpha_1 + \cdots, \quad c = \epsilon^2 c_0 + \epsilon^4 c_1 + \cdots. \tag{7.2.2}$$

The inviscid core region I

In this region, the disturbance expansions are given by (7.1.2),

$$\hat{u} = F_0 + \epsilon^2 F_1 + \cdots, \quad \hat{v} = \epsilon G_0 + \epsilon^3 G_1 + \cdots, \quad \hat{p} = \epsilon^2 P_0 + \epsilon^4 P_1 + \cdots, \tag{7.2.3}$$

and the governing leading order equations by (7.1.3),

$$\mathrm{i}\alpha_0 F_0 + \frac{\mathrm{d}G_0}{\mathrm{d}r} + \frac{G_0}{r} = 0, \quad \mathrm{i}\alpha_0 U_{00} F_0 + G_0 \frac{\mathrm{d}U_{00}}{\mathrm{d}r} = 0, \quad \mathrm{i}\alpha_0 U_{00} G_0 + \frac{\mathrm{d}P_0}{\mathrm{d}r} = 0. \tag{7.2.4a,b,c}$$

These are solved to yield (7.1.4),

$$F_0 = \frac{A_0}{r}\frac{\mathrm{d}U_{00}}{\mathrm{d}r}, \quad G_0 = -\frac{\mathrm{i}\alpha_0 A_0}{r}\,U_{00}, \quad P_0 = \hat{P}_0 + \alpha_0^2 A_0 I(r), \tag{7.2.5}$$

where $I(r)$ is as defined in (6.1.11) and A_0 is taken to be real.

The solutions for G_1 and P_1 are as in (7.1.5),

$$G_1(r) = -\mathrm{i}\alpha_0 A_1 \frac{U_{00}}{r} + \text{imaginary terms}, \quad P_1(r) = P_+^{(1)} + \alpha_0^2 A_1 I(r) + \text{real terms}, \tag{7.2.6}$$

where A_1 and $P_+^{(1)}$ are unknown complex constants.

Inviscid shear layer II+

This layer contains a critical layer where the base velocity is equal to the wavespeed of the neutral mode. The expansions in this region are given by (7.1.13a),

$$U_0 = \epsilon^2\lambda_+^{(0)}Y_+ + \epsilon^4\left(\lambda_+^{(10)}Y_+^2 + \lambda_+^{(1)}Y_+\right) + \cdots, \quad r = 1 - \epsilon^2 Y_+, \tag{7.2.7a}$$

$$\hat{u} = u_+^{(0)} + \cdots, \quad \hat{v} = -\epsilon^3 v_+^{(0)} - \epsilon^5 v_+^{(1)} + \cdots, \quad \hat{p} = \epsilon^2 p_+^{(0)} + \epsilon^4 p_+^{(1)} + \cdots. \tag{7.2.7b}$$

The leading order equations to be solved, subject to matching the core, are identical to (7.1.14),

$$\mathrm{i}\alpha_0 u_+^{(0)} + \frac{\mathrm{d}v_+^{(0)}}{\mathrm{d}Y_+} = 0, \tag{7.2.8a}$$

$$\mathrm{i}\alpha_0\left(\lambda_+^{(0)}Y_+ - c_0\right)u_+^{(0)} + \lambda_+^{(0)}v_+^{(0)} + \mathrm{i}\alpha_0 p_+^{(0)} = 0, \tag{7.2.8b}$$

$$\frac{\mathrm{d}p_+^{(0)}}{\mathrm{d}Y_+} = 0. \tag{7.2.8c}$$

These have solutions (7.1.16):

$$u_+^{(0)} = -A_0\lambda_+^{(0)}, \quad v_+^{(0)} = \mathrm{i}\alpha_0 A_0\left(\lambda_+^{(0)}Y_+ - c_0\right) - \frac{\mathrm{i}\alpha_0\hat{P}_0}{\lambda_+^{(0)}}, \quad p_+^{(0)} = \hat{P}_0. \tag{7.2.9}$$

Enforcing the inviscid impermeability condition, we obtain the pressure-displacement relation (7.1.17),

$$A_0 c_0 + \frac{\hat{P}_0}{\lambda_+^{(0)}} = 0. \tag{7.2.10}$$

The equations describing the dynamics at the next order are provided in (7.1.18). With $\zeta_+ = \lambda_+^{(0)} Y_+ - c_0$, (7.1.21) gives

$$v_+^{(1)} = \mathrm{i}\alpha_0 A_+^{(1)} \zeta_+ - \frac{\mathrm{i}\alpha_0 P_+^{(1)}}{\lambda_+^{(0)}} - \frac{\mathrm{i}\alpha_0 \hat{P}_0}{\lambda_+^{(0)}} \left(\frac{2\lambda_+^{(10)}}{\lambda_+^{(0)2}} + \frac{1}{\lambda_+^{(0)}} \right) \zeta_+ \log(\zeta_+) + \text{imaginary terms}, \quad \zeta_+ \neq 0. \tag{7.2.11}$$

Matching this to the core region (7.2.6),

$$\mathrm{Im}\left\{ A_+^{(1)} \right\} = \mathrm{Im}\{A_1\}. \tag{7.2.12}$$

Viscous wall layer III+

The expansions in this region are as in (7.1.29), with

$$\hat{u} = \bar{u}_+ + \cdots, \quad \hat{v} = -\epsilon^5 \bar{v}_+ - \cdots, \quad \hat{p} = \epsilon^2 \bar{p}_+ + \cdots, \tag{7.2.13a}$$

$$U_0 = \epsilon^4 \lambda_+^{(0)} \bar{y}_+ + \cdots, \quad r = 1 - \epsilon^4 \bar{y}_+. \tag{7.2.13b}$$

and we seek a solution to the leading order governing equations (7.1.30)

$$\mathrm{i}\alpha_0 \bar{u}_+ + \frac{\mathrm{d}\bar{v}_+}{\mathrm{d}\bar{y}_+} = 0, \tag{7.2.14a}$$

$$\frac{\mathrm{d}^2 \bar{u}_+}{\mathrm{d}\bar{y}_+^2} + \mathrm{i}\alpha_0 c_0 \bar{u}_+ - \mathrm{i}\alpha_0 \bar{p}_+ = 0, \tag{7.2.14b}$$

$$\frac{\mathrm{d}\bar{p}_+}{\mathrm{d}\bar{y}_+} = 0. \tag{7.2.14c}$$

The flow quantities must satisfy no-slip conditions on the outer cylinder and must match the inviscid shear region, and thus must be of the form (7.1.31)

$$\bar{u}_+ = \frac{\hat{P}_0}{c_0} \left[1 - \exp(-m_+ \bar{y}_+) \right], \quad \bar{v}_+ = -\frac{\mathrm{i}\alpha_0 \hat{P}_0}{c_0} \left[\bar{y}_+ + \frac{\exp(-m_+ \bar{y}_+)}{m_+} - \frac{1}{m_+} \right], \tag{7.2.15}$$
$$\bar{p}_+ = \hat{P}_0, \quad m_+ = (1 - \mathrm{i}) \left(\tfrac{1}{2} \alpha_0 c_0 \right)^{1/2}.$$

Matching the real part of the normal velocity disturbance to the inviscid shear layer, we obtain the same pressure-displacement relation as in (7.1.32):

$$-\frac{\hat{P}_0}{c_0 (2\alpha_0 c_0)^{1/2}} = c_0 \,\mathrm{Im}\{A_1\} + \frac{\mathrm{Im}\left\{ P_+^{(1)} \right\}}{\lambda_+^{(0)}} + \frac{\hat{P}_0}{\lambda_+^{(0)}} \left(\frac{2\lambda_+^{(10)}}{\lambda_+^{(0)2}} + \frac{1}{\lambda_+^{(0)}} \right) \pi c_0. \tag{7.2.16}$$

We reiterate that, thus far, the analysis has been identical to that in the previous upper branch structure consisting of two critical layers. We now move onto the lower layers.

Inviscid shear layer II-

The vital difference in this upper-branch structure is the behaviour of the normal velocity in this layer as we approach the inner cylinder. Unlike in Section 7.1, we take $(V_0 - c_0) > 0$, so we will **not** have a critical layer in this region. We will later see that this stipulation is supported by the solutions c_0 of our resulting eigenrelation.

Using the principle of maximal interactions, we balance the inertial and pressure terms in the axial momentum equation (2.3.11b) of the linearised disturbance equations (2.3.11),

$$\mathrm{i}\alpha(U_0 - c)\hat{u} \sim \alpha\hat{p}, \tag{7.2.17}$$

and deduce that $(r - \delta) = O(\epsilon^2)$. Thus we write $r = \delta + \epsilon^2 Y_-$ for an order one variable Y_-. Motivated by matching the solutions of the core (7.2.5), the expansions in this lower shear region are the same as in (7.1.34),

$$U_0 = \epsilon^2\left(V_0 + \lambda_-^{(0)}Y_-\right) + \epsilon^4\left(\lambda_-^{(10)}Y_-^2 + \lambda_-^{(1)}Y_-\right) + \cdots, \quad r = \delta + \epsilon^2 Y_-, \tag{7.2.18a}$$

$$\hat{u} = u_-^{(0)} + \cdots, \quad \hat{v} = -\epsilon^3 v_-^{(0)} - \epsilon^5 v_-^{(1)} + \cdots, \quad \hat{p} = \epsilon^2 p_-^{(0)} + \epsilon^4 p_-^{(1)} + \cdots. \tag{7.2.18b}$$

These satisfy the leading order equations described in (7.1.35),

$$\frac{\mathrm{d}v_-^{(0)}}{\mathrm{d}Y_-} - \mathrm{i}\alpha_0 u_-^{(0)} = 0, \tag{7.2.19a}$$

$$\mathrm{i}\alpha_0\left(\lambda_-^{(0)}Y_- + V_0 - c_0\right)u_-^{(0)} + \mathrm{i}\alpha_0 p_-^{(0)} - \lambda_-^{(0)}v_-^{(0)} = 0, \tag{7.2.19b}$$

$$\frac{\mathrm{d}p_-^{(0)}}{\mathrm{d}Y_-} = 0, \tag{7.2.19c}$$

subject to matching the core, and have solutions (7.1.36) and (7.1.38)

$$u_-^{(0)} = \frac{A_0\lambda_-^{(0)}}{\delta}, \quad v_-^{(0)} = \frac{\mathrm{i}\alpha_0 A_0}{\delta}\zeta_- + \frac{\mathrm{i}\alpha_0}{\lambda_-^{(0)}}\left(\hat{P}_0 + \alpha_0^2 A_0 I(\delta)\right), \quad p_-^{(0)} = \hat{P}_0 + \alpha_0^2 A_0 I(\delta) \tag{7.2.20}$$

for $\zeta_- = \lambda_-^{(0)}Y_- + V_0 - c_0$. At the next order, the disturbance quantities are governed by (7.1.39). The pressure $p_-^{(1)}$ term is given by (7.1.40),

$$p_-^{(1)} = P_-^{(1)} \tag{7.2.21}$$

where

$$\mathrm{Im}\left\{P_-^{(1)}\right\} = \mathrm{Im}\left\{P_+^{(1)}\right\} + \alpha_0^2\,\mathrm{Im}\{A_1\}I(\delta) \tag{7.2.22}$$

upon matching (7.2.21) to the core using (7.2.6). This relation is identical to (7.1.41).

The normal velocity $v_-^{(1)}$ is described by (7.1.42),

$$v_-^{(1)} = \frac{\mathrm{i}\alpha_0}{\lambda_-^{(0)}}\left(\frac{2\lambda_-^{(10)}}{{\lambda_-^{(0)}}^2} - \frac{1}{\delta\lambda_-^{(0)}}\right)\left(\hat{P}_0 + \alpha_0^2 A_0 I(\delta)\right)\zeta_- \log(\zeta_-) - \mathrm{i}\alpha_0 A_-^{(1)}\zeta_- + \frac{\mathrm{i}\alpha_0 P_-^{(1)}}{\lambda_-^{(0)}} + \text{imaginary terms}, \quad (7.2.23)$$

where we recall $\zeta_- = \lambda_-^{(0)} Y_- + V_0 - c_0$. The normal velocity disturbance does not exhibit a singularity in the log term as $\zeta_- > 0$ throughout this region (since $c_0 - V_0 > 0$). We emphasise that this is the crucial difference between this analysis and that of the upper-branch structure with two critical layers.

As we approach the inner cylinder then, we have

$$\mathrm{Re}\left\{v_-^{(1)}\right\} \to -\alpha_0(V_0 - c_0)\frac{\mathrm{Im}\{A_1\}}{\delta} - \frac{\alpha_0\,\mathrm{Im}\left\{P_-^{(1)}\right\}}{\lambda_-^{(0)}} \quad (7.2.24)$$

instead of (7.1.45). We note the absence of the term involving π, which had arisen due to the phase shift upon crossing the lower critical layer in the upper-branch structure of Section 7.1.

Viscous wall layer III-

The thickness of this layer can be determined by requiring a balance in the inertial term $\mathrm{i}\alpha(U_0 - c)\hat{u}$ and viscous term $R^{-1}\hat{u}''$ in the linearised axial momentum equation (2.3.11b). We find

$$(r - \delta) = O(\epsilon^4). \quad (7.2.25)$$

The expansions here are the same as in (7.1.47),

$$U_{00} = \epsilon^4\lambda_-^{(0)}\bar{y} + \epsilon^8\lambda_-^{(10)}\bar{y}^2 + \cdots, \quad U_{01} = V_0 + \epsilon^4\lambda_-^{(1)}\bar{y} + \cdots, \quad r = \delta + \epsilon^4\bar{y}_-, \quad (7.2.26a)$$

$$\hat{u} = \bar{u}_-^{(0)} + \epsilon^2\bar{u}_-^{(1)}\cdots, \quad \hat{v} = -\epsilon^3\bar{v}_-^{(0)} - \epsilon^5\bar{v}_-^{(1)} - \cdots, \quad \hat{p} = \epsilon^2\bar{p}_-^{(0)} + \epsilon^4\bar{p}_-^{(1)}\cdots. \quad (7.2.26b)$$

The leading order terms satisfy equations (7.1.48),

$$\frac{\mathrm{d}\bar{v}_-^{(0)}}{\mathrm{d}\bar{y}_-} = 0, \qquad \frac{\mathrm{d}^2\bar{u}_-^{(0)}}{\mathrm{d}\bar{y}^2} - \mathrm{i}\alpha_0\,\bar{p}_-^{(0)} + \lambda_-^{(0)}\bar{v}_-^{(0)} - \mathrm{i}\alpha_0\,(V_0 - c_0)\,\bar{u}_-^{(0)} = 0, \qquad \frac{\mathrm{d}\bar{p}_-^{(0)}}{\mathrm{d}\bar{y}_-} = 0, \quad (7.2.27a,b,c)$$

and have solutions similar to those of (7.1.49); we note that m_- has been modified from Section 7.1 to account for c_0 being less than V_0 in this structure. The solutions are thus

$$\bar{p}_-^{(0)} = \hat{P}_0 + \alpha_0^2 A_0 I(\delta), \quad v_-^{(0)} = \mathrm{i}\alpha_0 \left(\frac{A_0 (V_0 - c_0)}{\delta} + \frac{\hat{P}_0 + \alpha_0^2 A_0 I(\delta)}{\lambda_-^{(0)}} \right), \tag{7.2.28}$$

$$u_-^{(0)} = \tilde{A} \exp(-m_- \bar{y}) + \frac{A_0 \lambda_-^{(0)}}{\delta}, \tag{7.2.29}$$

where $\tilde{A}$ is defined in (7.1.59), (7.1.56) and $m_- = \frac{1}{\sqrt{2}}(1+\mathrm{i})\sqrt{\alpha_0 (V_0 - c_0)}$. The dynamic and kinematic boundary conditions applied on the inner cylinder remain unchanged from (7.1.55) and (7.1.58) respectively.

The pressure-displacement relation (7.1.60) is unchanged from Section 7.1, and we have

$$\frac{A_0 (V_0 - c_0)}{\delta} + \left(\hat{P}_0 + \alpha_0^2 A_0 I(\delta) \right) \left(\frac{1}{\lambda_-^{(0)}} - \frac{V_0 - c_0}{\widetilde{K}} \right) = 0. \tag{7.2.30}$$

where $\widetilde{K} = K_0 - {\alpha_0}^2 {c_0}^2 m_0$.

At the next order, the governing equations are identical to those of (7.1.61). The normal velocity at the next order possesses the solution (7.1.62),

$$\bar{v}_-^{(1)} = \mathrm{i}\alpha_0 \left[\frac{A_0 \lambda_-^{(0)} \bar{y}_-}{\delta} - \frac{\hat{P}_0 + \alpha_0^2 A_0 I(\delta)}{m_- (V_0 - c_0)} \exp(-m_- \bar{y}_-) \right] + \mathrm{i}\alpha_0 \tilde{D}, \tag{7.2.31}$$

where $\mathrm{Im}(\tilde{D})$ will now reflect the lack of a lower critical layer in this structure. $\mathrm{Im}(\tilde{D})$ is found by matching to the inviscid shear region (7.2.24), and in this structure, is given by

$$\mathrm{Im}\{\tilde{D}\} = (V_0 - c_0) \frac{\mathrm{Im}\{A_1\}}{\delta} + \frac{\mathrm{Im}\{P_-^{(1)}\}}{\lambda_-^{(0)}}, \tag{7.2.32}$$

the analogous result to (7.1.64). We remark that (7.1.64) includes a term involving π; this term is not present in (7.2.32) due to the lack of a lower critical layer here. As in Section 7.1, we find a solution for the next order axial velocity term $\bar{u}_-^{(1)}$ subject to the boundary conditions (7.1.66) and (7.1.69) on the inner cylinder. The details are the same as in (7.1.67)-(7.1.70), so we include only the key results here.

We obtain a second expression for $\mathrm{Im}(\tilde{D})$ (corresponding to (7.1.71)):

$$\mathrm{Im}\{\tilde{D}\} = \frac{\mathrm{Im}\{P_-^{(1)}\}}{\widetilde{K}} (V_0 - c_0) - \frac{\hat{P}_0 + \alpha_0^2 A_0 I(\delta)}{(V_0 - c_0)\sqrt{2\alpha_0 (V_0 - c_0)}}. \tag{7.2.33}$$

This is largely the same as (7.1.71), but reflects the modification to m_- in this structure.

Together, the expressions (7.2.32) and (7.2.33) for $\mathrm{Im}(\tilde{D})$ yield the pressure-displacement relation

$$\frac{\hat{P}_0 + \alpha_0^2 A_0 I(\delta)}{(V_0 - c_0)\sqrt{2\alpha_0 (V_0 - c_0)}} = -\frac{\mathrm{Im}\{A_1\}}{\delta}(V_0 - c_0) + \mathrm{Im}\left\{P_-^{(1)}\right\}\left(\frac{V_0 - c_0}{\widetilde{K}} - \frac{1}{\lambda_-^{(0)}}\right), \quad (7.2.34)$$

an adaptation of (7.1.72). With these modified pressure-displacement relations, we now seek an upper-branch eigenrelation corresponding to the structure one critical layer.

The relations (7.2.10) and (7.2.30) are unchanged from Section 7.1 and yield

$${\alpha_0}^2 = \frac{(c_0 - V_0)\gamma}{\delta I(\delta)} + \frac{c_0 \lambda_+^{(0)}}{I(\delta)}, \qquad \gamma = \left(\frac{1}{\lambda_-^{(0)}} + \frac{c_0 - V_0}{\widetilde{K}}\right)^{-1}, \quad (7.2.35\ \text{a, b})$$

which are identical to (7.1.73) and (7.1.74).

A linear combination of (7.2.16) and (7.2.34) elicits the eigenrelation

$$-\frac{\lambda_+^{(0)}}{c_0\sqrt{2\alpha_0 c_0}} + \frac{\gamma}{(V_0 - c_0)\sqrt{2\alpha_0 (V_0 - c_0)}}\left(1 - \frac{{\alpha_0}^2 I(\delta)}{c_0 \lambda_+^{(0)}}\right) = \left(\frac{2\lambda_+^{(10)}}{{\lambda_+^{(0)}}^2} + \frac{1}{\lambda_+^{(0)}}\right) c_0 \pi, \quad (7.2.36)$$

upon manipulation using with (7.2.10), (7.2.22) and (7.2.30).

As expected, this eigenrelation bears great similarity to (7.1.75). The term on the right-hand side of (7.2.36) is associated with the phase shift that arises as we cross the critical layer near the outer cylinder. Unlike (7.1.75), here we have no term associated with a lower critical layer.

Equations (7.2.35) and (7.2.36) can be solved for α_0 and c_0 numerically using MATLAB. Figure 7.2.3 illustrates a solution for the eigenrelation for varying $\widetilde{K}$ with fixed $\delta = 0.5$ and $V_0 = 0.2$. Increasing $\widetilde{K}$ from zero, we observe there exists a critical value $\widetilde{K}_c$ beyond which the solution ceases to exist. For our choice of δ and V_0 here, it appears that $\widetilde{K}_c \approx 0.2328$. As $\widetilde{K}$ approaches this critical value from below, the wavespeed c_0 of the neutral mode becomes small and tends to zero, whilst the wavenumber becomes large. Our numerical investigations also show $\gamma \to -\infty$ in this limit. It is worth remarking that this cut-off for $\widetilde{K}$ demonstrates that there is no analogous mode in the rigid case. We also note that figure 7.2.3 supports our earlier assumption that $c_0 < V_0$.

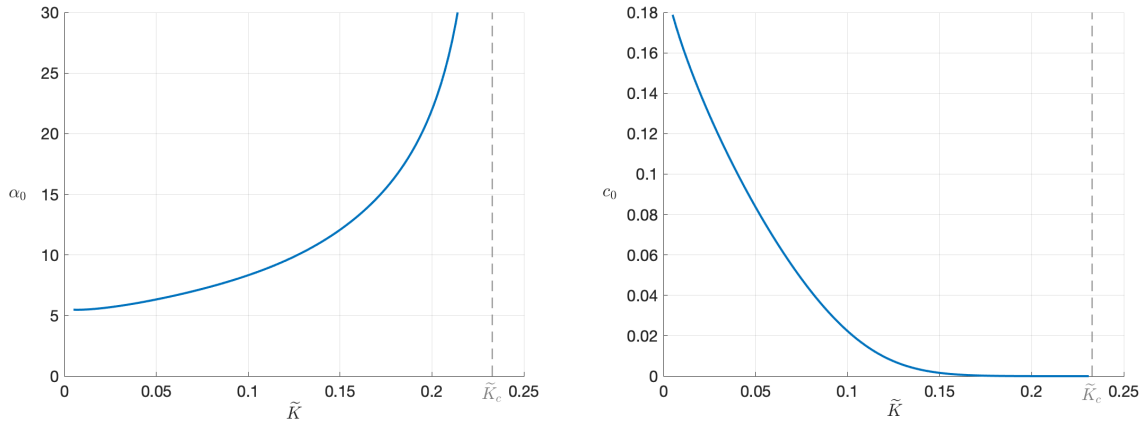

Figure 7.2.3: Illustration of the behaviour of the leading order wavenumber (left) and leading order wavespeed (right) as we vary $\widetilde{K}$ for an inner cylinder with $\delta = 0.5$ and $V_0 = 0.2$. The asymptote at $\widetilde{K} = \widetilde{K}_c$ is located at $\widetilde{K}_c \approx 0.2328$.

Behaviour of the upper-branch mode near the critical stiffness when $V_0 = O(1)$

We briefly consider the behaviour of the upper-branch structure (with only one critical layer) when V_0 is an order one quantity and $\widetilde{K}$ approaches from below the critical value beyond which the upper-branch eigenrelations (7.2.35, 7.2.36) have no solution.

Our expression for γ (7.2.35b) can be written as

$$\gamma = \frac{\lambda_-^{(0)}\widetilde{K}}{\widetilde{K} - \lambda_-^{(0)}V_0 + \lambda_-^{(0)}c_0}. \tag{7.2.37}$$

Our numerical results suggest that, near the critical stiffness with $V_0 = O(1)$, we have $\alpha_0 \to \infty$, $c_0 \to 0$ and $\gamma \to -\infty$. Upon use of (7.2.37), these considerations indicate that $\widetilde{K}$ is an order one quantity such that

$$\widetilde{K} = \widetilde{K}_c + \cdots, \qquad \widetilde{K}_c = \lambda_-^{(0)}V_0 \tag{7.2.38}$$

with

$$\widetilde{K} - \widetilde{K}_c \to 0^- \tag{7.2.39}$$

as we approach the critical stiffness. It is convenient to introduce a small positive parameter κ and write

$$\kappa = -\left(\widetilde{K} - \widetilde{K}_c\right), \qquad \kappa \to 0^+. \tag{7.2.40}$$

Consideration of γ using (7.2.37) reveals that

$$\gamma = -\lambda_-^{(0)}\,\widetilde{K}_c\,\kappa^{-1} + \cdots. \tag{7.2.41}$$

We have assumed here that κ is larger than c_0, and we will later show this is consistent with the analysis that follows.

The quadratic in α_0 (7.2.35a) elicits the balance

$$\alpha_0{}^2 \sim \frac{\lambda_-^{(0)} V_0 \, \widetilde{K}_c}{\delta I(\delta)} \, \kappa^{-1}, \tag{7.2.42}$$

which reveals that $\alpha_0 = O(\kappa^{-1/2})$ with

$$\alpha_0 = \sqrt{\frac{\lambda_-^{(0)} V_0 \, \widetilde{K}_c}{\delta I(\delta)}} \, \kappa^{-1/2} + \cdots . \tag{7.2.43}$$

We now focus our attention on the eigenrelation (7.2.36) to learn about the behaviour of c_0. We will consider each term in (7.2.36) individually. Using (7.2.43), the first term

$$-\frac{\lambda_+^{(0)}}{c_0 \sqrt{2\alpha_0 c_0}} = O\left(c_0{}^{-3/2} \, \alpha_0{}^{-1/2}\right) = O\left(c_0{}^{-3/2} \, \kappa^{1/4}\right). \tag{7.2.44}$$

The second term can be rewritten using (7.2.35a), and we see that

$$\frac{\gamma}{(V_0 - c_0)\sqrt{2\alpha_0 (V_0 - c_0)}} \left(1 - \frac{\alpha_0{}^2 I(\delta)}{c_0 \lambda_+^{(0)}}\right) = \frac{\gamma^2}{\delta c_0 \lambda_+^{(0)} \sqrt{2\alpha_0 (V_0 - c_0)}} = O\left(c_0^{-1} \, \kappa^{-7/4}\right) \tag{7.2.45}$$

upon recollection of (7.2.43). Finally, consideration of the third term illustrates

$$\left(\frac{2\lambda_+^{(10)}}{\lambda_+^{(0)2}} + \frac{1}{\lambda_+^{(0)}}\right) c_0 \pi = O\left(c_0\right). \tag{7.2.46}$$

Recalling that we seek a solution that has $c_0 \to 0$ and $\gamma \to -\infty$, it is apparent that the second term (7.2.45) becomes large and the third term (7.2.46) decays. We thus expect a balance between the first (7.2.44) and second (7.2.45) terms, which gives

$$c_0 = O(\kappa^4) \tag{7.2.47}$$

and, in particular,

$$c_0 = \frac{\lambda_+^{(0)4} \, \delta^2 \, V_0}{\lambda_-^{(0)4} \, \widetilde{K}_c^4} \, \kappa^4 + \cdots \tag{7.2.48}$$

after some manipulation. We remark that this is consistent with our earlier assumption that c_0 is smaller than κ.

It is of interest to compare the limiting behaviour found here to our solutions of the full eigenrelation (7.2.36) in figure 7.2.3. For the cylinder properties $\delta = 0.5$ and $V_0 = 0.2$, the expansion (7.2.38) gives $\widetilde{K} \approx 0.2328$ near the critical stiffness. This is consistent with our analysis of the full problem, where we observed $\widetilde{K}_c \approx 0.2328$ (see figure 7.2.3).

In order to illustrate the wave behaviour near the critical stiffness, we plot the leading order behaviour of the expansions

$$\alpha_0 = \sqrt{\frac{\lambda_-^{(0)} V_0 \, \widetilde{K}}{\delta I(\delta)}} \; \kappa^{-1/2} + \cdots, \qquad c_0 = \frac{\lambda_+^{(0)^4} \delta^2 \, V_0}{\lambda_-^{(0)^4} \, \widetilde{K}^4} \; \kappa^4 + \cdots \tag{7.2.49}$$

as $\kappa \to 0^+$ (that is, as $\widetilde{K}$ approaches $\widetilde{K}_c$ from below).

The orange dotted lines in figure 7.2.4 illustrate how the near-critical-stiffness wavenumber and wavespeed described in (7.2.49) vary with $\widetilde{K}$ as $\kappa \to 0$. The blue lines represent solutions α_0 and c_0 to the full eigenrelations (7.2.35), (7.2.36). As expected, agreement between the two approaches increases as $\widetilde{K}$ approaches the critical stiffness.

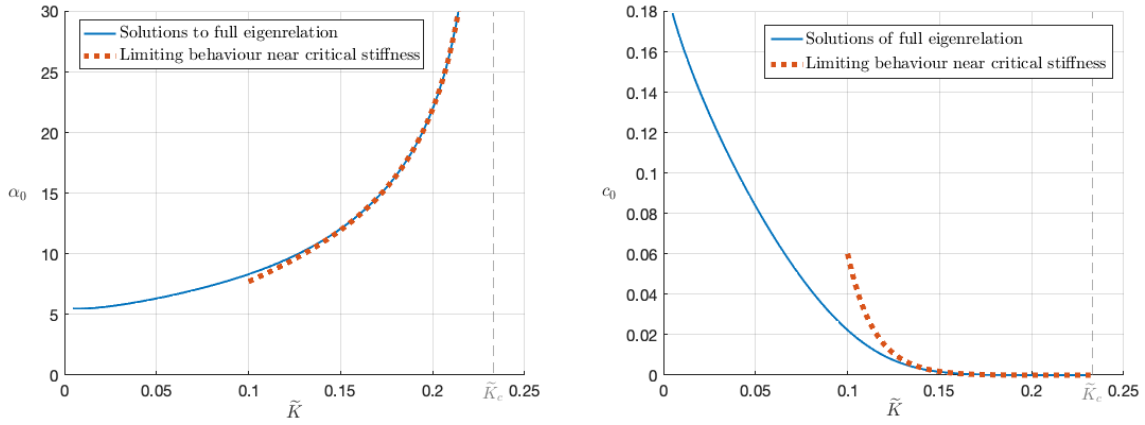

Figure 7.2.4: Illustration of the behaviour of the leading order wavenumber (left) and leading order wavespeed (right) as we vary $\widetilde{K}$ for an inner cylinder with $\delta = 0.5$ and $V_0 = 0.2$. Orange dotted lines represent the limiting behaviour described in (7.2.49). Blue lines represent solutions to the full eigenrelations (7.2.35), (7.2.36). The critical stiffness is located at $\widetilde{K}_c \approx 0.2328$.

Behaviour of the upper-branch mode as near the critical stiffness when V_0 becomes large

It is also of interest to examine the behaviour of the one-critical-layer upper-branch structure as $\widetilde{K}$ approaches its critical value $\widetilde{K}_c$ when V_0 is not constrained to be order one. Numerical investigations suggest that, in this limit, we have $\alpha_0 \to \infty$, $c_0 \to 0$ and $\gamma \to -\infty$.

In view of this, we introduce a positive parameter $\Gamma \gg 1$ and let

$$\gamma \sim -\gamma_0 \Gamma, \qquad \gamma_0 > 0. \tag{7.2.50}$$

Examining the expression for γ (7.2.35b) suggests that we take

$$\widetilde{K_c} = \lambda_-^{(0)} V_0 \tag{7.2.51}$$

with

$$V_0 \sim \bar{V}_0 \Gamma^a + \bar{V}_1 \Gamma^{a-1}, \qquad \widetilde{K} \sim \lambda_-^{(0)} \bar{V}_0 \Gamma^a - \bar{K}_1 \Gamma^{a-1} \tag{7.2.52}$$

where $\bar{K}_1 + \bar{V}_1 > 0$ and a will be determined in the analysis that follows. We assume $c_0 = o(\Gamma^{a-1})$ and confirm this during the course of our analysis. Using this, we find that γ_0 can be expressed as

$$\gamma_0 = \frac{{\lambda_-^{(0)}}^2 \bar{V}_0}{\bar{K}_1 + \bar{V}_1}. \tag{7.2.53}$$

Balancing the terms in the relation (7.2.35a) in the limit $\Gamma \to \infty$, we see the leading order wavenumber behaves as

$$\alpha_0 \sim \left(\frac{\gamma_0 \bar{V}_0}{\delta I(\delta)} \right)^{1/2} \Gamma^{\frac{a+1}{2}}. \tag{7.2.54}$$

It now remains to determine a. Substituting (7.2.35) into the eigenrelation (7.2.36), we write the eigenrelation as

$$-\frac{\lambda_+^{(0)}}{\sqrt{2\alpha_0 c_0}} + \frac{\gamma^2}{\sqrt{2\alpha_0 \left(V_0 - c_0\right)}} \frac{1}{\delta \lambda_+^{(0)}} = \left(\frac{2\lambda_+^{(10)}}{{\lambda_+^{(0)}}^2} + \frac{1}{\lambda_+^{(0)}} \right) \pi c_0^2 \tag{7.2.55}$$

Note that this equation is exact. We write the eigenrelation in this form to more easily identify the sizes of each term.

A balance between all three terms requires that

$$\Gamma^{-\frac{a+1}{4}} {c_0}^{-1/2} \sim \Gamma^{\frac{7-3a}{4}} \sim {c_0}^2, \tag{7.2.56}$$

which gives $a = {}^{39}/_{11}$ and

$$c_0 \sim \Gamma^{-5/11} \bar{c}_0. \tag{7.2.57}$$

Substitution of our expansions (7.2.50), (7.2.52), (7.2.53), (7.2.54) and (7.2.57) into the eigenrelation (7.2.55) reveals that $\bar{c}_0$ can be obtained by solving

$$\pi \left(\frac{2\lambda_+^{(10)}}{\lambda_-^{(0)}} + 1 \right) \left(2\bar{\alpha}_0 \bar{V}_0 \right)^{1/2} \bar{c}_0^{5/2} - \frac{\gamma_0^2}{\delta} \bar{c}_0^{1/2} + {\lambda_-^{(0)}}^2 \bar{V}_0^{1/2} = 0. \tag{7.2.58}$$

In the limit $\Gamma \to \infty$, we thus have

$$\alpha_0 \sim \Gamma^{25/11}\bar{\alpha}_0, \qquad c_0 \sim \Gamma^{-5/11}\bar{c}_0, \qquad V_0 \sim \Gamma^{39/11}\bar{V}_0, \qquad \widetilde{K} \sim \Gamma^{39/11}\lambda_-^{(0)}\bar{V}_0. \quad (7.2.59)$$

7.2.1 Upper-branch structure in the limit $\gamma \to -\infty$

The above analysis alludes to the existence of a new structure in the limit $\gamma \to -\infty$, and we now seek to determine the size of γ at which the upper-branch structure described in Section 7.2 breaks down. Guided by the behaviour in (7.2.59), we adopt the scalings

$$\alpha_0 \sim \Gamma^{25/11}\overline{\alpha}_0, \quad c_0 \sim \Gamma^{-5/11}\overline{c}_0, \quad (7.2.60)$$

$$V_0 \sim \Gamma^{39/11}\overline{V}_0, \quad \widetilde{K} \sim \Gamma^{39/11}\overline{K}, \quad \gamma \sim -\overline{\gamma}_0\Gamma, \quad \Gamma \to \infty. \quad (7.2.61)$$

Upon recollection that $\widetilde{K} = K_0 - {\alpha_0}^2{c_0}^2 m_0$, we take

$$K_0 = O(\Gamma^{39/11}), \quad m_0 = O(\Gamma^{-1/11}) \quad (7.2.62)$$

in order to preserve both the spring stiffness and mass of the inner cylinder in the quantity $\widetilde{K}$.

To facilitate our understanding of the new structure that arises, we identify scalings (in terms of Γ) for the disturbance quantities in the upper-branch structure. We endeavour to retain as many terms as possible in the Reynolds-number-independent equations governing the core region (7.2.4), inviscid shear layers (7.2.8), (7.2.19) and viscous wall layers (7.2.14), (7.2.27).

The inviscid core region I

In this region, our analysis pertains to the expansions (7.2.3), equations (7.2.4) and solutions F_0, G_0, P_0 in (7.2.5).

The linearity of the problem allows us to begin by taking $F_0 = O(1)$ in this region. In view of the solution for F_0, this determines A_0 to be such that $A_0 = O(1)$. A balance in the continuity equation (7.2.4a) with $\mathrm{i}\alpha_0 F_0 \sim {G_0}'(r)$ then requires $G_0 = O(\Gamma^{25/11})$. The radial momentum equation (7.2.4c) yields $P_0 = O(\Gamma^{50/11})$ upon enforcing the balance $\mathrm{i}\alpha_0 U_{00} G_0 \sim {P_0}'(r)$.

Writing $F_0 = \overline{F}_0$, $G_0 = \Gamma^{25/11}\overline{G}_0$ and $P_0 = \Gamma^{50/11}\overline{P}_0$, the equations (7.2.4) give

$$\mathrm{i}\overline{\alpha}_0\overline{F}_0 + \frac{\mathrm{d}\overline{G}_0}{\mathrm{d}r} + \frac{\overline{G}_0}{r} = 0, \tag{7.2.63a}$$

$$\mathrm{i}\overline{\alpha}_0 U_{00}\overline{F}_0 + \overline{G}_0\frac{\mathrm{d}U_{00}}{\mathrm{d}r} = 0, \tag{7.2.63b}$$

$$\mathrm{i}\overline{\alpha}_0 U_{00}\overline{G}_0 + \frac{\mathrm{d}\overline{P}_0}{\mathrm{d}r} = 0. \tag{7.2.63c}$$

These balances are identical to those in (7.2.4), though with barred variables now.

As we approach the outer cylinder, consideration of (7.2.5) shows

$$F_0 = O(1), \qquad G_0 = O(\Gamma^{25/11}(1-r)), \qquad P_0 = O(\hat{P}_0), \tag{7.2.64}$$

where the size of $\hat{P}_0$ will be determined in the analysis that follows. As $r \to \delta$,

$$F_0 = O(1), \qquad G_0 = O(\Gamma^{25/11}(r-\delta)), \qquad P_0 = O(\Gamma^{50/11}). \tag{7.2.65}$$

Inviscid shear layer II+

In this layer, our flow quantities correspond to the expansions (7.2.7), equations (7.2.8) and solutions (7.2.9). We have $(1-r) = \epsilon^2 Y_+$, where Y_+ is to be determined in terms of Γ.

To match with the core (7.2.64), we take $u_+ = O(1)$ in this region. This region contains a critical layer, so we balance the base velocity with the wavespeed. This reveals the thickness of the layer to be

$$(1-r) = O(R^{-2/11}\Gamma^{-5/11}) \tag{7.2.66}$$

so that in this region, $Y_+ = \Gamma^{-5/11}\overline{Y}_+$. This layer becomes thinner in the limit $\Gamma \to \infty$.

Preserving the terms in the axial momentum equation (7.2.8c), we take $v_+^{(0)} = O(\Gamma^{20/11})$ and $p_+^{(0)} = O(\Gamma^{-5/11})$. We substitute

$$u_+^{(0)} = \overline{u}_+^{(0)}, \qquad v_+^{(0)} = \Gamma^{20/11}\overline{v}_+^{(0)}, \qquad p_+^{(0)} = \Gamma^{-5/11}\overline{p}_+^{(0)}, \tag{7.2.67}$$

into (7.2.8), and the resulting leading order equations are

$$\mathrm{i}\overline{\alpha}_0\overline{u}_+^{(0)} + \frac{\mathrm{d}\overline{v}_+^{(0)}}{\mathrm{d}\overline{Y}_+} = 0, \tag{7.2.68a}$$

$$\mathrm{i}\overline{\alpha}_0\left(\lambda_+^{(0)}\overline{Y}_+ - \overline{c}_0\right)\overline{u}_+^{(0)} + \lambda_+^{(0)}\overline{v}_+^{(0)} + \mathrm{i}\overline{\alpha}_0\overline{p}_+^{(0)} = 0, \tag{7.2.68b}$$

$$\frac{\mathrm{d}\overline{p}_+^{(0)}}{\mathrm{d}\overline{Y}_+} = 0, \tag{7.2.68c}$$

subject to matching the core. These balances are the same as in (7.2.8), with barred variables instead.

Before we move onto the upper viscous layer, we comment on the size of $\hat{P}_0$. From (7.2.68c), it is apparent that $\overline{p}_+^{(0)}$ is constant with respect to $\overline{Y}_+$. Since the pressure disturbance must match the core (7.2.64), we require that $\hat{P}_0 = O(\Gamma^{-5/11})$.

Viscous wall layer III+

Our analysis in this layer focuses on the expansions (7.2.13) and equations (7.2.14). Here we have $(1-r) = \epsilon^4\bar{y}_+$, where $\bar{y}_+$ is to be determined in terms of Γ.

In this region, the pressure is constant (7.2.14c) and must match inviscid shear layer (7.2.67), so we take $\bar{p}_+ = O(\Gamma^{-5/11})$. With $\bar{u}_+ = O(1)$ to match the inviscid layer (7.2.67), we turn to the axial momentum equation (7.2.14b).

Striking the balance

$$\frac{\mathrm{d}^2\bar{u}_+}{\mathrm{d}\bar{y}_+^2} \sim \mathrm{i}\alpha_0 c_0\bar{u}_+ \sim \mathrm{i}\alpha_0\bar{p}_+$$

gives the thickness of the layer to be $(1-r) = O(R^{-4/11}\Gamma^{-10/11})$ with $\bar{y}_+ = \Gamma^{-10/11}\overline{Y}_+$ upon recollection that $\alpha_0 = O(\Gamma^{25/11})$ and $c_0 = O(\Gamma^{-5/11})$ (7.2.60). This layer becomes thinner in the limit $\Gamma \to \infty$.

The continuity equation (7.2.14a) then suggests that $\bar{v}_+ = O(\Gamma^{15/11})$. We thus write

$$\bar{u}_+ = \overline{U}_+, \qquad \bar{v}_+ = \Gamma^{15/11}\overline{V}_+, \qquad \bar{p}_+ = \Gamma^{-5/11}\overline{P}_+, \qquad \bar{y}_+ = \Gamma^{-10/11}\overline{Y}_+, \tag{7.2.69}$$

which, upon substitution into (7.2.14), reveals the equations

$$\mathrm{i}\overline{\alpha}_0\overline{U}_+ + \frac{\mathrm{d}\overline{V}_+}{\mathrm{d}\overline{Y}_+} = 0, \tag{7.2.70a}$$

$$\frac{\mathrm{d}^2\overline{U}_+}{\mathrm{d}\overline{Y}_+^2} + \mathrm{i}\overline{\alpha}_0\overline{c}_0\overline{U}_+ - \mathrm{i}\overline{\alpha}_0\overline{P}_+ = 0, \tag{7.2.70b}$$

$$\frac{\mathrm{d}\overline{P}_+}{\mathrm{d}\overline{Y}_+} = 0, \tag{7.2.70c}$$

subject to no-slip conditions on the outer cylinder and matching the inviscid shear layer. We note that these equations contain the same balances as in (7.2.14).

Inviscid shear layer II-

In this layer, we concentrate on the expansions (7.2.18) and equations (7.2.19). We have $r = \delta + \epsilon^2 Y_-$, where the size of Y_- will be determined in terms of Γ.

We expect that $u_-^{(0)} = O(1)$ and $p_-^{(0)} = O(\Gamma^{50/11})$, as suggested by the matching conditions from the core (7.2.65). Recalling that we have $\alpha_0 = O(\Gamma^{25/11})$ (7.2.60), we balance the inertia and pressure terms in the axial momentum equation (7.2.19b) to obtain $Y_- = O(\Gamma^{50/11})$ and $v_-^{(0)} = O(\Gamma^{75/11})$.

In consideration of these scalings, as well as those in (7.2.60) and (7.2.61), we substitute

$$u_-^{(0)} = \overline{u}_-, \qquad v_-^{(0)} = \Gamma^{75/11}\overline{v}_-, \qquad p_-^{(0)} = \Gamma^{50/11}\overline{p}_-, \qquad Y_- = \Gamma^{50/11}\overline{Y}_- \tag{7.2.71}$$

$$\alpha_0 = \Gamma^{25/11}\overline{\alpha}_0, \quad c_0 = \Gamma^{-5/11}\overline{c}_0, \quad V_0 = \Gamma^{39/11}\overline{V}_0, \tag{7.2.72}$$

into the equations (7.2.19).

This gives

$$\frac{\mathrm{d}\overline{v}_-}{\mathrm{d}\overline{Y}_-} - \mathrm{i}\overline{\alpha}_0\overline{u}_- = 0, \tag{7.2.73a}$$

$$\mathrm{i}\overline{\alpha}_0\lambda_-^{(0)}\overline{Y}_-\overline{u}_- + \mathrm{i}\overline{\alpha}_0\overline{p}_- - \lambda_-^{(0)}\overline{v}_- = 0, \tag{7.2.73b}$$

$$\frac{\mathrm{d}\overline{p}_-}{\mathrm{d}\overline{Y}_-} = 0, \tag{7.2.73c}$$

which are to be solved in conjunction to matching the core (7.2.65). Note that this layer becomes thicker in the limit $\Gamma \to \infty$. We see that these equations are not identical to (7.2.19); specifically, the sliding velocity V_0 and wavespeed c_0 have not been retained in the axial momentum equation (7.2.73b).

Viscous wall layer III-

In this layer, our analysis pertains to the expansions (7.2.26) and equations (7.2.27). We have $r = \delta + \epsilon^4 \bar{y}_-$ where the size of $\bar{y}_-$ is to be determined in terms of Γ.

We anticipate $\bar{p}_-^{(0)} = \Gamma^{50/11}\overline{P}_-$ and $\bar{v}_-^{(0)} = \Gamma^{75/11}\overline{V}_-$ to match the inviscid shear layer (7.2.71), and expect both quantities to be constant in this layer in view of the solutions (7.2.28).

With $\widetilde{K} = \Gamma^{39/11}\overline{K}$ (7.2.61), the dynamic boundary condition (7.1.55) suggests that $\bar{u}_-^{(0)} = \Gamma\,\overline{U}_-$ so that

$$\overline{P}_- = \frac{\overline{K}}{\lambda_-^{(0)}}\overline{U}_-. \tag{7.2.74}$$

The kinematic condition (7.1.58) reduces to

$$\mathrm{i}\overline{\alpha}_0\overline{V}_0\overline{U}_- - \lambda_-^{(0)}\overline{V}_- = 0 \tag{7.2.75}$$

in view of the scalings (7.2.60) and (7.2.61), which show $\alpha_0 = \Gamma^{25/11}\overline{\alpha}_0$, $c_0 = \Gamma^{-5/11}\overline{c}_0$ and $V_0 = \Gamma^{39/11}\overline{V}_0$.

To incorporate the inertial, pressure and viscous terms in the axial momentum equation (7.2.27c), we require $\bar{y}_- = \Gamma^{-32/11}\overline{Y}_-$.

Substituting

$$\bar{u}_-^{(0)} = \Gamma\,\overline{U}_-, \qquad \bar{v}_-^{(0)} = \Gamma^{75/11}\overline{V}_-, \qquad \bar{p}_-^{(0)} = \Gamma^{50/11}\overline{P}_-, \qquad \bar{y}_- = \Gamma^{-32/11}\overline{Y}_- \tag{7.2.76}$$

into (7.2.27), the governing equations in this limit are

$$\frac{\mathrm{d}\overline{V}_-}{\mathrm{d}\overline{Y}_-} = 0, \qquad \frac{\partial^2\overline{U}_-}{\partial\overline{Y}_-{}^2} - \mathrm{i}\overline{\alpha}_0\overline{P}_- + \lambda_-^{(0)}\overline{V}_- - \mathrm{i}\overline{\alpha}_0\overline{V}_0\overline{U}_- = 0, \qquad \frac{\mathrm{d}\overline{P}_-}{\mathrm{d}\overline{Y}_-} = 0. \tag{7.2.77}$$

We note the wavespeed c_0 is not retained in these equations, though the sliding velocity is included. The layer becomes thinner in the limit $\Gamma \to \infty$.

Structure breakdown

We illustrate the regions described above in figure 7.2.5. A natural next step is to investigate the size of Γ for which this structure breaks down.

To this end, we turn our attention back to the lower inviscid shear region, which becomes thicker in the limit $\Gamma \to \infty$. We specifically concentrate on the radial velocity disturbance

in our expansions (7.2.18), where we recall $\epsilon = R^{-1/11}$ so that

$$\hat{v} = -R^{-3/11} v_-^{(0)} - R^{-5/11} v_-^{(1)} + \cdots . \tag{7.2.78}$$

During the course of our analysis, we determined that $v_-^{(0)} = O(\Gamma^{75/11})$ (7.2.71) in the limit $\Gamma \to \infty$. It is worthwhile to also consider the expected size of $v_-^{(1)}$ in this limit. The solution to $v_-^{(1)}$ is given by (7.2.23), which is

$$v_-^{(1)} = \frac{\mathrm{i}\alpha_0}{\lambda_-^{(0)}} \left(\frac{2\lambda_-^{(10)}}{\lambda_-^{(0)2}} - \frac{1}{\delta \lambda_-^{(0)}} \right) \left(\hat{P}_0 + \alpha_0^2 A_0 I(\delta) \right) \zeta_- \log(\zeta_-) - \mathrm{i}\alpha_0 A_-^{(1)} \zeta_- + \frac{\mathrm{i}\alpha_0 P_-^{(1)}}{\lambda_-^{(0)}} + \text{imaginary terms}, \tag{7.2.79}$$

where we recall $\zeta_- = \lambda_-^{(0)} Y_- + V_0 - c_0$. We focus on the first term of this solution.

In the lower inviscid shear layer, we found that $Y_- = \Gamma^{50/11} \overline{Y}_-$ (7.2.71). It is also helpful to recall that we have found $A_0 = O(1)$, $\hat{P}_0 = O(\Gamma^{-5/11})$ in the limit $\Gamma \to \infty$ during our analysis of the core region and upper inviscid layer in Section 7.2.1. In addition, we have $\alpha_0 = O(\Gamma^{25/11})$, $c_0 = O(\Gamma^{-5/11})$, $V_0 = O(\Gamma^{39/11})$ from (7.2.60), (7.2.61).

Using this, we observe that the first term of $v_-^{(1)}$ (7.2.79) behaves as

$$\frac{\mathrm{i}\alpha_0}{\lambda_-^{(0)}} \left(\frac{2\lambda_-^{(10)}}{\lambda_-^{(0)2}} - \frac{1}{\delta \lambda_-^{(0)}} \right) \left(\hat{P}_0 + \alpha_0^2 A_0 I(\delta) \right) \zeta_- \log(\zeta_-) = O(\Gamma^{125/11} \log \Gamma) \tag{7.2.80}$$

We therefore expect the normal velocity $v_-^{(1)}$ to become larger in the limit $\Gamma \to \infty$. The expansion (7.2.78) can now be written as

$$\hat{v} = -R^{-3/11} \Gamma^{75/11} \overline{v}_- - R^{-5/11} \Gamma^{125/11} \log \Gamma \; \overline{v}_-^{(1)} \tag{7.2.81}$$

where $\overline{v}_-$ and $\overline{v}_-^{(1)}$ are order one in the limit $\Gamma \to \infty$.

We see that this expansion for $\hat{v}$ (7.2.81) is no longer well-ordered when

$$\Gamma = \frac{R^{1/25}}{(\log R)^{11/50}}. \tag{7.2.82}$$

At this size of Γ, our upper-branch structure no longer holds and

$$\alpha = O\left(\frac{1}{\sqrt{\log R}} \right), \quad c = O\left(\left(\frac{R}{\sqrt{\log R}} \right)^{-1/5} \right). \tag{7.2.83}$$

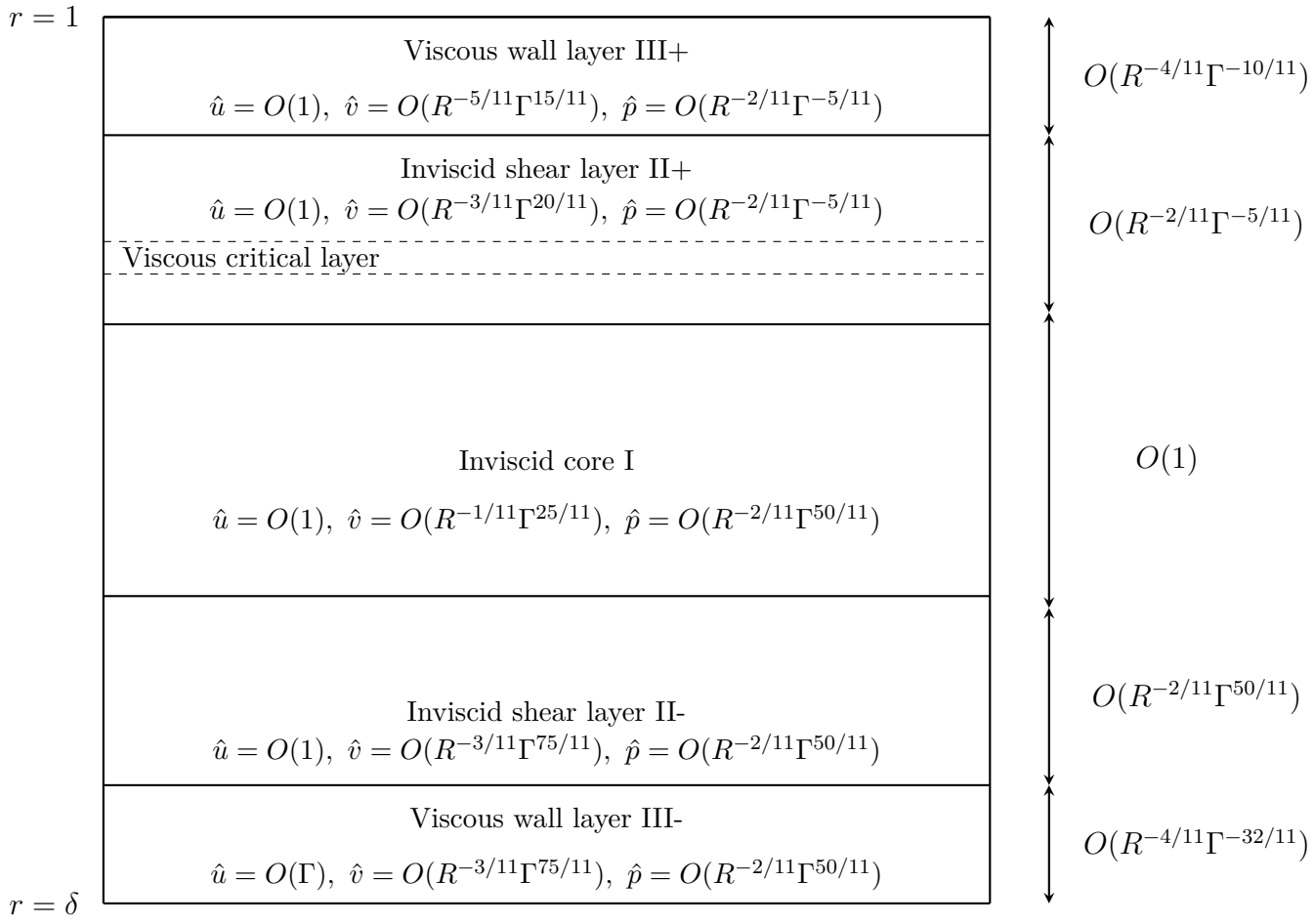

Figure 7.2.5: Schematic of the asymptotic structure of the upper branch mode with one critical layer, where $\alpha = O\left(R^{-1/11}\Gamma^{25/11}\right)$ and $c = O\left(R^{-2/11}\Gamma^{-5/11}\right)$. The cylinder properties are $V = O\left(R^{-2/11}\Gamma^{39/11}\right)$, $K = O\left(R^{20/11}\Gamma^{39/11}\right)$ and $m = O\left(R^{4/11}\Gamma^{-1/11}\right)$.

7.3 Summary

We began this chapter by studying an upper-branch structure with two critical layers (Section 7.1). We explored the influence of flexibility on this neutral mode, and found that this influence diminished as the sliding velocity of our inner cylinder was increased. This motivated us to investigate the structure in the limit $V_0 \to \infty$ (Section 7.1.1). Our results from this analysis suggested that the lower critical layer moves closer to the wall of the inner cylinder at increasingly large sliding velocities. We expect that the upper layers of this structure retain an upper-branch-type structure, while the lower layers become of a lower-branch-type structure. We will explore this in more depth in the next chapter. In Section 7.1.2, we went on to study the upper-branch mode in the large-wavenumber limit with $\widetilde{K} \to 0^-$.

In Section 7.2, we considered an upper-branch structure with the same scalings as in Section 7.1, but with the stipulation that the disturbance wavespeed is smaller than the sliding velocity of the inner cylinder. This means that there does not exist a critical layer near the inner cylinder wall. We found that this structure has a critical value $\widetilde{K}_c$ beyond which there exists no neutral mode, and as such, there is no rigid analogue to this structure. In Chapter 9, we will see an example of a numerical stability region corresponding to this structure. Examining the eigenrelations (7.2.35) and (7.2.36), we briefly explored the behaviour of the neutral mode when $\widetilde{K}$ is near the critical value $\widetilde{K}_c$ and V_0 is of order one. We also analysed the one-critical-layer upper-branch structure when $\widetilde{K} \sim \widetilde{K}_c$ and V_0 becomes large.

Chapter 8

An asymptotic approach at large Reynolds numbers: a hybrid analysis

Cowley and Smith [45] explored the stability properties of plane Poiseuille Couette flow at large Reynolds numbers using asymptotic techniques, and determined the scalings for a neutral mode that exhibits properties pertaining to both the lower-branch and upper-branch structures. In his detailed study of annular Poiseuille Couette flow, Walton [1] also investigated this neutral mode at large Reynolds numbers, coining the term 'hybrid' to describe such a structure.

Following the analysis of Walton [1], in Section 7.1.1 we considered an upper-branch structure in the limit $V_0 \to \infty$, where we recall that V_0 is such that $V = R^{-2/11}V_0$. We briefly revisit our findings here. When V_0 is increased sufficiently, we expect that the upper-branch structure breaks down with the critical layer in the lower inviscid shear layer (see figure 7.1.1) moving into the lower viscous wall layer, so that the lower layers form a lower-branch-type structure. We expect that the upper layers, however, remain unaffected and retain their upper-branch-type structure.

To enable us to find the scalings for the hybrid mode, we consider this new mode as an extension of the upper-branch mode with $V = R^{-2/11}V_0$ in the limit $V_0 \to \infty$. We emphasise that consideration of the limit $V_0 \to \infty$ will not pertain to a large sliding velocity V, owing to the scaling $V = R^{-2/11}V_0$. We confirm this in the subsequent analysis, where we determine the order of V_0 at which the upper-branch mode breaks down and find a distinguished scaling for the hybrid mode.

In view of this objective, we restate the limiting behaviour of the upper-branch mode as $V_0 \to \infty$, as found in (7.1.95), (7.1.96) (Chapter 7, Section 7.1.1):

$$\alpha \sim R^{-1/11}\alpha_0, \quad c \sim R^{-2/11}c_0, \quad K = R^{20/11}K_0, \quad m = R^{4/11}K_0, \quad V = R^{-2/11}V_0, \tag{8.0.1}$$

where

$$\alpha_0 \sim \left(\frac{\lambda_+^{(0)}}{I(\delta)}\right)^{1/2} V_0^{1/2}, \quad c_0 \sim V_0 + \tilde{\beta}_2 V_0^{-9/2}, \quad K_0 \sim \overline{k}_0 V_0^{-9/2}, \quad m_0 \sim \overline{m}_0 V_0^{-15/2}, \quad V_0 \to \infty, \tag{8.0.2}$$

with $\tilde{\beta}_2 > 0$ defined in (7.1.93).

When the scaled sliding velocity in the upper branch structure, V_0, becomes sufficiently large, we see from the asymptotic behaviour (8.0.2) that c_0 becomes very close to V_0. As this happens, we expect the lower critical layer of the upper-branch structure to move closer to the inner cylinder wall and eventually be situated in the lower viscous wall layer, whose thickness we will denote by q in the limit $V_0 \to \infty$.

The existence of a critical layer near the inner wall requires the basic velocity to be equal to the disturbance wavespeed in the vicinity of $r = \delta$. With the basic velocity expanding as

$$U_0 = V + \lambda_-^{(0)}(r - \delta) + \ldots \quad \text{as} \quad r \to \delta, \tag{8.0.3}$$

we have

$$U_0 - c \sim \lambda_-^{(0)}(r - \delta) + R^{-2/11}V_0 - R^{-2/11}c_0 \tag{8.0.4}$$

in view of the upper-branch scalings (8.0.1). In the limit $V_0 \to \infty$, this gives

$$U_0 - c \sim \lambda_-^{(0)} q - R^{-2/11}\tilde{\beta}_2 V_0^{-9/2} \tag{8.0.5}$$

upon use of (8.0.2) and thus, in order to have a critical layer, we require

$$q = O\left(R^{-2/11}V_0^{-9/2}\right). \tag{8.0.6}$$

With viscosity playing an important role in this region, we also expect a balance between the inertial and viscous terms of the linearised axial momentum equation (2.3.11b). For sufficiently large V_0, we have

$$\alpha = O(R^{-1/11}V_0^{1/2}) \quad \text{and} \quad U_0 - c = O(R^{-2/11}V_0^{-9/2}) \tag{8.0.7}$$

in consideration of (8.0.1), (8.0.2) and (8.0.5), (8.0.6) respectively. Therefore the balance

$$\mathrm{i}\alpha(U_0 - c)\hat{u} \sim \frac{1}{R}\frac{\mathrm{d}^2\hat{u}}{\mathrm{d}r^2} \tag{8.0.8}$$

requires

$$R^{-1/11}V_0^{1/2}R^{-2/11}V_0^{-9/2} \sim R^{-1}\left(R^{-2/11}V_0^{-9/2}\right)^{-2}. \tag{8.0.9}$$

This is achieved when

$$V_0 = O(R^{4/143}). \tag{8.0.10}$$

Recalling the scalings (8.0.2), we see then that our new structure arises when the disturbance wavespeed and wavenumber are of the size

$$\alpha_0 = O\left(V_0^{1/2}\right) = R^{2/143}, \quad c_0 = O\left(V_0\right) = R^{4/143}. \tag{8.0.11}$$

For the spring stiffness and mass described by (8.0.2), we have

$$K_0 = O\left(V_0^{-9/2}\right) = R^{-18/143}, \quad m_0 = O\left(V_0^{-15/2}\right) = R^{-30/143}, \tag{8.0.12}$$

which indicates that the inner cylinder has become more flexible.

In light of (8.0.11), (8.0.12) and the upper-branch scalings (8.0.1), the upper-branch structure transforms into a new regime in which

$$\alpha = O\left(R^{-1/11}R^{2/143}\right), \quad c = O\left(R^{-2/11}R^{4/143}\right), \tag{8.0.13a}$$

$$V = O\left(R^{-2/11}R^{4/143}\right), \quad K = O\left(R^{20/11}R^{-18/143}\right), \quad m = O\left(R^{4/11}R^{-30/143}\right). \tag{8.0.13b}$$

This can be written as

$$\alpha = O\left(R^{-1/13}\right), \quad c = O\left(R^{-2/13}\right), \tag{8.0.14a}$$

$$V = O\left(R^{-2/13}\right), \quad K = O\left(R^{22/13}\right), \quad m = O\left(R^{2/13}\right). \tag{8.0.14b}$$

Following the terminology of Walton [1], these will be known as our hybrid scalings and we convey this behaviour through the expansions

$$V = \epsilon^2\overline{V}_0, \quad \alpha = \epsilon\overline{\alpha}_0 + \epsilon^3\overline{\alpha}_1, \quad c = \epsilon^2\overline{c}_0 + \epsilon^4\overline{c}_1, \quad \overline{c}_0 = \overline{V}_0, \quad K = \epsilon^{-22}\overline{K}_0, \quad m = \epsilon^{-2}\overline{m}_0, \tag{8.0.15}$$

where we have introduced order one barred variables and the small parameter ϵ is now given by

$$\epsilon = R^{-1/13}. \tag{8.0.16}$$

We remark that these are the scalings found by Cowley and Smith [45] in the planar case.

We now move onto analysing the flow quantities in each region of the hybrid structure.

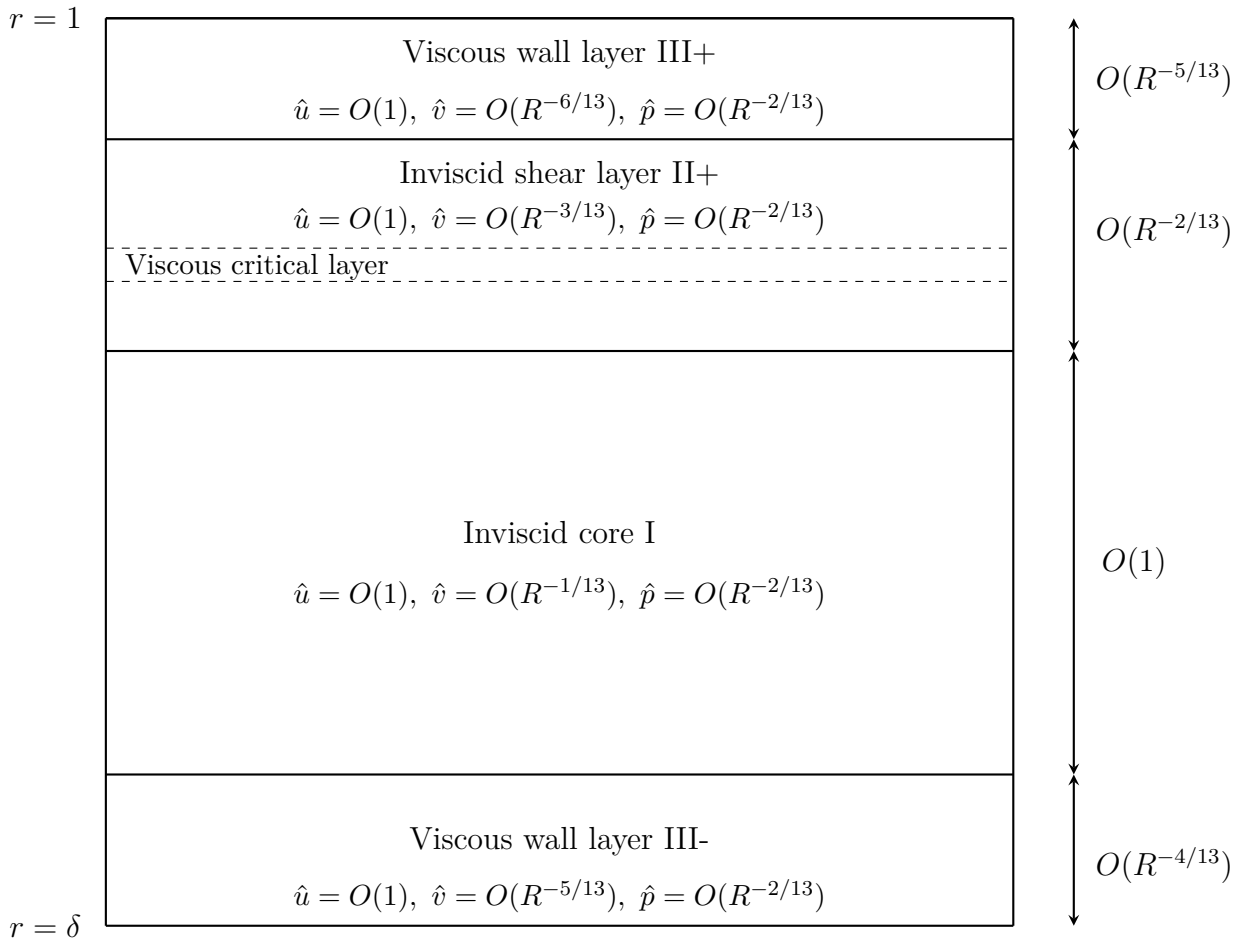

Figure 8.0.1: Schematic of the asymptotic structure of the hybrid mode, where $\alpha = O\left(R^{-1/13}\right)$ and $c = O\left(R^{-2/13}\right)$. The cylinder properties are $V = O\left(R^{-2/13}\right)$, $K = O\left(R^{22/13}\right)$ and $m = O\left(R^{2/13}\right)$.

The core region

The dynamics that govern this region are identical to those in the core regions of the upper and lower branch structures with $\alpha = O(R^{-1/11})$ and $\alpha = O(R^{-1/7})$ respectively. Chapters 6 and 7 contain details of the analysis in this region, but we include the solutions here for completeness.

The expansions in this region are given by

$$\hat{u} = F_0 + \cdots, \quad \hat{v} = \epsilon G_0 + \epsilon^3 G_1 + \cdots, \quad \hat{p} = \epsilon^2 P_0 + \epsilon^4 P_1 + \cdots. \tag{8.0.17a}$$

Substituting these into the linearised disturbance equations (2.3.11) yields the governing equations (7.1.3) and (7.1.5) with α_0 replaced by $\overline{\alpha}_0$.

These have solutions

$$F_0 = \frac{A_0}{r}\frac{\mathrm{d}U_{00}}{\mathrm{d}r}, \tag{8.0.18a}$$

$$G_0 = -\mathrm{i}\overline{\alpha}_0 A_0 \frac{U_{00}}{r}, \quad G_1 = -\mathrm{i}\overline{\alpha}_0 A_1 \frac{U_{00}}{r} + \text{purely imaginary terms}, \tag{8.0.18b}$$

$$P_0 = \hat{P}_0 + \overline{\alpha}_0^2 A_0 I(r), \quad P_1 = P_+^{(1)} + \overline{\alpha}_0^2 A_1 I(r) + \text{purely real terms}, \tag{8.0.18c}$$

where A_0 is a real constant, A_1 and $P_+^{(1)}$ are unknown complex constants, and $I(r)$ is as defined in (6.1.11). We reiterate that these disturbance solutions (8.0.18) are identical to those of the upper-branch core (7.1.4, 7.1.6), with α_0 replaced by $\overline{\alpha}_0$.

The behaviour of these quantities as we approach the inner and outer cylinders provide matching conditions for the flow expansions in the neighbouring layers. As $r \to 1^-$,

$$F_0 \to -A_0\lambda_+^{(0)}, \quad G_0 \sim -\mathrm{i}\overline{\alpha}_0 A_0 \lambda_+^{(0)}(1-r), \quad P_0 \to \hat{P}_0, \tag{8.0.19a}$$

$$\mathrm{Re}\{G_1\} \sim \overline{\alpha}_0 \,\mathrm{Im}\{A_1\}\lambda_+^{(0)}(1-r), \quad \mathrm{Im}\{P_1\} \to \mathrm{Im}\left\{P_+^{(1)}\right\}. \tag{8.0.19b}$$

Similarly, as $r \to \delta^+$,

$$F_0 \to \frac{A_0\lambda_-^{(0)}}{\delta}, \quad G_0 \sim -\frac{\mathrm{i}\overline{\alpha}_0 A_0 \lambda_-^{(0)}}{\delta}(r-\delta), \quad P_0 \to \hat{P}_0 + \overline{\alpha}_0^2 A_0 I(\delta), \tag{8.0.20a}$$

$$\mathrm{Re}\{G_1\} \sim \frac{\overline{\alpha}_0 \,\mathrm{Im}\{A_1\}\lambda_-^{(0)}}{\delta}(r-\delta), \quad \mathrm{Im}\{P_1\} \to \mathrm{Im}\left\{P_+^{(1)}\right\} + \overline{\alpha}_0^2 \,\mathrm{Im}\{A_1\} I(\delta). \tag{8.0.20b}$$

Upper inviscid shear layer

The inviscid shear region here is largely the same as its analogue in the upper branch structure (see figure 7.1.1 of Section 7.1).

In order to have a critical layer in this region, the basic velocity must be of the same order as the disturbance wavespeed. Since $U_0 \sim \lambda_+^{(0)}(1-r)$ here and $c = O(\epsilon^2)$ (8.0.15), we require $(1-r) = O(\epsilon^2)$ and write $r = 1 - \epsilon^2 Y_+$. In view of the matching conditions (8.0.19), the flow quantities are then expanded as

$$\hat{u} = u_+^{(0)} + \cdots, \quad \hat{v} = -\epsilon^3 v_+^{(0)} - \epsilon^5 v_+^{(1)} + \cdots, \quad \hat{p} = \epsilon^2 p_+^{(0)} + \epsilon^4 p_+^{(1)} + \cdots. \tag{8.0.21}$$

Substituting the expansions (8.0.21) into (2.3.11), to leading order our governing equations are given by (7.1.14), with α_0 and c_0 replaced with $\overline{\alpha}_0$ and $\overline{c}_0$ respectively. Solving these subject to matching the core (8.0.19), we find that the expansion terms are given by

$$u_+^{(0)} = -A_0\lambda_+^{(0)}, \qquad v_+^{(0)} = \mathrm{i}\overline{\alpha}_0 A_0\left(\lambda_+^{(0)} Y_+ - \overline{c}_0\right) - \frac{\mathrm{i}\overline{\alpha}_0 \hat{P}_0}{\lambda_+^{(0)}}, \qquad p_+^{(0)} = \hat{P}_0. \tag{8.0.22}$$

We apply a condition of zero normal flow as $Y_+ \to 0$, and consequently obtain our first displacement-pressure relationship,

$$A_0\overline{c}_0 + \frac{\hat{P}_0}{\lambda_+^{(0)}} = 0. \tag{8.0.23}$$

Since $u_+^{(0)}$ and $p_+^{(0)}$ are constant with respect to Y_+, these quantities remain order one as we approach the outer cylinder.

At the next order, the substitution of (8.0.21) into (2.3.11) yields the governing equations (7.1.18), where α_0, α_1, c_0 and c_1 are replaced with analogous barred variables. Taking into account the matching conditions (8.0.19), we introduce $\zeta_+ = \lambda_+^{(0)} Y_+ - \overline{c}_0$ and obtain the solutions

$$p_+^{(1)} = P_+, \tag{8.0.24a}$$

$$v_+^{(1)} = \mathrm{i}\overline{\alpha}_0 A_+^{(1)}\zeta_+ - \frac{\mathrm{i}\overline{\alpha}_0 P_+}{\lambda_+^{(0)}} - \frac{\mathrm{i}\overline{\alpha}_0\hat{P}_0}{\lambda_+^{(0)}}\left(\frac{2\lambda_+^{(10)}}{{\lambda_+^{(0)}}^2} + \frac{1}{\lambda_+^{(0)}}\right)\zeta_+\log(\zeta_+) + \text{imaginary terms}, \quad \zeta_+ \neq 0 \tag{8.0.24b}$$

where $A_+^{(1)}$ is an unknown complex constant and

$$\mathrm{Im}(P_+) = \mathrm{Im}\left\{P_+^{(1)}\right\}. \tag{8.0.25}$$

A critical layer manifests where $\zeta_+ = 0$ to smooth out the singularity that arises in the logarithmic term of $v_+^{(1)}$. As we cross the critical layer, there exists a phase jump of magnitude π in the logarithmic term. We express this by writing $\log(\zeta_+) = \log|\zeta_+|$ for $\zeta_+ > 0$, and $\log(\zeta_+) = \log|\zeta_+| - \mathrm{i}\pi$ for $\zeta_+ < 0$. The details of such layers have been studied by, for example, Lin [15], Stuart [16] and Reid [17].

In order to find a relation between the constants A_1 and $A_+^{(1)}$, we impose matching between the real part of G_1 as $r \to 1$ in the core (8.0.19b) and the real part of $v_+^{(1)}$ (8.0.24b) as $Y_+ \to \infty$ in the inviscid shear layer. This gives

$$\mathrm{Im}\left\{A_+^{(1)}\right\} = \mathrm{Im}\{A_1\}. \tag{8.0.26}$$

It will be useful to determine the behaviour of $v_+^{(1)}$ as we approach the outer cylinder.

In consideration of (8.0.26) and the phase shift mentioned above, we find that

$$\mathrm{Re}\Big\{v_+^{(1)}\Big\} \to \frac{\overline{\alpha}_0\bar{c}_0\hat{P}_0}{\lambda_+^{(0)}}\left(\frac{2\lambda_+^{(10)}}{\lambda_+^{(0)2}}+\frac{1}{\lambda_+^{(0)}}\right)\pi+\overline{\alpha}_0\bar{c}_0\,\mathrm{Im}\{A_1\}+\frac{\overline{\alpha}_0\,\mathrm{Im}\Big\{P_+^{(1)}\Big\}}{\lambda_+^{(0)}} \quad \text{as} \quad Y_+\to 0. \tag{8.0.27}$$

Thus far, our analysis has not differed from that of the upper-branch structure. This will no longer be the case in the upper viscous wall layer, which we study presently.

Upper viscous wall layer

The quantities $\hat{u}$ and $\hat{p}$ approach the viscous layer with orders 1 and ϵ^2 respectively, as seen from the expansions (8.0.21) and solutions (8.0.22). Motivated by this, we take $\hat{u}=O(1)$ and $\hat{p}=O(\epsilon^2)$ in this region.

We also enforce a dominant balance between the inertia and viscous terms in the axial momentum equation (2.3.11b). Letting $\tilde{q}$ denote the thickness of the layer, we see that

$$\mathrm{i}\alpha\,(U_0-c)\,\hat{u}\sim\frac{1}{R}\frac{\mathrm{d}^2\hat{u}}{\mathrm{d}r^2} \tag{8.0.28}$$

gives

$$\tilde{q}\sim\epsilon^5 \tag{8.0.29}$$

since $\alpha=O(\epsilon)$, $c=O(\epsilon^2)$ (8.0.15) and the base velocity is much smaller than the disturbance wavespeed in this region. The wall layer here is thus thinner than the upper viscous wall layer of the upper-branch structure, which had thickness $R^{-4/11}$ (see figure 7.1.1). The continuity equation (2.3.11a) then suggests that $\alpha\hat{u}\sim{}^{\hat{v}}\!/_{\tilde{q}}$, yielding

$$\hat{v}\sim\epsilon^6. \tag{8.0.30}$$

Under consideration of (8.0.21) and (8.0.27), it may appear that the normal velocity in the inviscid shear layer approaches the viscous layer with an order of ϵ^5. To resolve the mismatch of scalings as suggested by (8.0.30), it must be the case that $\mathrm{Re}\Big\{v_+^{(1)}\Big\}\to 0$ as $Y_+\to 0$ in the inviscid shear region. Thus we have

$$\frac{\bar{c}_0\hat{P}_0}{\lambda_+^{(0)}}\left(\frac{2\lambda_+^{(10)}}{\lambda_+^{(0)2}}+\frac{1}{\lambda_+^{(0)}}\right)\pi+\bar{c}_0\,\mathrm{Im}\{A_1\}+\frac{\mathrm{Im}\Big\{P_+^{(1)}\Big\}}{\lambda_+^{(0)}}=0 \tag{8.0.31}$$

upon use of (8.0.27). This expression provides us with our second displacement-pressure relationship.

This completes our analysis for the upper layers of the hybrid structure.

Next, we explore the lower viscous layer and seek further relations relating the unknown constants $\hat{P}_0$, $P_+^{(1)}$, A_0 and A_1.

Lower viscous wall layer

We will see that the dynamics of this viscous layer will have some resemblance to the lower-branch structure. In this region, we have

$$U_0 - c \sim \lambda_-^{(0)}(r-\delta) + \epsilon^2\left(\overline{V}_0 - \overline{c}_0\right) - \epsilon^4\overline{c}_1. \tag{8.0.32}$$

Recalling that $\overline{V}_0 = \overline{c}_0$ (8.0.15), the existence of a critical layer requires that $(r-\delta) = O(\epsilon^4)$ and so we write $r = \delta + \epsilon^4 y_-$ for an order one variable y_-. This is as expected from (8.0.6) and (8.0.10). To enable us to find the disturbance expansions in this region, we recall the behaviour of the core disturbance as $r \to \delta$ (8.0.20):

$$F_0 \to \frac{A_0\lambda_-^{(0)}}{\delta}, \qquad G_0 \sim -\epsilon^4\frac{\mathrm{i}\overline{\alpha}_0 A_0\lambda_-^{(0)}}{\delta}y_-, \qquad P_0 \to \hat{P}_0 + \overline{\alpha}_0{}^2 A_0 I(\delta). \tag{8.0.33a}$$

In view of the core expansions (8.0.17), this motivates the scalings

$$\hat{u} = u_-^{(0)}, \quad \hat{v} = \epsilon^5 v_-^{(0)}, \quad \hat{p} = \epsilon^2 p_-^{(0)} + \epsilon^4 p_-^{(1)}, \tag{8.0.34}$$

which evoke the dominant balances $\mathrm{i}\alpha\hat{u} \sim \hat{v}'$ in the continuity equation (2.3.11a) and $\alpha(U_0 - c)\hat{u} \sim R^{-1}\hat{u}''$ in the momentum equation (2.3.11b). Substituting (8.0.34) into the linearised disturbance equations (2.3.11) gives

$$p_-^{(0)} = 0 \tag{8.0.35}$$

and, upon matching with the core (8.0.33), unveils the relation

$$\hat{P}_0 = -\overline{\alpha}_0{}^2 A_0 I(\delta). \tag{8.0.36}$$

In conjunction with (8.0.23), the relation (8.0.36) explicitly relates $\overline{\alpha}_0$ to $\overline{c}_0$, and defines the leading order wavenumber term to be

$$\overline{\alpha}_0 = \left(\frac{\overline{c}_0\lambda_+^{(0)}}{I(\delta)}\right)^{1/2}. \tag{8.0.37}$$

Since $\overline{c}_0 = \overline{V}_0$ (8.0.15), we can write

$$\overline{\alpha}_0 = \left(\frac{\overline{V}_0\lambda_+^{(0)}}{I(\delta)}\right)^{1/2}, \qquad \overline{c}_0 = \overline{V}_0. \tag{8.0.38}$$

This is consistent with the upper-branch behaviour (8.0.2) in the limit $V_0 \to \infty$. We remark that the leading order disturbance wavenumber and wavespeed are independent of the cylinder compliance, and the expressions (8.0.38) are identical to that which was found in the rigid case by Walton [1].

We now seek to understand how compliance affects the hybrid structure, and we aim for an eigenrelation for the wavespeed correction c_1.

From substitution of (8.0.34) into the linearised disturbance equations (2.3.11), we further learn that the next order pressure term $p_-^{(1)}$ does not vary in y_-. Matching to the core disturbance (8.0.20b), we specifically have

$$\mathrm{Im}\left\{p_-^{(1)}\right\} = \mathrm{Im}\left\{P_+^{(1)}\right\} + \overline{\alpha}_0{}^2\,\mathrm{Im}\{A_1\}I(\delta). \tag{8.0.39}$$

Before continuing, it is worthwhile to rewrite $\mathrm{Im}\left\{p_-^{(1)}\right\}$ using (8.0.31) and (8.0.38). After some manipulation, we obtain

$$\mathrm{Im}\{p_-^{(1)}\} = -\hat{P}_0\overline{V}_0\left(\frac{2\lambda_+^{(10)}}{\lambda_+^{(0)\,2}} + \frac{1}{\lambda_+^{(0)}}\right)\pi. \tag{8.0.40}$$

Using (8.0.36) to write $\hat{P}_0$ in terms of A_0, this reveals

$$\mathrm{Im}\{p_-^{(1)}\} = \overline{\alpha}_0{}^2 I(\delta)\overline{V}_0 A_0\left(\frac{2\lambda_+^{(10)}}{\lambda_+^{(0)\,2}} + \frac{1}{\lambda_+^{(0)}}\right)\pi. \tag{8.0.41}$$

In the analysis that follows, we will seek a second relation between $\mathrm{Im}\{p_-^{(1)}\}$ and A_0.

The substitution of (8.0.34) into (2.3.11) also elicits the pair of coupled equations

$$\mathrm{i}\overline{\alpha}_0 u_-^{(0)} + \frac{\mathrm{d}v_-^{(0)}}{\mathrm{d}y_-} = 0, \tag{8.0.42a}$$

$$\mathrm{i}\overline{\alpha}_0\left(\lambda_-^{(0)}y_- - \overline{c}_1\right)u_-^{(0)} + \lambda_-^{(0)}v_-^{(0)} = -\mathrm{i}\overline{\alpha}_0 p_-^{(1)} + \frac{\mathrm{d}^2u_-^{(0)}}{\mathrm{d}y_-^2}, \tag{8.0.42b}$$

which are reminiscent of the lower-branch analysis and enable us to find the leading order velocity terms. With (8.0.33) in mind, these are to be solved subject to the matching condition

$$u_-^{(0)} \to \frac{A_0\lambda_-^{(0)}}{\delta} \quad \text{as} \quad Y_+ \to \infty. \tag{8.0.43}$$

After some manipulation, the coupled equations (8.0.42) can be combined to yield a third-order differential equation given by

$$\frac{\mathrm{d}^3u_-^{(0)}}{\mathrm{d}y_-^3} - \mathrm{i}\overline{\alpha}_0\left(\lambda_-^{(0)}y_- - \overline{c}_1\right)\frac{\mathrm{d}u_-^{(0)}}{\mathrm{d}y_-} = 0. \tag{8.0.44}$$

Upon making the substitution $\tau = \frac{\mathrm{d}u_-^{(0)}}{\mathrm{d}y_-}$, this reduces to a second-order equation in τ. Next, we perform a linear change of variables with $\xi = ay_- + b$, where

$$a = \left(\mathrm{i}\overline{\alpha}_0\lambda_-^{(0)}\right)^{1/3} \quad \text{and} \quad b = -\frac{\mathrm{i}\overline{\alpha}_0\bar{c}_1}{\left(\mathrm{i}\overline{\alpha}_0\lambda_-^{(0)}\right)^{2/3}}. \tag{8.0.45}$$

Under this transformation, (8.0.44) becomes the well-known Airy equation,

$$\frac{\mathrm{d}^2\tau}{\mathrm{d}\xi^2} - \xi\tau = 0. \tag{8.0.46}$$

It is reasonable to expect that τ remains bounded as $\xi \to \infty$, and this leads us to the solution

$$\frac{\mathrm{d}u_-^{(0)}}{\mathrm{d}y_-} = C \cdot \mathrm{Ai}(\xi), \tag{8.0.47}$$

where C is a constant to be determined and Ai is the Airy function of the first kind. Integrating this differential equation with respect to y_- and subsequently imposing the matching condition (8.0.43) reveals that

$$C = \frac{a}{\kappa(b)}\left(\frac{A_0\lambda_-^{(0)}}{\delta} - u_-^{(0)}(0)\right), \tag{8.0.48}$$

and hence $u_-^{(0)}$ is found to possess the solution

$$u_-^{(0)}(y_-) = \frac{1}{\kappa(b)}\left(\frac{A_0\lambda_-^{(0)}}{\delta} - u_-^{(0)}(0)\right)\int_b^\xi \mathrm{Ai}(\xi)\mathrm{d}\xi + u_-^{(0)}(0), \qquad \kappa(b) = \int_b^\infty \mathrm{Ai}(\xi)\mathrm{d}\xi. \tag{8.0.49}$$

Differentiating this twice with respect to y_-, we note that

$$\frac{\mathrm{d}^2u_-^{(0)}}{\mathrm{d}y_-^2} = \frac{\left(\mathrm{i}\overline{\alpha}_0\lambda_-^{(0)}\right)^{2/3}}{\kappa(b)}\left(\frac{A_0\lambda_-^{(0)}}{\delta} - u_-^{(0)}(0)\right)\mathrm{Ai}'(\xi). \tag{8.0.50}$$

Thus far, the effects of flexibility have not entered the hybrid structure. The boundary conditions (2.3.13, 2.3.14) on the inner cylinder, which are

$$\mathrm{i}\alpha\left(V - c\right)\hat{u}(\delta) + \hat{v}(\delta)U_0'(\delta) = 0, \tag{8.0.51a}$$

$$\hat{p}(\delta) = \frac{2}{R}\hat{v}'(\delta) + \left(-\alpha^2c^2m + \frac{K}{R^2}\right)\frac{\hat{u}(\delta)}{U_0{}'(\delta)}, \tag{8.0.51b}$$

allow us to determine the sizes of K and m that enable the compliance of the cylinder to penetrate the structure at leading order. We wish to evoke the balance

$$\hat{p}(\delta) \sim R^{-2}K\hat{u}(\delta) \sim \alpha^2c^2m\hat{u}(\delta) \tag{8.0.52}$$

in (8.0.51b).

From the scalings (8.0.15), (8.0.16) and (8.0.34), we note that $R^{-2} = \epsilon^{26}$, $\alpha^2 c^2 = O(\epsilon^6)$, $\hat{u} = O(1)$ and $\hat{p} = O(\epsilon^4)$, since $p_-^{(0)} = 0$ (8.0.35). We therefore prescribe

$$K = O(\epsilon^{-22}), \quad m = O(\epsilon^{-2}), \tag{8.0.53}$$

which is as suggested in (8.0.15), and write $K = \epsilon^{-22}\overline{K}_0$ and $m = \epsilon^{-2}\overline{m}_0$ for order one quantities $\overline{K}_0$ and $\overline{m}_0$. With this scaling, the conditions (8.0.51) at leading order are expressed as

$$u_-^{(0)}(0) = \frac{\lambda_-^{(0)}}{\overline{K}} p_-^{(1)}, \tag{8.0.54a}$$

$$-\mathrm{i}\overline{\alpha}_0 \bar{c}_1 u_-^{(0)}(0) + \lambda_-^{(0)} v_-^{(0)}(0) = 0, \tag{8.0.54b}$$

with $\overline{K} = \overline{K}_0 - \overline{\alpha}_0^2\, \bar{c}_0^2\, \overline{m}_0$. Recall that $p_-^{(1)}$ is constant in y_-, so that $p_-^{(1)}(0) = p_-^{(1)}$. The axial momentum equation (8.0.42b) evaluated at $y_- = 0$ allows us to form another relationship on the boundary:

$$-\mathrm{i}\overline{\alpha}_0 \bar{c}_1 u_-^{(0)}(0) + \lambda_-^{(0)} v_-^{(0)}(0) = -\mathrm{i}\overline{\alpha}_0 p_-^{(1)} + \left.\frac{\mathrm{d}^2 u_-^{(0)}}{\mathrm{d}y_-^2}\right|_{y_-=0} \tag{8.0.55a}$$

Using the kinematic condition (8.0.54b) and our expression for the second derivative of $u_-^{(0)}$ (8.0.50), this simplifies to

$$\mathrm{i}\overline{\alpha}_0 p_-^{(1)} = \frac{\left(\mathrm{i}\overline{\alpha}_0 \lambda_-^{(0)}\right)^{2/3}}{\kappa(b)} \left(\frac{A_0 \lambda_-^{(0)}}{\delta} - u_-^{(0)}(0) \right) \mathrm{Ai}'(b). \tag{8.0.56}$$

We introduce a variable s_- such that $b = -\mathrm{i}^{1/3} s_-$ and recall the function $g(s_-)$ is defined as

$$g(s_-) = \mathrm{i}^{5/3}\, \frac{\mathrm{Ai}'(-\mathrm{i}^{1/3} s_-)}{\kappa(-\mathrm{i}^{1/3} s_-)}. \tag{8.0.57}$$

Expressing $u_-^{(0)}(0)$ in terms of $p_-^{(1)}$ using (8.0.54a), we now write (8.0.56) as

$$p_-^{(1)} \left[\frac{{\lambda_-^{(0)}}^{5/3}}{\overline{K}} g(s_-) - {\overline{\alpha}_0}^{1/3} \right] = \frac{{\lambda_-^{(0)}}^{5/3} A_0}{\delta} g(s_-) \tag{8.0.58}$$

upon use of (8.0.57) and rearrangement of the resulting relation.

We recall that we have an expression that relates the imaginary part of $p_-^{(1)}$ with A_0 (8.0.41). Our goal now is to use (8.0.58) to form a second such relation, also without the involvement of the real part of $p_-^{(1)}$. To this end, we let

$$Z_1 = p_-^{(1)}, \quad Z_2 = \frac{{\lambda_-^{(0)}}^{5/3}}{\overline{K}} g(s_-) - {\overline{\alpha}_0}^{1/3}, \quad Z_3 = \frac{{\lambda_-^{(0)}}^{5/3} A_0}{\delta} g(s_-), \tag{8.0.59}$$

and we rewrite equation (8.0.58) in the form

$$Z_1 Z_2 = Z_3. \tag{8.0.60}$$

We take the real and imaginary parts of this complex equation to form two separate real-valued equations. An appropriate linear combination of these allows us to form the relation

$$\mathrm{Im}\{Z_1\}\,\mathrm{Re}\{Z_2\} + \left(\frac{\mathrm{Re}\{Z_3\} + \mathrm{Im}\{Z_1\}\,\mathrm{Im}\{Z_2\}}{\mathrm{Re}\{Z_2\}}\right)\mathrm{Im}\{Z_2\} = \mathrm{Im}\{Z_3\}, \tag{8.0.61}$$

which is independent of $\mathrm{Re}\{Z_1\}$, as desired. Before continuing, we revisit our expression for $\mathrm{Im}\{p_-^{(1)}\}$ (8.0.41) to write

$$\mathrm{Im}\{Z_1\} = \overline{\alpha}_0{}^2 I(\delta)\overline{V}_0 A_0 \left(\frac{2\lambda_+^{(10)}}{\lambda_+^{(0)\,2}} + \frac{1}{\lambda_+^{(0)}}\right)\pi. \tag{8.0.62}$$

Substitution of the expressions (8.0.59) and (8.0.62) into (8.0.61) culminates in the hybrid eigenrelation

$$\overline{V}_0^2\pi\left(\frac{2\lambda_+^{(10)}}{\lambda_+^{(0)}} + 1\right)\left(\frac{\lambda_-^{(0)\,10/3}}{\overline{K}^2}(\mathrm{Im}\{g(s_-)\})^2 + \left[\frac{\lambda_-^{(0)\,5/3}}{\overline{K}}\,\mathrm{Re}\{g(s_-)\} - \left(\frac{\lambda_+^{(0)}}{I(\delta)}\right)^{1/6}\overline{V}_0^{1/6}\right]^2\right)$$
$$+\frac{\lambda_-^{(0)\,5/3}}{\delta}\,\mathrm{Im}\{g(s_-)\}\overline{V}_0^{1/6}\left(\frac{\lambda_+^{(0)}}{I(\delta)}\right)^{1/6} = 0 \tag{8.0.63}$$

after simplification with (8.0.38), with $g(s_-)$ defined in (8.0.57) and

$$\overline{K} = \overline{K}_0 - \frac{\lambda_+^{(0)}\,\overline{V}_0^3}{I(\delta)}\,\overline{m}_0. \tag{8.0.64}$$

Fixing $\overline{V}_0$, $\overline{K}_0$, $\overline{m}_0$ and δ, we wish to solve the above relation numerically for s_-. To achieve this, we plot the left-hand side of (8.0.63) as a function of s_- and graphically determine for which approximate values of s_- the left-hand side of (8.0.63) is zero. These provide initial guesses for the roots of the eigenrelation, and we refine these using a MATLAB solver.

Once we have obtained the roots s_- of (8.0.63), we are able to find the wavespeed correction c_1 as follows. Recalling that $b = -\mathrm{i}^{1/3}s_-$, with b defined in (8.0.45), s_- takes the form

$$s_- = \frac{\overline{\alpha}_0\overline{c}_1}{\left(\overline{\alpha}_0\lambda_-^{(0)}\right)^{2/3}}. \tag{8.0.65}$$

Rearranging this and using (8.0.38), we find the wavespeed correction $\bar{c}_1$ to be

$$\bar{c}_1 = \frac{s_- {\lambda_-^{(0)}}^{2/3}}{{\overline{\alpha}_0}^{1/3}} = \frac{s_- {\lambda_-^{(0)}}^{2/3}}{{\overline{V}_0}^{1/6}} \left(\frac{I(\delta)}{\lambda_+^{(0)}} \right)^{1/6}. \tag{8.0.66}$$

To obtain the rigid analogue of eigenrelation (8.0.63), we examine the relation as $\overline{K} \to \infty$ with $\overline{\alpha}_0 = O(1)$, $\bar{c}_1 = O(1)$ and $\overline{V}_0 = O(1)$. In this limit, (8.0.63) reduces to

$$\overline{V}_0^{13/6} = -\left(\frac{\lambda_+^{(0)}}{I(\delta)} \right)^{-1/6} \frac{{\lambda_-^{(0)}}^{5/3}}{\pi\delta} \left(\frac{2\lambda_+^{(10)}}{\lambda_+^{(0)}} + 1 \right)^{-1} \mathrm{Im}(g(s_-)) \tag{8.0.67}$$

upon rearrangement, which is precisely that which was found in the rigid case by Walton [1].

For fixed $\delta = 0.6$, figure 8.0.2 depicts solutions $\bar{c}_1$ of the rigid eigenrelation (8.0.66), (8.0.67) as $\overline{V}_0$ varies. For comparison, we also illustrate solutions $\bar{c}_1$ of the flexible eigenrelation (8.0.63), (8.0.66) against $\overline{V}_0$ for the values $\overline{K} = 5$ and $\overline{K} = 10$. For the rigid case, Walton [1] found that there exists a critical value of $\overline{V}_0$, say $\overline{V}_c$, beyond which there exist no solutions for the hybrid mode. Below this velocity, there typically exists two solutions for $\bar{c}_1$, though there is a small range of $\overline{V}_0$ where four solutions exist. We observe that the general structure of the solution is unchanged as we decrease $\overline{K}$ from the rigid limit, however the critical velocity $\overline{V}_c$ decreases with $\overline{K}$. We emphasise that we have considered only positive values of $\overline{K}$ here.

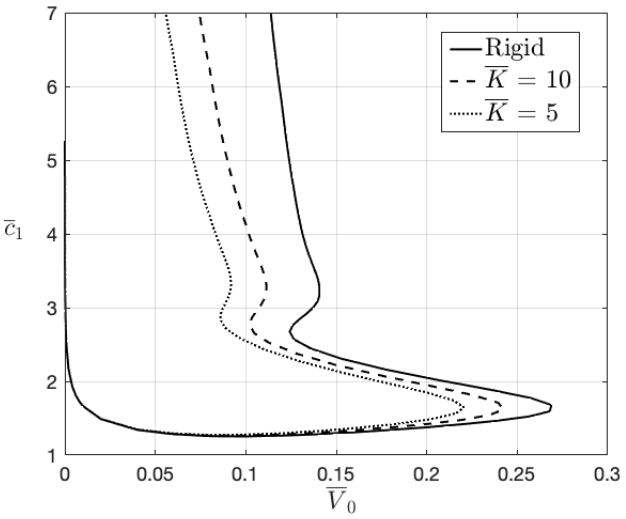

Figure 8.0.2: Fixing $\delta = 0.6$, each curve in this figure depicts solutions of the eigenrelation (8.0.63) for fixed $\overline{K}$ as $\overline{V}_0$ varies. This is done for two choices of $\overline{K}$. The rigid solution is included for comparison.

In summary, we have considered a so-called hybrid asymptotic structure whose lower and upper layers are reminiscent of a lower-branch-type and an upper-branch-type structure respectively. To conclude this chapter, we recall that the compliance of the inner cylinder does not affect the leading order wavenumber or wavespeed of neutral modes belonging to this hybrid structure. This is unlike the situation with the lower-branch and upper-branch modes. We did find, however, that the critical value $\overline{V}_c$ below which there exists a solution on this scaling is influenced by the value of $\overline{K}$.

In the next chapter, we will compare results from the asymptotic analysis in Chapters 6-8 with stability regions obtained numerically from the circular Orr-Sommerfeld equation (2.4.3).

Chapter 9

Comparisons of numerical and asymptotic results

In this chapter, we compare the results from our asymptotic analysis with those from our numerical computations, anticipating that agreement between the two approaches improves as the Reynolds number R becomes large. We begin by reviewing our asymptotic findings and then discuss how these can be used to predict neutral curves in the (R, α) plane for a given radius ratio δ, sliding velocity V, spring stiffness K and mass m.

9.1 Summary of asymptotic results

To recapitulate the work done in Chapters 6-8, we have established five distinguished scalings for the wavenumber α and wavespeed c associated with the linearised disturbance problem (2.3.11) subject to the flexibility conditions (2.3.12, 2.3.13, 2.3.14). We briefly recollect these below.

S1. (Chapter 6, Section 6.1). The three-zone lower-branch scaling with

$$\alpha = R^{-1/7}\alpha_0 + \cdots, \quad c = R^{-2/7}c_0 + \cdots, \tag{9.1.1a}$$

$$V = R^{-2/7}V_0, \quad K = R^{12/7}K_0, \quad m = R^{4/7}m_0, \tag{9.1.1b}$$

has the associated eigenrelation (6.1.50), which we repeat below:

$$\frac{\left(\lambda_-^{(0)}\right)^{5/3} g(s_-)}{\tilde{K}}\left[\alpha_0^{7/3} I(\delta) + \left(\lambda_+^{(0)}\right)^{5/3} g(s_+)\right] = \alpha_0^{1/3}\left[\alpha_0^{7/3} I(\delta) + \left(\lambda_+^{(0)}\right)^{5/3} g(s_+) + \frac{\left(\lambda_-^{(0)}\right)^{5/3} g(s_-)}{\delta}\right], \quad (9.1.2)$$

with $\widetilde{K}$ defined as

$$\widetilde{K} = K_0 - \alpha_0^2 c_0^2 m_0, \quad (9.1.3)$$

and the function g defined in (6.1.47) as

$$g(s) = \mathrm{i}^{5/3}\frac{\mathrm{Ai}'(-\mathrm{i}^{1/3}s)}{\kappa(-\mathrm{i}^{1/3}s)}. \quad (9.1.4)$$

The variables s_+ and s_- are given by (6.1.48),

$$s_+ = \frac{\alpha_0 c_0}{\left(\alpha_0 \lambda_+^{(0)}\right)^{2/3}} \quad \text{and} \quad s_- = \frac{\alpha_0\left(c_0 - V_0\right)}{\left(\alpha_0 \lambda_-^{(0)}\right)^{2/3}}. \quad (9.1.5)$$

For $V \neq 0$, it is convenient to write this in the form (6.1.52), which is

$$\mathrm{t}(s_+, s_-)\left[(\mathrm{t}(s_+, s_-))^7 I(\delta) + \frac{1}{\delta} {V_0}^7 \left(\lambda_-^{(0)}\right)^{5/3} g(s_-) + {V_0}^7 \left(\lambda_+^{(0)}\right)^{5/3} g(s_+)\right] = \frac{1}{\widetilde{K}}\left[(\mathrm{t}(s_+, s_-))^7 I(\delta) V_0 \left(\lambda_-^{(0)}\right)^{5/3} g(s_-) + {V_0}^8 \left(\lambda_+^{(0)}\right)^{5/3}\left(\lambda_-^{(0)}\right)^{5/3} g(s_+) g(s_-)\right], \quad V_0 \neq 0, \quad (9.1.6)$$

where

$$\mathrm{t}(s_+, s_-) = \left(\lambda_+^{(0)}\right)^{2/3} s_+ - \left(\lambda_-^{(0)}\right)^{2/3} s_- \quad (9.1.7)$$

and

$$\widetilde{K} = K_0 - \frac{{s_+}^2 \left(\lambda_+^{(0)}\right)^{4/3} (\mathrm{t}(s_+, s_-))^4}{{V_0}^4} m_0. \quad (9.1.8)$$

The rigid analogues of (9.1.2) and (9.1.6) are respectively given by

$$\alpha_0^{7/3} I(\delta) + \left(\lambda_+^{(0)}\right)^{5/3} g(s_+) + \frac{\left(\lambda_-^{(0)}\right)^{5/3} g(s_-)}{\delta} = 0, \quad (9.1.9)$$

and, with $V_0 \neq 0$,

$$\left(\left(\lambda_+^{(0)}\right)^{2/3} s_+ - \left(\lambda_-^{(0)}\right)^{2/3} s_-\right)^7 I(\delta) + {V_0}^7\left(\frac{1}{\delta}\left(\lambda_-^{(0)}\right)^{5/3} g(s_-) + \left(\lambda_+^{(0)}\right)^{5/3} g(s_+)\right) = 0, \quad (9.1.10)$$

as seen in Walton [1].

S2. (Chapter 6, Section 6.2). A three-zone lower-branch structure emerges for neutral modes with $K - \alpha^2 c^2 m < 0$. This has the scalings

$$\alpha = \overline{\alpha}_0 + \cdots, \quad c = R^{-1/3}\,\overline{c}_0 + \cdots, \quad V = R^{-1/3}\,\overline{V}_0, \quad K = R^{5/3}\,\overline{K}_0, \quad m = R^{1/3}\,\overline{m}_0. \tag{9.1.11a}$$

The leading order wavenumber and wavespeed can be determined through the relations (6.2.36), (6.2.38):

$$\overline{\alpha}_0{}^{1/3} = \frac{\left(\lambda_-^{(0)}\right)^{5/3}}{\overline{K_0} - \overline{\alpha}_0{}^2\overline{c}_0{}^2\overline{m}_0}\, g(s_0), \qquad \overline{c}_0 = \overline{V}_0 + \frac{\lambda_-^{(0)\,2/3} s_0}{\overline{\alpha}_0{}^{1/3}}, \tag{9.1.12}$$

where $s_0 \approx 2.2972$ is such that $\mathrm{Im}(g(s_0)) = 0$.

S3. (Chapter 7, Section 7.1). The five-zone upper-branch structure consisting of two critical layers has $c > V$ with the scalings

$$\alpha = R^{-1/11}\alpha_0 + \cdots, \quad c = R^{-2/11}c_0 + \cdots, \tag{9.1.13a}$$

$$V = R^{-2/11}V_0, \quad K = R^{20/11}K_0, \quad m = R^{4/11}m_0. \tag{9.1.13b}$$

The eigenrelation arising from this structure is given by

$$\begin{aligned}\frac{\lambda_+^{(0)}}{c_0\sqrt{2\alpha_0 c_0}} - \frac{\gamma}{(c_0 - V_0)\sqrt{2\alpha_0\,(c_0 - V_0)}}\left(1 - \frac{\alpha_0{}^2 I(\delta)}{c_0\lambda_+^{(0)}}\right) \\ - \frac{\gamma}{\lambda_-^{(0)}}\left(1 - \frac{\alpha_0{}^2 I(\delta)}{c_0\lambda_+^{(0)}}\right)\left(\frac{2\lambda_-^{(10)}}{\lambda_-^{(0)\,2}} - \frac{1}{\delta\lambda_-^{(0)}}\right)(c_0 - V_0)\,\pi + \left(\frac{2\lambda_+^{(10)}}{\lambda_+^{(0)\,2}} + \frac{1}{\lambda_+^{(0)}}\right)c_0\pi = 0,\end{aligned} \tag{9.1.14}$$

which is to be solved in conjunction with the relation

$$\alpha_0{}^2 = \frac{(c_0 - V_0)\,\gamma}{\delta I(\delta)} + \frac{c_0\lambda_+^{(0)}}{I(\delta)}, \tag{9.1.15}$$

where

$$\gamma = \left(\frac{1}{\lambda_-^{(0)}} + \frac{c_0 - V_0}{\widetilde{K}}\right)^{-1}, \qquad \widetilde{K} = K_0 - \alpha_0^2 c_0^2 m_0. \tag{9.1.16}$$

These are equations (7.1.73), (7.1.74) and (7.1.75) of Section 7.1. In the rigid scenario, the appropriate relations to solve are detailed by Walton [1], and are given by (9.1.14) and (9.1.15) with γ now defined as

$$\gamma = \lambda_-^{(0)}. \tag{9.1.17}$$

S4. (Chapter 7, Section 7.2). Similar to structure *S3*, this upper-branch structure also comprises of five zones. The distinguishing feature between the two structures is the size of the disturbance wavespeed in relation to the cylinder sliding velocity. For this structure with only one critical layer, we have $c < V$. The scalings are unchanged from *S3*, so we have

$$\alpha = R^{-1/11}\alpha_0 + \cdots, \quad c = R^{-2/11}c_0 + \cdots, \tag{9.1.18a}$$

$$V = R^{-2/11}V_0, \quad K = R^{20/11}K_0, \quad m = R^{4/11}m_0. \tag{9.1.18b}$$

The eigenrelation pertaining to this structure is a modification of that of *S3*, owing to the lack of a critical layer near the inner cylinder. The leading order wavenumber and wavespeed are related by the equations

$$-\frac{\lambda_+^{(0)}}{c_0\sqrt{2\alpha_0 c_0}} + \frac{\gamma}{(V_0 - c_0)\sqrt{2\alpha_0\,(V_0 - c_0)}}\left(1 - \frac{{\alpha_0}^2 I(\delta)}{c_0\lambda_+^{(0)}}\right) = \left(\frac{2\lambda_+^{(10)}}{{\lambda_+^{(0)}}^2} + \frac{1}{\lambda_+^{(0)}}\right)c_0\pi \tag{9.1.19}$$

and

$${\alpha_0}^2 = \frac{(c_0 - V_0)\,\gamma}{\delta I(\delta)} + \frac{c_0\lambda_+^{(0)}}{I(\delta)}, \tag{9.1.20}$$

where

$$\gamma = \left(\frac{1}{\lambda_-^{(0)}} + \frac{c_0 - V_0}{\widetilde{K}}\right)^{-1}, \qquad \widetilde{K} = K_0 - \alpha_0^2\, c_0^2\, m_0. \tag{9.1.21}$$

These are equations (7.2.36) and (7.2.35) of Section 7.2. As discussed in Section 7.2, this structure has no rigid counterpart.

S5. (Chapter 8). The last of our discussed structures, the hybrid structure, was found to have scalings

$$\alpha = R^{-1/13}\,\overline{\alpha}_0 + \cdots, \quad c = R^{-2/13}\,\overline{c}_0 + R^{-4/13}\,\overline{c}_1 + \cdots, \tag{9.1.22a}$$

$$V = R^{-2/13}\,\overline{V}_0, \quad K = R^{22/13}\,\overline{K}_0, \quad m = R^{2/13}\,\overline{m}_0. \tag{9.1.22b}$$

The leading order wavenumber and wavespeed are given by

$$\overline{\alpha}_0 = \left(\frac{\overline{V}_0\lambda_+^{(0)}}{I(\delta)}\right)^{1/2}, \qquad \overline{c}_0 = \overline{V}_0. \tag{9.1.23}$$

Introducing

$$\overline{K} = \overline{K}_0 - \frac{\lambda_+^{(0)}\,\overline{V}_0^3}{I(\delta)}\,\overline{m}_0, \tag{9.1.24}$$

the wavespeed correction $\bar{c}_1$ can be found by solving

$$\overline{V}_0^2\pi\left(\frac{2\lambda_+^{(10)}}{\lambda_+^{(0)}}+1\right)\left(\frac{{\lambda_-^{(0)}}^{10/3}}{\overline{K}^2}(\mathrm{Im}\{g(s_-)\})^2+\left[\frac{{\lambda_-^{(0)}}^{5/3}}{\overline{K}}\,\mathrm{Re}\{g(s_-)\}-\left(\frac{\lambda_+^{(0)}}{I(\delta)}\right)^{1/6}\overline{V}_0^{1/6}\right]^2\right)$$
$$=-\frac{{\lambda_-^{(0)}}^{5/3}}{\delta}\,\mathrm{Im}\{g(s_-)\}\overline{V}_0^{1/6}\left(\frac{\lambda_+^{(0)}}{I(\delta)}\right)^{1/6}, \quad (9.1.25)$$

for s_- and subsequently applying the relation

$$\bar{c}_1=\frac{s_-{\lambda_-^{(0)}}^{2/3}}{{\overline{V}_0}^{1/6}}\left(\frac{I(\delta)}{\lambda_+^{(0)}}\right)^{1/6}. \quad (9.1.26)$$

These relations are (8.0.38), (8.0.63) and (8.0.66) of Chapter 8.

The rigid analogue of the hybrid structure is given by (9.1.23) and (9.1.26) with

$$\overline{V}_0^{13/6}=-\left(\frac{\lambda_+^{(0)}}{I(\delta)}\right)^{-1/6}\frac{{\lambda_-^{(0)}}^{5/3}}{\pi\delta}\left(\frac{2\lambda_+^{(10)}}{\lambda_+^{(0)}}+1\right)^{-1}\mathrm{Im}(g(s_-)), \quad (9.1.27)$$

as found by Walton [1].

9.2 Application of asymptotic results

Given a cylinder of radius ratio δ, sliding velocity V, spring stiffness K and mass m, we compute the leading order wavenumber and wavespeed of our neutral disturbance(s) at a specified Reynolds number using the relevant eigenrelation from structures *S1* - *S5* (Section 9.1). We repeat this for various large Reynolds numbers, eventually forming a predicted neutral curve in the (R,α) plane. We illustrate this by way of an example, beginning with a stationary cylinder.

Consider the numerically obtained stability regions of a rigid inner cylinder with the properties $\delta=0.7$ and $V=0$, as depicted by the shaded region in figure 9.2.1a. At large Reynolds numbers, the lower and upper branches of the neutral curve are governed by the rigid analogues of structures *S1* and *S3* respectively. The relevant eigenrelations are thus (9.1.5, 9.1.10) and (9.1.14, 9.1.15, 9.1.17), with $\alpha R^{1/7}$ and $\alpha R^{1/11}$ tending to constants on the lower and upper branches respectively [1]. When $V=0$, the lower and upper eigenrelations admit a unique solution [1].

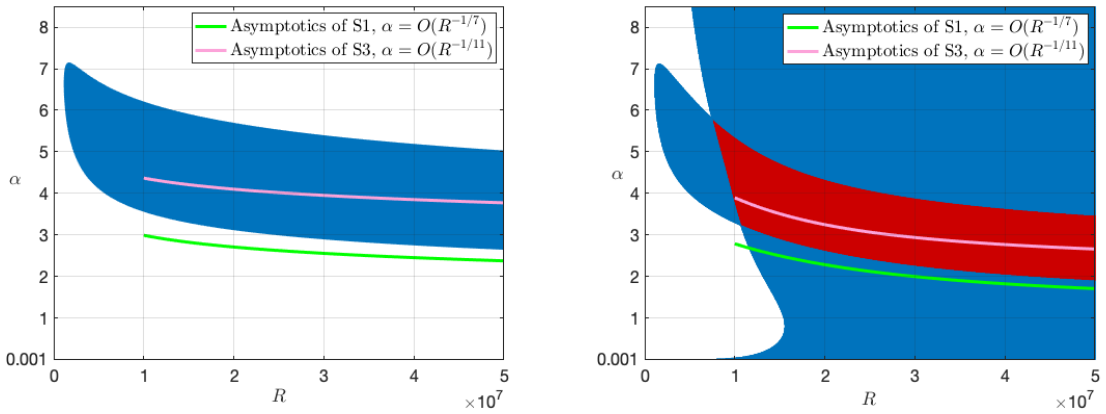

(a) Rigid cylinder with $\delta = 0.7,\ V = 0$.

(b) Flexible cylinder with $\delta = 0.7,\ V = 0,\ K = 5 \times 10^{11}$ and $m = 0.1$.

Figure 9.2.1: Comparison of numerical stability regions (shaded) with asymptotic results (pink and green curves).

In the scenario of a flexible cylinder, eigenrelations (9.1.6) and (9.1.14) describe the lower and upper branches of the neutral curve of the modified flow-based mode shown in figure 9.2.1b. The asymptotic curves pertaining to this mode when $K = 5 \times 10^{11}$ with $m = 0.1$ are illustrated in figure 9.2.1b. When solving eigenrelations (9.1.6) and (9.1.14) for a cylinder with given K and m, it is important to note that K_0 and m_0 vary along the neutral curve, according to $K_0 = R^{-12/7}K$ and $m_0 = R^{-4/7}m$ along the lower branch and $K_0 = R^{-20/11}K$ and $m_0 = R^{-4/11}m$ along the upper branch. As anticipated, agreement between the numerical and asymptotic computations increases as the Reynolds numbers becomes larger.

We note that the lower-branch asymptotic curve provides a considerably superior approximation than the upper-branch asymptotic curve. We remark that this does not seem unreasonable. In his study of the stability of plane Poiseuille flow, Reid [17] noticed the existence of a 'kink' in the upper branch of the neutral curve at a well-defined Reynolds number. He also found a similar kink in the neutral curve for the asymptotic suction boundary layer profile. Some years later, Healey [77] found the presence of a kink in the upper branch of the neutral curve describing the linear stability of a flat-plate boundary layer. It is possible that such a kink exists in compliant APCF too, say at $R = R^*$, in which case we would expect that the upper-branch asymptotic structure $S3$ describes the upper branch of the neutral curve for Reynolds numbers greater than R^*.

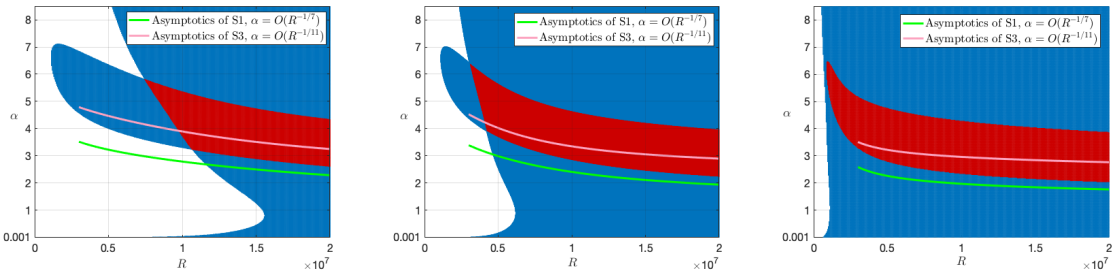

(a) (b) (c)

Figure 9.2.2: Comparison of numerical stability regions (blue and red shading) with asymptotic results from $S1$ and $S3$ (pink and green curves). The inner cylinder is stationary, with $\delta = 0.7$, $m = 0.1$ and (a) $K = 5 \times 10^{11}$, (b) $K = 1 \times 10^{11}$, (c) $K = 5 \times 10^9$.

Depicted in figure 9.2.2 are the stability regions corresponding to a stationary cylinder with $\delta = 0.7$ and varying K. As the spring stiffness decreases, we expect from our numerical computations that the band of unstable wavenumbers pertaining to the modified flow-based mode sinks in α. Figure 9.2.2 shows that this behaviour is indeed captured by our asymptotic results.

When V increases, the situation becomes more complicated. For a flexible inner cylinder with $\delta = 0.7$, $K = 5 \times 10^{11}$ and $m = 0.1$, we solve the lower-branch eigenrelation (9.1.6) of $S1$ at various Reynolds numbers for $V = 0.0025$, $V = 0.005$ and $V = 0.01$. As the Reynolds number increases along a lower branch neutral curve for a given δ, V, K and m, the appropriate V_0 with which to solve the eigenrelation (9.1.6) increases, whilst the appropriate K_0 and m_0 decrease.

Solving (9.1.6) with $\delta = 0.7$, $V_0 = R^{2/7}V$, $K_0 = R^{-12/7}K$ and $m_0 = R^{-4/7}m$ as the Reynolds number ranges from $R = 1 \times 10^7$ to $R = 5 \times 10^7$ culminates in the solutions for s_+ and s_- depicted in figures 9.2.3(a,b), 9.2.4(a,b) and 9.2.5(a,b). With $\widetilde{K}$ as defined in (9.1.3), solutions marked with a cross ($\times$) have $\widetilde{K} < 0$, whilst solutions marked with a filled circle ($\bullet$) have $\widetilde{K} > 0$. At a given Reynolds number, solutions s_+ and s_- belonging to the same solution pair (s_+, s_-) are plotted in the same colour.

Using the definitions of s_+ and s_- (9.1.5), we are able to solve for α_0 and form curves in the (R, α) plane. These curves are shown in figures 9.2.3c, 9.2.4c and 9.2.5c. The colour of each curve illustrates from which pair of solutions (s_+, s_-) the curve arises. For example, the green asymptotic curve of figure 9.2.3c corresponds to the green solutions for s_+ and s_- in figures 9.2.3(a,b).

In figure 9.2.3, we see the lower-branch eigenrelation admits two solutions for the Reynolds numbers shown when $V = 0.0025$ (and $\delta = 0.7,\ K = 5 \times 10^{11},\ m = 0.1$). The solutions depicted in blue crosses have $\widetilde{K} < 0$. The corresponding asymptotic curve exists in the (R, α) plane at wavenumbers larger than those displayed in 9.2.3c, and so is not shown.

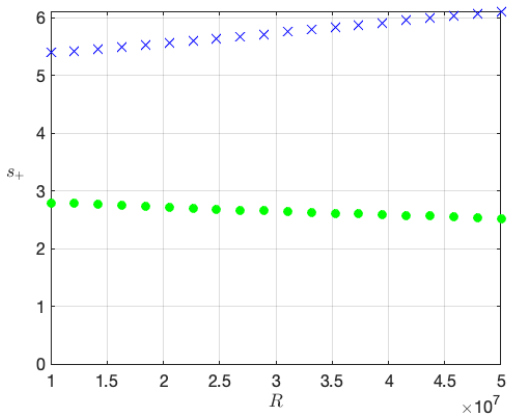

(a) Solutions s_+ of $S1$

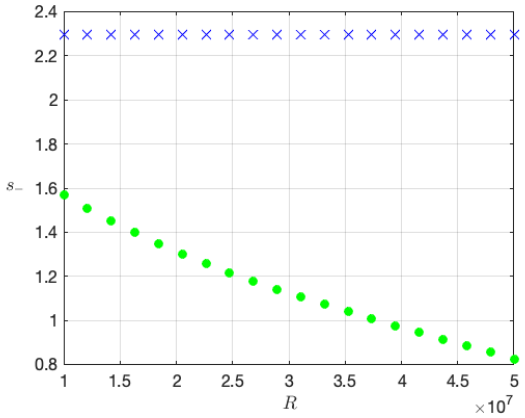

(b) Solutions s_- of $S1$

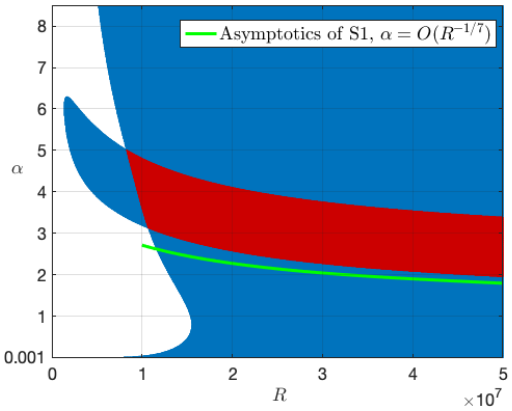

(c) Asymptotic curve of $S1$

Figure 9.2.3: The inner cylinder has properties $\delta = 0.7, K = 5 \times 10^{11}$, $m = 0.1$ and $V = 0.0025$. Figures (a) and (b) illustrate solutions s_+ and s_- of (9.1.6) for various Reynolds numbers. At a given Reynolds number, solutions s_+ and s_- belonging to the same solution pair (s_+, s_-) are plotted in the same colour. Solutions marked with a cross (x) have $\widetilde{K} < 0$, whilst solutions marked with a filled circle (•) have $\widetilde{K} > 0$. Figure (c) shows a comparison of numerical stability regions (blue and red shading) with asymptotic results. The green asymptotic curve in figure (c) corresponds to the green solution pairs (s_+, s_-) in figures (a) and (b).

Once V increases to $V = 0.005$, we see that the behaviour of the solution with $\widetilde{K} > 0$ changes considerably. In particular, s_- becomes negative beyond $R \approx 3.1 \times 10^7$ (see figure 9.2.4b). From the definition of s_- (9.1.5), this means that we must have $c_0 < V_0$. For solutions with $s_- < 0$, the lower-branch structure $S1$ consists of only one critical layer, which is embedded in the viscous wall layer near the outer cylinder.

The change in behaviour in our asymptotic results is also reflected in the numerical computations, where it appears that the red region, which contains two unstable modes, is splitting (figure 9.2.4c). As before, the neutral curve corresponding to the solutions (s_+, s_-) depicted in blue crosses exist at wavenumbers beyond the scope of figure 9.2.4c.

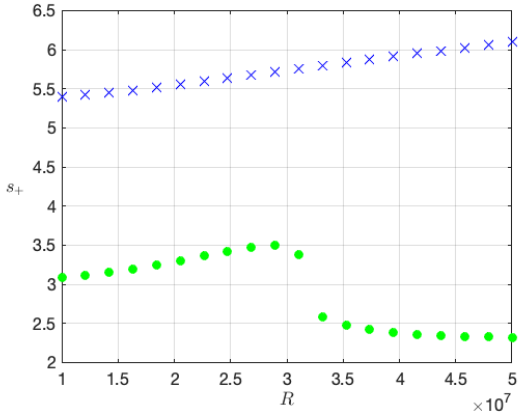

(a) Solutions s_+ of $S1$

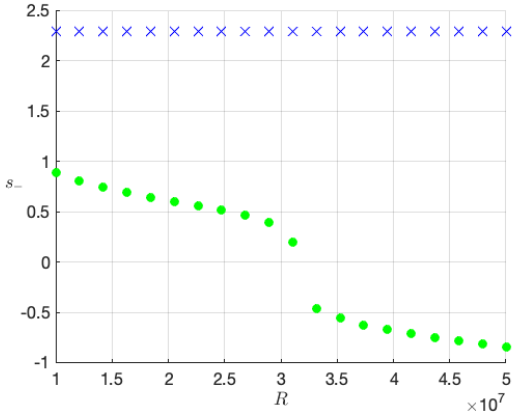

(b) Solutions s_- of $S1$

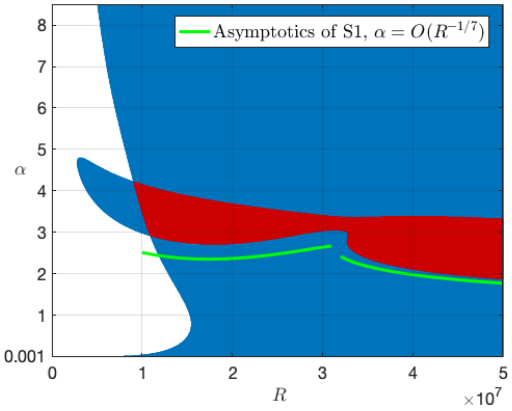

(c) Asymptotic curves of $S1$

Figure 9.2.4: The inner cylinder has properties $\delta = 0.7, K = 5 \times 10^{11}$, $m = 0.1$ and $V = 0.005$. Figures (a) and (b) illustrate solutions s_+ and s_- of (9.1.6) for various Reynolds numbers. At a given Reynolds number, solutions s_+ and s_- belonging to the same solution pair (s_+, s_-) are plotted in the same colour. Solutions marked with a cross (x) have $\widetilde{K} < 0$, whilst solutions marked with a filled circle (•) have $\widetilde{K} > 0$. Figure (c) shows a comparison of numerical stability regions (blue and red shading) with asymptotic results. The green asymptotic curve in figure (c) corresponds to the green solution pairs (s_+, s_-) in figures (a) and (b).

Increasing V further to $V = 0.01$, we find the existence of many more pairs of solutions (s_+, s_-). These are shown in figures 9.2.5a and 9.2.5b. We observe that the red and orange solutions merge and subsequently disappear as R is increased. It is interesting to observe that this is reflected in our numerical results (figure 9.2.5c), which reveal a closed stability region where $R < 1 \times 10^7$. The red and orange asymptotic curves in the (R, α) plane (figure 9.2.5c) describe this closed stability region, and meet at $R \approx 1 \times 10^7$.

The significance of the grey and black solution pairs (s_+, s_-) (figures 9.2.5a, 9.2.5b) is unclear from looking at the numerical stability regions of figure 9.2.5c. However, our asymptotic results are only valid for $R \gg 1$ and it is possible that we are simply not at high enough Reynolds numbers to appropriately capture these modes. In figure 9.2.5c, we have opted not to illustrate the asymptotic curves corresponding to these solutions.

In figures 9.2.5a and 9.2.5b, the solutions in green emerge at $R \approx 1.6 \times 10^7$. With $s_- < 0$, these solutions correspond to neutral modes with $c_0 < V_0$. As seen by the green asymptotic curve in figure 9.2.5c, these solutions seem to accurately predict the emergence and subsequent behaviour of the corresponding numerically obtained stability region.

In light blue crosses, we illustrate a lower-branch mode with $\widetilde{K} < 0$ and s_- deviating from $s_- \approx 2.2972$ as the Reynolds number becomes larger. We see evidence for this mode at larger wavenumbers, which we anticipate has moved off the scaling of *S2* and onto that of *S1* as the Reynolds number increases. To explore this further, we plot the asymptotic curve of $S2$ (see the pink curve in figure 9.2.5c) and observe the curve deviates from the numerical results as R becomes larger. In contrast, the asymptotic curve corresponding to the light blue solutions shows consistently excellent agreement with the numerical results shown. Though there is some doubt in the numerical stability calculations for modes with large wavenumbers, we opted to illustrate stability regions for $\alpha \leq 10$ for this choice of V. This is to showcase the asymptotic solutions that describe the upper unstable region in red.

In addition to these lower-branch solutions, we seek solutions of the upper-branch eigenrelation (9.1.19) belonging to structure *S4* for the range $2 \times 10^7 < R < 5 \times 10^7$. These solutions are shown by the yellow curve in figure 9.2.5c. We recall the structure *S4* has only one critical layer, and has no rigid counterpart. The agreement between the asymptotic curve and numerical results increases as R becomes larger.

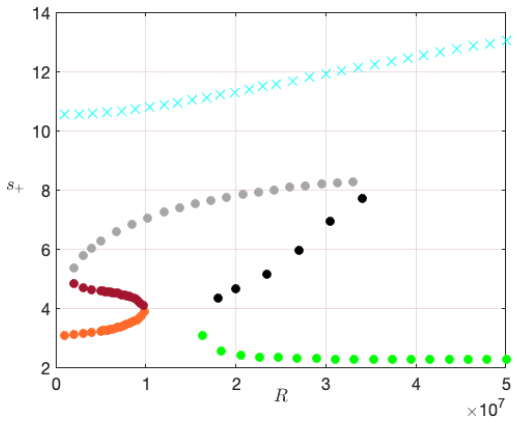

(a) Solutions s_+ of $S1$

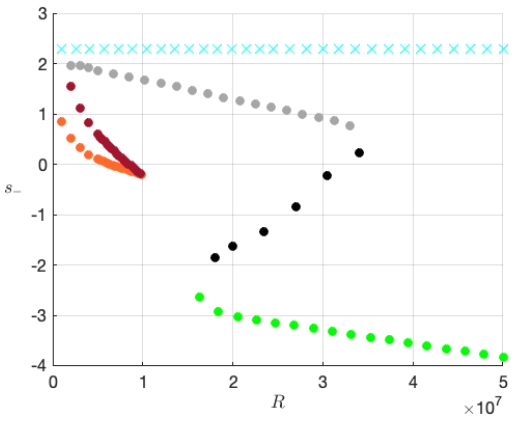

(b) Solutions s_- of $S1$

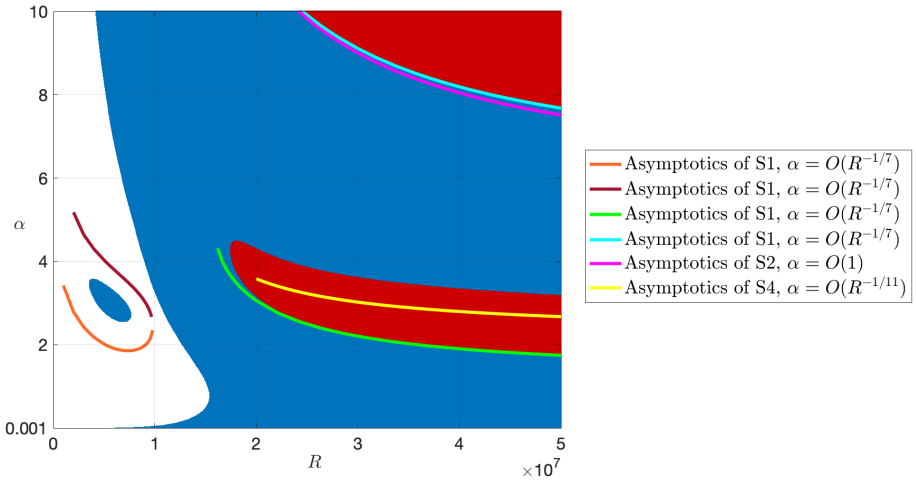

(c) Asymptotic curves of $S1 - S4$

Figure 9.2.5: The inner cylinder has properties $\delta = 0.7$, $K = 5 \times 10^{11}$, $m = 0.1$ and $V = 0.01$. Figures (a) and (b) illustrate solutions s_+ and s_- of (9.1.6) for various Reynolds numbers. At a given Reynolds number, solutions s_+ and s_- belonging to the same solution pair (s_+, s_-) are plotted in the same colour. Solutions marked with a cross (x) have $\widetilde{K} < 0$, whilst solutions marked with a filled circle (•) have $\widetilde{K} > 0$. Figure (c) shows a comparison of numerical stability regions (blue and red shading) with asymptotic results. The orange, red, green and light blue asymptotic curves in figure (c) respectively correspond to the orange, red, green and light blue solution pairs (s_+, s_-) in figures (a) and (b).

9.3 Summary

To summarise the work in this chapter, we have seen numerical evidence for neutral modes belonging to structures $S1$-$S4$. We found that the asymptotic results of structures $S1$ and $S3$ appropriately captured the numerical behaviour of the flow-based mode as K was decreased for a stationary inner cylinder (figure 9.2.2).

Increasing the sliding velocity of the inner cylinder, the situation became more complicated. Our asymptotic results accurately reflected the 'splitting' of the red stability region (figure 9.2.4c) when $V = 0.005$. Increasing V further, we found the existence of additional asymptotic solutions.

In general, we have found good agreement between the asymptotic and numerical results. It remains to understand the significance of the lower-branch solutions depicted in grey and black in figures 9.2.5a and 9.2.5b. It would also be of interest to compare results from our numerical method with those from our hybrid structure $S5$.

Thus far, we have explored the stability properties of compliant APCF with respect to infinitesimal disturbances of amplitude Δ. In the next chapter, we increase the size of the disturbance so that nonlinear terms of order $O(\Delta^2)$ may no longer be neglected. We will move away from the cylindrical geometry of APCF and will investigate vortex-wave interaction in planar Couette flow when the lower wall is flexible.

Chapter 10

Vortex-wave interaction in planar Couette flow with a flexible lower wall

The framework of vortex-wave interaction theory was developed by Hall and Smith [30, 31, 32, 33], Bennett, Hall and Smith [34], Smith and Walton [35], Walton and Smith [36]. The contribution from the waves may be of either the inviscid Rayleigh-type or the viscous Tollmien-Schlichting-type.

An example of the former has been considered by Hall and Sherwin [37] in plane Couette flow. The interaction involving waves of a Tollmien-Schlichting-type has been studied by Hall and Smith [31] in incompressible boundary layers and Blackaby [78] in compressible boundary layer flows. Other works include those by Walton and Smith [79] for the boundary layer over a flat surface, and more recently, Dempsey and Walton [38] in the case of the asymptotic suction boundary layer.

Vortex-wave interaction is a rich field that has been the subject of much research. The list of works given above is by no means exhaustive.

10.1 Problem Formulation

In this chapter, we consider the flow of an incompressible fluid through a region bounded by an upper rigid wall and lower flexible wall. The upper and lower walls of the channel move in the streamwise direction with constant velocity V^* and $-V^*$ respectively. The fluid has kinematic viscosity ν^* and constant density ρ^*. Unlike in the previous chapters, there is no external pressure gradient applied to the flow.

This flow is readily described by a Cartesian coordinate system with (x^*, y^*, z^*) measured in the streamwise, normal and spanwise directions respectively. The dimensional flow velocities in these respective directions are given by (u^*, v^*, w^*). We denote the dimensional pressure of the fluid by p^*.

The upper wall is located at $y^* = h^*$. We use the spring-backed plate model to describe the flexibility of the lower wall, which we assume flexes only in the normal direction. The position of the lower wall y_s^* is given by

$$y_s^* = -h^* + \eta^*(x^*, z^*, t^*), \tag{10.1.1}$$

where $y^* = -h^*$ is the position of the lower wall when unflexed, and η^* is the displacement of the wall due to its flexibility. The displacement η^* is dependent on the streamwise and spanwise positions along the wall, and also on the time t^*.

We non-dimensionalise our lengthscales using the undisturbed channel half-width, and our velocities using the streamwise velocity of the upper wall:

$$(x^*,\ y^*,\ z^*) = h^*(x, y, z), \qquad \eta^* = h^*\eta, \qquad (u^*, v^*, w^*) = V^*(u, v, w). \tag{10.1.2}$$

Our pressure and time are non-dimensionalised as

$$p^* = \rho^* {V^*}^2 p, \quad t^* = \frac{h^*}{V^*} t. \tag{10.1.3}$$

Using the non-dimensionalisation (10.1.2) and (10.1.3), the Navier Stokes equations governing our flow are

$$\frac{\partial u}{\partial x} + \frac{\partial v}{\partial y} + \frac{\partial w}{\partial z} = 0, \tag{10.1.4a}$$

$$\frac{\partial u}{\partial t} + u\frac{\partial u}{\partial x} + v\frac{\partial u}{\partial y} + w\frac{\partial u}{\partial z} = -\frac{\partial p}{\partial x} + \frac{1}{R}\left[\frac{\partial^2 u}{\partial x^2} + \frac{\partial^2 u}{\partial y^2} + \frac{\partial^2 u}{\partial z^2}\right], \tag{10.1.4b}$$

$$\frac{\partial v}{\partial t} + u\frac{\partial v}{\partial x} + v\frac{\partial v}{\partial y} + w\frac{\partial v}{\partial z} = -\frac{\partial p}{\partial y} + \frac{1}{R}\left[\frac{\partial^2 v}{\partial x^2} + \frac{\partial^2 v}{\partial y^2} + \frac{\partial^2 v}{\partial z^2}\right], \tag{10.1.4c}$$

$$\frac{\partial w}{\partial t} + u\frac{\partial w}{\partial x} + v\frac{\partial w}{\partial y} + w\frac{\partial w}{\partial z} = -\frac{\partial p}{\partial z} + \frac{1}{R}\left[\frac{\partial^2 w}{\partial x^2} + \frac{\partial^2 w}{\partial y^2} + \frac{\partial^2 w}{\partial z^2}\right], \tag{10.1.4d}$$

where the Reynolds number R is defined as

$$R = \frac{V^* h^*}{\nu^*}. \tag{10.1.5}$$

The flow quantities are to satisfy appropriate no-slip conditions on the channel walls. On the upper wall, these are expressed by

$$u = 1, \qquad v = 0, \qquad w = 0 \qquad \text{on} \quad y = 1. \tag{10.1.6}$$

We now seek to form boundary conditions on the lower wall, which has the non-dimensional position

$$y_s(x,z,t) = -1 + \eta(x,z,t), \tag{10.1.7}$$

as seen from (10.1.1) and (10.1.2). Since the wall flexes only in the normal direction, the streamwise and spanwise velocities are simply

$$u = -1, \quad w = 0 \qquad \text{on} \quad y = y_s. \tag{10.1.8}$$

We revisit the kinematic and dynamic conditions of Chapter 2 (see equations (2.1.7b) and (2.1.10)), adapting them to the planar flow of interest here. The kinematic boundary condition allows us to relate the motion of the fluid with the motion of the wall, and we have

$$v = \frac{\partial \eta}{\partial t} + u\frac{\partial \eta}{\partial x} + w\frac{\partial \eta}{\partial z} \qquad \text{on} \quad y = y_s. \tag{10.1.9}$$

The final condition we apply on the lower wall is the dynamic condition, which we obtain by balancing the forces acting on the wall. The use of a spring-backed plate model [54, 55] proposes

$$m\frac{\partial^2 \eta}{\partial t^2} = -p + \frac{2}{R}\frac{\partial v}{\partial y} - \frac{1}{R^2}K\eta, \tag{10.1.10}$$

where m and K are the non-dimensional mass and spring constant (by Hooke's law) per unit area. We have made use of the non-dimensionalisation

$$m^* = \rho^* h^* m, \qquad K^* = \frac{\rho^* {\nu^*}^2}{{h^*}^3}K. \tag{10.1.11}$$

Before we study the existence of vortex-wave interaction in our flow, we consider the nature of the base flow in the absence of any external disturbances. We suppose that the flexibility of the lower wall does not affect the base flow, denoted by (u_b, v_b, w_b). Under this assumption, the base flow satisifies

$$u_b = 1, \quad v_b = 0, \quad w_b = 0 \qquad \text{on} \quad y = 1, \tag{10.1.12a}$$

$$u_b = -1, \quad v_b = 0, \quad w_b = 0 \qquad \text{on} \quad y = -1. \tag{10.1.12b}$$

An exact solution of the Navier-Stokes equations (10.1.4) subject to (10.1.12) is provided by the unidirectional flow known as plane Couette flow:

$$u_b = y, \quad v_b = 0, \quad w_b = 0. \tag{10.1.13}$$

In the previous chapters of this thesis, we conducted a linear stability analysis and perturbed our base flow with infinitesimal disturbances of amplitude Δ. Nonlinear terms of order Δ^2 were thus assumed to be negligible. In this chapter, we consider the flow at

asymptotically large Reynolds numbers and increase the amplitude of our disturbance so that nonlinear terms can no longer be neglected. We determine the size of Δ at which the nonlinear self-interaction of the wave induces an order one perturbation to our basic state via a self-sustaining process.

Known as vortex-wave interaction at high Reynolds numbers, this process comprises three interacting components: travelling waves, a roll flow, and a streak flow. Three-dimensional travelling waves propagating in the streamwise direction nonlinearly self-interact to force a flow in the cross-stream plane, which we call the roll flow. The rolls in turn drive a flow in the streamwise direction, the streak. As we will see later, this streak then supports the existence of neutrally stable travelling waves, and the process continues.

The roll and streak flows are steady and independent of the streamwise distance. Together, the roll/streak flow is referred to as a vortex flow. We assume the vortex flow, denoted by (U_v, V_v, W_v), satisfies the conditions

$$U_v = 1, \quad V_v = 0, \quad W_v = 0 \quad \text{on} \quad y = 1, \tag{10.1.14a}$$

$$U_v = -1, \quad V_v = 0, \quad W_v = 0 \quad \text{on} \quad y = -1. \tag{10.1.14b}$$

The streak flow, with both normal and spanwise dependencies, is taken to be an order one quantity.

10.2 Derivation of vortex-wave interaction equations

We investigate the existence of a vortex-wave interaction in this flow by examining three regions of the flow in which different physical processes dominate: a core region surrounded by two viscous wall layers. Before we begin our analysis, we briefly describe our approach.

We consider the vortex flow $(U_v(y,z), V_v(y,z), W_v(y,z))$ superimposed with travelling waves of amplitude Δ,

$$\Delta \hat{q}(y,z) \mathrm{e}^{\mathrm{i}\alpha(x-ct)} + c.c. \tag{10.2.1}$$

Our objective is to identify, in terms of the Reynolds number, the critical size of Δ that leads to the self-sustaining vortex/wave interaction described above. To enable this, we seek the required scalings of the vortex and wave in each asymptotic region, emphasising that the size of Δ is chosen so as to induce order one spanwise fluctuations in the streak.

Assuming that the streak flow U_v found in the core behaves regularly as we approach the channel walls, we have

$$U_v = 1 + \lambda_+(z)\,(y-1) + \cdots, \qquad U_v = -1 + \lambda(z)\,(y+1) + \cdots \tag{10.2.2a}$$

near the upper and lower walls respectively, where

$$\lambda_+(z) = \left.\frac{\partial U_v}{\partial y}\right|_{y=1}, \quad \lambda(z) = \left.\frac{\partial U_v}{\partial y}\right|_{y=-1}. \tag{10.2.3}$$

The scalings for the wave component in our interaction are motivated by the analysis of our lower branch structure where $\alpha = O(1)$ (see Chapter 6, Section 6.2). With this in mind, we take the wavenumber and wavespeed to be

$$\alpha = \alpha_0 + \cdots, \quad c = -1 + R^{-1/3}c_0 + \cdots. \tag{10.2.4}$$

where α_0 and c_0 are order one quantities.

The lower wall layer

We commence our analysis in the layer near the lower flexible wall. As mentioned above, the work in the lower branch structure where $\alpha = O(1)$ (Section 6.2) guides our scalings here. The wave quantities (u_w, v_w, w_w, p_w) thus expand as

$$\begin{aligned} u_w \sim \Delta u_- \mathrm{e}^{\mathrm{i}\alpha(x-ct)} + c.c, \quad v_w \sim \Delta R^{-1/3} v_- \mathrm{e}^{\mathrm{i}\alpha(x-ct)} + c.c, \\ w_w \sim \Delta w_- \mathrm{e}^{\mathrm{i}\alpha(x-ct)} + c.c, \quad p_w \sim \Delta R^{-1/3} p_- \mathrm{e}^{\mathrm{i}\alpha(x-ct)} + c.c. \end{aligned} \tag{10.2.5}$$

with

$$y = y_s + R^{-1/3}\bar{y}, \tag{10.2.6}$$

and

$$K = R^{5/3}K_0, \quad m = R^{1/3}m_0. \tag{10.2.7}$$

We also assume that the displacement $\eta(x,z)$ to the lower wall assumes a normal-mode form,

$$\eta(x,z) = \Delta\hat{\eta}(z)\mathrm{e}^{\mathrm{i}\alpha(x-ct)} + c.c, \tag{10.2.8}$$

where we have assumed that $\Delta \ll R^{-1/3}$ so that the perturbation is much smaller than the thickness of this layer.

We anticipate the wave self-interacts to force the roll/streak flow (U_v, V_v, W_v) and thus enforce the balances

$$v_w \frac{\partial w_w^*}{\partial y} \sim R^{-1} \frac{\partial^2 U_v}{\partial y^2}, \qquad u_w \frac{\partial w_w^*}{\partial x} \sim R^{-1} \frac{\partial^2 W_v}{\partial y^2} \tag{10.2.9}$$

in the streamwise (10.1.4b) and spanwise (10.1.4d) momentum equations respectively. With use of (10.2.5) and (10.2.6), this leads to the scalings

$$U_v = -1 + R^{-1/3}\lambda(z)\bar{y} + \cdots + \Delta^2 R^{1/3}\overline{u}_v + \cdots, \qquad W_v = \Delta^2 R^{1/3}\overline{w}_v + \cdots. \tag{10.2.10}$$

The first two terms in the expansion for $\overline{U}_v$ account for the contribution of the streak flow from the core, as expressed in (10.2.2).

Finally, the continuity equation (10.1.4a) suggests we take

$$\frac{\partial V_v}{\partial y} \sim \frac{\partial W_v}{\partial z}, \tag{10.2.11}$$

which gives

$$V_v = \Delta^2 \overline{v}_v \tag{10.2.12}$$

after consideration of (10.2.6) and (10.2.10).

The expansions in this region are thus

$$u = -1 + R^{-1/3}\lambda(z)\bar{y} + \Delta\, u_-(y,z)\, e^{\mathrm{i}\alpha(x-ct)} + \cdots + \Delta^2 R^{1/3}\,\overline{u}_v(y,z) + \cdots + c.c, \tag{10.2.13a}$$

$$v = \Delta R^{-1/3}\, v_-(y,z)\, e^{\mathrm{i}\alpha(x-ct)} + \cdots + \Delta^2\,\overline{v}_v(y,z) + \cdots + c.c, \tag{10.2.13b}$$

$$w = \Delta\, w_-(y,z)\, e^{\mathrm{i}\alpha(x-ct)} + \cdots + \Delta^2 R^{1/3}\,\overline{w}_v(y,z) + \cdots + c.c, \tag{10.2.13c}$$

$$p = \Delta R^{-1/3}\, p_-(y,z)\, e^{\mathrm{i}\alpha(x-ct)} + \cdots + \Delta^2 R^{-2/3}\,\overline{p}_v(y,z) + \cdots + c.c. \tag{10.2.13d}$$

With the assumption $\Delta \ll R^{-1/3}$, substitution into the Navier-Stokes equations (10.1.4) shows that the wave equations in this region are identical to those of Smith [80], and are given by

$$\mathrm{i}\alpha_0 u_- + \frac{\partial v_-}{\partial \bar{y}} + \frac{\partial w_-}{\partial z} = 0, \tag{10.2.14a}$$

$$\mathrm{i}\alpha_0 u_-\,(\lambda(z)\bar{y} - c_0) + \lambda(z) v_- + \lambda'(z)\bar{y} w_- = -\mathrm{i}\alpha_0 p_- + \frac{\partial^2 u_-}{\partial \bar{y}^2}, \tag{10.2.14b}$$

$$\frac{\partial p_-}{\partial \bar{y}} = 0, \tag{10.2.14c}$$

$$\mathrm{i}\alpha_0 w_-\,(\lambda(z)\bar{y} - c_0) = -\frac{\mathrm{d}p_-}{\mathrm{d}z} + \frac{\partial^2 w_-}{\partial \bar{y}^2}. \tag{10.2.14d}$$

From these equations, we see how the shear imparted by the streak flow drives the wave. The boundary conditions (10.1.8), (10.1.9) and (10.1.10) reveal that the wave satisfies the following boundary conditions on the compliant wall situated at $\bar{y} = 0$:

$$u_-(0,z) + \hat{\eta}(z)\lambda(z) = 0, \tag{10.2.15a}$$

$$v_-(0,z) = -\mathrm{i}\alpha_0 c_0 \hat{\eta}(z), \tag{10.2.15b}$$

$$w_-(0,z) = 0, \tag{10.2.15c}$$

$$p_-(0,z) = \left(\alpha_0^2 m_0 - K_0\right)\hat{\eta}(z). \tag{10.2.15d}$$

Manipulating these to eliminate $\hat{\eta}$, we obtain

$$\mathrm{i}\alpha_0 c_0 u_-(0,z) - \lambda(z) v_-(0,z) = 0, \tag{10.2.16a}$$

$$w_-(0,z) = 0, \tag{10.2.16b}$$

$$p_-(0,z) = \frac{1}{\lambda(z)}\left(K_0 - {\alpha_0}^2 m_0\right) u_-(0,z). \tag{10.2.16c}$$

It is reasonable to impose that

$$u_-(y,z) \to 0, \quad w_-(y,z) \to 0 \quad \text{as } y \to \infty, \tag{10.2.17}$$

and this will match the core behaviour described later.

Our goal now is to form a differential equation for the wave pressure $p_-(z)$. The subsequent analysis follows the work of Smith [80]. From the pressure wave equation (10.2.14c), it is clear that

$$p_- = p_-(z). \tag{10.2.18}$$

Introducing

$$\xi = (\mathrm{i}\alpha_0\lambda)^{1/3}\,\bar{y} - \frac{\mathrm{i}\alpha_0 c_0}{(\mathrm{i}\alpha_0\lambda)^{2/3}}, \tag{10.2.19}$$

we may write the spanwise wave momentum equation (10.2.14d) as a non-homogeneous Airy differential equation, specifically

$$\frac{\partial^2 w_-}{\partial \xi^2} - \xi w_- = \frac{1}{(\mathrm{i}\alpha_0\lambda)^{2/3}}\frac{\mathrm{d}p_-}{\mathrm{d}z}. \tag{10.2.20}$$

After imposing conditions (10.2.16b) and (10.2.17), we find the solution for w_- to be

$$w_- = \frac{1}{(\mathrm{i}\alpha_0\lambda)^{2/3}}\frac{\mathrm{d}p}{\mathrm{d}z}\left[L(\xi) - \frac{L(\xi_0)}{\mathrm{Ai}(\xi_0)}\mathrm{Ai}(\xi)\right], \qquad \xi_0 = -\frac{\mathrm{i}\alpha_0 c_0}{(\mathrm{i}\alpha_0\lambda)^{2/3}}, \tag{10.2.21}$$

where L has the form

$$L(\xi) = \mathrm{Ai}(\xi) \int_0^\xi \frac{1}{\mathrm{Ai}^2(q)} \int_\infty^q \mathrm{Ai}(q_1)\mathrm{d}q_1\mathrm{d}q \tag{10.2.22}$$

and is a particular solution of the forced Airy equation

$$L''(\xi) - \xi L(\xi) = 1. \tag{10.2.23}$$

Differentiating the streamwise wave momentum equation (10.2.14b) with respect to $\bar{y}$ and using the continuity equation (10.2.14a) to eliminate v_-, we obtain

$$\mathrm{i}\alpha_0 \left(\lambda(z)\bar{y} - c_0\right) \frac{\partial u_-}{\partial \bar{y}} - \frac{\partial^3 u_-}{\partial \bar{y}^3} = \lambda(z)\frac{\partial w_-}{\partial z} - \frac{\mathrm{d}\lambda}{\mathrm{d}z}\left(w_- + \bar{y}\frac{\partial w_-}{\partial \bar{y}}\right). \tag{10.2.24}$$

Upon substitution of the solution for w_- (10.2.21), and subsequent manipulation, we may write

$$\left(\frac{\partial^2}{\partial \xi^2} - \xi\right)\frac{\partial u_-}{\partial \xi} = (\mathrm{i}\alpha_0\lambda)^{-1/3}\left[C_0 L(\xi) + C_1\mathrm{Ai}(\xi) + 4C_2\xi L'(\xi) + C_3\xi\mathrm{Ai}'(\xi)\right], \tag{10.2.25}$$

where

$$C_0 = -(\mathrm{i}\alpha_0\lambda)^{-4/3}\left(\lambda\frac{\mathrm{d}^2 p_-}{\mathrm{d}z^2} - \frac{5}{3}\frac{\mathrm{d}\lambda}{\mathrm{d}z}\frac{\mathrm{d}p_-}{\mathrm{d}z}\right), \tag{10.2.26a}$$

$$C_1 = -C_0\frac{L(\xi_0)}{\mathrm{Ai}(\xi_0)} - \frac{2}{3}(\mathrm{i}\alpha_0\lambda)^{-4/3}\frac{\mathrm{d}\lambda}{\mathrm{d}z}\frac{\mathrm{d}p_-}{\mathrm{d}z}\xi_0\left(\frac{L'(\xi_0)}{\mathrm{Ai}(\xi_0)} - \frac{L(\xi_0)}{\mathrm{Ai}(\xi_0)^2}\mathrm{Ai}'(\xi_0)\right), \tag{10.2.26b}$$

$$C_2 = \frac{1}{6}(\mathrm{i}\alpha_0\lambda)^{-4/3}\frac{\mathrm{d}\lambda}{\mathrm{d}z}\frac{\mathrm{d}p_-}{\mathrm{d}z}, \tag{10.2.26c}$$

$$C_3 = -4C_2\frac{L(\xi_0)}{\mathrm{Ai}(\xi_0)}. \tag{10.2.26d}$$

To help us in solving (10.2.25), we use the properties of $\mathrm{Ai}(\xi)$ and $L(\xi)$ to obtain the results

$$\left(\frac{\mathrm{d}^2}{\mathrm{d}\xi^2} - \xi\right)\mathrm{Ai}'(\xi) = \mathrm{Ai}(\xi), \qquad \left(\frac{\mathrm{d}^2}{\mathrm{d}\xi^2} - \xi\right)\left(\frac{\xi^2\mathrm{Ai}(\xi)}{4} - \frac{\mathrm{Ai}'(\xi)}{2}\right) = \xi\mathrm{Ai}'(\xi), \tag{10.2.27a}$$

$$\left(\frac{\mathrm{d}^2}{\mathrm{d}\xi^2} - \xi\right)L'(\xi) = L(\xi), \qquad \left(\frac{\mathrm{d}^2}{\mathrm{d}\xi^2} - \xi\right)(\xi L''(\xi) - 2L'(\xi)) = 4\xi L'(\xi). \tag{10.2.27b}$$

In view of these relations, we find

$$\frac{\partial u_-}{\partial \bar{y}} = C_0 L'(\xi) + C_1 \mathrm{Ai}'(\xi) + C_2 \left[\xi L''(\xi) - 2L'(\xi)\right] + C_3 \left[\frac{\xi^2}{4}\mathrm{Ai}(\xi) - \frac{1}{2}\mathrm{Ai}'(\xi)\right] + (\mathrm{i}\alpha_0\lambda)^{1/3} C_4 \mathrm{Ai}(\xi), \quad (10.2.28)$$

where C_4 is unknown.

Evaluating the streamwise momentum equation (10.2.14b) at $\bar{y} = 0$ and applying the boundary conditions (10.2.16a), (10.2.16b) reveals that

$$\frac{\partial^2 u_-}{\partial \bar{y}^2} = \mathrm{i}\alpha_0 p_-(z) \quad \text{on} \quad \bar{y} = 0. \quad (10.2.29)$$

Upon differentiation of (10.2.28), this gives

$$\frac{\mathrm{i}\alpha_0 p_-(z)}{(\mathrm{i}\alpha_0\lambda)^{1/3}} = C_0 L''(\xi_0) + C_1 \mathrm{Ai}''(\xi_0) + C_2 \left[\xi_0 L'''(\xi_0) - L''(\xi_0)\right] + \frac{1}{4} C_3 {\xi_0}^2 \mathrm{Ai}'(\xi_0) + (\mathrm{i}\alpha_0\lambda)^{1/3} C_4 \mathrm{Ai}'(\xi_0). \quad (10.2.30)$$

The subsequent part of this analysis differs from the work of Smith [80] as we do not impose that the streamwise velocity is zero on the wall $\bar{y} = 0$. As we will see, this leads to an additional term in the wave pressure equation. Integrating (10.2.28) with respect to ξ between ξ_0 and infinity, we use the behaviour of $\mathrm{Ai}(\xi)$, $L(\xi)$ and their derivatives as $\xi \to \infty$ to simplify the resulting expression. The boundary condition (10.2.16c) then illustrates that

$$(\mathrm{i}\alpha_0\lambda)^{1/3} \frac{\lambda p_-(z)}{K_0 - {\alpha_0}^2 m_0} = C_0 L(\xi_0) + C_1 \mathrm{Ai}(\xi_0) + C_2 \left[\xi_0 L'(\xi_0) - 3L(\xi_0)\right] + C_3 \left[\frac{\xi_0}{4}\mathrm{Ai}'(\xi_0) - \frac{3}{4}\mathrm{Ai}(\xi_0)\right] - (\mathrm{i}\alpha_0\lambda)^{1/3} C_4 \kappa(\xi_0). \quad (10.2.31)$$

It is useful to note that

$$\frac{\mathrm{d}}{\mathrm{d}\xi}\left[\mathrm{Ai}(\xi)L'(\xi) - L(\xi)\mathrm{Ai}'(\xi)\right] = \mathrm{Ai}(\xi), \quad (10.2.32)$$

which can be established using the equations for $\mathrm{Ai}(\xi)$ and $L(\xi)$. Upon integration, (10.2.32) yields

$$\mathrm{Ai}(\xi_0)L'(\xi_0) - L(\xi_0)\mathrm{Ai}'(\xi_0) = -\kappa(\xi_0). \quad (10.2.33)$$

Eliminating C_4 from (10.2.30) and (10.2.31), and making use of relation (10.2.33), we see that the wave pressure satisfies

$$\frac{\mathrm{d}^2 p_-}{\mathrm{d}z^2} - \frac{1}{\lambda(z)}\frac{\mathrm{d}\lambda}{\mathrm{d}z}\mathscr{F}(s)\frac{\mathrm{d}p_-}{\mathrm{d}z} + \left[-{\alpha_0}^2 + \frac{(\alpha_0\lambda(z))^{5/3}}{K_0 - \alpha_0{}^2 m_0} g(s)\right] p_-(z) = 0, \tag{10.2.34}$$

where $g(s)$ and $\mathscr{F}(s)$ are defined as

$$g(s) = \mathrm{i}^{5/3}\frac{\mathrm{Ai}'(-\mathrm{i}^{1/3}s)}{\kappa(-\mathrm{i}^{1/3}s)}, \qquad \mathscr{F}(s) = \frac{3}{2} + \frac{-\mathrm{i}^{1/3}s}{2\mathrm{Ai}(-\mathrm{i}^{1/3}s)}\left(-\mathrm{i}^{1/3}s\kappa(-\mathrm{i}^{1/3}s) + \mathrm{Ai}'(-\mathrm{i}^{1/3}s)\right), \tag{10.2.35}$$

with $s = \mathrm{i}^{5/3}\xi_0$ and ξ_0 defined in (10.2.21). We impose that the wave pressure is 2π periodic in z, so that

$$p_-(0) = p_-(2\pi), \qquad \left.\frac{\mathrm{d}p_-}{\mathrm{d}z}\right|_{z=0} = \left.\frac{\mathrm{d}p_-}{\mathrm{d}z}\right|_{z=2\pi}. \tag{10.2.36}$$

We remark that (10.2.34) illustrates the effect of the streak on the wave via the shear term, $\lambda(z)$.

Before we examine the roll/streak behaviour in the lower layer, we determine the behaviour of the wave as we approach the core. In the limit $\bar{y} \to \infty$, the spanwise wave equation (10.2.14d) evokes the balance

$$\mathrm{i}\alpha_0 w_-\lambda(z)\bar{y} \sim -\frac{\mathrm{d}p_-}{\mathrm{d}z},$$

which, upon rearrangement, reveals that

$$w_- \sim \frac{\mathrm{i}}{\alpha_0\lambda(z)}\frac{\mathrm{d}p_-}{\mathrm{d}z}\frac{1}{\bar{y}}. \tag{10.2.37}$$

This behaviour can be verified using our solution for w_-, shown in (10.2.21). Striking the balance

$$\mathrm{i}\alpha_0 u_- \sim -\frac{\partial w_-}{\partial z}$$

in the continuity equation (10.2.14a) then yields

$$u_- \sim -\frac{1}{\alpha_0{}^2\lambda(z)^2}\left(\lambda(z)\frac{\mathrm{d}^2 p_-}{\mathrm{d}z^2} - \frac{\mathrm{d}\lambda}{\mathrm{d}z}\frac{\mathrm{d}p_-}{\mathrm{d}z}\right)\frac{1}{\bar{y}}. \tag{10.2.38}$$

Finally, the streamwise momemtum equation (10.2.14b) with the balance

$$\lambda(z)v_- \sim -\mathrm{i}\alpha_0 p_- - \frac{\mathrm{d}\lambda}{\mathrm{d}z}\,\bar{y}\,w_- - \mathrm{i}\alpha_0 u_-\lambda(z)\bar{y}$$

elucidates the behaviour

$$v_- \sim \frac{\mathrm{i}}{\alpha_0\lambda(z)}\left(\frac{\mathrm{d}^2 p_-}{\mathrm{d}z^2} - \frac{2}{\lambda(z)}\frac{\mathrm{d}\lambda}{\mathrm{d}z}\frac{\mathrm{d}p_-}{\mathrm{d}z} - {\alpha_0}^2 p_-(z)\right) \tag{10.2.39}$$

as we approach the core.

Substituting the flow expansions (10.2.13) into the Navier-Stokes equations (10.1.4), we observe the wave self-interacts to force a roll/streak flow governed by

$$\frac{\partial\overline{v}_v}{\partial\bar{y}} + \frac{\partial\overline{w}_v}{\partial z} = 0, \tag{10.2.40a}$$

$$v_-\frac{\partial u_-^*}{\partial\bar{y}} + v_-^*\frac{\partial u_-}{\partial\bar{y}} + \lambda(z)\overline{v}_v + w_-\frac{\partial u_-^*}{\partial z} + w_-^*\frac{\partial u_-}{\partial z} + \frac{\mathrm{d}\lambda}{\mathrm{d}z}\bar{y}\,\overline{w}_v = \frac{\partial^2\overline{u}_v}{\partial\bar{y}^2}, \tag{10.2.40b}$$

$$\mathrm{i}\alpha_0 u_-^* v_- - \mathrm{i}\alpha_0 u_- v_-^* + v_-\frac{\partial v_-^*}{\partial\bar{y}} + v_-^*\frac{\partial v_-}{\partial\bar{y}} + w_-\frac{\partial v_-^*}{\partial z} + w_-^*\frac{\partial v_-}{\partial z} = \frac{\partial^2\overline{v}_v}{\partial\bar{y}^2} - \frac{\partial\overline{p}_v}{\partial\bar{y}}, \tag{10.2.40c}$$

$$\mathrm{i}\alpha_0 u_-^* w_- - \mathrm{i}\alpha_0 u_- w_-^* + v_-\frac{\partial w_-^*}{\partial\bar{y}} + v_-^*\frac{\partial w_-}{\partial\bar{y}} + w_-\frac{\partial w_-^*}{\partial z} + w_-^*\frac{\partial w_-}{\partial z} = \frac{\partial^2\overline{w}_v}{\partial\bar{y}^2}. \tag{10.2.40d}$$

It now remains to ascertain the behaviour of the roll as we approach the core. Considering the spanwise roll equation (10.2.40d) in conjunction with the wave behaviour as $\bar{y}\to\infty$ (10.2.37)-(10.2.39), we obtain

$$\frac{\partial^2\overline{w}_v}{\partial\bar{y}^2} \sim -\frac{q}{\bar{y}^2} \quad \text{as} \quad \bar{y}\to\infty, \tag{10.2.41}$$

after considerable algebra, where

$$q = \frac{1}{{\alpha_0}^2\lambda(z)^2}\left[{\alpha_0}^2\frac{\mathrm{d}}{\mathrm{d}z}\left(p_-p_-^*\right) + \frac{\mathrm{d}}{\mathrm{d}z}\left(\frac{\mathrm{d}p_-}{\mathrm{d}z}\frac{\mathrm{d}p_-^*}{\mathrm{d}z}\right)\right]. \tag{10.2.42}$$

From this, we observe that we may take

$$\overline{w}_v \sim -q\log\bar{y} \quad \text{as} \quad \bar{y}\to\infty. \tag{10.2.43}$$

so that the compliance of the lower wall has a leading order effect on the core forcing.

In view of the scalings (10.2.6) and (10.2.10), the spanwise roll W_v thus approaches the core region with the behaviour

$$W_v \sim -\frac{q}{3}\Delta^2 R^{1/3}\log R. \tag{10.2.44}$$

To conclude this section, we remark that the roll solution in the lower layer should latch onto that in the core; it is this imposition that allows for the nonlinear self-interaction of the wave in the lower layer to affect the core via a boundary forcing, and hence determines the size of Δ.

The core region

As an initial step in determining the flow behaviour, we seek to establish the roll/streak and wave equations that govern this region. The limiting behaviour of the wave (10.2.37)-(10.2.39) in the lower viscous layer as we approach the core suggests that our wave components expand as

$$u_w \sim \Delta R^{-1/3} F_0 \mathrm{e}^{\mathrm{i}\alpha(x-ct)} + c.c, \quad v_w \sim \Delta R^{-1/3} G_0 \mathrm{e}^{\mathrm{i}\alpha(x-ct)} + c.c,$$
$$w_w \sim \Delta R^{-1/3} H_0 \mathrm{e}^{\mathrm{i}\alpha(x-ct)} + c.c, \quad p_w \sim \Delta R^{-1/3} P_0 \mathrm{e}^{\mathrm{i}\alpha(x-ct)} + c.c. \tag{10.2.45}$$

In this region, we expect the roll flow (V_v, W_v) to be such that nonlinear terms in the streamwise momentum equation (10.1.4b) become significant at leading order. With the streak U_v being order one, we enforce the balance

$$V_v \frac{\partial U_v}{\partial y} \sim W_v \frac{\partial U_v}{\partial z} \sim R^{-1} \frac{\partial^2 U_v}{\partial y^2}, \tag{10.2.46}$$

obtaining $W_v = O(R^{-1})$ and $V_v = O(R^{-1})$. A balance between the pressure and nonlinear inertia terms in the spanwise momentum equation (10.1.4d) yields

$$W_v \frac{\partial W_v}{\partial z} \sim \frac{\partial P_v}{\partial z}, \tag{10.2.47}$$

so that $P_v = O(R^{-2})$. Writing

$$U_v = u_v + \cdots, \quad V_v = R^{-1} v_v(y,z) + \cdots, \tag{10.2.48}$$
$$W_v = R^{-1} w_v(y,z) + \cdots, \quad P_v = R^{-2} p_v(y,z) + \cdots, \tag{10.2.49}$$

the flow expansions in the core region are thus

$$u = u_v(y,z) + \cdots + \Delta R^{-1/3} F_0(y,z)\, e^{\mathrm{i}\alpha(x-ct)} + \cdots + c.c, \tag{10.2.50a}$$
$$v = R^{-1} v_v(y,z) + \cdots + \Delta R^{-1/3} G_0(y,z)\, e^{\mathrm{i}\alpha(x-ct)} + \cdots + c.c, \tag{10.2.50b}$$
$$w = R^{-1} w_v(y,z) + \cdots + \Delta R^{-1/3} H_0(y,z)\, e^{\mathrm{i}\alpha(x-ct)} + \cdots + c.c, \tag{10.2.50c}$$
$$p = R^{-2} p_v(y,z) + \cdots + \Delta R^{-1/3} P_0(y,z)\, e^{\mathrm{i}\alpha(x-ct)} + \cdots + c.c. \tag{10.2.50d}$$

Upon substitution of (10.2.50) into the Navier-Stokes equations (10.1.4), we obtain equations encapsulating the wave behaviour:

$$\mathrm{i}\alpha_0 F_0 + \frac{\partial G_0}{\partial y} + \frac{\partial H_0}{\partial z} = 0, \tag{10.2.51a}$$

$$\mathrm{i}\alpha_0 F_0(u_v + 1) + G_0\frac{\partial u_v}{\partial y} + H_0\frac{\partial u_v}{\partial z} = -\mathrm{i}\alpha_0 P_0, \tag{10.2.51b}$$

$$\mathrm{i}\alpha_0 G_0(u_v + 1) = -\frac{\partial P_0}{\partial y}, \tag{10.2.51c}$$

$$\mathrm{i}\alpha_0 H_0(u_v + 1) = -\frac{\partial P_0}{\partial z}. \tag{10.2.51d}$$

These can be manipulated to form the equation

$$\frac{\partial^2 P_0}{\partial y^2} + \frac{\partial^2 P_0}{\partial z^2} - {\alpha_0}^2 P_0 = \frac{2}{u_v(y,z)+1}\frac{\partial u_v}{\partial y}\frac{\partial P_0}{\partial y} + \frac{2}{u_v(y,z)+1}\frac{\partial u_v}{\partial z}\frac{\partial P_0}{\partial z}, \tag{10.2.52}$$

a three-dimensional generalisation of the Rayleigh pressure equation that shows the wave pressure is being driven by the streak.

This to be solved subject to the typical inviscid impermeability condition

$$G_0 = 0 \quad \text{on} \quad y = 1, \tag{10.2.53}$$

which, using (10.2.51c), is equivalent to

$$\frac{\partial P_0}{\partial y} = 0 \quad \text{on} \quad y = 1. \tag{10.2.54}$$

We look for solutions to the wave equations (10.2.51a), (10.2.52) near $y = 1$, obtaining

$$P_0 \sim P_+(z) + \frac{1}{2}\left({\alpha_0}^2 P_+(z) - P_+''(z)\right)(y-1)^2,$$

$$F_0 \sim -\frac{P_+(z)}{2}, \quad G_0 \sim \frac{\mathrm{i}}{2\alpha_0}\left({\alpha_0}^2 P_+(z) - P_+''(z)\right)(y-1), \quad H_0 \sim \frac{\mathrm{i}}{2\alpha_0}P_+'(z). \tag{10.2.55}$$

$P_+(z)$ is the wave pressure at $y = 1$. These form the matching conditions for the upper wall layer, which we will discuss shortly.

As we approach the lower wall, we have

$$P_0 \sim p_-(z) + \frac{1}{2}\left(p_-''(z) - \frac{2\lambda'(z)}{\lambda(z)}p_-'(z) - {\alpha_0}^2 p_-(z)\right)(y+1)^2, \tag{10.2.56a}$$

$$F_0 \sim -\frac{1}{\alpha_0^2\lambda(z)^2}\left(\lambda(z)p_-''(z) - \lambda'(z)p_-'(z)\right)\frac{1}{y+1}, \tag{10.2.56b}$$

$$G_0 \sim \frac{\mathrm{i}}{\alpha_0\lambda(z)}\left(p_-''(z) - \frac{2\lambda'(z)}{\lambda(z)}p_-'(z) - {\alpha_0}^2 p_-(z)\right), \tag{10.2.56c}$$

$$H_0 \sim \frac{\mathrm{i}p_-'(z)}{\alpha_0\lambda(z)}\frac{1}{y+1}, \tag{10.2.56d}$$

where $p_-(z)$ has been taken to be the wave pressure at $y=-1$ to match the lower viscous layer. These are consistent with the limiting behaviour shown in (10.2.37)-(10.2.39).

Moving onto the roll/streak flow, substitution of the expansions (10.2.50) into the Navier-Stokes equations (10.1.4) yields the governing equations

$$\frac{\partial v_v}{\partial y} + \frac{\partial w_v}{\partial z} = 0, \tag{10.2.57a}$$

$$v_v\frac{\partial u_v}{\partial y} + w_v\frac{\partial u_v}{\partial z} = \frac{\partial^2 u_v}{\partial y^2} + \frac{\partial^2 u_v}{\partial z^2}, \tag{10.2.57b}$$

$$v_v\frac{\partial v_v}{\partial y} + w_v\frac{\partial v_v}{\partial z} = -\frac{\partial p_v}{\partial y} + \frac{\partial^2 v_v}{\partial y^2} + \frac{\partial^2 v_v}{\partial z^2}, \tag{10.2.57c}$$

$$v_v\frac{\partial w_v}{\partial y} + w_v\frac{\partial w_v}{\partial z} = -\frac{\partial p_v}{\partial z} + \frac{\partial^2 w_v}{\partial y^2} + \frac{\partial^2 w_v}{\partial z^2}. \tag{10.2.57d}$$

In view of the presumed behaviour (10.2.2), these are to be solved subject to

$$u_v \to 1,\ w_v \to 0,\ v_v \to 0 \text{ as } y \to 1. \tag{10.2.58a}$$

$$u_v \to -1,\ v_v \to 0 \text{ as } y \to -1. \tag{10.2.58b}$$

The boundary condition for w_v on the lower wall is less straightforward, and requires an examination of the roll behaviour in the lower viscous layer as we approach the core. In particular, we turn our attention to the matching condition (10.2.44).

Our initial goal is to determine the appropriate size of Δ. Having established the core roll is such that $W_v = R^{-1}w_v$, the required balance (10.2.44) reveals that

$$R^{-1}w_v \sim -\frac{q}{3}\Delta^2 R^{1/3}\log R. \tag{10.2.59}$$

This pins down Δ to be

$$\Delta \sim \frac{R^{-2/3}}{\sqrt{\log R}}, \tag{10.2.60}$$

and supplies the spanwise roll boundary condition

$$w_v \to -\frac{q(z)}{3} \quad \text{as} \quad y \to -1. \tag{10.2.61}$$

where q is defined in (10.2.42) with

$$\lambda(z) = \left.\frac{\partial u_v}{\partial y}\right|_{y=-1}. \tag{10.2.62}$$

With this choice of Δ, the influence of the wave in the lower layer is transmitted to the core region through the roll forcing described in (10.2.61). The roll flow then drives a streak with cross-stream dependence, as seen in (10.2.57b). The spanwise variation in the shear of the streak then feeds into the wave, the impact of which is highlighted in the wave pressure equation (10.2.34) of the lower layer. If a solution to (10.2.34) exists, we can see that it is possible to sustain this vortex/wave interaction. Before we seek such a solution, we study the behaviour of the flow near the upper wall for completeness, though this behaviour plays no role in the vortex-wave interaction at leading order.

The upper Stokes layer

To identify the flow dynamics in the region, we first describe the behaviour of the flow quantities in the core as we approach the upper wall. The streak and roll solutions found in the core satisfy the required no-slip conditions on the upper wall. Performing Taylor expansions of the core quantities about $y = 1$ and subsequently substituting these into the continuity equation (10.1.4a) allows us to see the roll/streak behaviour in this Stokes layer:

$$U_v = 1 + \lambda_+(z)\,(y-1) + \cdots, \tag{10.2.63a}$$

$$V_v = -\frac{R^{-1}}{2}\omega'(z)(y-1)^2 + \cdots, \qquad W_v = R^{-1}\omega(z)(y-1) + \cdots, \tag{10.2.63b}$$

where

$$\omega(z) = \left.\frac{\partial w_v}{\partial y}\right|_{y=1}. \tag{10.2.64}$$

The purpose of this Stokes layer then is to reduce the wave velocities to zero on the upper wall. Denoting the thickness of this layer by h, we anticipate that the wave quantities

have sizes

$$u_w = O\left(\frac{R^{-1}}{\sqrt{\log R}}\right), \quad v_w = O\left(\frac{R^{-1}h}{\sqrt{\log R}}\right), \quad w_w = O\left(\frac{R^{-1}}{\sqrt{\log R}}\right), \quad p_w = O\left(\frac{R^{-1}}{\sqrt{\log R}}\right). \tag{10.2.65}$$

as a result of the matching conditions (10.2.55) from the core.

In this layer, we seek a balance between the inertial and viscous wave contributions in the streamwise momentum equation (10.1.4b):

$$\frac{\partial u_w}{\partial t} + U_v \frac{\partial u_w}{\partial x} \sim R^{-1} \frac{\partial^2 u_w}{\partial y^2}. \tag{10.2.66}$$

This requires that $R^{-1}h^{-2} = O(1)$, and gives the thickness of the layer to be of the order $R^{-1/2}$.

Writing

$$u_w = \frac{R^{-1}}{\sqrt{\log R}}\, u_+, \quad v_w = \frac{R^{-3/2}}{\sqrt{\log R}}\, v_+, \quad w_w = \frac{R^{-1}}{\sqrt{\log R}}\, w_+, \tag{10.2.67a}$$

$$p_w = \frac{R^{-1}}{\sqrt{\log R}}\, p_+, \quad y = 1 - R^{-1/2}\,\bar{y}_+, \tag{10.2.67b}$$

our expansions in this region are taken to be

$$u = 1 - R^{-1/2}\,\bar{y}\,\lambda_+^{(0)}(z) + \cdots + \frac{R^{-1}}{\sqrt{\log R}}\, u_+(y,z)\mathrm{e}^{\mathrm{i}\alpha(x-ct)} + \cdots + c.c, \tag{10.2.68a}$$

$$v = \frac{R^{-3/2}}{\sqrt{\log R}}\, v_+(y,z)\mathrm{e}^{\mathrm{i}\alpha(x-ct)} + \cdots + c.c, \tag{10.2.68b}$$

$$w = \frac{R^{-1}}{\sqrt{\log R}}\, w_+(y,z)\mathrm{e}^{\mathrm{i}\alpha(x-ct)} + \cdots + c.c, \tag{10.2.68c}$$

$$p = \frac{R^{-1}}{\sqrt{\log R}}\, p_+(y,z)\mathrm{e}^{\mathrm{i}\alpha(x-ct)} + \cdots + c.c. \tag{10.2.68d}$$

Substituting these expansions into the Navier-Stokes equations (10.1.4), we obtain the wave equations

$$\mathrm{i}\alpha_0 u_+ - \frac{\partial v_+}{\partial \bar{y}_+} + \frac{\partial w_+}{\partial z} = 0, \tag{10.2.69a}$$

$$\frac{\partial^2 u_+}{\partial \bar{y}_+^2} - 2\mathrm{i}\alpha_0 u_+ = \mathrm{i}\alpha_0 p_+, \tag{10.2.69b}$$

$$p_+ = p_+(z), \tag{10.2.69c}$$

$$\frac{\partial^2 w_+}{\partial \bar{y}_+^2} - 2\mathrm{i}\alpha_0 w_+ = \frac{\mathrm{d}p_+}{\mathrm{d}z}. \tag{10.2.69d}$$

These are solved subject to no-slip conditions on $\bar{y}_+ = 0$ and matching conditions (10.2.55) as $\bar{y}_+ \to \infty$, giving

$$u_+ = -\frac{P_+(z)}{2}\left(1 - \mathrm{e}^{-m\bar{y}_+}\right), \quad v_+ = \frac{\mathrm{i}}{2\alpha_0}\left(P_+''(z) - \alpha_0^2 P_+(z)\right)\left(\bar{y}_+ + \frac{\mathrm{e}^{-m\bar{y}_+}}{m} - \frac{1}{m}\right),$$
$$w_+ = \frac{\mathrm{i}P_+'(z)}{2\alpha_0}\left(1 - \mathrm{e}^{-m\bar{y}_+}\right), \quad p_+ = P_+(z), \tag{10.2.70a}$$
$$m = \sqrt{\alpha_0}(1+\mathrm{i}).$$

This completes the formulation of the three-zone asymptotic structure, and we now concentrate on finding solutions to the vortex-wave interaction equations, which we restate here for convenience.

We seek a solution to the core vortex equations (10.2.57),

$$\frac{\partial v_v}{\partial y} + \frac{\partial w_v}{\partial z} = 0, \tag{10.2.71a}$$
$$v_v\frac{\partial u_v}{\partial y} + w_v\frac{\partial u_v}{\partial z} = \frac{\partial^2 u_v}{\partial y^2} + \frac{\partial^2 u_v}{\partial z^2}, \tag{10.2.71b}$$
$$v_v\frac{\partial v_v}{\partial y} + w_v\frac{\partial v_v}{\partial z} = -\frac{\partial p_v}{\partial y} + \frac{\partial^2 v_v}{\partial y^2} + \frac{\partial^2 v_v}{\partial z^2}, \tag{10.2.71c}$$
$$v_v\frac{\partial w_v}{\partial y} + w_v\frac{\partial w_v}{\partial z} = -\frac{\partial p_v}{\partial z} + \frac{\partial^2 w_v}{\partial y^2} + \frac{\partial^2 w_v}{\partial z^2}. \tag{10.2.71d}$$

which are to be solved subject to (10.2.58),

$$u_v \to -1, \ v_v \to 0, \ w_v \to -\frac{q(z)}{3} \text{ as } y \to -1. \tag{10.2.72}$$

The wave influences the spanwise roll flow through the boundary conditions (10.2.72), with $q(z)$ being defined in (10.2.42):

$$q = \frac{1}{{\alpha_0}^2\lambda(z)^2}\left[{\alpha_0}^2\frac{\mathrm{d}}{\mathrm{d}z}\left(p_- p_-^*\right) + \frac{\mathrm{d}}{\mathrm{d}z}\left(\frac{\mathrm{d}p_-}{\mathrm{d}z}\frac{\mathrm{d}p_-^*}{\mathrm{d}z}\right)\right]. \tag{10.2.73}$$

The wave pressure p_- is governed by the the pressure equation (10.2.34)

$$\frac{\mathrm{d}^2 p_-}{\mathrm{d}z^2} - \frac{1}{\lambda(z)}\frac{\mathrm{d}\lambda}{\mathrm{d}z}\mathscr{F}(s)\frac{\mathrm{d}p_-}{\mathrm{d}z} + p_-(z)\left[-{\alpha_0}^2 + \frac{(\alpha_0\lambda(z))^{5/3}}{K_0 - {\alpha_0}^2 m_0}g(s)\right] = 0, \tag{10.2.74}$$

with $s = \mathrm{i}^{5/3}\xi_0$ and ξ_0 defined in (10.2.21). The functions $g(s)$ and $\mathscr{F}(s)$ are defined in (10.2.35). The pressure equation (10.2.74) is to be solved subject to periodic boundary conditions

$$p_-(0) = p_-(2\pi), \qquad \left.\frac{\mathrm{d}p_-}{\mathrm{d}z}\right|_{z=0} = \left.\frac{\mathrm{d}p_-}{\mathrm{d}z}\right|_{z=2\pi}. \tag{10.2.75}$$

We see (10.2.74) is influenced by the streak flow via the presence of the shear term $\lambda(z)$,

$$\lambda(z) = \left.\frac{\partial u_v}{\partial y}\right|_{y=-1}. \tag{10.2.76}$$

We make initial progress in solving these interactive equations by assuming that the wave forcing is small. We then turn to numerical methods to obtain a solution when the size of this forcing is gradually increased.

10.3 An analytic approach: small wave expansion

Our focus lies in solving the core roll equations (10.2.57) subject to the conditions (10.2.58b) and (10.2.61), where q is defined in (10.2.42) and p_- is a solution to the pressure equation (10.2.34). This solution is influenced by the streak flow, which in turn is forced by the roll.

It is a difficult task to solve this interactive system analytically. We make progress by considering a wave forcing in the lower layer that has small amplitude and is of the form

$$p_-(z) = \delta p_0 \cos(\beta z) + \cdots, \tag{10.3.1}$$

where δ is small, p_0 is a complex constant and β is real.

Since δ is small, we anticipate that the streak will be a perturbation to planar Couette flow, so that $u_v = y + \cdots$. The shear term $\lambda(z)$ is thus taken to be unity at leading order. Writing

$$\alpha_0 = \overline{\alpha}_0 + \cdots, \quad c_0 = \overline{c}_0 + \cdots, \quad \lambda(z) = 1 + \cdots, \quad s = \overline{s}_0 + \cdots, \tag{10.3.2}$$

an order of magnitude analysis of the pressure wave equation (10.2.34) results in the following relation for the leading order wavenumber:

$$-\overline{\alpha}_0^2 + \frac{\overline{\alpha}_0^{5/3} g(\overline{s}_0)}{K_0 - \overline{\alpha}_0^2 m_0} = \beta^2. \tag{10.3.3}$$

We remark that the middle term on the left-hand side of (10.2.34) does not contribute at leading order.

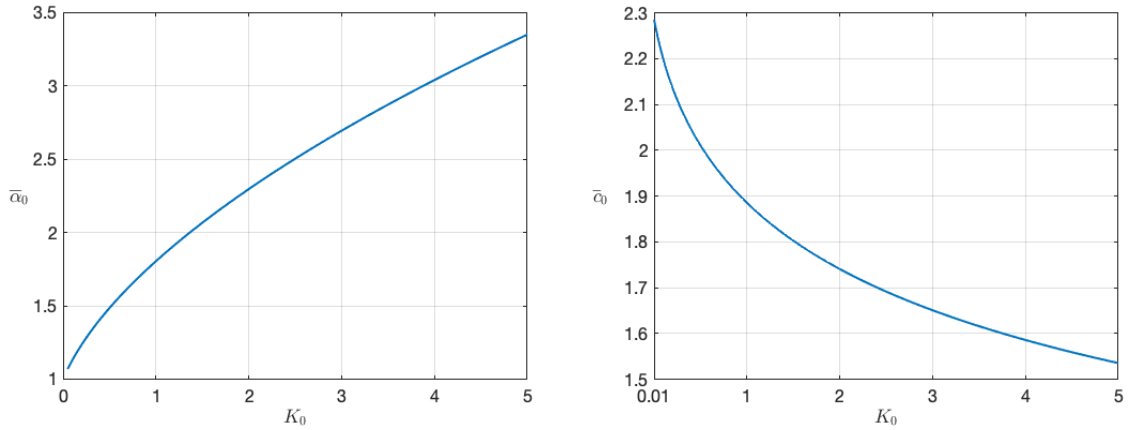

Figure 10.3.1: Depiction of $\overline{\alpha}_0$ (left) and $\overline{c}_0$ (right) as K_0 varies, for fixed $m_0 = 0.5$ and $\beta = 1$.

In order for relation (10.3.3) to hold, we require $g(s)$ (10.2.35) to be real at leading order, so that $\mathrm{Im}(g(\overline{s}_0)) = 0$. This reveals that $\overline{s}_0 \approx 2.2972$ (see figure A.0.1). It is possible to write (10.3.3) as a 12^{th} order polynomial in $\overline{\alpha_0}^{1/3}$, specifically

$$m_0\overline{\alpha}_0^4 + (\beta^2 m_0 - K_0)\overline{\alpha}_0^2 + g(\overline{s}_0)\overline{\alpha}_0^{5/3} - \beta^2 K_0 = 0. \tag{10.3.4}$$

This can thus be readily solved using a polynomial root solver, and we find that there exists at least one positive solution for $\overline{\alpha}_0^{1/3}$, and hence $\overline{\alpha}_0$. Recalling $s = \mathrm{i}^{5/3}\xi_0$ for ξ_0 defined in (10.2.21), s is given by

$$s = \frac{\alpha_0 c_0}{(\alpha_0 \lambda)^{2/3}}. \tag{10.3.5}$$

We use this to solve for $\overline{c}_0$ and obtain

$$\overline{c}_0 = \frac{\overline{s}_0}{\overline{\alpha}_0^{1/3}}. \tag{10.3.6}$$

In figure 10.3.1, we illustrate solutions of (10.3.3) and (10.3.6) for the leading order wavenumber and wavespeed when K_0 varies with fixed $m_0 = 0.5$ and $\beta = 1$. We see that $\overline{\alpha}_0$ increases as the lower plate becomes more rigid, whilst $\overline{c}_0$ appears to decrease.

In the remainder of this section, we will focus on a pressure disturbance wave with spanwise wavenumber $\beta = 1$, that is

$$p_-(z) = \delta p_0 \cos(z) + \cdots, \tag{10.3.7}$$

and investigate the vortex-wave interaction that arises.

To leading order, this form of p_- yields

$$q(z) = \delta^2 q_0 \sin(2z) + \cdots, \quad q_0 = \frac{|p_0|^2 (1 - \overline{\alpha}_0^2)}{\overline{\alpha}_0^2} \tag{10.3.8}$$

upon recollection of the definition of $q(z)$ (10.2.42).

We investigate how this forcing drives the roll/streak solution in the core. In light of the boundary condition (10.2.61), the scaling of $q(z)$ suggests that the core quantity w_v is such that $w_v = O(\delta^2)$. The continuity equation (10.2.71a) then indicates that $v_v = O(\delta^2)$, and after considering the streak equation (10.2.57b), we take $u_v = y + O(\delta^2)$. Finally, the normal momentum equation (10.2.57c) suggests $p_v = O(\delta^2)$.

We thus write

$$u_v = y + \delta^2 u_1(y,z) + \cdots, \qquad v_v = \delta^2 v_1(y,z) + \cdots, \tag{10.3.9}$$

$$w_v = \delta^2 w_1(y,z) + \cdots, \qquad p_v = \delta^2 p_1(y,z) + \cdots. \tag{10.3.10}$$

Substituting these scalings into the core equations (10.2.57), the leading order roll/streak equations governing the core region are the linear equations

$$\frac{\partial v_1}{\partial y} + \frac{\partial w_1}{\partial z} = 0, \tag{10.3.11a}$$

$$\frac{\partial^2 u_1}{\partial y^2} + \frac{\partial^2 u_1}{\partial z^2} = v_1, \tag{10.3.11b}$$

$$\frac{\partial^2 v_1}{\partial y^2} + \frac{\partial^2 v_1}{\partial z^2} = \frac{\partial p_1}{\partial y}, \tag{10.3.11c}$$

$$\frac{\partial^2 w_1}{\partial y^2} + \frac{\partial^2 w_1}{\partial z^2} = \frac{\partial p_1}{\partial z}. \tag{10.3.11d}$$

These are subject to the matching conditions (10.2.58) and (10.2.61), giving

$$u_1 \to 0, \quad v_1 \to 0, \quad w_1 \sim -\frac{1}{3}|p_0|^2 \left(\frac{1}{\overline{\alpha}_0^2} - 1\right) \sin(2z) \quad \text{as } y \to -1 \tag{10.3.12}$$

as we approach the flexible surface, and

$$u_1 \to 0, \quad v_1 \to 0, \quad w_1 \to 0 \quad \text{as } y \to 1 \tag{10.3.13}$$

as we approach the rigid surface.

The form of q (10.3.8) suggests an ansatz for $w_1(y,z)$ that behaves as

$$w_1 = -\frac{1}{3}|p_0|^2 \left(\frac{1}{\overline{\alpha}_0^2} - 1\right) \frac{\mathrm{d}F}{\mathrm{d}y} \sin(2z), \tag{10.3.14}$$

where $F(y)$ is to be determined. The continuity equation (10.3.11a) then requires

$$v_1 = \frac{2}{3}|p_0|^2 \left(\frac{1}{\overline{\alpha}_0^2} - 1\right) F(y)\cos(2z). \tag{10.3.15}$$

Cross-differentiation of (10.3.11c) and (10.3.11d) to eliminate the roll pressure results in the third order partial differential equation

$$\frac{\partial^3 v_1}{\partial z^3} + \frac{\partial^3 v_1}{\partial y^2 \partial z} - \frac{\partial^3 w_1}{\partial y \partial z^2} - \frac{\partial^3 w_1}{\partial y^3} = 0. \tag{10.3.16}$$

Substituting w_1 and v_1, we obtain a fourth order homogeneous differential equation for $F(y)$, namely

$$\frac{\mathrm{d}^4 F}{\mathrm{d}y^4} - 8\frac{\mathrm{d}^2 F}{\mathrm{d}y^2} + 16F(y) = 0. \tag{10.3.17}$$

The boundary conditions (10.3.12) and (10.3.13) necessitate that

$$F(-1) = 0, \qquad F(1) = 0, \qquad F'(-1) = 1, \qquad F'(1) = 0. \tag{10.3.18}$$

Solving for $F(y)$, we find

$$F(y) = C_1 \mathrm{e}^{2y} + C_2 \mathrm{e}^{-2y} + C_3 y \mathrm{e}^{2y} + C_4 y \mathrm{e}^{-2y}, \tag{10.3.19}$$

where

$$\begin{aligned} C_1 &= -\frac{9 - \mathrm{e}^{-8}}{\mathrm{e}^6 - 66\mathrm{e}^{-2} + \mathrm{e}^{-10}}, \quad C_2 = \frac{1 + 7\mathrm{e}^{-8}}{\mathrm{e}^2 - 66\mathrm{e}^{-6} + \mathrm{e}^{-14}}, \\ C_3 &= \frac{7 + \mathrm{e}^{-8}}{\mathrm{e}^6 - 66\mathrm{e}^{-2} + \mathrm{e}^{-10}}, \quad C_4 = \frac{1 - 9\mathrm{e}^{-8}}{\mathrm{e}^2 - 66\mathrm{e}^{-6} + \mathrm{e}^{-14}}. \end{aligned} \tag{10.3.20}$$

The roll flow forces the streak, as described by the streak equation (10.3.11b). Solving (10.3.11b) subject to (10.3.12) and (10.3.13), we then have

$$u_1 = -\frac{1}{3}|p_0|^2 \left(\frac{1}{\overline{\alpha}_0^2} - 1\right) R(y)\cos(2z), \tag{10.3.21}$$

where

$$R(y) = C_5 \mathrm{e}^{2y} + C_6 \mathrm{e}^{-2y} + \left[-\frac{C_3}{4}y^2 + \left(\frac{C_3}{8} - \frac{C_1}{2}\right)y\right]\mathrm{e}^{2y} + \left[\frac{C_4}{4}y^2 + \left(\frac{C_4}{8} + \frac{C_2}{2}\right)y\right]\mathrm{e}^{-2y}, \tag{10.3.22}$$

$$C_5 = -\frac{39 + 90\mathrm{e}^{-8} - \mathrm{e}^{-16}}{8\left(\mathrm{e}^6 - 67\mathrm{e}^{-2} + 67\mathrm{e}^{-10} - \mathrm{e}^{-18}\right)}, \quad C_6 = \frac{3 + 130\mathrm{e}^{-8} - 5\mathrm{e}^{-16}}{8\left(\mathrm{e}^2 - 67\mathrm{e}^{-6} + 67\mathrm{e}^{-14} - \mathrm{e}^{-22}\right)}. \tag{10.3.23}$$

We are now able to determine the behaviour of $\lambda_1(z)$ as

$$\lambda_1(z) = \frac{\partial u_1}{\partial y}\bigg|_{y=-1} = \overline{\lambda}_1 \cos(2z), \tag{10.3.24}$$

where

$$\overline{\lambda}_1 = -\frac{1}{3}|p_0|^2 \left(\frac{1}{\overline{\alpha}_0^2} - 1\right)\left(\frac{1}{8} - \frac{24 + 40\mathrm{e}^{-8}}{\mathrm{e}^8 - 67 + 67\mathrm{e}^{-8} - \mathrm{e}^{-6}}\right). \tag{10.3.25}$$

A maximal-interactions approach when exploring the pressure wave equation (10.2.34) suggests the expansions

$$\alpha_0 = \overline{\alpha}_0 + \delta^2\overline{\alpha}_1 + \cdots, \qquad c_0 = \overline{c}_0 + \delta^2\overline{c}_1 + \cdots, \tag{10.3.26a}$$

$$p_-(z) = \delta p_0 \cos(z) + \delta^3 p_-^{(1)}(z) + \cdots. \tag{10.3.26b}$$

Upon substitution of (10.3.26), the pressure equation (10.2.34) yields at the next order

$$p_-^{(1)\prime\prime}(z) + p_-^{(1)}(z) = L_1 \sin(2z)\sin(z) + L_2\cos(z) + L_3\cos(2z)\cos(z) \tag{10.3.27}$$

where

$$L_1 = 2p_0\mathscr{F}(\overline{s}_0)\overline{\lambda}_1, \tag{10.3.28}$$

$$\begin{aligned} L_2 = -p_0\Bigg[&- 2\overline{\alpha}_0\,\overline{\alpha}_1 + \frac{2m_0}{\left(K_0 - \overline{\alpha}_0^2 m_0\right)^2} g(\overline{s}_0)\overline{\alpha}_0^{8/3}\overline{\alpha}_1 \\ &+ \frac{1}{K_0 - \overline{\alpha}_0^2 m_0}\overline{\alpha}_0^{5/3} g'(\overline{s}_0)\left(\overline{\alpha}_0^{1/3}\overline{c}_1 + \frac{\overline{c}_0\,\overline{\alpha}_1}{3\overline{\alpha}_0^{2/3}}\right) + \frac{5}{3(K_0 - \overline{\alpha}_0^2 m_0)} g(\overline{s}_0)\overline{\alpha}_0^{2/3}\overline{\alpha}_1\Bigg], \end{aligned} \tag{10.3.29}$$

$$L_3 = \frac{-p_0\overline{\lambda}_1}{3(K_0 - \overline{\alpha}_0^2 m_0)}\left[5g(\overline{s}_0)\overline{\alpha}_0^{5/3} - 2g'(\overline{s}_0)\overline{\alpha}_0^2\overline{c}_0\right], \tag{10.3.30}$$

with $g(s)$ and $\mathscr{F}(s)$ defined in (10.2.35).

The corrections $\overline{\alpha}_1$ and $\overline{c}_0$ are determined by imposing the appropriate boundary conditions on $p_-^{(1)}(z)$. Since the pressure equation (10.2.34) is linear, we may take

$$p_-(0) = p_-(2\pi) = \delta p_0 \tag{10.3.31}$$

without loss of generality. We also require $p_1'(z)$ to be periodic. Therefore we impose

$$p_-^{(1)}(0) = p_-^{(1)}(2\pi) = 0, \qquad p_-^{(1)\prime}(0) = p_-^{(1)\prime}(2\pi). \tag{10.3.32}$$

We seek an even solution to (10.3.27), which leads us to

$$p_-^{(1)}(z) = \frac{L_3 - L_1}{16}\left(\cos(z) - \cos(3z)\right), \tag{10.3.33}$$

where we have enforced

$$L_1 + 2L_2 + L_3 = 0. \tag{10.3.34}$$

in order to satisfy the conditions (10.3.32).

This complex-valued equation is linear in $\overline{\alpha}_1$ and $\overline{c}_1$. For a fixed spring stiffness and mass, the relation (10.3.34) provides us with two equations that can be solved uniquely for $\overline{\alpha}_1$ and $\overline{c}_1$. These solutions are depicted in figure 10.3.2 for various K_0 and fixed $m_0 = 0.5$, $p_0 = 1$ and $\beta = 1$. Both $\overline{\alpha}_1$ and $\overline{c}_1$ are negative for small values of K_0, and eventually become positive as K_0 is increased.

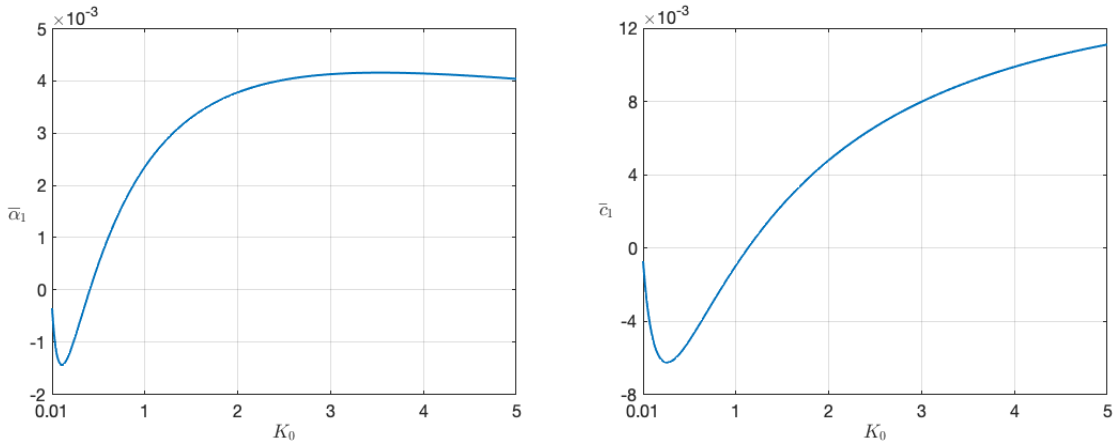

Figure 10.3.2: Depiction of $\overline{\alpha}_1$ (left) and $\overline{c}_1$ (right) as K_0 varies, for fixed $p_0 = 1, m_0 = 0.5$ and $\beta = 1$.

The pressure solution (10.3.33) enables us to determine the forcing q at the subsequent order:

$$q = \delta^2 q_0 \sin(2z) + \delta^4\left(q_{11}\sin(2z) + q_{12}\sin(4z)\right) + \cdots, \tag{10.3.35}$$

with

$$q_{11} = \frac{(L_3 - L_1)p_0^* + (L_3^* - L_1^*)p_0}{4\overline{\alpha}_0^2} - \frac{2|p_0|^2\,\overline{\alpha}_1}{\overline{\alpha}_0^3}, \tag{10.3.36a}$$

$$q_{12} = \overline{\lambda}_1|p_0|^2\left(1 - \frac{1}{\overline{\alpha}_0^2}\right) + \frac{(L_3 - L_1)p_0^*}{8}\left(1 - \frac{3}{\overline{\alpha}_0^2}\right) + \frac{(L_3^* - L_1^*)p_0}{8}\left(1 - \frac{3}{\overline{\alpha}_0^2}\right). \tag{10.3.36b}$$

Guided by the matching condition (10.2.61) between the core and lower wall layer, we anticipate that $w_v = \delta^2 w_1(y,z) + \delta^4 w_2(y,z) + \cdots$. It is possible to repeat the process carried out above to obtain higher order terms in our roll/streak expansions.

10.4 Numerical Investigations

The analytical work in the previous section guides our numerical exploration of the self-sustaining processes in the flow.

We briefly give an overview of our numerical method here, and discuss each step in more detail in the subsequent sections. Our procedure involves iterating over the core region's boundary forcing $q(z)$ for a fixed spring stiffness and mass. Given an initial guess $q(z)$, the nonlinear core roll equations (10.2.71, 10.2.72) are solved using a fixed point iteration scheme. This is done via a Fourier decomposition of the flow components in z, and a finite differencing method in y. Once we have the roll solution, we are able to determine the behaviour of the streak and thus find $\lambda(z)$ through use of (10.2.76). This is fed into the wave pressure equation (10.2.74). We now look for α_0 and c_0 such that equation (10.2.74) admits an even, periodic solution for the wave pressure in the lower wall layer with $p_-(0) = \delta$ for some fixed real δ. This solution to $p_-(z)$ is used to calculate an updated $q(z)$ using (10.2.73), and we repeat this procedure until q converges. This process comprises of a fixed point iteration scheme for $q(z)$.

For small values of δ, the initial guess used for q is provided by our small amplitude analysis in Section 10.3, specifically expression (10.3.8) with use of (10.3.4). For larger δ, a more appropriate initial guess is the converged $q(z)$ from the solution for a slightly smaller value of δ. This procedure forms a continuation in δ.

10.4.1 Core roll/streak solution

This section details the procedure for solving the core roll equations (10.2.71), which we repeat here for ease:

$$\frac{\partial v_v}{\partial y} + \frac{\partial w_v}{\partial z} = 0, \tag{10.4.1a}$$

$$v_v \frac{\partial u_v}{\partial y} + w_v \frac{\partial u_v}{\partial z} = \frac{\partial^2 u_v}{\partial y^2} + \frac{\partial^2 u_v}{\partial z^2}, \tag{10.4.1b}$$

$$v_v \frac{\partial v_v}{\partial y} + w_v \frac{\partial v_v}{\partial z} = -\frac{\partial p_v}{\partial y} + \frac{\partial^2 v_v}{\partial y^2} + \frac{\partial^2 v_v}{\partial z^2}, \tag{10.4.1c}$$

$$v_v \frac{\partial w_v}{\partial y} + w_v \frac{\partial w_v}{\partial z} = -\frac{\partial p_v}{\partial z} + \frac{\partial^2 w_v}{\partial y^2} + \frac{\partial^2 w_v}{\partial z^2}. \tag{10.4.1d}$$

These are to be solved subject to the conditions (10.2.72)

$$u_v \to -1,\ w_v \to -\frac{q(z)}{3},\ v_v \to 0 \text{ as } y \to -1, \tag{10.4.2a}$$

$$u_v \to 1,\ w_v \to 0,\ v_v \to 0 \text{ as } y \to 1, \tag{10.4.2b}$$

where $q(z)$ is considered to be a prescribed function here.

We first describe how we solve for the roll flow, and subsequently detail the solution procedure for the streak flow.

Calculating the roll flow

With some manipulation, cross-differentiation of (10.4.1c) and (10.4.1d) to eliminate the roll pressure and subsequent use of the continuity equation (10.4.1a) results in

$$v_v\frac{\partial^2 v_v}{\partial y\partial z} + w_v\frac{\partial^2 v_v}{\partial z^2} - v_v\frac{\partial^2 w_v}{\partial y^2} - w_v\frac{\partial^2 w_v}{\partial y\partial z} = 2\frac{\partial^3 v_v}{\partial y^2\partial z} + \frac{\partial^3 v_v}{\partial z^3} - \frac{\partial^3 w_v}{\partial y^3}. \tag{10.4.3}$$

We begin by expanding the flow components in Fourier series:

$$u_v = y + \tilde{U}_0(y) + \sum_{n=1}^{N} U_n(y)\,\mathrm{e}^{\mathrm{i}nz} + \sum_{n=1}^{N} U_n^*(y)\,\mathrm{e}^{-\mathrm{i}nz}, \tag{10.4.4a}$$

$$v_v = V_0(y) + \sum_{n=1}^{N} V_n(y)\,\mathrm{e}^{\mathrm{i}nz} + \sum_{n=1}^{N} V_n^*(y)\,\mathrm{e}^{-\mathrm{i}nz}, \tag{10.4.4b}$$

$$w_v = W_0(y) + \sum_{n=1}^{N} W_n(y)\,\mathrm{e}^{\mathrm{i}nz} + \sum_{n=1}^{N} W_n^*(y)\,\mathrm{e}^{-\mathrm{i}nz}, \tag{10.4.4c}$$

$$p_v = P_0(y) + \sum_{n=1}^{N} P_n(y)\,\mathrm{e}^{\mathrm{i}nz} + \sum_{n=1}^{N} P_n^*(y)\,\mathrm{e}^{-\mathrm{i}nz}. \tag{10.4.4d}$$

The behaviour of the 0^{th} harmonic $V_0(y)$ can be determined analytically, and then used to simplify our expressions for the higher harmonics. We therefore begin by seeking a solution for V_0. Substituting the decomposition (10.4.4b) into the continuity equation (10.4.1a) and matching condition (10.4.2a), the behaviour V_0 is found to be governed by

$$\frac{\mathrm{d}V_0}{\mathrm{d}y} = 0, \quad V_0(-1) = 0, \tag{10.4.5a}$$

which reveals that $V_0 \equiv 0$ for $-1 \le y \le 1$.

With this simplification, substitution of (10.4.4c) into (10.4.1d) gives

$$\frac{\mathrm{d}^2 W_0}{\mathrm{d}y^2} = \sum_{n=1}^{N} V_n^* \frac{\mathrm{d}W_n}{\mathrm{d}y} + c.c.. \tag{10.4.6}$$

The boundary conditions for W_0 will be specified shortly.

Substitution of (10.4.4) into (10.4.1a) and (10.4.3) results in the following set of nonlinear partial differential equations for the higher harmonics in the roll flow. The appropriate boundary conditions arise from (10.4.2). The higher harmonics are governed by

$$\frac{\mathrm{d}V_n}{\mathrm{d}y} + \mathrm{i}nW_n(y) = 0 \quad (n = 1, \cdots, N), \tag{10.4.7a}$$

$$\begin{aligned}
&\frac{\mathrm{d}^3 W_n}{\mathrm{d}y^3} - \mathrm{i}nW_0 \frac{\mathrm{d}W_n}{\mathrm{d}y} - 2\mathrm{i}n \frac{\mathrm{d}^2 V_n}{\mathrm{d}y^2} - n^2 W_0 V_n - \frac{\mathrm{d}^2 W_0}{\mathrm{d}y^2} V_n + \mathrm{i}n^3 V_n \\
&+ \sum_{k=1}^{n-1} \left\{ \mathrm{i}(n-k) V_k \frac{\mathrm{d}V_{n-k}}{\mathrm{d}y} - (n-k)^2 V_{n-k} W_k - V_k \frac{\mathrm{d}^2 W_{n-k}}{\mathrm{d}y^2} - \mathrm{i}(n-k) W_k \frac{\mathrm{d}W_{n-k}}{\mathrm{d}y} \right\} \\
&+ \sum_{k=n+1}^{N} \left\{ -\mathrm{i}(k-n) V_k \frac{\mathrm{d}V_{k-n}^*}{\mathrm{d}y} - (k-n)^2 V_{k-n}^* W_k - V_k \frac{\mathrm{d}^2 W_{k-n}^*}{\mathrm{d}y^2} + \mathrm{i}(k-n) W_k \frac{\mathrm{d}W_{k-n}^*}{\mathrm{d}y} \right\} \\
&+ \sum_{k=1}^{N-n} \left\{ \mathrm{i}(k+n) V_k^* \frac{\mathrm{d}V_{k+n}}{\mathrm{d}y} - (k+n)^2 V_{k+n} W_k^* - V_k^* \frac{\mathrm{d}^2 W_{k+n}}{\mathrm{d}y^2} - \mathrm{i}(k+n) W_k^* \frac{\mathrm{d}W_{k+n}}{\mathrm{d}y} \right\} = 0, \\
&\qquad (n = 2, ..., N-1)
\end{aligned} \tag{10.4.7b}$$

The equations encapsulating the behaviour of W_1 and W_N are respectively given by

$$\begin{aligned}
&\frac{\mathrm{d}^3 W_1}{\mathrm{d}y^3} - \mathrm{i}W_0 \frac{\mathrm{d}W_1}{\mathrm{d}y} - 2\mathrm{i} \frac{\mathrm{d}^2 V_1}{\mathrm{d}y^2} + \mathrm{i}V_0 \frac{\mathrm{d}V_1}{\mathrm{d}y} - W_0 V_1 - \frac{\mathrm{d}^2 W_0}{\mathrm{d}y^2} V_1 + \mathrm{i}V_1 + \\
&\sum_{k=2}^{N} \left\{ -\mathrm{i}(k-1) V_k \frac{\mathrm{d}V_{k-1}^*}{\mathrm{d}y} - (k-1)^2 V_{k-1}^* W_k - V_k \frac{\mathrm{d}^2 W_{k-1}^*}{\mathrm{d}y^2} + \mathrm{i}(k-1) W_k \frac{\mathrm{d}W_{k-1}^*}{\mathrm{d}y} \right\} + \\
&\sum_{k=1}^{N-1} \left\{ \mathrm{i}(k+1) V_k^* \frac{\mathrm{d}V_{k+1}}{\mathrm{d}y} - (k+1)^2 V_{k+1} W_k^* - V_k^* \frac{\mathrm{d}^2 W_{k+1}}{\mathrm{d}y^2} - \mathrm{i}(k+1) W_k^* \frac{\mathrm{d}W_{k+1}}{\mathrm{d}y} \right\} = 0,
\end{aligned} \tag{10.4.8a}$$

$$\begin{aligned}
&\frac{\mathrm{d}^3 W_N}{\mathrm{d}y^3} - \mathrm{i}NW_0 \frac{\mathrm{d}W_N}{\mathrm{d}y} - 2\mathrm{i}N \frac{\mathrm{d}^2 V_N}{\mathrm{d}y^2} - N^2 W_0 V_N - \frac{\mathrm{d}^2 W_0}{\mathrm{d}y^2} V_N + \mathrm{i}N^3 V_N \\
&+ \sum_{k=1}^{N-1} \left\{ \mathrm{i}(N-k) V_k \frac{\mathrm{d}V_{N-k}}{\mathrm{d}y} - (N-k)^2 V_{N-k} W_k - V_k \frac{\mathrm{d}^2 W_{N-k}}{\mathrm{d}y^2} - \mathrm{i}(N-k) W_k \frac{\mathrm{d}W_{N-k}}{\mathrm{d}y} \right\} = 0.
\end{aligned} \tag{10.4.8b}$$

This system of equations is subject to

$$V_n(-1) = 0, \quad V_n(1) = 0 \quad (n = 1, ..., N), \tag{10.4.9a}$$

$$W_n(-1) = -\frac{1}{3}q_n, \quad W_n(1) = 0 \quad (n = 0, ..., N), \tag{10.4.9b}$$

where q_n is the amplitude of the n^{th} harmonic of $q(z)$. Specifically,

$$q = q_0 + \sum_{n=1}^{N} q_n \mathrm{e}^{\mathrm{i}nz} + \sum_{n=1}^{N} q_n^* \mathrm{e}^{-\mathrm{i}nz}. \tag{10.4.10}$$

Discretising the domain in the wall normal direction with J equally-spaced points, we define

$$y_j = -1 + (j-1)h, \quad h = \frac{2}{J-1} \quad (j = 1, ..., J). \tag{10.4.11}$$

With this discretisation, y_1 corresponds to the lower compliant wall and y_J to the upper rigid wall. The boundary conditions (10.4.9) thus become

$$V_n(y_1) = 0, \quad V_n(y_J) = 0 \quad (n = 1, ..., N), \tag{10.4.12a}$$

$$W_n(y_1) = -\frac{1}{3}q_n, \quad W_n(y_J) = 0 \quad (n = 0, ..., N), \tag{10.4.12b}$$

We use a second-order finite differencing method to approximate the derivatives in (10.4.6)-(10.4.8). A central difference scheme was used for interior points, whilst a one-sided scheme was used for points near the boundaries when appropriate.

Moving all nonlinear terms in these discretised equations to the right-hand side, we can transform our system into the matrix equation

$$\mathbf{A}\mathbf{x} = \mathbf{f}(\mathbf{x}), \tag{10.4.13}$$

where the vector $\mathbf{x}$ has length $2(N+1)J$ and contains the unknowns of our system:

$$\mathbf{x}_{2nJ+j} = V_n(y_j), \quad \mathbf{x}_{2nJ+J+j} = W_n(y_j) \quad n = 0, .., N, \;\; j = 1, ..., J. \tag{10.4.14}$$

The square matrix $\mathbf{A}$ of order $2(N+1)J$ is fully known and pertains only to the linear terms in our discretised equations. Of length $2(N+1)J$, the vector $\mathbf{f}(\mathbf{x})$ contains the nonlinear terms of the equations. We briefly detail their composition here. Rows $(2nJ+1)$ and $(2nJ+J)$ correspond to the boundary conditions for V_n at $y = y_1$ and $y = y_J$ respectively. The intermediate rows (i.e rows $(2nJ+j)$ for $j = 2, ..., J-1$) correspond to the n^{th} harmonic discretised continuity equation at $y = y_j$. The remaining rows are associated with the spanwise harmonics in a similar manner, with rows $(2nJ+J+1)$ and $(2nJ+J+J)$ being reserved for the boundary conditions of W_n at $y = y_1$ and $y = y_J$ respectively. Rows $(2nJ+J+j)$ for $j = 2, ..., J-1$ correspond to the discretised equations governing W_n at $y = y_j$.

Along each row of the matrix $\mathbf{A}$, the coefficient of $V_n(y_j)$ in the appropriate discretised equation belongs in column $2nJ + j$ and similarly, the coefficient of $W_n(y_j)$ belongs in column $2nJ + J + j$.

We solve for the roll flow using a fixed point iteration method so that at each iteration k, we have

$$\mathbf{A}\mathbf{x}^{(k)} = \mathbf{f}(\mathbf{x}^{(k-1)}), \quad k = 1, 2, ... \tag{10.4.15}$$

We use an inbuilt MATLAB function to solve (10.4.15) for $\mathbf{x}^{(k)}$. One possible choice for the initial guess $\mathbf{x}^{(0)}$ is given by neglecting all non-linear terms and solving $\mathbf{A}\mathbf{x}^{(0)} = \mathbf{b}$, where $\mathbf{b}$ is a vector containing information only about the roll boundary conditions. Specifically, we have

$$\mathbf{b}_{2nJ+J+1} = -\frac{1}{3}q_n \tag{10.4.16}$$

with all other entries being zero. If the value of δ is not small, it is reasonable to use the converged roll solution for a slightly smaller value of δ as the initial guess $\mathbf{x}^{(0)}$.

At the k^{th} iteration, we calculate the energy

$$E^{(k)}(y_j) = \sum_{n=0}^{N} \left\{ \left| V_n^{(k)}(y_j) \right|^2 + \left| W_n^{(k)}(y_j) \right|^2 \right\}, \quad j = 1, .., J-1 \tag{10.4.17}$$

and continue iterating on the roll flow solution until the quantity

$$\max_{1 \le j \le J-1} \frac{E^{(k)}(y_j) - E^{(k-1)}(y_j)}{E^{(k-1)}(y_j)} \tag{10.4.18}$$

is below a desired tolerance.

Once this fixed-point iteration scheme converges, we have a solution for the roll flow and can seek the behaviour of the streak flow. Typically, less than 10 iterations were required for convergence.

Calculating the streak flow

To determine the streak behaviour, it is convenient to define the sums

$$S_1(n; y) = \sum_{k=1}^{n-1} \left\{ -V_k \frac{\mathrm{d}U_{n-k}}{\mathrm{d}y} - \mathrm{i}(n-k) W_k U_{n-k} \right\}, \tag{10.4.19a}$$

$$S_2(n; y) = \sum_{k=n+1}^{N} \left\{ -V_k \frac{\mathrm{d}U_{k-n}^*}{\mathrm{d}y} + \mathrm{i}(k-n) W_k U_{k-n}^* \right\}, \tag{10.4.19b}$$

$$S_3(n; y) = \sum_{k=1}^{N-n} \left\{ -V_k^* \frac{\mathrm{d}U_{k+n}}{\mathrm{d}y} - \mathrm{i}(k+n) W_k^* U_{k+n} \right\}. \tag{10.4.19c}$$

Using this, upon substitution of the Fourier decomposition (10.4.4a) into the core streak equation (10.4.1b), we find that the streamwise harmonics are governed by

$$\frac{\mathrm{d}^2\tilde{U}_0}{\mathrm{d}y^2} + S_2(0;y) + S_3(0;y) = 0, \tag{10.4.20a}$$

$$\frac{\mathrm{d}^2U_1}{\mathrm{d}y^2} - U_1 - \mathrm{i}W_0U_1 - V_1\frac{\mathrm{d}\tilde{U}_0}{\mathrm{d}y} + S_2(1;y) + S_3(1;y) = V_1, \tag{10.4.20b}$$

$$\frac{\mathrm{d}^2U_n}{\mathrm{d}y^2} - n^2U_n - \mathrm{i}nW_0U_n - V_n\frac{\mathrm{d}\tilde{U}_0}{\mathrm{d}y} + S_1(n;y) + S_2(n;y) + S_3(n;y) = V_n \quad (n = 2, ..., N-1) \tag{10.4.20c}$$

$$\frac{\mathrm{d}^2U_N}{\mathrm{d}y^2} - N^2U_N - \mathrm{i}NW_0U_N - V_N\frac{\mathrm{d}\tilde{U}_0}{\mathrm{d}y} + S_1(N;y) = V_N. \tag{10.4.20d}$$

The corresponding boundary conditions are found by substitution of (10.4.4a) into (10.4.2):

$$\tilde{U}_0(1) = \tilde{U}_0(-1) = 0, \qquad U_n(1) = U_n(-1) = 0 \qquad (n = 1, ..., N). \tag{10.4.21}$$

Since the roll flow is now fully known, these $(N+1)$ equations are linear in the unknown, streak harmonics. We therefore use a different method to that used for the roll flow.

In order to accommodate the conjugated U_n in our numerical method, we consider this as a system containing $(2N+2)$ unknowns to be found, namely $\tilde{U}_0$, U_1, ..., U_N, $\tilde{U}_0^*$, U_1^*, ..., U_N^*. Solving for both U_n and U_n^* allows us to conveniently form a matrix equation that accommodates the coefficients of U_n and U_n^* in equations (10.4.20). We will discuss this matrix equation shortly.

We therefore need to supplement our system with another $(N+1)$ equations, along with the appropriate boundary conditions. These can be found by taking the conjugate of equations (10.4.20) and conditions (10.4.21):

$$\frac{\mathrm{d}^2\tilde{U}_0^{\,*}}{\mathrm{d}y^2} + S_2^*(0;y) + S_3^*(0;y) = 0, \tag{10.4.22a}$$

$$\frac{\mathrm{d}^2U_1^*}{\mathrm{d}y^2} - U_1^* + \mathrm{i}W_0^*U_1^* - V_1^*\frac{\mathrm{d}\tilde{U}_0^{\,*}}{\mathrm{d}y} + S_2^*(1;y) + S_3^*(1;y) = V_1^*, \tag{10.4.22b}$$

$$\frac{\mathrm{d}^2U_n^*}{\mathrm{d}y^2} - n^2U_n^* + \mathrm{i}nW_0^*U_n^* - V_n^*\frac{\mathrm{d}\tilde{U}_0^{\,*}}{\mathrm{d}y} + S_1^*(n;y) + S_2^*(n;y) + S_3^*(n;y) = V_n^* \quad (n = 2, ..., N-1) \tag{10.4.22c}$$

$$\frac{\mathrm{d}^2U_N^*}{\mathrm{d}y^2} - N^2U_N^* + \mathrm{i}NW_0^*U_N^* - V_N^*\frac{\mathrm{d}\tilde{U}_0^{\,*}}{\mathrm{d}y} + S_1^*(N;y) = V_N^*. \tag{10.4.22d}$$

$$\tilde{U}_0^{\,*}(1) = \tilde{U}_0^{\,*}(-1) = 0, \quad U_n^*(1) = U_n^*(-1) = 0 \quad (n = 1, ..., N). \tag{10.4.23}$$

We again use a second-order finite difference method, opting to use a central scheme for interior points and one-sided schemes near the boundaries. We discretise our domain $1 \leq y \leq 1$ using the same normal locations y_j (10.4.11) as used when solving for our roll flow. This choice ensures that the roll flow is known at the appropriate locations and no interpolation is necessary.

Upon finite differencing (10.4.20)-(10.4.23), we can write down the system as the matrix equation

$$\mathbf{Su} = \mathbf{t}. \tag{10.4.24}$$

Here, $\mathbf{S}$ is a known square matrix of size $2(N+1)J$, whose structure we discuss shortly. The vector of unknowns $\mathbf{u}$ is of length $2(N+1)J$ and is such that

$$\mathbf{u}_j = \tilde{U}_0(y_j), \quad \mathbf{u}_{(N+1)J+j} = \tilde{U}_0^*(y_j), \tag{10.4.25a}$$

$$\mathbf{u}_{nJ+j} = U_n(y_j), \quad \mathbf{u}_{(N+1)J+nJ+j} = U_n^*(y_j) \tag{10.4.25b}$$

for $n = 1, ..., N,\ j = 1, ..., J$. A fully known vector of length $2(N+1)J$, $\mathbf{t}$ is given by

$$\mathbf{t}_j = 0, \quad \mathbf{t}_{(N+1)J+j} = 0, \tag{10.4.26a}$$

$$\mathbf{t}_{nJ+j} = V_n(y_j), \quad \mathbf{t}_{(N+1)J+nJ+j} = V_n^*(y_j) \tag{10.4.26b}$$

for $n = 1, ..., N,\ j = 1, ..., J$.

Turning back to the matrix $\mathbf{S}$, rows $(nJ+1)$ and $(nJ+J)$ correspond to the boundary conditions for U_n (10.4.21), whilst rows $(J(N+1)+nJ+1)$ and $(J(N+1)nJ+J)$ correspond to the boundary conditions for U_n^* (10.4.23). The equations (10.4.20) and (10.4.22) are described in the intermediate rows $(nJ+j)$ and $(J(N+1)+nJ+j)$ respectively. Finally, entries in the $(nJ+j)$ and $(J(N+1)+nJ+j)$ columns correspond to coefficients of $U_n(y_j)$ and $U_n^*(y_j)$ in the appropriate equation or boundary condition.

With $\mathbf{S}$ and $\mathbf{t}$ defined, we may now solve for $\mathbf{u}$ using an in-built MATLAB solver.

Once we have the solution for the streak, we can calculate $\lambda(z)$ using (10.2.76), which we recall is given by

$$\lambda(z) = \left.\frac{\partial u_v}{\partial y}\right|_{y=-1}. \tag{10.4.27}$$

Linking the roll/streak and wave flows, this key equation yields

$$\lambda(z) = 1 + \tilde{U_0}'(-1) + \sum_{n=1}^{N} U_n'(-1)\mathrm{e}^{\mathrm{i}nz} + \sum_{n=1}^{N} U_n^{*\prime}(-1)\mathrm{e}^{-\mathrm{i}nz}. \tag{10.4.28}$$

10.4.2 Solving the pressure wave equation

In this section, we discuss how to determine α_0 and c_0 such that the pressure wave equation (10.2.74) admits an even, 2π periodic solution. We restate the equation governing the wave pressure, along with the associated boundary conditions, for ease. Having defined

$$g(s) = \mathrm{i}^{5/3}\frac{\mathrm{Ai}'(-\mathrm{i}^{1/3}s)}{\kappa(-\mathrm{i}^{1/3}s)}, \qquad \mathscr{F}(s) = \frac{3}{2} + \frac{-\mathrm{i}^{1/3}s}{2\mathrm{Ai}(-\mathrm{i}^{1/3}s)}\left(-\mathrm{i}^{1/3}s\kappa(-\mathrm{i}^{1/3}s) + \mathrm{Ai}'(-\mathrm{i}^{1/3}s)\right), \tag{10.4.29}$$

we are to solve

$$\frac{\mathrm{d}^2 p_-}{\mathrm{d}z^2} - \frac{\mathrm{d}p_-}{\mathrm{d}z}\frac{\lambda'(z)}{\lambda(z)}\mathscr{F}(s) + p_-\left[-{\alpha_0}^2 + \frac{(\alpha_0\lambda(z))^{5/3}}{K_0 - \alpha_0{}^2 m_0}g(s)\right] = 0, \tag{10.4.30}$$

subject to the periodic boundary conditions

$$p_-(0) = p_-(2\pi), \qquad \left.\frac{\mathrm{d}p_-}{\mathrm{d}z}\right|_{z=0} = \left.\frac{\mathrm{d}p_-}{\mathrm{d}z}\right|_{z=2\pi}. \tag{10.4.31}$$

Since (10.4.30) is linear in $p_-(z)$, we impose that

$$p_-(0) = \delta \tag{10.4.32}$$

where δ is real, without loss of generality. Recall that we seek an even solution for $p_-(z)$, so that $p_-(z) = p_-(-z)$. Using the chain rule,

$$p_-'(z) = -p_-'(-z). \tag{10.4.33}$$

Evaluating this at $z = 0$ implies that we must have

$$p_-'(0) = 0. \tag{10.4.34}$$

Before demonstrating our numerical procedure, we reformulate our aims here: we seek α_0 and c_0 such that equation (10.4.30) admits a solution in the domain $0 \le z \le \pi$ with initial conditions (10.4.32) and (10.4.34), such that the constraint $p_-'(\pi) = 0$ is satisfied. We may then reflect this solution (about $z = \pi$) to obtain the continuous behaviour of the pressure from $z = \pi$ to $z = 2\pi$. Imposing this reflection about $z = \pi$ assures that the periodic boundary conditions (10.4.31) are satisfied and that the pressure is even about $z = 0$:

$$p_-(z) = p_-(2\pi + z) = p_-(\pi + (\pi + z)) = p_-(\pi - (\pi + z)) = p_-(-z), \tag{10.4.35}$$

where the first equality follows from the periodicity of p_-, and the third from the evenness of p_- about $z = \pi$.

Having posed our problem, we detail our numerical procedure. We begin by choosing an initial guess for α_0 and c_0. For small δ, an appropriate initial guess arises from solving the analytical small-δ equations (10.3.3) and (10.3.6) with $\beta = 1$. Over the domain $0 \leq z \leq \pi$, we then solve the pressure equation (10.4.30) with initial conditions

$$p_-(0) = \delta, \quad p_-'(0) = 0 \tag{10.4.36}$$

using a 4^{th} order Runge-Kutta method, which we describe shortly. Once we have a solution for p_-, we calculate the values

$$\Sigma_1(\alpha_0, c_0) = \text{Re}(p_-'(\pi)), \quad \Sigma_2(\alpha_0, c_0) = \text{Im}(p_-'(\pi)). \tag{10.4.37}$$

We repeat this procedure, iterating over α_0 and c_0 using the Newton-Raphson method until the values Σ_1 and Σ_2 are sufficiently close to zero so that we have achieved $p_-'(\pi) = 0$ to within some specified tolerance.

The Newton-Raphson method makes use of a Jacobian of derivatives. We do not describe the method here, but we provide an example of how we approximate these derivatives:

$$\frac{\partial \Sigma_1}{\partial \alpha_0}(\bar{\alpha}_0, \bar{c}_0) \approx \frac{\Sigma_1(\bar{\alpha}_0 + \Delta\alpha_0, \bar{c}_0) - \Sigma_1(\bar{\alpha}_0, \bar{c}_0)}{\Delta\alpha_0} \tag{10.4.38}$$

where $\Delta\alpha_0$ is a small perturbation to $\bar{\alpha}_0$.

We now briefly discuss how we solve (10.4.30) subject to (10.4.36). A second order differential equation for p_-, we introduce the substitution

$$r_1(z) = p_-(z), \qquad r_2(z) = p_-'(z) \tag{10.4.39}$$

to convert (10.4.30) into a system of two first order differential equations,

$$r_1'(z) = r_2(z), \qquad r_2'(z) = \frac{\lambda'(z)}{\lambda(z)}\mathscr{F}(s)\, r_2 - \left(-{\alpha_0}^2 + \frac{(\alpha_0\lambda(z))^{5/3}}{K_0 - {\alpha_0}^2 m_0} g(s)\right) r_1, \tag{10.4.40}$$

with initial conditions arising from (10.4.36)

$$r_1(0) = \delta, \quad r_2(0) = 0. \tag{10.4.41}$$

Discretising our spanwise domain $0 \leq z \leq \pi$ using M intervals of equal length, the distance between each point is given by

$$h = \frac{\pi}{M} \tag{10.4.42}$$

and we have

$$z_m = m \cdot h, \quad m = 0, ..., M. \tag{10.4.43}$$

We then use a 4^{th} order Runge-Kutta method to march $r_1(z)$ and $r_2(z)$ from $z = 0$ to $z = \pi$, according to the equations (10.4.40). This entails evaluating $\lambda(z)$ and $\lambda'(z)$ at the points $z = z_m$ and $z = z_m + \frac{h}{2}$. From our solution of the roll flow, we have $\lambda(z)$ in the form of a Fourier decomposition (10.4.28), and we are able to calculate the sum on the right hand side of (10.4.28) for various z.

It is also worth noting that s is dependent on $\lambda(z)$, with

$$s(z) = \frac{{\alpha_0}^{1/3} c_0}{\lambda(z)^{2/3}}. \tag{10.4.44}$$

Therefore $\mathscr{F}(s)$ and $g(s)$ must also be evaluated at the relevant spanwise locations. In order to do this, we formulate differential equations that govern $\mathscr{F}(s)$ and $g(s)$ (see appendix A). Defining

$$s_{\max} = \max_{m=0,..,M} s(z_m), \tag{10.4.45}$$

we solve these equations over the interval $0 \leq s \leq s_{\max}$ and interpolate the solutions to $s = s(z_m)$ and $s = s(z_m + \frac{h}{2})$.

Finally, to complete this section, we discuss how to obtain the forcing q. Once we have reflected the solutions r_1 and r_2 about $z = \pi$, we acquire solutions for the wave pressure and its derivative over the interval $0 \leq z \leq 2\pi$. We can then ascertain the values of q at the spanwise locations

$$z_m = m \cdot h \quad \text{for} \quad h = \frac{\pi}{M}, \quad m = 0, ..., 2M \tag{10.4.46}$$

by using the relation (10.2.42)

$$q = \frac{1}{{\alpha_0}^2 \lambda(z)^2} \left[{\alpha_0}^2 \frac{\mathrm{d}}{\mathrm{d}z} \left(p_- p_-^* \right) + \frac{\mathrm{d}}{\mathrm{d}z} \left(\frac{\mathrm{d}p_-}{\mathrm{d}z} \frac{\mathrm{d}p_-^*}{\mathrm{d}z} \right) \right]. \tag{10.4.47}$$

This forcing will be fed into our roll flow solver, which requires q to be in the form of a Fourier decomposition,

$$q = q_0 + \sum_{n=1}^{N} q_n \mathrm{e}^{\mathrm{i}nz} + \sum_{n=1}^{N} q_n^* \mathrm{e}^{-\mathrm{i}nz}. \tag{10.4.48}$$

To manipulate q into the appropriate form, we calculate the Fourier coefficients using

$$q_0 = \frac{1}{2\pi} \int_0^{2\pi} q(z) \mathrm{d}z, \quad q_n = \frac{1}{2\pi} \int_0^{2\pi} q(z) \mathrm{e}^{-\mathrm{i}nz} \mathrm{d}z. \tag{10.4.49}$$

We approximate these integrals using Simpson's rule. For example,

$$q_0 \approx \frac{h}{6\pi} \left[q(z_0) + q(z_{2M}) + 4 \sum_{j=1}^{M} q(z_{2j-1}) + 2 \sum_{j=1}^{M-1} q(z_{2j}) \right]. \tag{10.4.50}$$

The q_n are computed in a similar manner.

10.4.3 Numerical results

Having detailed each aspect of our numerical procedure, we now illustrate numerical solutions to the vortex-wave interaction equations (10.2.71)-(10.2.76). Our focus lies in investigating how the roll/streak flow is influenced by increasing the amplitude δ of the wave pressure $p_-(z)$, where we recall

$$p_-(0) = p_-(2\pi) = \delta. \tag{10.4.51}$$

For our numerical method, we use N harmonics in our Fourier decomposition of the vortex flow, where $N = 20$ unless otherwise stated. This was found to sufficiently resolve the solutions shown here. We find two families of solutions, each with different characteristics. We are able to categorise the solutions as emerging from either zero amplitude ($\delta = 0$) or finite amplitude (say, $\delta = \delta_e$). We will refer to these as Type I and Type II solutions respectively.

Consider a lower wall with the properties $K_0 = 1$ and $m_0 = 0.1$. In figure 10.4.1, we compare Type I solutions α_0 and c_0 from our numerical computations with the results from our small-δ expansion (Section 10.3) as δ increases. We see good agreement between the two approaches when δ is small. While the magnitudes of the maximum and minimum values of the shear $\lambda(z)$ and boundary forcing $q(z)$ increase considerably with increasing δ, they both broadly appear to retain their shape (figure 10.4.2). A similar trend occurs in the normal roll and streak flow: the magnitude of vortex flow has been greatly amplified, but the rolls and streak remain regularly spaced in the spanwise direction as δ increases to $\delta = 1.7$ (see figures 10.4.3 and 10.4.4). We remark that the roll flow is concentrated towards the lower flexible wall. We are unable to continue this solution of the vortex-wave interaction equations to larger values of δ for these particular wall properties. We do, however, find the existence of a Type II solution for these same wall properties. We will see shortly that, for certain values of δ, the Type I and Type II solutions co-exist.

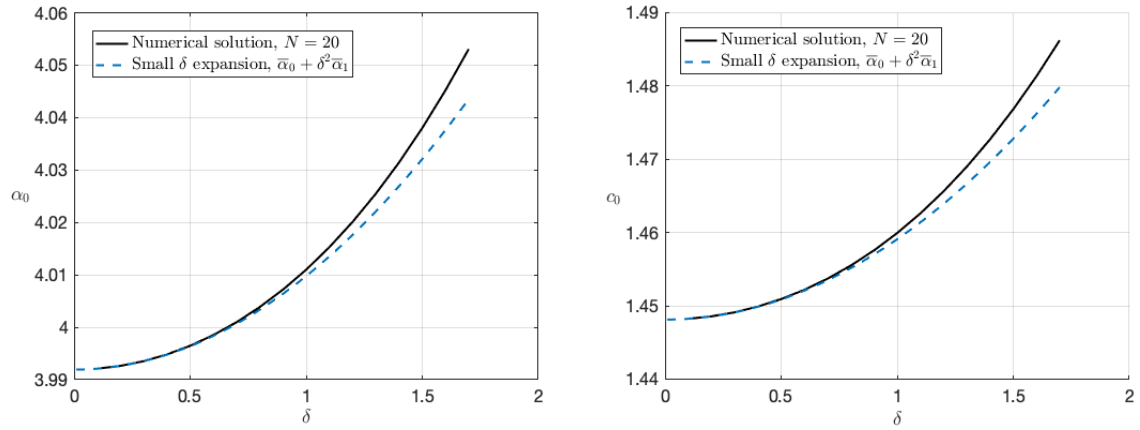

Figure 10.4.1: Comparison of Type I numerical and 'small-δ' solutions of α_0 (left) and c_0 (right) as δ varies. The cylinder properties are $K_0 = 1,\ m_0 = 0.1$. For the small-δ expansion, we take $p_0 = 1$ without loss of generality and $\beta = 1$.

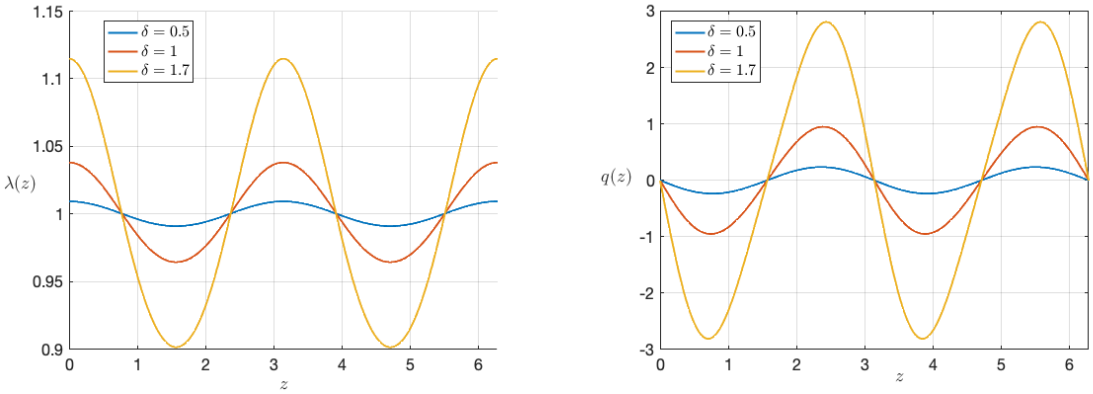

Figure 10.4.2: Type I solution. Plots of the (numerically obtained) shear $\lambda(z)$ (left) and $q(z)$ (right) for various δ. The cylinder properties are $K_0 = 1,\ m_0 = 0.1$.

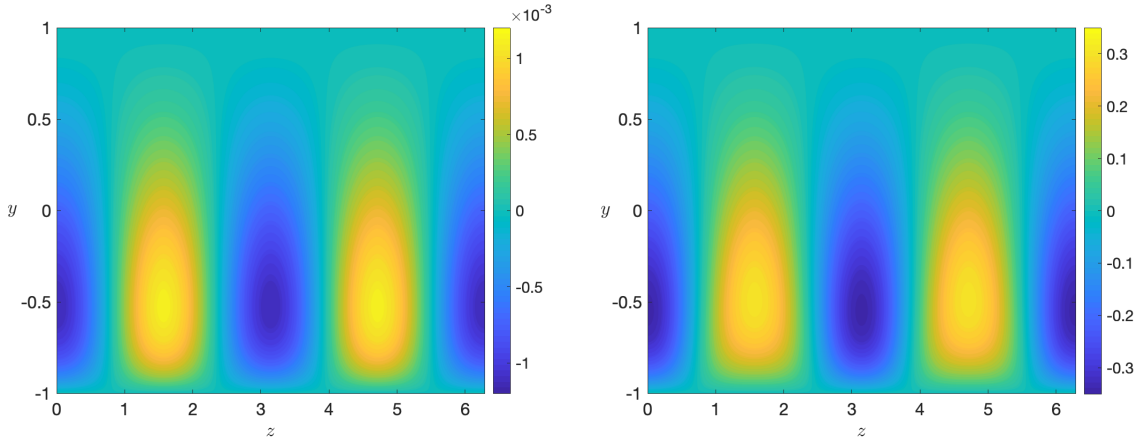

(a) $\delta = 0.1$ (b) $\delta = 1.7$

Figure 10.4.3: Type I solution. Plots of the (numerically obtained) normal roll flow for various δ. The cylinder properties are $K_0 = 1,\ m_0 = 0.1$. Note the colourmaps are different for each figure.

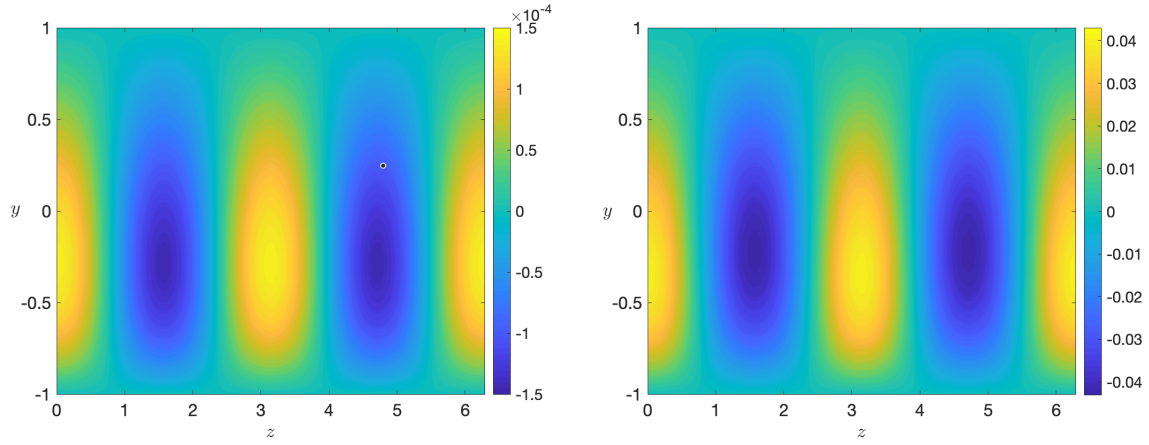

(a) $\delta = 0.1$ (b) $\delta = 1.7$

Figure 10.4.4: Type I solution. Plots of (numerically obtained) streak flow for various δ. Specifically, we plot $(U_v - y)$. The cylinder properties are $K_0 = 1,\ m_0 = 0.1$. Note the colourmaps are different for each figure.

Before continuing, it is worth remarking that the pressure equation (10.2.74) admits the solution

$$p_- \equiv \delta \quad \text{for} \quad 0 \leq z \leq 2\pi \tag{10.4.52}$$

with α_0 and c_0 satisfying

$$-{\alpha_0}^2 + \frac{{\alpha_0}^{5/3}}{K_0 - {\alpha_0}^2 m_0} g(s_0) = 0, \quad c_0 = \frac{s_0}{\alpha_0^{1/3}}, \quad s_0 \approx 2.2972, \tag{10.4.53}$$

where s_0 is such that

$$\operatorname{Im} g(s_0) = 0. \tag{10.4.54}$$

This solution, as described by (10.4.52) and (10.4.53), does not generate a roll/streak flow.

The Type II solution found for the cylinder properties $K_0 = 1$ and $m_0 = 0.1$ appears to bifurcate from the solution $p_- \equiv \delta$ (10.4.52) at finite amplitude ($\delta_e \approx 1.3$), and is shown in figure 10.4.5. The maximum magnitude of $\lambda(z)$ and $q(z)$ increase significantly as δ is increased (figure 10.4.6). This solution is vastly different to the Type I solution. We see that the Type II-associated $\lambda(z)$ and $q(z)$ have no even or odd symmetry about $z = \pi/2$ or $z = 3\pi/2$, and the peak of the Type II shear does not exceed the value 1.

We observe that the roll flow is concentrated towards the lower wall more so than the streak, as seen in figures 10.4.7 and 10.4.8. We also notice fewer rolls than in the Type I solution (see figure 10.4.3) for the same wall properties. Furthermore, the Type II rolls appear to extend closer to the lower flexible wall than the Type I rolls for the values of δ shown.

As δ increases, the Type II-associated $q'(z)$ becomes closer to zero at $z = \pi$ (figure 10.4.6). The roll centred about $z = \pi$ begins to 'split' into two distinct rolls that have increasing intensity (figure 10.4.7). In figure 10.4.8, we see the contours in the most negative region of the streak flow begin to pull apart and the spanwise variations in the streak become more intense.

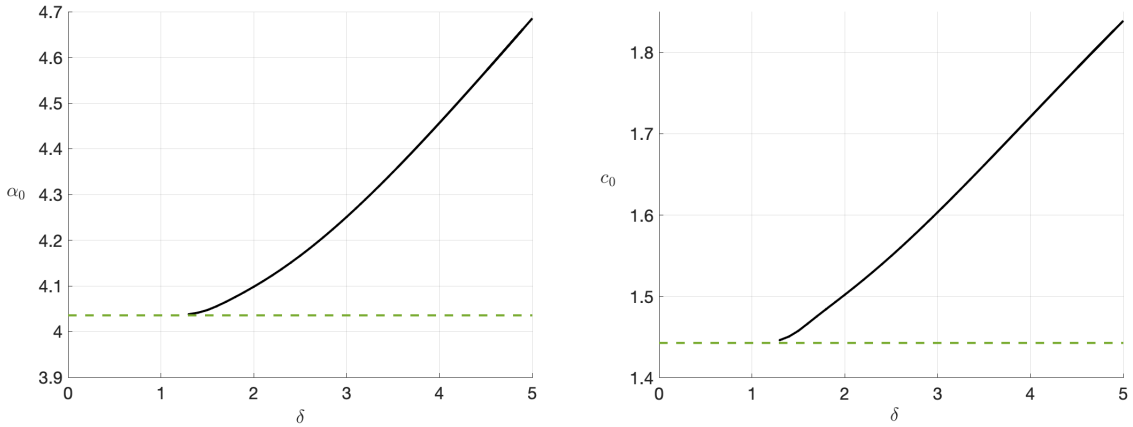

Figure 10.4.5: Type II solution. The black curves depict solutions α_0 and c_0 to the vortex-wave interaction equations when the cylinder properties are $K_0 = 1,\ m_0 = 0.1$. The green dashed line represents the constant pressure wave solution (10.4.52) with α_0 and c_0 as in (10.4.53).

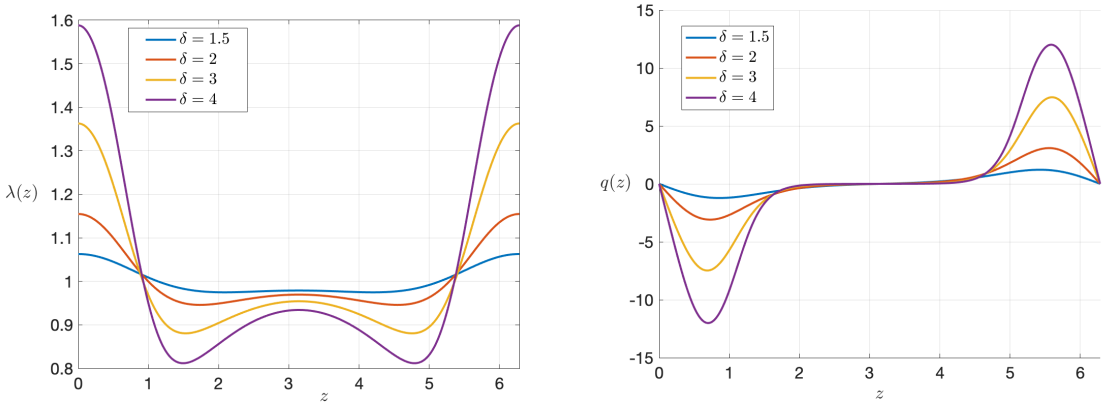

Figure 10.4.6: Type II solution. Plots of the (numerically obtained) shear $\lambda(z)$ (left) and $q(z)$ (right) for various δ. The cylinder properties are $K_0 = 1,\ m_0 = 0.1$.

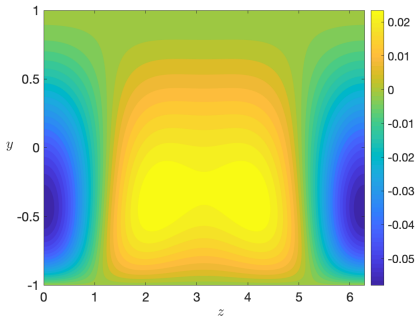

(a) $\delta = 1.3$

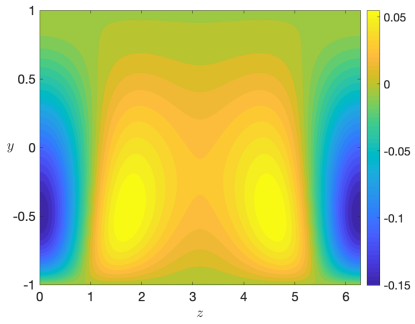

(b) $\delta = 1.5$

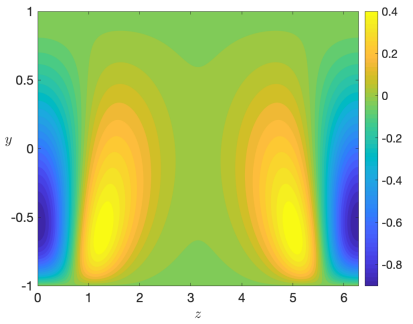

(c) $\delta = 3$

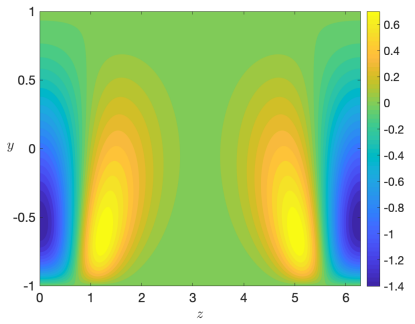

(d) $\delta = 4$

Figure 10.4.7: Type II solution. Plots of the (numerically obtained) normal roll flow for various δ. The cylinder properties are $K_0 = 1,\ m_0 = 0.1$.

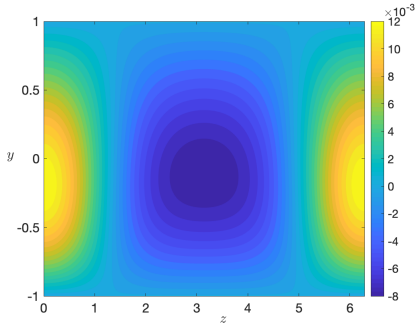

(a) $\delta = 1.3$

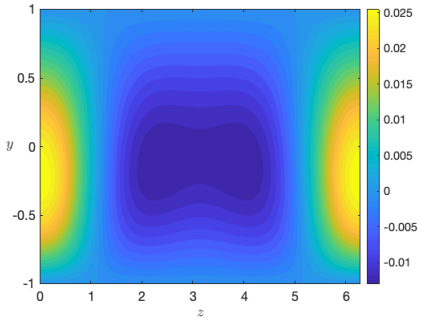

(b) $\delta = 1.5$

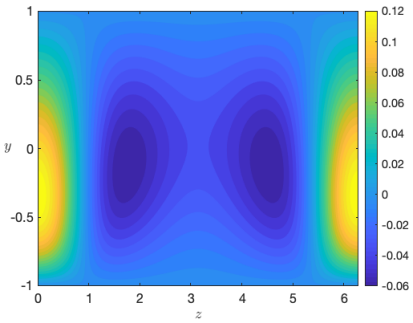

(c) $\delta = 3$

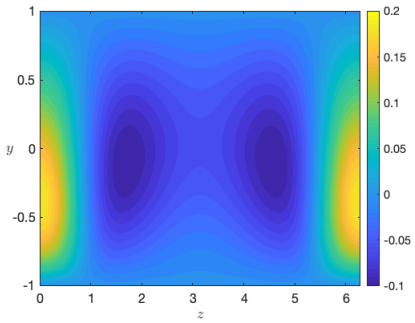

(d) $\delta = 4$

Figure 10.4.8: Type II solution. Plots of (numerically obtained) streak flow for various δ. Specifically, we plot $(U_v - y)$. The cylinder properties are $K_0 = 1,\ m_0 = 0.1$.

Increasing the mass of the flexible lower wall, we explore the vortex flow for a wall with the properties $K_0 = 1$ and $m_0 = 1$. Figures 10.4.9-10.4.12 depict Type I solutions to the vortex-wave interaction equations (10.2.71)-(10.2.76). These originate at zero amplitude, $\delta = 0$. We see good agreement with results from the 'small δ' expansion when δ is small. Unlike the case $m_0 = 0.1$, α_0 and c_0 now decrease with increasing δ.

As δ increases in figure 10.4.10, we see that the shape of $q(z)$ deviates from what is expected by our 'small-δ' expansion. This is particularly noticeable around $z = \pi$.

In figure 10.4.11, the spanwise variation of the roll flow increases near the lower wall as δ is increased; the negative roll centred at $z = \pi$ appears to change shape and to spread over a larger spanwise extent. In addition to this, an increase in δ results in the positive rolls becoming more concentrated towards the lower wall. By $\delta = 3$, the roll solution has become highly disturbed. Though the streak flow increases in intensity with increasing δ, its shape remains largely unaffected (see figure 10.4.12).

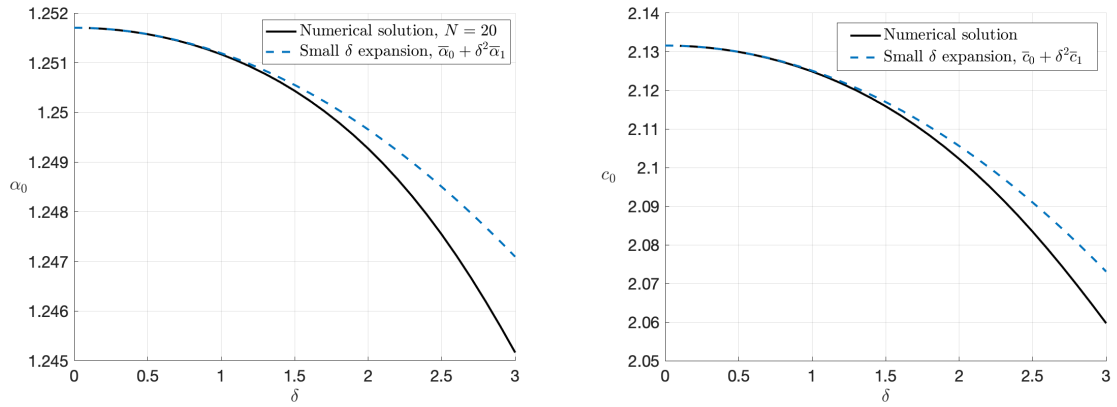

Figure 10.4.9: Comparison of Type I numerical and 'small-δ' solutions of α_0 (left) and c_0 (right) as δ varies. The cylinder properties are $K_0 = 1,\ m_0 = 1$.

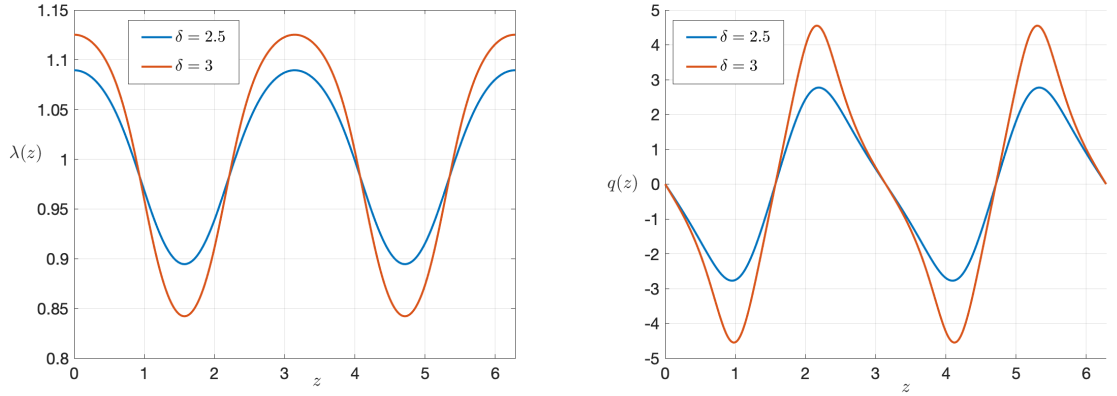

Figure 10.4.10: Type I solution. Plots of the (numerically obtained) shear $\lambda(z)$ (left) and $q(z)$ (right) for various δ. The cylinder properties are $K_0 = 1,\ m_0 = 1$. *We have used $N = 24$ harmonics for $\delta = 3$ so as to ensure adequate resolution.

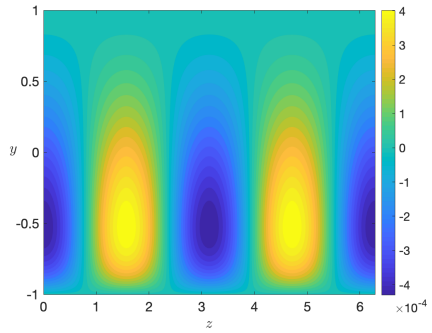

(a) $\delta = 0.1$

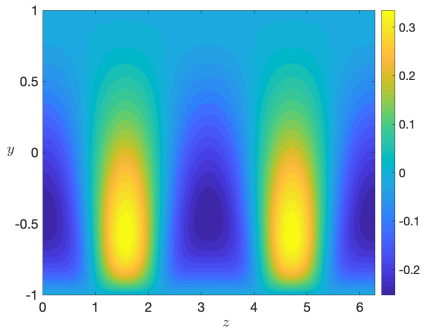

(b) $\delta = 2.5$

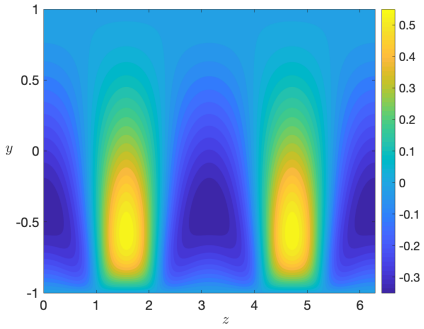

(c) $\delta = 3^*$

Figure 10.4.11: Type I solution. Plots of the (numerically obtained) normal roll flow for various δ. The cylinder properties are $K_0 = 1,\ m_0 = 1$. *We have used $N = 24$ harmonics to generate this figure so as to ensure adequate resolution.

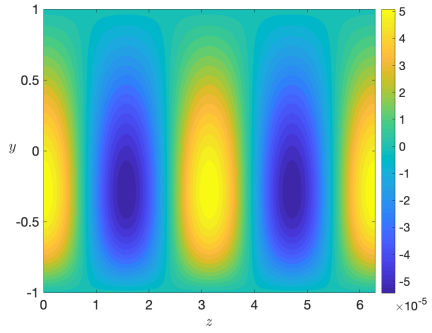

(a) $\delta = 0.1$

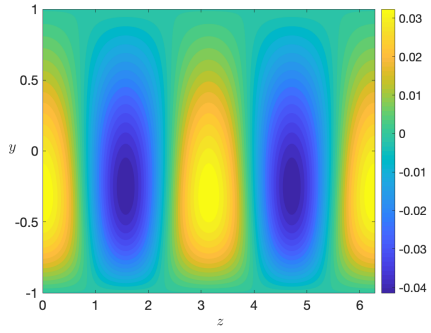

(b) $\delta = 2.5$

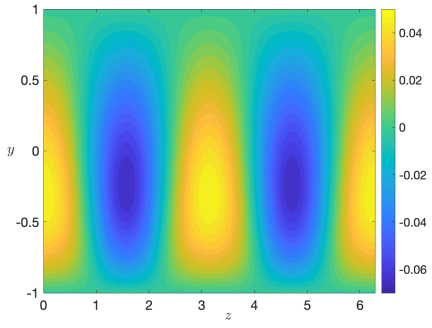

(c) $\delta = 3^*$

Figure 10.4.12: Type I solution. Plots of (numerically obtained) streak flow for various δ. Specifically, we plot $(U_v - y)$. The cylinder properties are $K_0 = 1,\ m_0 = 1$. *We have used $N = 24$ harmonics to generate this figure so as to ensure adequate resolution.

A Type II solution emerges at finite amplitude, with $\delta_e \approx 3.25$. It is thus evident that δ_e is dependent on the mass of the lower wall. Figure 10.4.13 shows that the shapes of $\lambda(z)$ and $q(z)$ at $\delta = 4.25$ are very dissimilar to those of the Type II solution corresponding to $m = 0.1$ (figure 10.4.6). In this case, the shear term $\lambda(z)$ has only one trough and no peaks. In addition, the forcing $q(z)$ has a steepening gradient near $z = \pi$ with an increase in δ. These differences are reflected in the vortex flow, which is illustrated in figures 10.4.14 and 10.4.15. In contrast with the Type II rolls when $m_0 = 0.1$, we do not see a roll 'splitting' into two distinct rolls here ($m_0 = 1$).

We consider again figures 10.4.14 and 10.4.15 for $K_0 = 1$ and $m_0 = 1$. As δ is increased to $\delta = 4.25$, the rolls are no longer equally spaced along the spanwise direction, with the positive roll becoming more localised around $z = \pi$. The effect of increasing δ is less prominent on the shape of the streak, but we note that its intensity has increased greatly and the negative region appears slightly more concentrated about $z = \pi$.

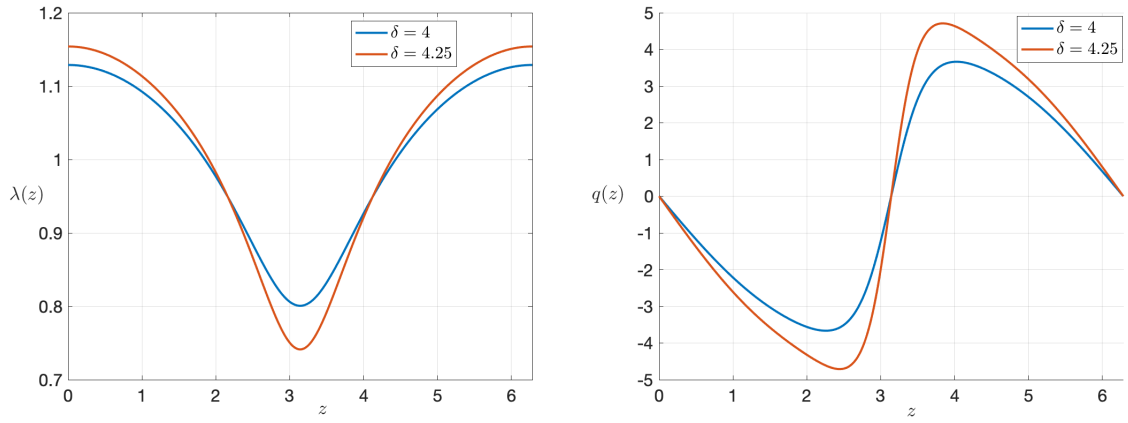

Figure 10.4.13: Type II solution. Plots of the (numerically obtained) shear $\lambda(z)$ (left) and $q(z)$ (right) for various δ. The cylinder properties are $K_0 = 1$, $m_0 = 1$.

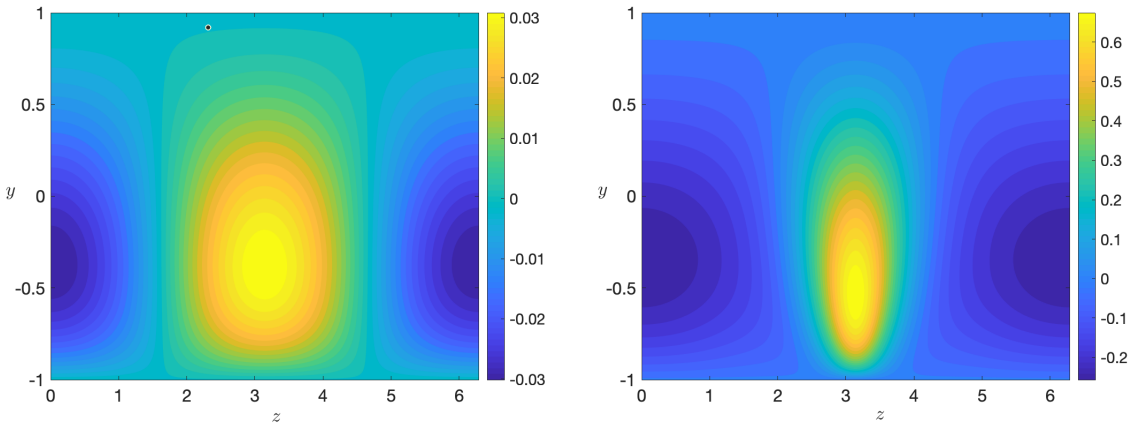

(a) $\delta = 3.25$ (b) $\delta = 4.25$

Figure 10.4.14: Type II solution. Plots of the (numerically obtained) normal roll flow for various δ. The cylinder properties are $K_0 = 1,\ m_0 = 1$. Note the colourmaps are different for each figure.

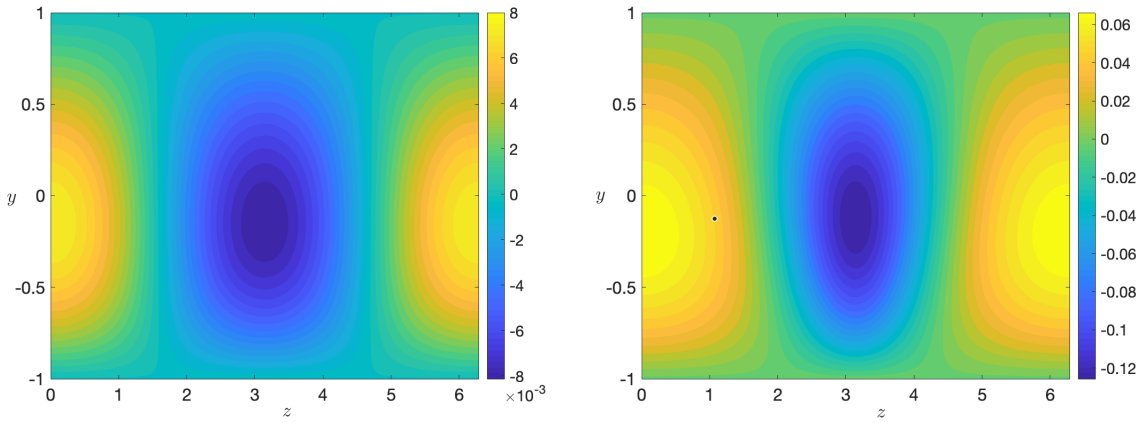

(a) $\delta = 3.25$ (b) $\delta = 4.25$

Figure 10.4.15: Type II solution. Plots of (numerically obtained) streak flow for various δ. Specifically, we plot $(U_v - y)$. The cylinder properties are $K_0 = 1,\ m_0 = 1$. Note the colourmaps are different for each figure.

In summary, we have seen the existence of highly nonlinear solutions to the vortex-wave interaction equations (10.2.71)-(10.2.76). Generally, we have found that the roll flow $V_v(y, z)$ is concentrated towards the lower flexible wall, and is more greatly affected by an increase in δ than the streak flow. We have seen two families of solutions. Type I solutions emerge from zero amplitude ($\delta = 0$) and behave as expected from our 'small-δ analytical results (Section 10.3) when δ is small. In contrast, Type II solutions emerge at finite amplitude ($\delta = \delta_e$). The Type II solution appears to be immensely affected by the mass of the flexible wall. The effect of varying the spring stiffness of the wall has not been studied here, though it is of interest.

10.5 Summary

We give a brief overview of this chapter, which focuses on vortex-wave interaction in planar Couette flow with a lower flexible wall. During the course of our analysis, we have seen that the nonlinear self-interaction of the wave in the lower viscous wall layer affects the core region via a boundary forcing for the roll flow. This roll flow drives a streak flow, and the spanwise variation in this streak flow influences the wave in the lower viscous layer.

The vortex-wave interaction equations (10.2.71)-(10.2.76) that govern this self-sustaining process are difficult to solve analytically. In order to make analytical progress, we assumed that the wave has small amplitude in the lower viscous wall layer and we subsequently found leading order solutions for the roll and streak flow. This work partly guided our numerical investigation of the equations (10.2.71)-(10.2.76), which illustrated the co-existence of two families of finite-amplitude solutions with different flow structures.

Chapter 11

Conclusions and Future Work

The focus of this thesis has broadly been concerned with two areas: the linear stability of annular Poiseuille-Couette flow (APCF) to axisymmetric disturbances when the inner cylinder is flexible (Chapters 2-9), and vortex-wave interaction in planar Couette flow with a lower flexible wall (Chapter 10).

In Chapter 2, we formulated the linear stability problem of APCF, modelling the flexible inner cylinder using a spring-backed plate model [55]. We subsequently formed the linearised disturbance equations, and the cylindrical version of the Orr-Sommerfeld problem on which our numerical computations in Chapter 3 hinged.

In Chapter 3, we presented neutral stability curves of compliant APCF for various inner cylinder properties, such as spring stiffness, mass, radius ratio and sliding velocity. For a stationary inner cylinder, we found that an increase in flexibility caused the 'flow-based instability' present in the rigid case to have a narrower band of unstable wavenumbers. Our numerical calculations also show the presence of a compliance-related mode that is nonexistent in the scenario of a rigid inner cylinder. The situation becomes more complicated with increasing sliding velocity, where we see the existence of further compliance-related instabilities. We remark, however, that this does not mean these instabilities do not exist for a stationary flexible cylinder. Our investigations also suggest that the critical Reynolds number of the flow in the limit $\alpha \to 0$ is unaffected by the cylinder mass.

Motivated by our numerical findings, in Chapter 4 we explored the circular Orr-Sommerfeld equation and determined the values of δ and V for which a compliance-related instability exists in the long-wave limit. Where this is the case, we were able to calculate the critical Reynolds number of the instability in this limit, which we analytically confirmed is independent of the cylinder mass.

In Chapter 5, we followed the methods of Yeo and Dowling [66], Yeo [67], Kumaran [68] and Shankar and Kumaran [69] to prove theorems pertaining to the inviscid linear stability of compliant APCF. We provided necessary conditions for instability, in addition to wavespeed bounds for unstable modes. As a result of our boundary conditions, our theorems are weaker than their classical counterparts for the planar flow over rigid boundaries.

In Chapters 6-8, we studied the linearised disturbance equations for asymptotically large Reynolds numbers. We discussed the effects of flexibility on the lower-branch, upper-branch and hybrid modes of the rigid case, which was studied by Walton [1]. In addition to these, we found the existence of structures that do not have rigid counterparts. Chapter 9 compares results from this analysis to our numerical computations at finite Reynolds numbers, and we generally found good agreement between the two approaches.

Finally, in Chapter 10, we moved away from the cylindrical geometry used thus far, and turned our attention to planar Couette flow with a flexible lower wall. The amplitude of a three-dimensional travelling wave perturbation was increased to a critical size so as to alter our basic flow to a streaky flow. We demonstrated that the nonlinear self-interaction of the wave forces a roll flow, which in turn drives a streak flow that supports the existence of neutrally stable waves. After deriving the vortex-wave interaction equations, we used a numerical approach to illustrate the co-existence of two finite-amplitude states with different flow structures.

There are many more avenues to explore with this research. For example, our research has been concerned with the linear stability of compliant APCF to axisymmetric disturbances. With Squire's theorem not applicable to our annular flow, it would be insightful to consider also stability with respect to non-axisymmetric disturbances.

Our spring-backed plate model for a flexible surface constrains motion due to flexibility to the normal direction. Shankar and Kumaran [81] have demonstrated that the inclusion of tangential motion can induce instability in wall modes that is not captured by a wall that moves only normally. Though the spring-backed plate model has been used extensively, more sophisticated models have also been used to describe wall deformability. These include linear and neo-Hookean viscoelastic solid models, the latter of which has been used by Gaurav and Shankar [82] and Patne and Shankar [83, 84] in the case of pressure-driven flow through a channel with deformable walls. It would be interesting to see the effect of using these models for APCF with a flexible inner cylinder.

We investigated the inviscid linear stability of compliant APCF as a means to understand the viscous problem at large Reynolds numbers. Synge [85] provides eigenvalue bounds for solutions to the Orr-Sommerfeld equation for planar flow over rigid boundaries. These results were extended by Joseph [86, 87], who also considered the stability of parallel flow in round pipes. More recently, Pavithra and Subbiah [88] found eigenvalue bounds for axial flows through an annular region between two cylinders. The formulation of these bounds for the case of a flexible inner cylinder would be a worthwhile pursuit.

The end of our thesis pertained to vortex-wave interaction in planar Couette flow with a lower flexible wall. In view of the work carried out in our earlier chapters, a natural next step would be to consider vortex-wave interaction in the cylindrical geometry of compliant APCF and to see whether the non-uniqueness found in the planar case is also present in the more complicated geometry.

Appendix A

Governing equations for $g(s)$ and $\mathscr{F}(s)$

Following the methods of Walton and Patel [89], we calculate values of the functions $g(s)$ and $\mathscr{F}(s)$ appearing the pressure wave equation (10.2.74) by forming and solving the differential equations described below.

The function $g(s)$ has been defined as

$$g(s) = \mathrm{i}^{5/3} \frac{\mathrm{Ai}'(-\mathrm{i}^{1/3}s)}{\kappa(-\mathrm{i}^{1/3}s)}, \tag{A.0.1}$$

where

$$\kappa(-\mathrm{i}^{1/3}s) = \int_{-\mathrm{i}^{1/3}s}^{\infty} \mathrm{Ai}\left(\xi_-\right) \mathrm{d}\xi_-. \tag{A.0.2}$$

In figure A.0.1 we illustrate how the real and imaginary parts of $g(s)$ vary with s.

Differentiating (A.0.1) using the chain and product rules, it can be shown with some manipulation that

$$\mathrm{i}^{5/3} g'(s) = \frac{\mathrm{Ai}(-\mathrm{i}^{1/3}s)}{\kappa(-\mathrm{i}^{1/3}s)} \left(s + g(s)\right). \tag{A.0.3}$$

Upon differentiation, this leads to a second order differential equation for $g(s)$ after further simplification:

$$g''(s) = -\mathrm{i}\left(s + g(s)\right) g(s) + \frac{2\left(g'(s)\right)^2 + g'(s)}{s + g(s)}. \tag{A.0.4}$$

Using (A.0.1) and (A.0.3), we are able to form two initial conditions subject to which (A.0.4) should be solved.

Noting that

$$\kappa(0) = \int_0^{\infty} \mathrm{Ai}(\xi)\mathrm{d}\xi = \frac{1}{3}, \tag{A.0.5}$$

we find

$$g(0) = -\frac{3\mathrm{Ai}'(0)}{\mathrm{i}^{1/3}}, \qquad g'(0) = 9\ \mathrm{Ai}'(0)\ \mathrm{Ai}(0). \tag{A.0.6a}$$

The equation (A.0.1) can be solved subject to (A.0.6) using, for example, a Runge-Kutta method.

In some parts of this thesis, we have calculated $g(s)$ by direct integration of κ (A.0.2) using MATLAB's *vpaintegral* function.

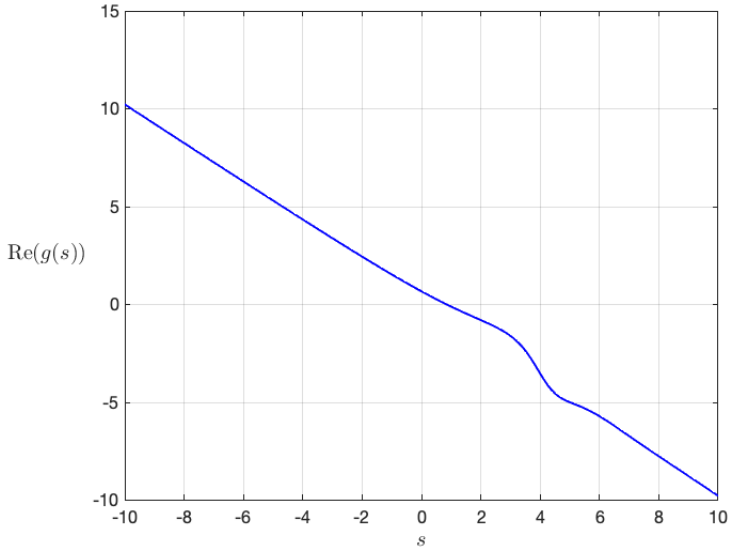

(a) Plot of $\mathrm{Re}(g(s))$ against s

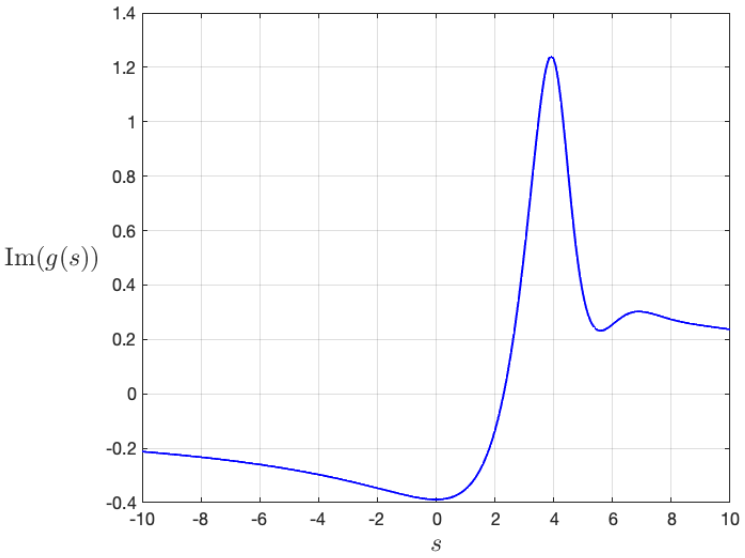

(b) Plot of $\mathrm{Im}(g(s))$ against s

Figure A.0.1: Illustration of $\mathrm{Re}(g(s))$ and $\mathrm{Im}(g(s))$ against s. For these figures, $g(s)$ was calculated by direct integration of κ (A.0.2) using MATLAB's *vpaintegral* function.

Now we consider the function $\mathscr{F}(s)$,

$$\mathscr{F}(s) = \frac{3}{2} + \frac{-\mathrm{i}^{1/3}s}{2\mathrm{Ai}(-\mathrm{i}^{1/3}s)}\left(-\mathrm{i}^{1/3}s\kappa(-\mathrm{i}^{1/3}s) + \mathrm{Ai}'(-\mathrm{i}^{1/3}s)\right), \tag{A.0.7}$$

Following Walton and Patel [89], we introduce a function $h(s)$ such that

$$\mathscr{F}(s) = \frac{3}{2} + s\,h(s). \tag{A.0.8}$$

With differentiation and manipulation, it can be shown that $h(s)$ satisfies

$$h''(s) = 2h'(s)\left[\frac{s\,h'(s) - h(s)}{s\,h(s) + 1/2}\right] + \mathrm{i}\left(\frac{1}{2} + s\,h(s)\right) \tag{A.0.9}$$

subject to

$$h(0) = \frac{-\mathrm{i}^{1/3}\mathrm{Ai}'(0)}{2\mathrm{Ai}(0)}, \qquad h'(0) = \frac{\mathrm{i}^{2/3}}{2}\left[\frac{1}{3\mathrm{Ai}(0)} - \left(\frac{\mathrm{Ai}'(0)}{\mathrm{Ai}(0)}\right)^2\right]. \tag{A.0.10}$$

This system can also be solved for $h(s)$ using a Runge-Kutta method, and the solution can then be used to find $\mathscr{F}(s)$ using (A.0.8).

Appendix B

Wavespeed expansion for a neutral disturbance in the long-wave limit

In Chapter 4, we sought a neutral-mode solution to the Orr-Sommerfeld problem (4.0.1 4.0.2) in the limit $\alpha \to 0$. In this appendix, we examine the second order term in the wavespeed expansion (4.0.9) and demonstrate that a neutral disturbance in the long-wave limit must have $c_1 = 0$.

For convenience, we restate the relevant Orr-Sommerfeld problem below:

$$(U_0 - c)\left(\phi'' - \frac{\phi'}{r} - \alpha^2\phi\right) + \phi\left(\frac{U_0'}{r} - U_0''\right) = \frac{1}{\mathrm{i}\alpha R}\left(\phi^{(4)} - \frac{2\phi^{(3)}}{r} + \left(\frac{3}{r^2} - 2\alpha^2\right)\phi'' + \left(\frac{2\alpha^2}{r} - \frac{3}{r^3}\right)\phi' + \alpha^4\phi\right), \quad \text{(B.0.1)}$$

is to be solved subject to the boundary conditions

$$\phi(1) = 0, \quad \text{(B.0.2a)}$$

$$\phi'(1) = 0, \quad \text{(B.0.2b)}$$

$$(c - V)\,\phi'(\delta) + U_0'(\delta)\,\phi(\delta) = 0, \quad \text{(B.0.2c)}$$

$$\left[\frac{2\mathrm{i}\alpha}{R}\left(\frac{3}{2}U_0'(\delta) + \frac{c - V}{\delta}\right) - \left(\frac{K}{R^2} - \alpha^2 c^2 m\right)\right]\phi'(\delta) = \frac{\mathrm{i}U_0'(\delta)}{\alpha R}\left[\phi^{(3)}(\delta) - \frac{\phi''(\delta)}{\delta} + \frac{\phi'(\delta)}{\delta^2}\right], \quad \text{(B.0.2d)}$$

where V is chosen so that $U_0'(\delta) \neq 0$. Primes ($'$) denote differentiation with respect to r. The base flow U_0 (2.2.2) is given by

$$U_0(r) = 1 - r^2 + \frac{(V - 1 + \delta^2)}{\log\delta}\,\log r, \quad \delta \leq r \leq 1. \quad \text{(B.0.3)}$$

We recall that the eigenfunction ϕ has been normalised so that $\phi(\delta) = 1$. Following the expansions (4.0.4) and (4.0.9), we write

$$R = R_0 + \cdots, \qquad \phi = \phi_0 + \alpha R_0\, \phi_1 + \cdots, \qquad c = c_0 + \alpha c_1 + \cdots. \tag{B.0.4}$$

In Chapter 4, we determined that ϕ_0 and c_0 are given by (4.0.8) and (4.0.11) respectively. We then commented that we must have $c_1 = 0$, and used this assumption to determine ϕ_1 and R_0. Our goal here is to prove that c_1 is indeed zero.

Substitution of the expansions (B.0.4) into the kinematic boundary condition (B.0.2c) results in

$$(c_0 - V)\ \phi_1'(\delta) + c_1\phi_0'(\delta) + U_0'(\delta)\,\phi_1(\delta) = 0. \tag{B.0.5}$$

Taking the real part of (B.0.5) gives

$$(c_0 - V)\ \mathrm{Re}\{\phi_1'(\delta)\} + \mathrm{Re}\{c_1\}\phi_0'(\delta) + U_0'(\delta)\ \mathrm{Re}\{\phi_1(\delta)\} = 0, \tag{B.0.6}$$

where $\mathrm{Re}\{\cdot\}$ denotes the real part. If ϕ_1 is purely imaginary, equation (B.0.6) indicates that c_1 must have zero real part since $\phi_0'(\delta)$ is non-zero. With this in mind, we seek to understand the behaviour of ϕ_1.

Recalling that ϕ_1 is described by the inhomogenous differential equation given in (4.0.12), we write

$$\phi_1'''' - \frac{2}{r}\phi_1''' + \frac{3}{r^2}\phi_1'' - \frac{3}{r^3}\phi_1' = \mathrm{i}\,\overline{\mathcal{M}}(r) \tag{B.0.7}$$

where $\overline{\mathcal{M}}(r)$ is a purely real function given by

$$\overline{\mathcal{M}}(r) = (U_0 - c_0)\left(\phi_0'' - \frac{\phi_0'}{r}\right) + \left(\frac{U_0'}{r} - U_0''\right)\phi_0. \tag{B.0.8}$$

As a fourth order differential equation, (B.0.7) requires four boundary conditions. Upon substitution of the expansions (B.0.4) into the boundary conditions (B.0.2a), (B.0.2b) and (B.0.2d), we see that ϕ_1 must satisfy

$$\phi_1(1) = 0, \tag{B.0.9a}$$

$$\phi_1'(1) = 0, \tag{B.0.9b}$$

$$\mathrm{i}\frac{K}{R^2}\phi_0'(\delta) = U_0'(\delta)\left[\phi_1^{(3)}(\delta) - \frac{\phi_1''(\delta)}{\delta} + \frac{\phi_1'(\delta)}{\delta^2}\right]. \tag{B.0.9c}$$

We also impose the normalisation condition $\phi(\delta) = 1$, which gives the fourth condition

$$\phi_1(\delta) = 0. \tag{B.0.10}$$

Assuming ϕ_1 is a complex-valued function, we write

$$\phi_1 = \eta + \mathrm{i}\mu \tag{B.0.11}$$

for real-valued functions η and μ.

With the goal of determining η, we take the real part of (B.0.7) and see that η is governed by the equation

$$\eta'''' - \frac{2}{r}\eta''' + \frac{3}{r^2}\eta'' - \frac{3}{r^3}\eta' = 0. \tag{B.0.12}$$

The real parts of (B.0.9) and (B.0.10) give the boundary conditions

$$\eta(1) = 0, \quad \eta'(1) = 0, \quad \eta'''(\delta) - \frac{\eta''(\delta)}{\delta} + \frac{\eta'(\delta)}{\delta^2} = 0, \quad \eta(\delta) = 0. \tag{B.0.13}$$

Solving (B.0.12) subject to (B.0.12) leads to

$$\eta \equiv 0. \tag{B.0.14}$$

This demonstrates that ϕ_1 has no real part. Let us now investigate the wavespeed c_1. The kinematic condition (B.0.6) reveals that

$$\mathrm{Re}\{c_1\} = 0. \tag{B.0.15}$$

As we are seeking a description of a neutral mode disturbance, we must also have $\mathrm{Im}\{c\} = 0$ and hence $\mathrm{Im}\{c_1\} = 0$. Paired with equation (B.0.15), this indicates that we have $c_1 = 0$.

Bibliography

[1] Walton, A. G. Stability of circular Poiseuille–Couette flow to axisymmetric disturbances. Journal of Fluid Mechanics, 500:169–210, 2004.

[2] Rohatgi, A. Webplotdigitizer - Web Based Plot Digitizer: Version 4.6. URL https://automeris.io/WebPlotDigitizer, 2022.

[3] Drazin, P. G. and Reid, W. H. Hydrodynamic Stability. Cambridge Mathematical Library. Cambridge University Press, 2 edition, 2004.

[4] Schmid, P. J. and Henningson, D. S. Stability and transition in shear flows. Applied mathematical sciences ; 142. Springer, New York, 2000.

[5] Pope, S. B. Turbulent Flows. Cambridge University Press, 2000.

[6] Reynolds, O. An experimental investigation of the circumstances which determine whether the motion of water shall be direct or sinuous, and of the law of resistance in parallel channels. Philosophical Transactions of the Royal society of London, (174):935–982, 1883.

[7] Romanov, V. A. Stability of plane-parallel Couette flow. Functional analysis and its applications, 7(2):137–146, 1973.

[8] Tillmark, N. and Alfredsson, P. H. Experiments on transition in plane Couette flow. Journal of Fluid Mechanics, 235:89–102, 1992.

[9] Orszag, S. A. Accurate solution of the Orr–Sommerfeld stability equation. Journal of Fluid Mechanics, 50(4):689–703, 1971.

[10] Carlson, D. R., Widnall, S. E., and Peeters, M. F. A flow-visualization study of transition in plane Poiseuille flow. Journal of Fluid Mechanics, 121:487–505, 1982.

[11] Squire, H. B. On the stability for three-dimensional disturbances of viscous fluid flow between parallel walls. Proceedings of the Royal Society of London. Series A, Containing Papers of a Mathematical and Physical Character, 142(847):621–628, 1933.

[12] Rayleigh, Lord. On the stability, or instability, of certain fluid motions. Proceedings of the London Mathematical Society, 1(1):57–72, 1879.

[13] Howard, L. N. Note on a paper of John W. Miles. Journal of Fluid Mechanics, 10(4):509–512, 1961.

[14] Tollmien, W. Über die entstehung der turbulenz, Nachr. Ges. Wiss. Göttingen Math.-Phys. Kl II, 21, 1929.

[15] Lin, C. C. The Theory of Hydrodynamic Stability. Cambridge University Press, 1955.

[16] Stuart, J. T. Hydrodynamic stability. In Laminar boundary layers. (Ed. Rosenhead, L.), Oxford University Press, 1963.

[17] Reid, W. H. The stability of parallel flows. In Basic developments in fluid dynamics, volume 1. (Ed. Holt, M.). Academic Press New York, 1965.

[18] Benney, D. J. and Bergeron, R. F. A New Class of Nonlinear Waves in Parallel Flows. Studies in Applied Mathematics, 48:181–204, 1969.

[19] Davis, R. E. On the high Reynolds number flow over a wavy boundary. Journal of Fluid Mechanics, 36(2):337–346, 1969.

[20] Haberman, R. Critical Layers m Parallel Flows. Studies in Applied Mathematics, 51(2):139–161, 1972.

[21] Nagata, M. Three-dimensional finite-amplitude solutions in plane Couette flow: bifurcation from infinity. Journal of Fluid Mechanics, 217:519–527, 1990.

[22] Waleffe, F. Three-dimensional coherent states in plane shear flows. Physical Review Letters, 81(19):4140, 1998.

[23] Waleffe, F. Exact coherent structures in channel flow. Journal of Fluid Mechanics, 435:93–102, 2001.

[24] Waleffe, F. Proposal for a self-sustaining process in shear flows (Unpublished). Center for Turbulence Research manuscript, 1990.

[25] Waleffe, F., Kim, J., and Hamilton, J. M. On the origin of streaks in turbulent shear flows. In Turbulent Shear Flows 8, pages 37–49. Springer, 1993.

[26] Hamilton, J. M., Kim, J., and Waleffe, F. Regeneration mechanisms of near-wall turbulence structures. Journal of Fluid Mechanics, 287:317–348, 1995.

[27] Waleffe, F. On a self-sustaining process in shear flows. Physics of Fluids, 9(4):883–900, 1997.

[28] Faisst, H. and Eckhardt, B. Traveling Waves in Pipe Flow. Phys. Rev. Lett., 91:224502, Nov 2003.

[29] Wedin, H. and Kerswell, R. R. Exact coherent structures in pipe flow: travelling wave solutions. Journal of Fluid Mechanics, 508:333–371, 2004.

[30] Hall, P. and Smith, F. T. The nonlinear interaction of Tollmien-Schlichting waves and Taylor-Göertler vortices in curved channel flows. Proceedings of the Royal Society of London Series A, 417(1853):255–282, June 1988.

[31] Hall, P. and Smith, F. T. Nonlinear Tollmien-Schlichting/vortex interaction in boundary layers. European Journal of Mechanics B-fluids, 8:179–205, 1989.

[32] P. Hall and Smith, F. T. Near-planar TS waves and longitudinal vortices in channel flow: nonlinear interaction and focussing. In Instability and Transition, ICASE/ NASA LaRC Series, pages 5–39. Springer, 1990.

[33] Hall, P. and Smith, F. T. On strongly nonlinear vortex/wave interactions in boundary-layer transition. Journal of Fluid Mechanics, 227:641–666, 1991.

[34] Bennett, J., Hall, P., and Smith, F. T. The strong nonlinear interaction of Tollmien–Schlichting waves and Taylor–Görtler vortices in curved channel flow. Journal of Fluid Mechanics, 223:475–495, 1991.

[35] Smith, F. T. and Walton, A. G. Nonlinear interaction of near-planar TS waves and longitudinal vortices in boundary-layer transition. Mathematika, 36(2):262–289, 1989.

[36] Walton, A. G. and Smith, F. T. Properties of strongly nonlinear vortex/Tollmien–Schlichting-wave interactions. Journal of Fluid Mechanics, 244:649–676, 1992.

[37] Hall, P. and Sherwin, S. Streamwise vortices in shear flows: harbingers of transition and the skeleton of coherent structures. Journal of Fluid Mechanics, 661:178–205, 2010.

[38] Dempsey, L. J. and Walton, A. G. Vortex/Tollmien–Schlichting wave interaction states in the asymptotic suction boundary layer. The Quarterly Journal of Mechanics and Applied Mathematics, 70(3):187–213, 2017.

[39] Mott, J. E. and Joseph, D. D. Stability of parallel flow between concentric cylinders. The Physics of Fluids, 11(10):2065–2073, 1968.

[40] Mahadevan, R. and Lilley, G. M. The stability of axial flow between concentric cylinders to asymmetric disturbances. In In AGARD Laminar-Turbulent Transition 10 p (SEE N78-14316 05-34), 1977.

[41] Heaton, C. J. Linear instability of annular Poiseuille flow. Journal of Fluid Mechanics, 610:391–406, 2008.

[42] Potter, M. C. Stability of plane Couette–Poiseuille flow. Journal of Fluid Mechanics, 24(3):609–619, 1966.

[43] Hains, F. D. Stability of Plane Couette-Poiseuille Flow. The Physics of Fluids, 10(9):2079–2080, 1967.

[44] Reynolds, W. C. and Potter, M. C. Finite-amplitude instability of parallel shear flows. Journal of Fluid Mechanics, 27(3):465–492, 1967.

[45] Cowley, S. J. and Smith, F. T. On the stability of Poiseuille-Couette flow: a bifurcation from infinity. Journal of Fluid Mechanics, 156:83–100, 1985.

[46] Sadeghi, V. M. and Higgins, B. G. Stability of sliding Couette–Poiseuille flow in an annulus subject to axisymmetric and asymmetric disturbances. Physics of Fluids A: Fluid Dynamics, 3(9):2092–2104, 1991.

[47] Gittler, Ph. Stability of axial Poiseuille-Couette flow between concentric cylinders. Acta Mechanica, 101(1-4):1–13, 1993.

[48] Walton, A. G. The nonlinear instability of thread-annular flow at high Reynolds number. Journal of Fluid Mechanics, 477:227–257, 2003.

[49] Frei, Ch., Lüscher, P., and Wintermantel, E. Thread-annular flow in vertical pipes. Journal of Fluid Mechanics, 410:185–210, 2000.

[50] Max O Kramer. Boundary-layer stabilization by distributed damping. Journal of the Aerospace Sciences, 27(1):69–69, 1960.

[51] Benjamin, T. B. Effects of a flexible boundary on hydrodynamic stability. Journal of Fluid Mechanics, 9(4):513–532, 1960.

[52] Benjamin, T. B. The threefold classification of unstable disturbances in flexible surfaces bounding inviscid flows. Journal of Fluid Mechanics, 16(3):436–450, 1963.

[53] Landahl, M. T. On the stability of a laminar incompressible boundary layer over a flexible surface. Journal of Fluid Mechanics, 13(4):609–632, 1962.

[54] Carpenter, P. W. and Garrad, A. D. The hydrodynamic stability of flow over Kramer-type compliant surfaces. Part 1. Tollmien-Schlichting instabilities. Journal of Fluid Mechanics, 155:465–510, 1985.

[55] Carpenter, P. W. and Garrad, A. D. The hydrodynamic stability of flow over Kramer-type compliant surfaces. Part 2. Flow-induced surface instabilities. Journal of Fluid Mechanics, 170:199–232, 1986.

[56] Carpenter, P. W., Gaster, M., and Willis, G. J. K. A numerical investigation into boundary layer stability on compliant surfaces. Numerical Methods in Laminar and Turbulent Flow, pages 166–172, 1983.

[57] Davies, C. and Carpenter, P. W. Instabilities in a plane channel flow between compliant walls. Journal of Fluid Mechanics, 352:205–243, 1997.

[58] Nagata, M. and Cole, T. R. On the stability of plane Poiseuille flow between compliant boundaries. WIT Transactions on Modelling and Simulation, 22, 1999.

[59] Lebbal, S., Alizard, F., and Pier, B. Revisiting the linear instabilities of plane channel flow between compliant walls. Phys. Rev. Fluids, 7:023903, Feb 2022.

[60] Alexander, J. P., Kirk, T. L., and Papageorgiou, D. T. Stability of falling liquid films on flexible substrates. Journal of Fluid Mechanics, 900:A40, 2020.

[61] Gajjar, J. S. B. and Sibanda, P. The hydrodynamic stability of channel flow with compliant boundaries. Theoretical and computational fluid dynamics, 8(2):105–129, 1996.

[62] Kumaran, V., Fredrickson, G. H., and Pincus, P. A. Flow induced instability of the interface between a fluid and a gel at low reynolds number. Journal De Physique Ii, 4:893–911, 1994.

[63] Kumaran, V. Stability of the viscous flow of a fluid through a flexible tube. Journal of Fluid Mechanics, 294:259–281, 1995.

[64] Shankar, V. and Kumaran, V. Weakly nonlinear stability of viscous flow past a flexible surface. Journal of Fluid Mechanics, 434:337–354, 2001.

[65] Høiland, E. On two-dimensional perturbation of linear flow. Geofys. Publ. 18, 1953.

[66] Yeo, K. S. and Dowling, A. P. The stability of inviscid flows over passive compliant walls. Journal of Fluid Mechanics, 183:265–292, 1987.

[67] Yeo, K. S. Note on the inviscid stability of flow over a compliant wall. Journal of Fluid Mechanics, 279:165–168, 1994.

[68] Kumaran, V. Stability of an inviscid flow in a flexible tube. Journal of Fluid Mechanics, 320:1–18, 1996.

[69] Shankar, V. and Kumaran, V. Stability of fluid flow in a flexible tube to non-axisymmetric disturbances. Journal of Fluid Mechanics, 407:291–314, 2000.

[70] Hains, F. D. and Price, J. F. Effect of a flexible wall on the stability of Poiseuille flow. Physics of Fluids, 5(3):365–365, 1962.

[71] Green, C. H. and Ellen, C. H. The stability of plane Poiseuille flow between flexible walls. Journal of Fluid Mechanics, 51(2):403–416, 1972.

[72] Walton, A. G. The linear and nonlinear stability of thread-annular flow. Philosophical Transactions of the Royal Society A: Mathematical, Physical and Engineering Sciences, 363(1830):1223–1233, 2005.

[73] Drazin, P. G. and Howard, L. N. Hydrodynamic stability of parallel flow of inviscid fluid. In Advances in applied mechanics, volume 9, pages 1–89. Elsevier, 1966.

[74] Lin, C. C. On the stability of two-dimensional parallel flows. III. Stability in a viscous fluid. Quarterly of Applied Mathematics, 3(4):277–301, 1946.

[75] Cowley, S. J. and Wu, X. Asymptotic approaches to transition modelling. Progress in Transition Modelling, 1994.

[76] Abramowitz, M. and Stegun, I. A. Handbook of mathematical functions with formulas, graphs, and mathematical tables, volume 55. US Government printing office, 1964.

[77] J. J. Healey. On the neutral curve of the flat-plate boundary layer: comparison between experiment, Orr–Sommerfeld theory and asymptotic theory. Journal of Fluid Mechanics, 288:59–73, 1995.

[78] Blackaby, N. D. Tollmien-Schlichting/vortex interactions in compressible boundary-layer flows. IMA Journal of Applied Mathematics, 53(2):191–214, 05 1994.

[79] Walton, A. G. and Smith, F. T. Properties of strongly nonlinear vortex/Tollmien–Schlichting-wave interactions. Journal of Fluid Mechanics, 244:649–676, 1992.

[80] Smith, F. T. Instability of flow through pipes of general cross-section, Part 1. Mathematika, 26(2):187–210, 1979.

[81] Shankar, V. and Kumaran, V. Stability of wall modes in fluid flow past a flexible surface. Physics of fluids, 14(7):2324–2338, 2002.

[82] Gaurav and Shankar, V. Stability of pressure-driven flow in a deformable neo-Hookean channel. Journal of Fluid Mechanics, 659:318–350, 2010.

[83] Patne, R. and Shankar, V. Stability of flow through deformable channels and tubes: implications of consistent formulation. Journal of Fluid Mechanics, 860:837–885, 2019.

[84] Patne, R. and Shankar, V. Stability of plane Poiseuille flow of a Bingham fluid through a deformable neo-Hookean channel. Phys. Rev. Fluids, 4:083302, Aug 2019.

[85] Synge, J. L. Hydrodynamical stability. Semicentenn. Publ. Amer. Math. Soc, 2:227–269, 1938.

[86] Joseph, D. D. Eigenvalue bounds for the Orr-Sommerfeld equation. Journal of Fluid Mechanics, 33(3):617–621, 1968.

[87] Joseph, D. D. Eigenvalue bounds for the Orr—Sommerfeld equation. Part 2. Journal of Fluid Mechanics, 36(4):721–734, 1969.

[88] Pavithra, P. and Subbiah, M. Eigenvalue bounds for the circular orr-sommerfeld problem of hydrodynamic stability. The Journal of Analysis, pages 1–22, 2022.

[89] Walton, A. G. and Patel, R. A. Singularity formation in the strongly nonlinear wide-vortex/Tollmien–Schlichting-wave interaction equations. Journal of Fluid Mechanics, 400:265–293, 1999.